

26



**AD-A232 425**

THE FLORIDA STATE UNIVERSITY  
COLLEGE OF ARTS AND SCIENCES

INITIALIZATION OF CLOUD AND RADIATION  
IN THE  
FLORIDA STATE UNIVERSITY  
GLOBAL SPECTRAL MODEL

DTIC  
ELECTE  
MAR 07 1991  
S D D

By

ALLAN MEREDITH WEINER

A Dissertation submitted to the  
Department of Meteorology  
in partial fulfillment of the  
requirements for the degree of  
Doctor of Philosophy

DISPATCHED  
MAR 10 1991

Degree Awarded:  
Fall Semester, 1990

**91 3 05 100**

REPORT DOCUMENTATION PAGE			
1. AGENCY USE ONLY (Leave blank)	2. REPORT DATE 1990	3. REPORT TYPE AND DATES COVERED <del>XXXXXX</del> /DISSERTATION	
4. TITLE AND SUBTITLE Initialization of Cloud and Radiation in the Florida State University Global Spectral Model		5. FUNDING NUMBERS	
6. AUTHOR(S) Allan Meredith Weiner			
7. PERFORMING ORGANIZATION NAME(S) AND ADDRESS(ES) AFIT Student Attending: Florida State University		8. PERFORMING ORGANIZATION REPORT NUMBER AFIT/CI/CIA-90-038D	
9. SPONSORING MONITORING AGENCY NAME(S) AND ADDRESS(ES) AFIT/CI Wright-Patterson AFB OH 45433-6583		10. SPONSORING MONITORING AGENCY REPORT NUMBER	
11. SUPPLEMENTARY NOTES			
12a. DISTRIBUTION AVAILABILITY STATEMENT Approved for Public Release IAW 190-1 Distributed Unlimited ERNEST A. HAYGOOD, 1st Lt, USAF Executive Officer		12b. DISTRIBUTION CODE	
13. ABSTRACT (Maximum 200 words)			
14. SUBJECT TERMS		15. NUMBER OF PAGES 237	16. PRICE CODE
17. SECURITY CLASSIFICATION OF REPORT	18. SECURITY CLASSIFICATION OF THIS PAGE	19. SECURITY CLASSIFICATION OF ABSTRACT	20. LIMITATION OF ABSTRACT

## GENERAL INSTRUCTIONS FOR COMPLETING SF 298

The Report Documentation Page (RDP) is used in announcing and cataloging reports. It is important that this information be consistent with the rest of the report, particularly the cover and title page. Instructions for filling in each block of the form follow. It is important to **stay within the lines to meet optical scanning requirements.**

### **Block 1. Agency Use Only (Leave Blank)**

**Block 2. Report Date.** Full publication date including day, month, and year, if available (e.g. 1 Jan 88). Must cite at least the year.

**Block 3. Type of Report and Dates Covered.** State whether report is interim, final, etc. If applicable, enter inclusive report dates (e.g. 10 Jun 87 - 30 Jun 88).

**Block 4. Title and Subtitle.** A title is taken from the part of the report that provides the most meaningful and complete information. When a report is prepared in more than one volume, repeat the primary title, add volume number, and include subtitle for the specific volume. On classified documents enter the title classification in parentheses.

**Block 5. Funding Numbers.** To include contract and grant numbers; may include program element number(s), project number(s), task number(s), and work unit number(s). Use the following labels:

<b>C</b> - Contract	<b>PR</b> - Project
<b>G</b> - Grant	<b>TA</b> - Task
<b>PE</b> - Program Element	<b>WU</b> - Work Unit Accession No.

**Block 6. Author(s).** Name(s) of person(s) responsible for writing the report, performing the research, or credited with the content of the report. If editor or compiler, this should follow the name(s).

**Block 7. Performing Organization Name(s) and Address(es).** Self-explanatory.

**Block 8. Performing Organization Report Number.** Enter the unique alphanumeric report number(s) assigned by the organization performing the report.

**Block 9. Sponsoring/Monitoring Agency Name(s) and Address(es).** Self-explanatory.

**Block 10. Sponsoring/Monitoring Agency Report Number.** (If known)

**Block 11. Supplementary Notes.** Enter information not included elsewhere such as: Prepared in cooperation with...; Trans. of ..., To be published in .... When a report is revised, include a statement whether the new report supersedes or supplements the older report.

**Block 12a. Distribution/Availability Statement.** Denote public availability or limitation. Cite any availability to the public. Enter additional limitations or special markings in all capitals (e.g. NOFORN, REL, ITAR)

**DOD** - See DoDD 5230.24, "Distribution Statements on Technical Documents."

**DOE** - See authorities

**NASA** - See Handbook NHB 2200.2.

**NTIS** - Leave blank.

### **Block 12b. Distribution Code.**

**DOD** - DOD - Leave blank

**DOE** - DOE - Enter DOE distribution categories from the Standard Distribution for Unclassified Scientific and Technical Reports

**NASA** - NASA - Leave blank

**NTIS** - NTIS - Leave blank.

**Block 13. Abstract.** Include a brief (Maximum 200 words) factual summary of the most significant information contained in the report.

**Block 14. Subject Terms.** Keywords or phrases identifying major subjects in the report.

**Block 15. Number of Pages.** Enter the total number of pages.

**Block 16. Price Code.** Enter appropriate price code (NTIS only).

**Blocks 17. - 19. Security Classifications.** Self-explanatory. Enter U.S. Security Classification in accordance with U.S. Security Regulations (i.e., UNCLASSIFIED). If form contains classified information, stamp classification on the top and bottom of the page.

**Block 20. Limitation of Abstract.** This block must be completed to assign a limitation to the abstract. Enter either UL (unlimited) or SAR (same as report). An entry in this block is necessary if the abstract is to be limited. If blank, the abstract is assumed to be unlimited.

THE FLORIDA STATE UNIVERSITY  
COLLEGE OF ARTS AND SCIENCES

INITIALIZATION OF CLOUD AND RADIATION  
IN THE  
FLORIDA STATE UNIVERSITY  
GLOBAL SPECTRAL MODEL

By  
ALLAN MEREDITH WEINER

A Dissertation submitted to the  
Department of Meteorology  
in partial fulfillment of the  
requirements for the degree of  
Doctor of Philosophy

Degree Awarded:  
Fall Semester, 1990

Accession For	
NTIS	□
DTIC	□
Unannounced	□
Justification	
By	
Distribution	
Availability Code	
Dist	Availability Code
A-1	



The members of the Committee approve the dissertation of Allan M. Weiner defended on September 20, 1990.

*T N Krishnamurti*

---

T.N. Krishnamurti  
Professor Directing Dissertation

*E. C. Young*

---

E.C. Young  
Outside Committee Member

*J.J. Stephens*

---

J.J. Stephens  
Committee Member

*S.A. Stage*

---

S.A. Stage  
Committee Member

*N.E. LaSeur*

---

N.E. LaSeur  
Committee Member

## Dedication

This dissertation is dedicated to my family, whose support has been unfaltering through a very rough four years. For my wife, there will be no more "just one more hour before I come home." My son will soon learn to throw the football farther and harder. My daughter will have one more guest at her tea parties. I love you all very much and we will soon be a family again.

## Acknowledgements

I wish to express my sincere gratitude to Dr. T. N. Krishnamurti for his moral support and guidance during my stay at Florida State University. I also wish to thank my committee, Drs. J. J. Stephens, S. A. Stage, N. E. LaSeur, and E. C. Young, for their suggestions regarding this dissertation. I have also benefited from the technical assistance of Drs. H. S. Bedi, Xue, and P. C. Joshi. I have received many hours of computer assistance from Ms. D. Oosterhof, Mr. G. Daughenbaugh, and Mr. K. Ingles. Ms. R. Raymond has assisted in drafting the figures of this dissertation. I also wish to express my sincere appreciation to my colleague, fellow student, and friend S. Moten, who has spent innumerable hours studying with me.

The sponsorship of my time for this research was made possible by the Air Force Institute of Technology. The computer time for this research was made possible by grants from the Air Force Office of Scientific Research (grant # 88-NCC-098) and the National Center for Atmospheric Research (project # 3511071). Computations for this research were carried out on the Cray 2 at the Air Force Weapons Laboratory Computing Center, Kirkland Air Force Base, New Mexico and at the National Center for Atmospheric Research, Boulder, Colorado. Additional Computing was done on the Florida State University Cyber 835.

## TABLE OF CONTENTS

DEDICATION	iii
ACKNOWLEDGEMENTS	iv
LIST OF TABLES	vii
LIST OF FIGURES	vii
ABSTRACT	xxi
CHAPTER I	
INTRODUCTION	1
CHAPTER II	
THE FSUGSM	6
CHAPTER III	
DEFINITION OF CLOUDS	36

CHAPTER IV	
INITIALIZATION METHODS	56
CHAPTER V	
INITIALIZATION RESULTS	67
CHAPTER VI	
THE LONGWAVE RADIATIVE TRANSFER FORMULATION	102
CHAPTER VII	
MOIST STATIC STABILITY	122
CHAPTER VIII	
SENSITIVITY OF RAINFALL TO MOISTURE INITIALIZATION	207
CHAPTER IX	
SUMMARY AND CONCLUSIONS	226
REFERENCES	233
BIOGRAPHICAL SKETCH	237

## LIST OF TABLES

Table 3.1 Critical relative humidities and vertical extent for different cloud types.	38
Table 3.2 Table of points not converging and albedo when initializing data.	44
Table 3.3 Decision algorithm for the space and time, cloud versus clear test.	55
Table 6.1 Water vapor absorption parameters.	108
Table 6.2 15 $\mu\text{m}$ band parameters.	113
Table 6.3 Ozone Coefficients.	115

## LIST OF FIGURES

Figure 2.1 Schematic diagram showing the vertical staggering of levels where prognostic variables are defined for the 12 – level FSUGSM. Here S denotes dewpoint depression and all other variables have their usual meteorological meaning.

14

Figure 3.1 Cloud amount as a function of relative humidity in the FSUGSM.

40

Figure 3.2a The emittance of clouds as a function of temperature and pressure thickness (10 mb through 50 mb).

45

Figure 3.2b The emittance of clouds as a function of temperature and pressure thickness (60 mb through 100 mb).

46

Figure 3.2c The emittance of clouds as a function of temperature and pressure thickness (110 mb through 150 mb).

47

Figure 3.3a ISCCP total cloud fraction for July 4, 1983, 12GMT (legend in figure 3.3g)

51

Figure 3.3b ISCCP 1000 mb through 800 mb cloud fraction for July 4, 1983, 12GMT (legend in figure 3.3g)	51
Figure 3.3c ISCCP 800 mb through 600 mb cloud fraction for July 4, 1983, 12GMT (legend in figure 3.3g)	52
Figure 3.3d ISCCP 600 mb through 400 mb cloud fraction for July 4, 1983, 12GMT (legend in figure 3.3g)	52
Figure 3.3e ISCCP 400 mb through 200 mb cloud fraction for July 4, 1983, 12GMT (legend in figure 3.3g)	53
Figure 3.3f ISCCP 200 mb through 000 mb cloud fraction for July 4, 1983, 12GMT (legend in figure 3.3g)	53
Figure 3.3g Cloud fraction legend for ISCCP data.	54
Figure 4.1 Demonstration of situation where the false position method is slow to converge.	58
Figure 4.2 Example of the original and resultant moisture profiles due to the single parameter initialization scheme.	61

Figure 4.3 Example of the original and resultant moisture profiles due to the single parameter initialization scheme. 62

Figure 4.4 Conversion of random numbers from a rectangular distribution (a) to a gaussian distribution (b). 64

Figure 5.1 Verification of the control and moisture initialization experiments as a function of time. 68

Figure 5.2a through f Satellite observed OLR for the period 12 GMT July 27, 1979 through 12 GMT August 1, 1979. (Shading indicates areas of OLR less than  $240 \text{ Wm}^{-2}$ ). 71

Figure 5.3a through f OLR of the control experiment for the period 12 GMT July 27, 1979 through 12 GMT August 1, 1979. (Shading indicates areas of OLR less than  $240 \text{ Wm}^{-2}$ ). 75

Figure 5.4a through f OLR of the moisture initialization experiment for the period 12 GMT July 27, 1979 through 12 GMT August 1, 1979. (Shading indicates areas of OLR less than  $240 \text{ Wm}^{-2}$ ). 78

Figure 5.5a through g High clouds of the control experiment for the period 12 GMT July 27, 1979 through 12 GMT August 1, 1979. (Cloud legend in figure 5.5g)

84

Figure 5.6a through f High clouds of the moisture initialization experiment for the period 12 GMT July 27, 1979 through 12 GMT August 1, 1979. (Cloud legend in figure 5.5g)

87

Figure 5.7a through f Middle clouds of the control experiment for the period 12 GMT July 27, 1979 through 12 GMT August 1, 1979. (Cloud legend in figure 5.5g)

89

Figure 5.8a through f Middle clouds of the moisture initialization experiment for the period 12 GMT July 27, 1979 through 12 GMT August 1, 1979. (Cloud legend in figure 5.5g)

91

Figure 5.9a through f Low clouds of the control experiment for the period 12 GMT July 27, 1979 through 12 GMT August 1, 1979. (Cloud legend in figure 5.5g)

93

Figure 5.10a through f Low clouds of the moisture initialization experiment for the period 12 GMT July 27, 1979 through 12 GMT August 1, 1979. (Cloud legend in figure 5.5g)

95

Figure 5.11 Histogram of cloud verification for the ISCCP initialization. The control experiment is in the foreground and the moisture initialization experiment is in the background. 98

Figure 5.12 Histogram of cloud verification for the ISCCP forecast. The control experiment is in the foreground and the moisture initialization experiment is in the background. 99

Figure 6.1 Column model results for a standard tropical atmosphere with the old and new radiation models 120

Figure 6.2 Column model results for a standard tropical atmosphere with the old and new radiation models. The moisture of the lower levels has been modified to produce clouds. 121

Figure 7.1a and b Cross section of Typhoon Hope showing the  $y/z$  plane, from  $117^\circ$  East to  $137^\circ$  East along the  $21^\circ$  North latitude. The contours are of equivalent potential temperature and the vectors are the  $u-\omega$  wind vectors. Chart a is the control experiment and chart b is the moisture initialization experiment. 143

Figure 7.2a and b Cross section of the Indian monsoon, showing the  $x/z$  plane, from  $0^\circ$  North to  $20^\circ$  North along the  $65^\circ$  East meridian. The contours are of equivalent

potential temperature and the vectors are the  $v-\omega$  wind vectors. Chart a is the control experiment and chart b is the moisture initialization experiment.

146

Figure 7.3a and b Cross section of the Atlantic Ocean ITCZ, showing the  $x/z$  plane, from  $0^\circ$  North to  $20^\circ$  North along the  $25^\circ$  West meridian. The contours are of equivalent potential temperature and the vectors are the  $v-\omega$  wind vectors. Chart a is the control experiment and chart b is the moisture initialization experiment.

149

Figure 7.4a and b Cross section of Typhoon Hope showing the  $y/z$  plane, from  $117^\circ$  East to  $137^\circ$  East along the  $21^\circ$  North latitude. Contours are of the moist static stability tendency (negative areas are shaded). Chart a is the control experiment and chart b is the moisture initialization experiment.

153

Figure 7.4c and d Cross section of Typhoon Hope showing the  $y/z$  plane, from  $117^\circ$  East to  $137^\circ$  East along the  $21^\circ$  North latitude. Contours are of the vertical differential of the apparent heat source (negative areas are shaded). Chart c is the control experiment and chart d is the moisture initialization experiment.

155

Figure 7.4e and f Cross section of Typhoon Hope showing the  $y/z$  plane, from  $117^\circ$  East to  $137^\circ$  East along the  $21^\circ$  North latitude. Contours are of the vertical differential

of the apparent moisture sink (negative areas are shaded). Chart e is the control experiment and chart f is the moisture initialization experiment.

157

Figure 7.4g and h Cross section of Typhoon Hope showing the  $y/z$  plane, from  $117^\circ$  East to  $137^\circ$  East along the  $21^\circ$  North latitude. Contours are of the vertical differential of the three dimensional advection of the moist static energy (negative areas are shaded). Chart g is the control experiment and chart h is the moisture initialization experiment.

159

Figure 7.5a and b Cross section of the Indian monsoon, showing the  $x/z$  plane, from  $0^\circ$  North to  $20^\circ$  North along the  $65^\circ$  East meridian. The contours are of moist static stability tendency (negative areas are shaded). Chart a is the control experiment and chart b is the moisture initialization experiment.

161

Figure 7.5c and d Cross section of the Indian monsoon, showing the  $x/z$  plane, from  $0^\circ$  North to  $20^\circ$  North along the  $65^\circ$  East meridian. The contours are of the vertical differential of the apparent heat source (negative areas are shaded). Chart c is the control experiment and chart d is the moisture initialization experiment.

163

Figure 7.5e and f Cross section of the Indian monsoon, showing the  $x/z$  plane, from  $0^\circ$  North to  $20^\circ$  North along the  $65^\circ$  East meridian. The contours are of the vertical

differential of the apparent moisture sink (negative areas are shaded). Chart e is the control experiment and chart f is the moisture initialization experiment.

165

Figure 7.5g and h Cross section of the Indian monsoon, showing the  $x/z$  plane, from  $0^\circ$  North to  $20^\circ$  North along the  $65^\circ$  East meridian. The contours are of the vertical differential of the three dimensional advection of the moist static energy (negative areas are shaded). Chart g is the control experiment and chart h is the moisture initialization experiment.

167

Figure 7.6a and b Cross section of the Atlantic Ocean ITCZ, showing the  $x/z$  plane, from  $0^\circ$  North to  $20^\circ$  North along the  $25^\circ$  West meridian. The contours are of moist static stability tendency (negative areas are shaded). Chart a is the control experiment and chart b is the moisture initialization experiment.

169

Figure 7.6c and d Cross section of the Atlantic Ocean ITCZ, showing the  $x/z$  plane, from  $0^\circ$  North to  $20^\circ$  North along the  $25^\circ$  West meridian. The contours are of the vertical differential of the apparent heat source (negative areas are shaded). Chart c is the control experiment and chart d is the moisture initialization experiment.

171

Figure 7.6e and f Cross section of the Atlantic Ocean ITCZ, showing the  $x/z$  plane,

from 0° North to 20° North along the 25° West meridian. The contours are of the vertical differential of the apparent moisture sink (negative areas are shaded). Chart e is the control experiment and chart f is the moisture initialization experiment.

173

Figure 7.6g and h Cross section of the Atlantic Ocean ITCZ, showing the x/z plane, from 0° North to 20° North along the 25° West meridian. The contours are of the three dimensional advection of the moist static energy (negative areas are shaded). Chart g is the control experiment and chart h is the moisture initialization experiment.

175

Figure 7.7a, b, and c The apparent heat source as function of pressure level for the old radiation experiment at points A, B, and C. (See text for a description of the points.)

180

Figure 7.8a, b, and c The components of the apparent heat source as function of pressure level for the old radiation experiment at points A, B, and C. (See text for a description of the points.)

183

Figure 7.9a, b, and c The apparent heat source as function of pressure level of the control experiment at points A, B, and C. (See text for a description of the points.)

186

Figure 7.10a, b, and c The components of the apparent heat source as function of pressure level for the control experiment at points A, B, and C. (See text for a description of the points.) 189

Figure 7.11a, b, and c The apparent heat source as function of pressure level of the moisture initialization experiment at points A, B, and C. (See text for a description of the points.) 192

Figure 7.12a, b, and c The components of the apparent heat source as function of pressure level for the moisture initialization experiment at points A, B, and C. (See text for a description of the points.) 195

Figure 7.13 Longwave radiational cooling and clouds as a function pressure for Point C of the moisture initialization experiment. 198

Figure 7.14a, b, and c Radiative destabilization as a function of time as parcels for the three experiments approach the ITCZ. Chart a is the old radiation experiment, chart b is the control experiment, and chart c is the moisture initialization experiment. 199

Figure 7.15a, b, and c The apparent moisture sink as function of pressure level for the old radiation experiment at points A, B, and C. (See text for a description of the points.) 200

Figure 7.16a, b, and c The apparent moisture sink as function of pressure level for the moisture initialization experiment at points A, B, and C. (See text for a description of the points.)

204

Figure 8.1 a, b, and c Cumulative tropical rainfall for the period July 27, 1979 through August 1, 1979. Chart a is from the analysis of Krishnamurti *et al.* (1983), chart b is from the FSUGSM control experiment, and chart c is from the FSUGSM moisture initialization experiment.

213

Figure 8.1 d, e, and f Cumulative tropical rainfall for the period August 1, 1979 through August 6, 1979. Chart a is from the analysis of Krishnamurti *et al.* (1983), chart b is from the FSUGSM control experiment, and chart c is from the FSUGSM moisture initialization experiment.

214

Figure 8.2 Histogram of average cumulative rainfall for selected tropical areas. The foreground is the accumulated rainfall from July 27, 1979 through August 1, 1979. The background is the accumulated rainfall from August 1, 1979 through August 6, 1979.

215

Figure 8.3 a, b, and c Cumulative tropical rainfall for the period July 27, 1979 through August 1, 1979 computed from the method of Janowiak and Arkin (1990). Chart a uses the satellite observed OLR, chart b uses the OLR of the FSUGSM control experiment, and chart c uses the OLR of the FSUGSM moisture initialization

experiment.

218

Figure 8.3 d, e, and f Cumulative tropical rainfall for the period August 1, 1979 through August 6, 1979 computed from the method of Janowiak and Arkin (1990). Chart a uses the satellite observed OLR, chart b uses the OLR of the FSUGSM control experiment, and chart c uses the OLR of the FSUGSM moisture initialization experiment.

219

Figure 8.4 Histogram of average cumulative rainfall for selected tropical areas. The foreground is the accumulated rainfall from July 27, 1979 through August 1, 1979. The background is the accumulated rainfall from August 1, 1979 through August 6, 1979.

220

Figure 8.5 a, b, and c Cumulative tropical rainfall for the period July 27, 1979 through August 1, 1979 computed from the method of Krishnamurti *et al.* (1983). Chart a uses the satellite observed OLR, chart b uses the OLR of the FSUGSM control experiment, and chart c uses the OLR of the FSUGSM moisture initialization experiment.

222

Figure 8.5 d, e, and f Cumulative tropical rainfall for the period August 1, 1979 through August 6, 1979 computed from the method of Krishnamurti *et al.* (1983). Chart a uses the satellite observed OLR, chart b uses the OLR of the FSUGSM control experiment, and chart c uses the OLR of the FSUGSM moisture initialization

experiment.

223

Figure 8.6 Histogram of average cumulative rainfall for selected tropical areas. The foreground is the accumulated rainfall from July 27, 1979 through August 1, 1979. The background is the accumulated rainfall from August 1, 1979 through August 6, 1979.

224

INITIALIZATION OF CLOUD AND RADIATION  
IN THE  
FLORIDA STATE UNIVERSITY  
GLOBAL SPECTRAL MODEL

Allan M. Weiner, Ph. D.  
Florida State University, 1990  
Major Professor: T. N. Krishnamurti, Ph. D.

Satellite observed Outgoing Longwave Radiation (OLR) is used to initialize the clouds and radiation of the Florida State University Global Spectral Model. A one-parameter method and two different six-parameter methods of initialization are formulated. The one-parameter method is shown to be the most efficient and produce the best results.

The effects of the cloud and radiation initialization on a five day forecast are presented. The initialization procedure produces a better forecast of OLR than the control experiment by such a large extent that the five day forecast of the initialization experiment has approximately the same verification score as the initial data of the control experiment. The cloud forecasts (high, middle, and low) of the initialization experiment prominently show the cloud signatures of the monsoon, the Pacific and Atlantic Ocean ITCZs, and the African rainbelt, but the cloud signatures of the control experiment are weak or nonexistent. The moist static stability budgets show that the initialization procedure had a large impact on the forecast after five days of integration by producing a monsoon and typhoon that were stronger and better defined.

Additionally, radiative destabilization forcing budgets of the initialization experiment were an order of magnitude greater than the control experiment for the Atlantic Ocean ITCZ. The effect of initialization on precipitation forecasts was also investigated. It was found that the model precipitation decreased after initialization. This is attributed to the model formulation of precipitation, and a new formulation is suggested for further investigation.

## CHAPTER I

### INTRODUCTION

#### 1.1 Overview

The use of satellite observed Outgoing Longwave Radiation (OLR) in conjunction with a global spectral model is a recent concept which has gained usefulness in the past few years. Much of this research has dealt with climatological averages. Ramanathan (1987) has shown how OLR is used in many models and cites examples of how it is used in global, zonal, and regional intercomparisons between the computed and observed OLR. Paltridge (1987) reviewed four different climate models and their ability to match the five year average of the satellite observed OLR for the June and December months. He found that the interannual RMS variability was of the order of  $10 \text{ Wm}^{-2}$ , and the model difference was one and a half to two times that amount. Borger and Vernekar (1988) compared their climate model OLR with a nine year average of satellite observed OLR (June 1974 through November 1983). The global mean error was  $20 \text{ Wm}^{-2}$  too low, with the largest error in the middle and high latitudes, and the smallest error in the tropics. Slingo and Slingo (1988) used satellite observed OLR to study the effect of cloud radiative forcing on model simulations. They found that this forcing warms the upper troposphere by 4 K and cools the lower stratosphere by more than 6 K. It also accelerated the subtropical jet of the Northern

Hemisphere by over  $7 \text{ ms}^{-1}$  in the zonal mean. Harshvardhan *et al.* (1989) have used the UCLA/GLAS GCM to compare model-averaged OLR to satellite observed OLR for July 1979 and January 1980. They found their OLR to be slightly smaller than the observed data. They also found that since high clouds (common in the tropics) tend to warm the atmosphere (absorbing radiation from Earth's surface, while emitting only weakly) and low clouds (common in middle and high latitudes) tend to cool the atmosphere (absorbing primarily on their lower side, while emitting strongly upward and downward), the zonally averaged cloud radiative forcing necessitates a poleward transport of heat by the atmosphere, in addition to that required by latent heating and clear sky radiative cooling. The warming due to cloud radiative forcing in the tropics has a maximum of  $50 \text{ Wm}^{-2}$ . In the higher latitudes the cooling due to cloud radiative forcing has a maximum magnitude of  $30 \text{ Wm}^{-2}$ . Morcrette (1989) used satellite observed OLR to evaluate several changes to his global spectral model. These changes included modifications to the cloud emissivity definition and liquid water content formulation, as well as improving the temperature and pressure dependence of the longwave radiation. He found that these changes produced better agreement with satellite observed OLR; an increased contrast in OLR fields showing marked minima ( $< 200 \text{ Wm}^{-2}$ ) over convective areas and maxima ( $> 300 \text{ Wm}^{-2}$ ) over clear sky areas, rather than smoother values ( $230 \text{ Wm}^{-2}$  to  $285 \text{ Wm}^{-2}$ ) throughout the tropics.

Medium range global spectral model forecasts have also been compared with satellite observed OLR. Slingo *et al.* (1988) used the satellite observed OLR to improve their global forecast model by using these fields to identify the areas where their global spectral model had deficiencies. Through recognition of weak areas in their radiation budget, they made improvements to shallow cumulus convection and revised the formulation of subgrid scale turbulent exchanges. Charlock *et al.* (1988)

have computed the autocorrelation of satellite observed OLR with their model data. By varying the cloud amount in the global spectral model, they found that both the clear and full sky data displayed a rapid decay in the temporal correlation. They concluded that the variations of the full sky OLR were forced mostly by clouds. Puri and Miller (1990) have used satellite observed OLR in the specification of convective heating for the diabatic initialization routine of their global spectral model. They deduced heating rates from OLR data and used them in their diabatic normal modes initialization to derive an initialized divergence field. The moisture field is also modified so that the heating rates will be consistent with those used in the initialization. Their results show that this initialization procedure has the potential to reduce spinup time in the forecast model.

### 1.2 Statement of the problem

Arpe *et al.* (1985) have studied the forecast skill response to the quality of the analysis. They found that the forecast quality is dependent on two factors: 1. the quality of the analysis, and 2. the ability of the forecast model. The dominance of these two factors is time dependent. The errors due to the forecast model grew linearly between days one and six, while the errors due to the analysis grew exponentially during this time period. Therefore, the dominant cause of error for the short range forecast (day zero through day two) and after day five is the analysis, and between days two and five the dominant cause of error is the forecast model. This research focuses on the modification of the analysis in order to increase the FSUGSM forecast skill. Specifically, it concentrates on the modification of the cloud and radiation fields using satellite observed OLR as a basis for the modification. The cloud and radiation fields are not directly analyzed, but are computed from the moisture, temperature, and

pressure fields. When the computed OLR does not match the satellite observed OLR, the moisture is perturbed until there is agreement. After the initialization process is completed for all gridpoints, the computed OLR is verified against the satellite observed OLR. The FSUGSM then produces forecast fields of OLR which are verified against satellite observed OLR valid for the same time period. The diagnosed cloud forecast is qualitatively, but not quantitatively verified because there are no definitive cloud data bases to use for verification. The forecast clouds are representative of many other forecast fields, since they are the end result of many other processes in the model. The clouds depend on available moisture for their diagnosis, but other fields such temperature, pressure, vertical velocity, and horizontal wind advection all contribute to the forecast of clouds. By examining the cloud forecasts, it can be determined if synoptic features such as the monsoon and the ITCZ's of the Atlantic and Pacific Oceans have been correctly integrated. Other fields that may yield important qualitative information are the moist static stability, the apparent heat source, the apparent moisture sink, and the precipitation field. Because the profile of the moist static stability is similar to the profile of the equivalent potential temperature (Madden and Robitaille, 1970), vertical cross sections of atmospheric equivalent potential temperature are examined to discern the effect of initialization on the moist static stability. If the initialization does enhance the tropical synoptic features, then there should be stronger vertical gradients of equivalent potential temperature and/or greater organization of these gradients so that the unstable tropical air may be advected into the systems for intensification. The moist static stability tendency shows the local rate of change. A change in the initial moisture analysis has the potential to create large changes in the model due to largescale heating and moisture changes, therefore, the apparent heat source and apparent moisture sink are examined to determine how they

are affected by the initialization procedure. The precipitation field should also be sensitive to the initialization process. The equations for precipitation in the FSUGSM show that it will decrease as the cloud forecast accuracy increases due to a simultaneous decrease in the available moisture supply for precipitation.

## CHAPTER II

### THE FSUGSM

#### 2.1 Introduction

The FSUGSM was developed from the spectral model of Daley (1979). It is a global spectral model based on the primitive equations. The vertical coordinates are defined on sigma surfaces. The horizontal coordinates are latitude and longitude on a gaussian grid in real space. The spectral space representation is a 42 wave, triangular truncation. Section 2.2 discusses the dynamical processes of the model. Section 2.3 discusses the model's physical processes.

#### 2.2 Model dynamics

##### 2.2.1 The primitive equations

The FSUGSM uses the six primitive equations to forecast atmospheric motions. These equations are:

1.) The vorticity equation:

$$\frac{\partial \zeta}{\partial t} = -\nabla \cdot (\zeta + f)\mathbf{V} - \mathbf{k} \cdot \nabla \times (RT\nabla q + \sigma \frac{\partial \mathbf{V}}{\partial \sigma} - \mathbf{F})$$

(2.1)

2.) The divergence equation:

$$\frac{\partial D}{\partial t} = \mathbf{k} \cdot \nabla \times (\zeta + f) - \nabla \cdot (RT \nabla q + \dot{\sigma} \frac{\partial \mathbf{V}}{\partial \sigma} - F) - \nabla^2 (\Phi + \frac{\mathbf{V} \cdot \mathbf{V}}{2}) \quad (2.3)$$

3.) The thermodynamic equation:

$$\frac{\partial T}{\partial t} = -\nabla \cdot \mathbf{V} T + TD + \dot{\sigma} \gamma - \frac{RT}{C_p} (D + \frac{\partial \dot{\sigma}}{\partial \sigma}) + H_T \quad (2.3)$$

4.) The continuity equation:

$$\frac{\partial q}{\partial t} = -D - \frac{\partial \dot{\sigma}}{\partial \sigma} - \mathbf{V} \cdot \nabla q \quad (2.4)$$

5.) The hydrostatic equation:

$$\sigma \frac{\partial \Phi}{\partial \sigma} = -RT \quad (2.5)$$

6.) The moisture equation:

$$\frac{\partial S}{\partial t} = -\nabla \cdot \mathbf{V} S + SD - \dot{\sigma} \frac{\partial S}{\partial \sigma} + H_T - H_M - \left[ \frac{RT}{C_p} - \frac{RT_d^2}{\epsilon L} \right] \left[ D + \frac{\partial \dot{\sigma}}{\partial \sigma} - \frac{\dot{\sigma}}{\sigma} \right] \quad (2.6)$$

where:

$f$  = Coriolis parameter

$\mathbf{V}$  = horizontal vector wind

$\zeta$  = vertical component of vorticity =  $\mathbf{k} \cdot \nabla \times \mathbf{V}$

$D$  = horizontal divergence =  $\nabla \cdot \mathbf{V}$

$T$  = absolute temperature

$q = \ln p_s$

$\gamma$  = static stability =  $\frac{RT}{C_p \sigma} - \frac{\partial T}{\partial \sigma}$

$\sigma$  = vertical coordinate =  $\frac{p}{p_s}$

$\dot{\sigma}$  = vertical motion =  $(\sigma - 1) \left( \int_0^1 D d\sigma + \int_0^1 V d\sigma \cdot \nabla q \right) +$   
 $\int_{\sigma}^1 D d\sigma + \int_{\sigma}^1 V d\sigma \cdot \nabla q$

$\Phi$  = geopotential height

$F$  = horizontal frictional force per unit mass

$H_T$  = diabatic heating

$R$  = gas constant for dry air

$C_p$  = specific heat of dry air at constant pressure

$T_d$  = dew point temperature

$S$  = dew point depression =  $T - T_d$

$\epsilon$  = ratio of the molecular weight of water vapor to the effective  
molecular weight of dry air = 0.622

$L$  = latent heat of vaporization of water or ice

$H_M$  = moisture sources and sinks

In spherical form, with the wind vector converted into its components ( $U = u \cos \theta/a$  and  $V = v \cos \theta/a$ , where  $a$  is the radius of the earth) these equations are expressed as:

$$\frac{\partial \zeta}{\partial t} = -\alpha(A, B) \quad (2.7)$$

$$\frac{\partial D}{\partial t} + \nabla^2 P = \alpha(B, -A) - a^2 \nabla^2 E \quad (2.8)$$

$$\sigma \frac{\partial^2 P}{\partial t \partial \sigma} + R \gamma^* W = R \alpha(UT', VT') - RB_T \quad (2.9)$$

$$\frac{\partial q}{\partial t} - W_S = - \int_0^1 G d\sigma \quad (2.10)$$

$$\sigma \frac{\partial \Phi}{\partial \sigma} = -RT \quad (2.11)$$

$$\frac{\partial S}{\partial t} = -\alpha(US, VS) + B_S \quad (2.12)$$

where:

$$\alpha(X, Y) = \text{operator on } X \text{ and } Y = \frac{1}{\cos^2 \theta} \left[ \frac{\partial X}{\partial \lambda} + \cos \theta \frac{\partial Y}{\partial \theta} \right]$$

$$T^* = \text{initial horizontal mean} = T - T' = \frac{1}{4\pi} \int_{-\frac{\pi}{2}}^{+\frac{\pi}{2}} \int_0^{2\pi} T(\lambda, \theta, \sigma, t) \cos \theta d\lambda d\theta,$$

at  $t=0$

$$\gamma^* = \text{horizontal mean} = \gamma - \gamma'$$

$$A = (\zeta + f)U + \dot{\sigma} \frac{\partial V}{\partial \sigma} + \frac{RT'}{a^2} \cos \theta \frac{\partial q}{\partial \theta} - \cos \theta \frac{F_\theta}{a} \quad (2.13)$$

$$B = (\zeta + f)V - \dot{\sigma} \frac{\partial U}{\partial \sigma} - \frac{RT'}{a^2} \frac{\partial q}{\partial \lambda} + \cos \theta \frac{F_\lambda}{a} \quad (2.14)$$

$$G = \frac{1}{\cos^2 \theta} \left[ U \frac{\partial q}{\partial \lambda} + V \frac{\partial q}{\partial \theta} \right] \quad (2.15)$$

$$E = \frac{U^2 + V^2}{2 \cos^2 \theta} \quad (2.16)$$

$$\dot{\sigma} = (\sigma - 1) \left( \int_0^1 G d\sigma + \int_0^1 D d\sigma \right) + \int_{\sigma}^1 G d\sigma + \int_{\sigma}^1 D d\sigma \quad (2.17)$$

$$B_T = TD + \gamma \dot{\sigma} - \frac{RT}{C_p} \left( \int_0^1 G d\sigma + \int_0^1 D d\sigma \right) + \frac{RT}{C_p} G + H_T + \gamma^* \left[ \int_{\sigma}^1 G d\sigma + \int_0^1 G d\sigma \right] \quad (2.18)$$

$$B_S = SD - \dot{\sigma} \frac{\partial S}{\partial \sigma} + \left[ \frac{RT}{C_p} - \frac{RT_d^2}{\epsilon L} \right] \frac{\dot{\sigma}}{\sigma} + G - \int_0^1 G d\sigma - \int_0^1 D d\sigma + H_T + H_M \quad (2.19)$$

$$P = \Phi + RT^* \quad (2.20)$$

$$W = \int_{\sigma}^1 D d\sigma - \int_0^1 D d\sigma \quad (2.21)$$

$$W_S = W(\sigma=1) = - \int_0^1 D d\sigma \quad (2.22)$$

To close this system of equations, one more equation is generated:

$$\frac{\partial W}{\partial \sigma} + D = 0 \quad (2.23)$$

### 2.2.2 Spectral form of the primitive equations

The FSUGSM uses the primitive equations of the previous section in their spectral form. The vorticity, for example, may be expanded as:

$$\zeta = \sum_{m=-J}^J \sum_{l=|m|}^{|m|+J} \zeta_1^m(\sigma, t) Y_1^m(\lambda, \theta) \quad (2.24)$$

where

$\zeta_1^m(\sigma, t)$  = complex expansion coefficients

$Y_1^m(\lambda, \theta)$  = spherical harmonics =  $X_1^m(\sin\theta)\exp(im\lambda)$

$X_1^m(\sin\theta)$  = associated Legendre functions of the first kind of order  $m$

$m$  = east-west (zonal) wavenumber

$l$  = degree of the associated Legendre function

$J$  = triangular wavenumber truncation

The spectral form of the primitive equations may now be written as:

$$\frac{\partial \zeta_1^m}{\partial t} = - \left\{ \alpha(A, B) \right\}_1^m \quad (2.25)$$

$$\frac{\partial D_1^m}{\partial t} - a^{-2}l(l+1)P_1^m = \left\{ \alpha(b, -a) - a^2 \nabla^2 E \right\}_1^m \quad (2.26)$$

$$\sigma \frac{\partial^2 P_1^m}{\partial \sigma \partial t} + R\sigma^* W_1^m = R \left\{ \alpha(UT', VT') - B_T \right\}_1^m \quad (2.27)$$

$$\frac{\partial W_1^m}{\partial t} + D_1^m = \left\{ B_w \right\}_1^m \quad (2.28)$$

$$\frac{\partial q_1^m}{\partial t} - W_{s1}^m = - \int_0^1 G_1^m d\sigma \quad (2.29)$$

$$\frac{\partial S_1^m}{\partial t} = \left\{ -\alpha(US, VS) + B_S \right\}_1^m \quad (2.30)$$

where

$$\left\{ F \right\}_1^m = \text{operator} = \frac{1}{2\pi} \int_{-\pi/2}^{\pi/2} \int_0^{2\pi} F(\lambda, \theta, \sigma, t) Y_c^m(\lambda, \theta) \cos \theta d\lambda d\theta \quad (2.31)$$

$$\left\{ a^2 \nabla^2 E \right\}_1^m = -\frac{l(l+1)}{2\pi} \int_{-\pi/2}^{\pi/2} \int_0^{2\pi} \frac{U^2 + V^2}{a^2} Y_c^m d\lambda d\theta \quad (2.32)$$

The nonlinear terms are calculated on a Gaussian grid using a transform method, that involves projecting individual components of the nonlinear terms from spectral space to grid space and multiplying them. These products are then transformed back to spectral space to obtain nonlinear terms which are consistent with the spectral truncation and are alias free. It can be shown that for T-42 truncation the optimal number of equally spaced points along a Gaussian latitude is 128 for a fourier transform and that the number of Gaussian latitudes for a Legendre transform is 64. The calculations are done latitude by latitude, and the contributions to the Gaussian integral are accumulated successively over all latitudes in the manner of Eliassen *et al.* (1970).

The vorticity and moisture equations are solved using an explicit leapfrog scheme. The other equations contain terms which generate high frequency waves and are solved using the semi-implicit formulation of Robert *et al.* (1972). Pasch (1983) has shown that this method damps gravity waves, making it possible to use a timestep of 1200 seconds.

The vertical discretization of the FSUGSM is shown in figure 2.1. The levels are staggered with respect to the model variables. The variables defined on the sigma levels are the vorticity, divergence, and geopotential, while the temperature and dew point are defined on the intermediate sigma levels. The value of sigma at the intermediate levels is given by  $(\sigma_n * \sigma_{n+1})^{0.5}$ . This staggering of the kinematic and thermodynamic variables allows a second order-finite difference approximation of the vertical derivatives.

## 2.3 Model physical processes

### 2.3.1 Surface fluxes

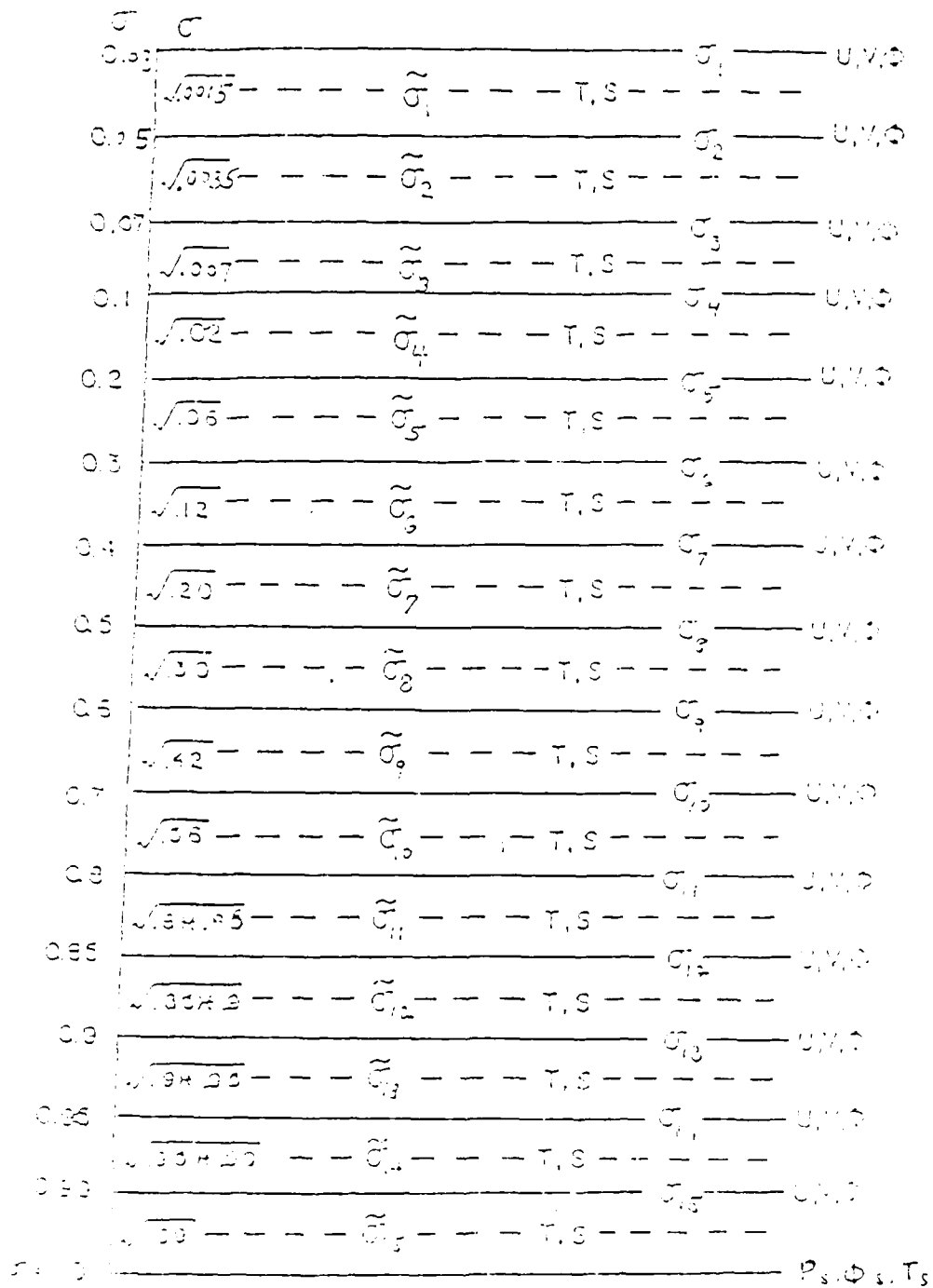
One form of boundary layer parameterization is based on the similarity theory of Monnin-Obukhov (1954). Louis (1979) has parameterized this theory for efficient use in a numerical model. The surface flux calculations of the FSUGSM are based on this work.

The surface fluxes of momentum, heat, and moisture are:

$$F_m = \rho u_*^2 \quad (2.33)$$

$$F_h = -\rho C_p u_* \theta_* \quad (2.34)$$

$$F_q = -\rho u_* q_* g_w \quad (2.35)$$



P AT ANY OF THESE LEVELS IS GIVEN BY  $\sigma * P_s$

Figure 2.1 Schematic diagram, showing the vertical staggering of levels where prognostic variables are defined for the 12 level FSUGSM. Here S denotes dew point depression and all other variables have their usual meteorological meaning.

where:

$F_m$  = momentum flux

$F_h$  = heat flux

$F_q$  = moisture flux

$u_*$  = friction velocity

$\theta_*$  = scale potential temperature

$q_*$  = scale moisture

$\rho$  = air density

$C_p$  = specific heat of dry air at constant pressure

$g_w$  = ground wetness

The surface fluxes may also be written in terms of the bulk aerodynamic formulae:

$$F_m = \rho C_m (\bar{u}_2 - \bar{u}_1)^2 \quad (2.36)$$

$$F_h = \rho C_p C_h (\bar{u}_2 - \bar{u}_1)^2 (\bar{\theta}_2 - \bar{\theta}_1) \quad (2.37)$$

$$F_q = \rho C_q (\bar{u}_2 - \bar{u}_1)^2 (\bar{q}_2 - \bar{q}_1) g_w \quad (2.38)$$

where the transfer coefficients are:

$$C_m = \frac{u_*^2}{(\bar{u}_2 - \bar{u}_1)^2} \quad (2.39)$$

$$C_h = \frac{u_* \theta_*}{(\bar{u}_2 - \bar{u}_1) (\bar{\theta}_2 - \bar{\theta}_1)} \quad (2.40)$$

$$C_q = \frac{u_* q_*}{(\bar{u}_2 - \bar{u}_1) (\bar{q}_2 - \bar{q}_1)} \quad (2.41)$$

Louis (1979) integrated the definitions of the friction velocity, the scale temperature, and the scale moisture as:

$$\frac{u_*^2}{(\bar{u}_2 - \bar{u}_1)^2} = \frac{k^2}{\left[ \ln(z/z_0) - \psi_m(z/L) + \psi_m(z_0/L) \right]^2} \quad (2.42)$$

$$\frac{u_* \theta_*}{(\bar{u}_2 - \bar{u}_1) (\bar{\theta}_2 - \bar{\theta}_1)} = \frac{-k}{R \left[ \ln(z/z_0) - \psi_h(z/L) + \psi_h(z_0/L) \right]}^* \quad (2.43)$$

$$\frac{k}{\left[ \ln(z/z_0) - \psi_m(z/L) + \psi_m(z_0/L) \right]}$$

$$\frac{u_* q_*}{(\bar{u}_2 - \bar{u}_1) (\bar{q}_2 - \bar{q}_1)} = \frac{-k}{R \left[ \ln(z/z_0) - \psi_q(z/L) + \psi_q(z_0/L) \right]}^* \quad (2.44)$$

$$\frac{k}{\left[ \ln(z/z_0) - \psi_m(z/L) + \psi_m(z_0/L) \right]}$$

where

$z_0$  = roughness length

$z$  = height of the lowest model level

$L$  = Monin–Obukhov scale length, given by Louis (1979) as:

$$= \frac{\bar{\theta}_u^2 \left[ \ln(z/z_0) - \psi_m(z/L) + \psi_h(z_0/L) \right]}{g\Delta\theta \left[ \ln(z/z_0) - \psi_m(z/L) + \psi_m(z_0/L) \right]^2}$$

$R$  = ratio of drag coefficient for momentum and heat in the neutral limit

$$= 0.74 \text{ (Businger } et al., 1971)$$

$$\psi_m(\zeta) = \ln \left[ \left[ \frac{1+x}{2} \right]^2 \left[ \frac{1+x^2}{2} \right] \right] - 2 \arctan x + \frac{\pi}{2}; \quad x = (1 - \gamma_m \zeta)^{0.25}$$

for unstable conditions

$$\psi_m(\zeta) = -\beta \zeta \text{ for stable conditions}$$

$$\psi_h(\zeta) = \ln \left[ \left[ \frac{1+y}{2} \right]^2 \right]; \quad y = (1 - \gamma_h \zeta)^{0.5} \text{ for unstable conditions}$$

$$\psi_h(\zeta) = -\beta \zeta/R \text{ for stable conditions}$$

$$\psi_q(\zeta) = \psi_h(\zeta)$$

The equations for the heat and moisture fluxes are similar from this point onward, and only the heat flux will be presented. The constants  $\gamma_m$ ,  $\gamma_h$ , and  $\beta$  are given by Businger *et al.* (1971) as 15., 9., and 4.7 respectively. The expression for the Monin–Obukhov scale height is an implicit relationship between the scale height and the bulk Richardson number for the layer:

$$Ri_b = \frac{gz\Delta\theta}{\bar{\theta}_u^2} \tag{2.45}$$

Louis (1979) solved these equations and fit them to analytical formulae. The formulae are:

$$\frac{u_*^2}{(u_1 - u_0)^2} = \frac{k^2}{\left[\ln \frac{z}{z_0}\right]^2} f_m(z/z_0, Ri_b) \quad (2.46)$$

$$\frac{u_* \theta_*}{(u_1 - u_0) (\theta_1 - \theta_0)} = \frac{1}{R} \frac{k^2}{\left[\ln \frac{z}{z_0}\right]^2} f_h(z/z_0, Ri_b) \quad (2.47)$$

where:

$$f = 1 - \frac{b Ri_b}{1 + c |Ri_b|^{0.5}} \quad (\text{for unstable conditions}) \quad (2.48)$$

$$f = \frac{1}{(1 + b' Ri_b)^2} \quad (\text{for stable conditions}) \quad (2.49)$$

$$c = C^* \frac{k^2}{\left[\ln \frac{z}{z_0}\right]^2} b (z/z_0)^{0.5} \quad (2.50)$$

The values of  $b$ ,  $b'$ , and  $C^*$  were chosen empirically by Louis (1979). The relation between  $b$  and  $b'$  was chosen so that the first derivative of  $f$  would be continuous between stable and unstable conditions:

$$b = 2b' = 9.4 \quad (2.51)$$

The value of  $C^*$  determines whether  $f$  is equal to  $f_m$  or  $f_h$  and  $f_q$ . A dimensional analysis of  $C^*$  yielded the values of 7.4 for momentum flux and 5.3 for heat and moisture fluxes.

Equations 2.46 and 2.47 may now be combined with equations 2.39 through

2.41 to yield the new transfer coefficients. For stable and neutral conditions ( $Ri_b \geq 0$ ):

$$C_m = \frac{k^2}{\left[\ln \frac{z}{z_0}\right]^2} \left[ 1 - \frac{Ri_b}{(1 + 4.6Ri_b)z} \right] \quad (2.52)$$

$$C_h = C_m \quad (2.53)$$

$$C_q = C_m \quad (2.54)$$

For unstable conditions ( $Ri_b < 0$ ):

$$C_m = \frac{k^2}{\left[\ln \frac{z}{z_0}\right]^2} \left[ 1 - \frac{9.4Ri_b}{1 + \left[ \frac{(7.4)k^2(9.4)(z/z_0)^{0.5}Ri_b^{0.5}}{[\ln(z/z_0)]^2} \right]} \right] \quad (2.55)$$

$$C_h = \frac{k^2}{\left[\ln \frac{z}{z_0}\right]^2} \left[ 1 - \frac{9.4Ri_b}{1 + \left[ \frac{(5.3)k^2(9.4)(z/z_0)^{0.5}Ri_b^{0.5}}{[\ln(z/z_0)]^2} \right]} \right] \quad (2.56)$$

$$C_q = \frac{k^2}{\left[\ln \frac{z}{z_0}\right]^2} \left[ 1 - \frac{9.4Ri_b}{1 + \left[ \frac{(5.3)k^2(9.4)(z/z_0)^{0.5}Ri_b^{0.5}}{[\ln(z/z_0)]^2} \right]} \right] \quad (2.57)$$

Equations 2.36 through 2.38 with equations 2.52 through 2.57 totally specify the fluxes of momentum, heat, and moisture. At the level  $z_0$ ,  $u_1$  is defined as zero and  $\theta_1$  is defined as the surface temperature. Manobianco (1988) lists the roughness length over land surfaces as:

$$z_0 = [0.15 + 0.2 \times 10^{-8} (2368.0 + 18.42h)^2] \quad (2.58)$$

where:

$h$  = height above sea level

The upper limit over land surfaces is 10 m. The roughness length over oceans is given by the formula of Charnock (1955):

$$z_0 = \frac{0.04u_*^2(z_0)}{g} \quad (2.59)$$

Since the friction velocity is a function of the roughness length, this equation is solved iteratively using equations 2.39, 2.55, and 2.59. Equation 2.39 is solved for the friction velocity using a first guess momentum transfer coefficient of 0.0011; this value of the friction velocity is used to calculate the roughness length in equation 2.59. The roughness length is then used to calculate a new momentum transfer coefficient in equation 2.55, which is used to start the iteration again at equation 2.39. The process is repeated until there is less than a 1% change in  $z_0$  over successive iterations. Manobianco (1988) states that three iterations are usually required for convergence. He has also found that a typical roughness length over the ocean is on the order of  $10^{-4}$ m. The variable  $z$  is taken as the first intermediate sigma level above the earth's surface. This corresponds to a  $\tilde{\sigma}_{12} = \sqrt{0.99}$ .

The ground wetness parameter is dependent upon whether the grid point is over land or ocean. Over oceans, it is set to unity. Over land, it is a function of the surface albedo:

$$g_w = 0.85 \{ 1 - \exp[-200(0.25 - \alpha)^2] \} \quad (2.60)$$

where:

$\alpha$  = surface albedo

The ground wetness parameter is constrained to lie within 0.0 and 0.85 (albedo larger than 25% or less than 10%). Pasch (1983) has found empirically that this formulation avoids excessively high moisture fluxes over tropical land areas.

### 2.3.2 Convection

#### 2.3.2.1 Deep cumulus convection and large scale condensation

The deep cumulus convection and large scale condensation of the FSUGSM are patterned after the work of Krishnamurti *et al.* (1983). The large scale supply of moisture is defined by:

$$I_1 = \frac{1}{g} \int_{pb}^{pt} \omega \frac{\partial q}{\partial p} dp \quad (2.61)$$

where:

$I_1$  = large scale supply of moisture

$\omega$  = large scale vertical velocity

$q$  = large scale specific humidity

$g$  = gravity

$pt$  = cloud top

$pb$  = cloud base

An additional source of moisture is now introduced to represent the nonmeasurable mesoscale (subgrid-scale) moisture supply,  $I\eta$ . The total moisture supply is then:

$$I = I_1(1 + \eta) \quad (2.62)$$

Following Kuo (1974), the rainfall and moistening rates may be expressed as:

$$R = I(1 - b) = I_1(1 + \eta)(1 - b) \quad (2.63)$$

$$M = Ib = I_1(1 + \eta)b \quad (2.64)$$

where:

$R$  = rainfall rate

$M$  = moistening rate

$b$  = moistening parameter

Krishnamurti *et al* (1983) write the supply of moisture required to produce a cloud as:

$$Q = Q_q + Q_\theta \quad (2.65)$$

where:

$$Q_q = \frac{1}{g} \int_{p_t}^{p_b} \frac{q_s - q}{\Delta\tau} dp \quad (2.66a)$$

$$Q_\theta = \frac{1}{g} \int_{p_t}^{p_b} \left[ \frac{C_p T(\theta_s - \theta)}{\Delta\tau} + \omega \frac{C_p T}{L\theta} \frac{\partial\theta}{\partial p} \right] dp \quad (2.66b)$$

The  $Q_q$  term is the moisture required to change an environmental humidity distribution from  $q$  to  $q_s$  in a time scale  $\Delta\tau$  (given by Krishnamurti *et al*, 1983, as 20 minutes). The first term of  $Q_\theta$  is the time required for establishment of a temperature  $T_s$  of a local moist adiabat in the same time scale. The second term of  $Q_\theta$  represents the moisture supply required to overcome the adiabatic cooling due to largescale ascent. It provides a smooth transition between the convective heating in the conditionally unstable atmosphere and the largescale condensation heating in the stable situation of saturated ascent.

Two additional proportionality factors are now defined:

$$a_\theta = \frac{I(1 - b)}{Q_\theta} = \frac{I_1(1 + \eta)(1 - b)}{Q_\theta} \quad (2.67)$$

$$a_q = \frac{Ib}{Q_q} = \frac{I_1(1 + \eta)b}{Q_q} \quad (2.68)$$

They may also be related to the convective heating and moistening rate as:

$$\frac{\partial\theta}{\partial t} = a_\theta \frac{(\theta_s - \theta)}{\Delta\tau} + \omega \frac{\partial\theta}{\partial p} \quad (2.69)$$

$$\frac{\partial q}{\partial t} = a_q \frac{(q_s - q)}{\Delta\tau} \quad (2.70)$$

All of the variables to determine the convective heating and moistening rates are known from the largescale, except  $\eta$  and  $b$  ( $a_\theta$  and  $a_q$  are determined directly from equations 2.67 and 2.68 once  $\eta$  and  $b$  are known). Krishnamurti *et al* (1983) determined these quantities in the following manner. Using the third phase of the GARP Atlantic Tropical Experiment, they regressed  $M/I_1$  and  $R/I_1$  against various

largescale variables such as vertical velocity, divergence, vertical shear of the horizontal wind, and vorticity. They found that the vertically averaged largescale vertical velocity and the 700 mb relative vorticity provided the best estimates. The regression equations used were:

$$\frac{M}{T_1} = a_1 \zeta_{700} + b_1 \bar{\omega} + c_1 \quad (2.71)$$

$$\frac{R}{T_1} = a_2 \zeta_{700} + b_2 \bar{\omega} + c_2 \quad (2.72)$$

The regression coefficients are time independent. Once determined, they may be used with the time dependent values of the vertically averaged vertical velocity and the 700 mb relative vorticity to produce different values of the mesoscale moisture source and moistening parameters. They are determined as:

$$b = \frac{a_1 \zeta + b_1 \bar{\omega} + c_1}{(a_1 + a_2) \zeta + (b_1 + b_2) \bar{\omega} + (c_1 + c_2)} \quad (2.73)$$

$$\eta = [(a_1 + a_2) \zeta + (b_1 + b_2) \bar{\omega} + (c_1 + c_2)] - 1 \quad (2.74)$$

### 2.3.2.2 Shallow cumulus convection

Shallow cumulus convection in the FSUGSM follows the scheme of Tiedtke (1984) who found that shallow cumulus convection is important to atmospheric flow. In the trade wind areas, shallow cumulus convection enhances the moisture supply to the atmosphere. As result of the enhanced moisture supply, the downstream diabatic heat sources and associated Hadley circulation are also enhanced. Through its effect on the Hadley circulation, shallow cumulus convection affects subtropical flow

(particularly the position of the Atlantic High).

For his shallow cumulus convection scheme, Tiedtke (1984) assumed that the net effect of convection could be attributed to the turbulent fluxes of heat and moisture:

$$\left[ \frac{\partial T}{\partial t} \right]_{\text{scc}} = \frac{1}{\bar{\rho} C_p} \frac{\partial H}{\partial z} \quad (2.74)$$

$$\left[ \frac{\partial \bar{q}}{\partial t} \right]_{\text{scc}} = \frac{1}{\bar{\rho}} \frac{\partial M}{\partial z} \quad (2.75)$$

where:

scc = denotes the effects due to shallow cumulus convection

$T$  = large scale temperature

$\bar{q}$  = large scale moisture

$\bar{\rho}$  = large scale density

$H$  = turbulent heat flux =  $C_p \bar{\rho} (p/p_0)^{\kappa} \frac{\partial \theta}{\partial z}$

$M$  = turbulent moisture flux =  $\bar{\rho} K_c \frac{\partial \bar{q}}{\partial z}$

$K_c$  = eddy diffusivity constant =  $10 \text{ ms}^{-1}$  in cloud;  $0 \text{ ms}^{-1}$  elsewhere

This parameterization scheme is used at points where the cloud base is below 700 mb and the air is conditionally unstable. The cloud top may not extend above 700 mb. This parameterization is a vertical diffusion scheme for the turbulent scale transport of heat and moisture by non-precipitating clouds.

### 2.3.3 Diffusion

#### 2.3.3.1 Horizontal diffusion

The horizontal diffusion in the FSUGSM follows the method of MacVean (1983). Spectral models, such as the FSUGSM, have an accumulation of energy near the truncation limit when performing non-linear integrations. This build up of energy can result in physically unrealistic solutions after a short integration time. Therefore, a diffusion scheme is incorporated to parameterize the effects of motion scales smaller than the truncation limit.

MacVean (1983) proposed a Laplacian type lateral diffusion of the form  $\kappa \nabla^4$  to dissipate the energy in the higher wavenumber components of vorticity, divergence, dewpoint depression, and temperature. The diffusion coefficient is expressed as a function of the e-folding diffusive decay time at total wavenumber  $n$  as:

$$\kappa = \{n(n + 1)a^{-2}\}^{-2} \tau(n)^{-1} \quad (2.76)$$

where:

$n$  = spectral wavenumber

$a$  = earth radius

$\tau(n)$  = time scale = (1 day)

The time scale of one day for the highest eight wavenumbers was found empirically by MacVean (1983). Using this formulation, the diffusion constant is equal to  $5.84 \text{ m}^4\text{s}^{-1}$ .

#### 2.3.3.2 Vertical diffusion

The vertical diffusion of the FSUGSM is extensively discussed by Manobianco

(1988). A summary of his discussion is presented here. The vertical eddy fluxes of momentum, heat, and moisture are parameterized as diffusive fluxes:

$$\frac{\partial \tau}{\partial t} = \frac{1}{\rho} \frac{\partial}{\partial z} \left[ \rho K \frac{\partial \tau}{\partial z} \right] \quad (2.77)$$

where:

$\tau = u, v, \theta, \text{ or } q$

$\rho = \text{density}$

$K = \text{diffusion constant} =$

$$K_m = l^2 \left| \frac{\partial V}{\partial z} \right| F_2 \text{ Ri} \quad (\text{momentum}) \quad (2.78)$$

$$K_{h,q} = l^2 \left| \frac{\partial V}{\partial z} \right| F_1 \text{ Ri} \quad (\text{heat, moisture}) \quad (2.79)$$

$$l = \text{mixing length} = kz / (1 + kz/\lambda) \quad (2.80)$$

$k = \text{Von Karman constant}$

$\lambda = \text{asymptotic mixing length}$

$= 150 \text{ m (momentum) or } 450 \text{ m (heat, moisture)}$

$$\text{Ri} = \text{Richardson number} = \frac{g}{\theta} \frac{\partial \theta}{\partial z} \left| \frac{\partial V}{\partial z} \right|^2 \quad (2.81)$$

$$F_1 = F_2 = 1 / (1 + 5 \text{ Ri})^2 \quad (\text{Ri} \geq 0) \quad (2.82)$$

$$F_1 = \frac{1 + 1.286 |\text{Ri}|^{0.5} - 8 \text{ Ri}}{1 + 1.286 |\text{Ri}|^{0.5}} \quad (\text{Ri} < 0) \quad (2.83)$$

$$F_2 = \frac{1 + 1.746 |\text{Ri}|^{0.5} - 8 \text{ Ri}}{1 + 1.746 |\text{Ri}|^{0.5}} \quad (\text{Ri} < 0) \quad (2.84)$$

The top boundary is set to zero. For stable conditions, the bottom boundary is set to the surface flux of momentum, heat, or moisture (see section 2.3.1) and for unstable

conditions it is set to zero.

The windshear in the Richardson number may cause problems in a stable atmosphere. If the wind shear approached zero, Ri would grow to a large value. This would produce eddy diffusivities approaching zero, with a corresponding large convergence of flux in the layer. To prevent this problem, the windspeed between two levels is limited to 1.0 ms<sup>-1</sup>.

Manobianco (1988) also states that equation 2.78 contains an implicit time scale on the order of  $k/\Delta z^2$ . He gives the threshold for the timescale as one day. If the square of the layer thickness divided by the eddy diffusivity is less than this time scale, the eddy diffusivity is recomputed as:

$$k_{m,h,q} = \Delta z^2 / 86400 \text{ s} \quad (2.85)$$

In this manner, the diffusive time scale will always be greater than or equal to one day.

#### 2.3.4 Radiation

The parameterization of radiation in the FSUGSM is divided into two parts: the longwave radiation and the shortwave radiation. The longwave radiation is discussed in detail in Chapter VI and will only be briefly discussed in this section. The shortwave radiation discussion follows.

The longwave parameterization of the FSUGSM is based on the scheme of Harshvardhan and Corsetti (1980). It assumes there are three principal absorbers in the longwave portion of the spectrum. They are water vapor, carbon dioxide, and ozone. Line by line spectral calculations are performed for the bands of water vapor and carbon dioxide and then fit to analytical functions. These functions are used by the

model to simulate line by line absorption in each of the bands. The ozone absorption follows calculations based on Lorentz line absorption.

The shortwave radiation parameterization of the FSUGSM is based on the scheme of the UCLA/GLAS GSM as described by Davies (1982) and Harshvardhan *et al* (1987). It allows water vapor, ozone, and surface absorption under a variety of conditions and sun angles. Water vapor absorption is calculated by the probability distribution of Lacis and Hansen (1974). Ozone absorption is also calculated by the method of Lacis and Hansen (1974).

For clear skies, the absorption due to water vapor is given by the probability distribution method of Lacis and Hansen (1974):

$$A_{wv}(y) = 1 - \int_0^1 p(k)e^{-ky}dk \quad (2.86)$$

where:

$A_{wv}(y)$  = shortwave absorption due to water vapor

$p(k)$  = probability distribution for the absorption coefficient

$p(k)dk$  = fraction of the incident flux that is associated with the absorption coefficient between  $k$  and  $k + dk$

$y$  = effective optical depth water vapor:

$$= \frac{M(\mu)}{g} \int_0^P q \left[ \frac{p}{p_0} \right]^n \left[ \frac{T_0}{T} \right]^{0.5} dp \quad (2.87)$$

$M$  = magnification factor

$g$  = gravity

$q$  = specific humidity

$p_0$  = reference pressure = 1013.25 mb

$T_0 = \text{reference temperature} = 273.16 \text{ K}$

$n = 1$

Lacis and Hansen (1974) have replaced the integral by the finite sum:

$$A_{wv}(y) = 1 - \int_0^1 p(k) e^{-ky} dk \cong \sum_{i=1}^I p(k_i) e^{-k_i y} \quad (2.88)$$

The values of  $p(k_i)$  and  $k_i$  are given by Davies (1983). Equation 2.88 is also used for the upward clear sky beam, except the optical depth is given by:

$$y^* = \frac{M(\mu)}{g} \int_0^{p_s} q \left[ \frac{p}{p_0} \right]^n \left[ \frac{T_0}{T} \right]^{0.5} dp + \frac{\sqrt{3}}{g} \int_p^{p_s} q \left[ \frac{p}{p_0} \right]^n \left[ \frac{T_0}{T} \right]^{0.5} dp \quad (2.89)$$

The net absorption by water vapor in a clear sky in the  $i$ th layer is then:

$$A_{wv} = \mu_0 S_0 \{ A_{wv}(y_{i+1}) - A_{wv}(y_i) + R_g(\mu) [A_{wv}(y^*_{i+1})] \} \quad (2.90)$$

where:

$S_0 = \text{solar flux at the top of the atmosphere}$

$R_g(\mu) = \text{ground albedo}$

In addition to calculating absorption in a cloudy sky, reflectance and

transmittance must also be determined. The complete set of equations for reflectance and transmittance as calculated by the delta-Eddington approximation is listed by Davies (1982). The direct radiation reflected and transmitted by a layer may be considered a source of diffuse radiation to the layers above and below it. The upwelling and downwelling radiation at each layer, as given by Harshvardhan *et al* (1987), is:

$$UO_i = \mu_0 S_i R_i(\mu_0) \quad i=1, \dots, n+1 \quad (2.91)$$

$$DO_i = \mu_0 S_i T_i(\mu_0) \quad i=1, \dots, n \quad (2.92)$$

where:

$UO$  = upwelling irradiance through level  $i$

$DO$  = downwelling diffuse irradiance through level  $i$

$R_i$  = reflectivity of layer  $i$  to unit diffuse radiation

$T_i$  = transmissivity of layer  $i$  to unit diffuse irradiance

$\mu_0 S_i$  = the direct solar flux incident on level  $i$

The downwelling diffuse radiation at level  $i+1$  due to all diffuse radiation that has not crossed level  $i$  is:

$$D1_{i+1} = (D1_i + UO_i CR_i) M_i T_i + DO_i \quad i=1, \dots, n+1 \quad (2.93)$$

where:

$CR_i$  = composite reflection coefficient of the atmosphere above  $i$

$M_i$  = magnification factor for multiple reflections

The upwelling diffuse radiation at  $i$  due to all diffuse radiation that has not previously crossed level  $i+1$  is:

$$U_{1i} = (D_{1i}R_i + U_{0i})M_i \quad i = 1, \dots, n+1 \quad (2.94)$$

Once  $D_{1i}$  and  $U_{1i}$  are found for all  $i$ , the total radiation crossing each level may be recursively calculated by:

$$U_i = U_{1i} + U_{i+1}T_iM_i \quad i = n, \dots, 1 \quad (2.95)$$

$$D_i = D_{1i} + U_iCR_i + \mu_0S_i \quad i = n+1, \dots, 1 \quad (2.96)$$

To obtain the broadband values, each of the spectral values calculated above are summed. The net flux convergence then gives the absorbed solar radiation.

The shortwave absorption by Earth's surface is the sum of the absorption in the spectral regions associated with significant water vapor absorption and the spectral regions of negligible water vapor absorption:

$$A_g = A_{g1} + A_{g2} \quad (2.97)$$

where:

$A_g$  = total surface absorption

$A_{g1}$  = surface absorption in the spectral region associated with

significant water vapor absorption (calculated differently for clear and cloudy skies)

$A_{g2}$  = surface absorption in the spectral regions of negligible water vapor absorption

For clear skies:

$$A_{g1} = \mu_0 S_0 [1 - R_g(\mu_0)] \sum_{i=1}^I p(k_i) e^{-k_i y} \quad (2.98)$$

$$A_{g2} = \mu_0 S_0 [0.647 - A_{oz}(m_r(\mu_0)x)] [1 - \bar{R}_g(\mu_0)] \quad (2.99)$$

where:

$R_g$  = ground albedo

$\bar{R}_g$  = albedo of the ground and the atmosphere above

For cloudy skies,  $A_{g1}$  is obtained by multiplying the transmission function at the ground by  $(1 - \bar{R}_g(\mu_0))$ .

The ozone absorption is calculated by the method of Lacis and Hansen (1974). The absorption is divided into two bands: the weak visual band (Chapius Band) and the ultraviolet band (Hartley and Huggins band). The absorption is:

$$A_{oz}(x) = A_{uv}(x) + A_{vis}(x) \quad (2.100)$$

Lacis and Hansen have fit the frequency integrated absorption curves for ozone to

analytical expressions:

$$A_{uv} = \frac{1.082x}{(1.0 + 138.6x)^{0.805}} + \frac{0.0658x}{1.0 + (103.6x)^3} \quad (2.101)$$

$$A_{vis} = \frac{0.02118x}{1.0 + 0.042x + 0.000323x^2} \quad (2.102)$$

where:

$x_1$  = ozone amount traversed by the direct solar beam to reach the  $l$ th layer =  $u_1M$

$u_1$  = amount of ozone in a vertical column above the  $l$ th layer

$M$  = magnification factor, accounting for the slant path and refraction

$$= \frac{35}{1224 \mu_0^2 + 1} \quad (2.103)$$

The ozone path traversed by the diffuse radiation illuminating the  $l$ th layer from below is:

$$x_1^* = u_tM + 1.9(u_t - u_1) \quad (2.104)$$

where:

$u_t$  = the total ozone amount above the reflecting layer

The total absorption of shortwave radiation in a layer due to ozone is then:

$$A_{\text{boz}} = \mu_0 S_0 \{ A_{\text{oz}}(x_{l+1}) - A_{\text{oz}}(x_l) + \bar{R}(\mu_0) [A_{\text{oz}}(x_1^*) - A_{\text{oz}}(x_{l+1}^*)] \} \quad (2.105)$$

where:

$\bar{R}(\mu_0)$  = the albedo of the reflecting region, including the effective albedo of the lower atmosphere and the ground reflectivity.

## CHAPTER III

### DEFINITION OF CLOUDS

#### 3.1 Overview

A numerical forecast model and a satellite provide different types of cloud information. In a numerical model, the cloud amount can be formulated by two criteria: the moisture content of a layer and the vertical distribution of the moisture. The cloud amount in an individual layer is determined by its relative humidity. The cloud amount through several layers is determined by the random overlap of the clouds in the individual layers. Satellite cloud observation, however, is limited by a lack of knowledge of cloud amount at all levels. When a satellite observes a column of clouds, it can view only the unobstructed cloud tops. It cannot gather information through the overlapping layers of clouds. Therefore, when a comparison is made between model diagnosed clouds and satellite observed clouds, suitable procedures must to be developed to determine cloud amounts in individual layers from limited satellite information. Section 3.2 discusses the determination of clouds in a numerical model (in a layer and in a column), and also the emittance of high clouds. Section 3.3 discusses satellite observed clouds (the ISCCP data set), and procedures to determine cloud amounts through a column from this data.

## 3.2 Clouds in a numerical model

### 3.2.1 Clouds in a layer

Clouds in a single layer are classified by their type (high, middle, or low) and amount (0.0 through 100.0%). The type of cloud is defined by its height in sigma levels, which may vary with latitude (see Table 3.1). Clouds are not defined for sigma levels below low cloud bases or above high cloud tops.

The amount of a cloud type in an individual layer is assumed to be a function of the relative humidity, which is dependent on the moisture, temperature, and pressure. The critical relative humidities used in the formulation of cloud amounts are given in Table 3.1. Below the critical relative humidity, the cloud amount is defined as zero. Above the critical relative humidity, the cloud amount is given by a quadratic function:

$$C = \left[ \frac{RH - RHC}{1.0 - RHC} \right]^2 \quad (3.1)$$

where:

C = fractional cloud amount

RH = relative humidity of the layer

RHC = critical relative humidity for the particular cloud type

The cloud amount is squared to ensure a bimodal distribution of clouds, as found in nature. (To ensure realistic amounts, the fractional cloud amount is constrained to be within the bounds of zero and one.) This formulation is similar to the one used by ECMWF (Norquist, 1988). However, at ECMWF the critical relative humidity varies with the sigma surfaces according to the following relation:

$$RHC = 1 - 2\sigma + 2\sigma^2 + 3\sigma^{0.5} (1 - 3\sigma + 2\sigma^2) \quad (3.2)$$

Table 3.1. Critical Relative Humidities and Vertical Extent for Different Cloud Types.

---



---

<u>CLOUD TYPE</u>	<u>CRITICAL RH</u>	<u>VERTICAL EXTENT</u> <u>(SIGMA LEVEL)</u>
Low Cloud	0.66	0.9 – 0.7
Middle Cloud	0.50	0.7 – 0.4
High Cloud	0.40	0.4 – 0.3 (High Latitudes)
High Cloud	0.40	0.4 – 0.2 (Middle Latitudes)
High Cloud	0.40	0.4 – 0.1 (Low Latitudes)

---

An example of low, middle, and high clouds as given by this definition is shown in Figure 3.1. It can easily be seen that for all three cloud types, the 0.0% cloud amount begins at the critical relative humidity. The cloud amount then rises slowly with large changes in relative humidity. Approaching 100% clouds, the slope decreases, so that small changes in relative humidity produce large changes in cloud amount.

### 3.2.2 Clouds in a column

Specification of cloud type and amount is an integral part of the radiation scheme of the FSUGSM. To compute the cloud amounts through the columns, moisture values at each level of the FSUGSM are supplied to the radiation model. Because of computational constraints, some portions of the radiation scheme cannot afford to have as many cloud levels as the FSUGSM has sigma levels. To overcome this problem, the model has only three types of clouds; low, middle, and high. The vertical extent of each cloud category in terms of sigma level is given in Table 3.1. The relative humidity within each cloud layer is the pressure weighted mean relative humidity of the individual layers.

The total cloud in a column from level  $i$  to level  $j$  is then one minus the product of the cloud-free line of sight for each level through the column:

$$C_{ij} = 1.0 - \prod_{n=i}^j (1.0 - C_n) \quad (3.3)$$

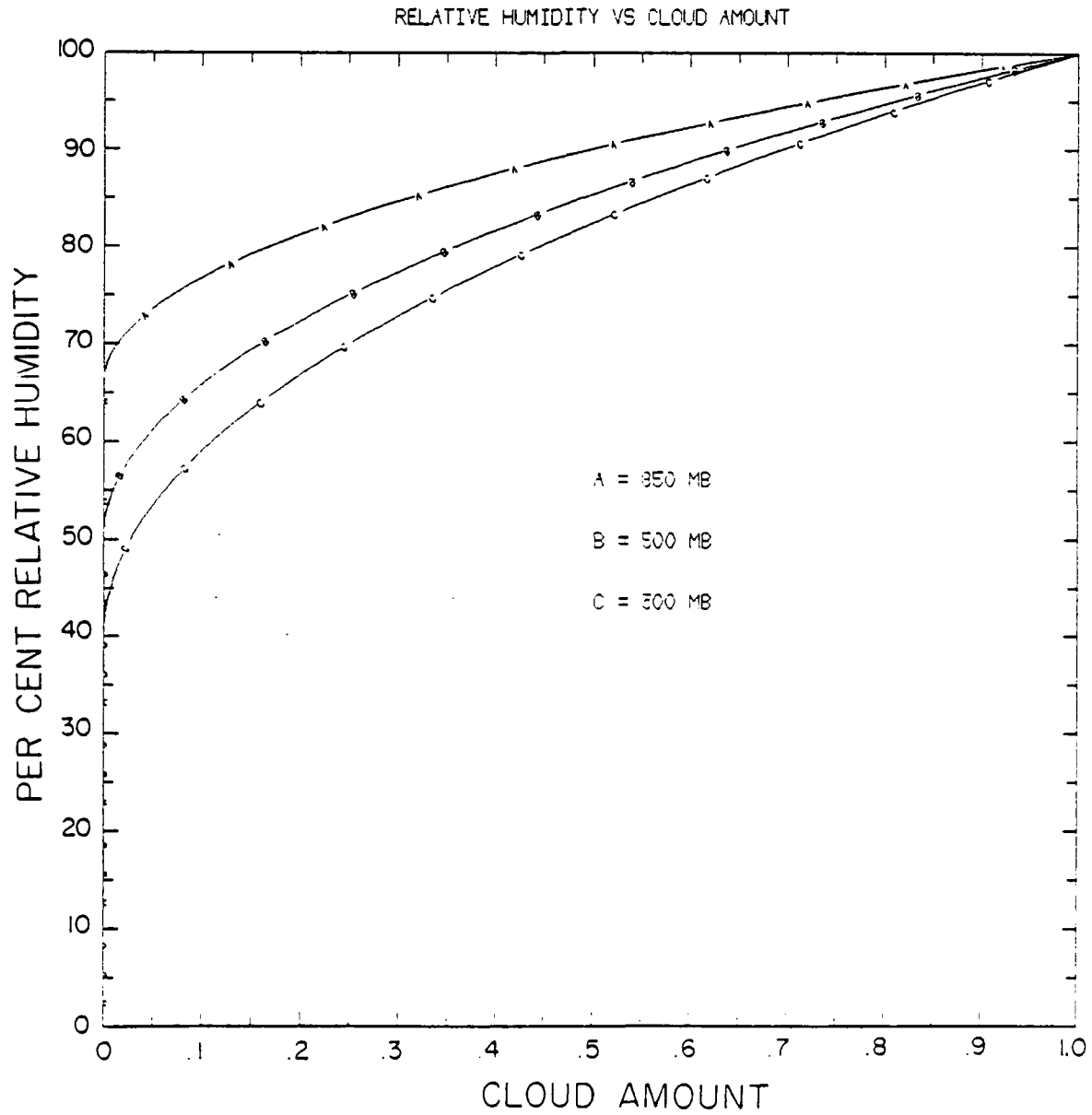


Figure 3.1 Cloud amount as a function of relative humidity in the FSUGSM.

where:

$$C_{ij} = \text{total cloud amount in the column from levels } i \text{ to } j$$

$$C_n = \text{cloud amount at level } n$$

This procedure assumes that clouds are randomly overlapped throughout the column. (As before, the total cloud amount is constrained to be between 0.0 and 1.0.) This is a modification of the maximum overlap method used by Harshvardhan and Corsetti (1984) in the UCLA/GLAS GCM. (In that GCM, maximum overlap is also averaged with the random overlap.)

### 3.2.3 Cloud Emittance

The longwave emittance of a cloud may be defined as:

$$\epsilon_{IR} = 1.0 - \exp(-D * \tau_{IR}) \quad (3.4)$$

where:

$$\epsilon_{IR} = \text{longwave emittance}$$

$$D = \text{diffusivity factor}$$

$$\tau_{IR} = \text{longwave optical depth}$$

Platt and Harshvardhan (1988) have empirically defined the diffusivity factor as 1.5.

The shortwave cloud optical depth may be defined as:

$$\tau_{SW} = B(T + T_0)^2 * DPC \quad (3.5)$$

where:

$$\tau_{SW} = \text{shortwave cloud optical depth}$$

B = constant

T = cloud temperature

T<sub>0</sub> = reference temperature

DPC = cloud pressure thickness

Platt and Harshvardhan (1988) also have empirically determined the values of B and T<sub>0</sub> as: B = 1.6 X 10<sup>-4</sup> and T<sub>0</sub> = -82.5°C. In addition, they also state that the shortwave cloud optical depth may be related to the longwave cloud optical depth through the following:

$$\beta = \tau_{SW}/\tau_{IR} = 2.0 \quad (3.6)$$

Using this relation, the above equations may be combined to yield:

$$\epsilon_{IR} = 1.0 - \exp(-.75 * \tau_{SW}) \quad (3.7)$$

Two things are now accomplished: the shortwave and the longwave radiation schemes have been tied together, and there is a method for evaluating the emittance of clouds.

The emissivity of low and middle clouds is unity. However, there is no agreed upon value for the emissivity of high clouds. Platt and Dilley (1981) have measured high cloud emittance using a ruby lidar and an IR radiometer. Their results show that more than 50% of high clouds should have an emittance of less than 0.3, while only 7% of high clouds have an emittance of greater than 0.70. On the other hand, Slingo *et al.* (1988) used an emittance of 0.6 for all high clouds in the ECMWF model.

The FSUGSM computes the longwave cloud emittance by equation 3.7. It was found that the empirical value of the constant B, determined by Platt and Harshvardhan (1988) did not give optimal results with the FSUGSM. Table 3.2 shows several values of the constant B and the results of initialization using this value. The baseline reference for comparison is taken from satellite observed OLR for the OLR comparisons and from a study by Hartmann *et al.* (1986) for the albedo comparisons. According to Hartmann *et al.* (1986), the tropical albedo for the month of July, 1979 was 27 %. The experimental tropical albedo, found by varying the constant B, were all slightly higher than this. Since the in albedo was insensitive to a change in B (a spread of albedo of less than 5 % with several orders of magnitude change in B), it was deemed a poor choice for determining a proper value of the constant B. The change in B did have a significant effect on the number of points converging during moisture initialization. At the value of  $2 \times 10^{-4}$ , the number of points not converging was 246. When a value of  $2 \times 10^{-2}$  was used 100% convergence was achieved. Accordingly, this value was used in the remainder of the experiments. With a value of B established, there is now a means to determine the emissivity of clouds in the FSUGSM. Figure 3.2 shows the emittance of clouds as a function of temperature and pressure thickness. Due to the vertical discretization of the model, most of the high clouds would have an emissivity of 1.0.

### 3.3 Clouds Observed by a Satellite – ISCCP clouds

Satellites look down and detect cloud tops. Therefore, no additional cloud information is available below the level of the highest cloud top. Through a complex decision tree (Krishnamurti *et al.*, 1988), each satellite pixel is labeled either clear or cloudy.

Table 3.2 Table of points not converging and albedo when initializing data.

Tropical Albedo (Total Points) (1446)	Tropical Points Not Converging (Total Points) (2816)	Constant B
29.40	246	$2.0 \times 10^{-4}$
30.08	63	$2.0 \times 10^{-3}$
30.67	5	$7.0 \times 10^{-3}$
30.85	0	$2.0 \times 10^{-2}$
30.86	0	$2.0 \times 10^{-1}$

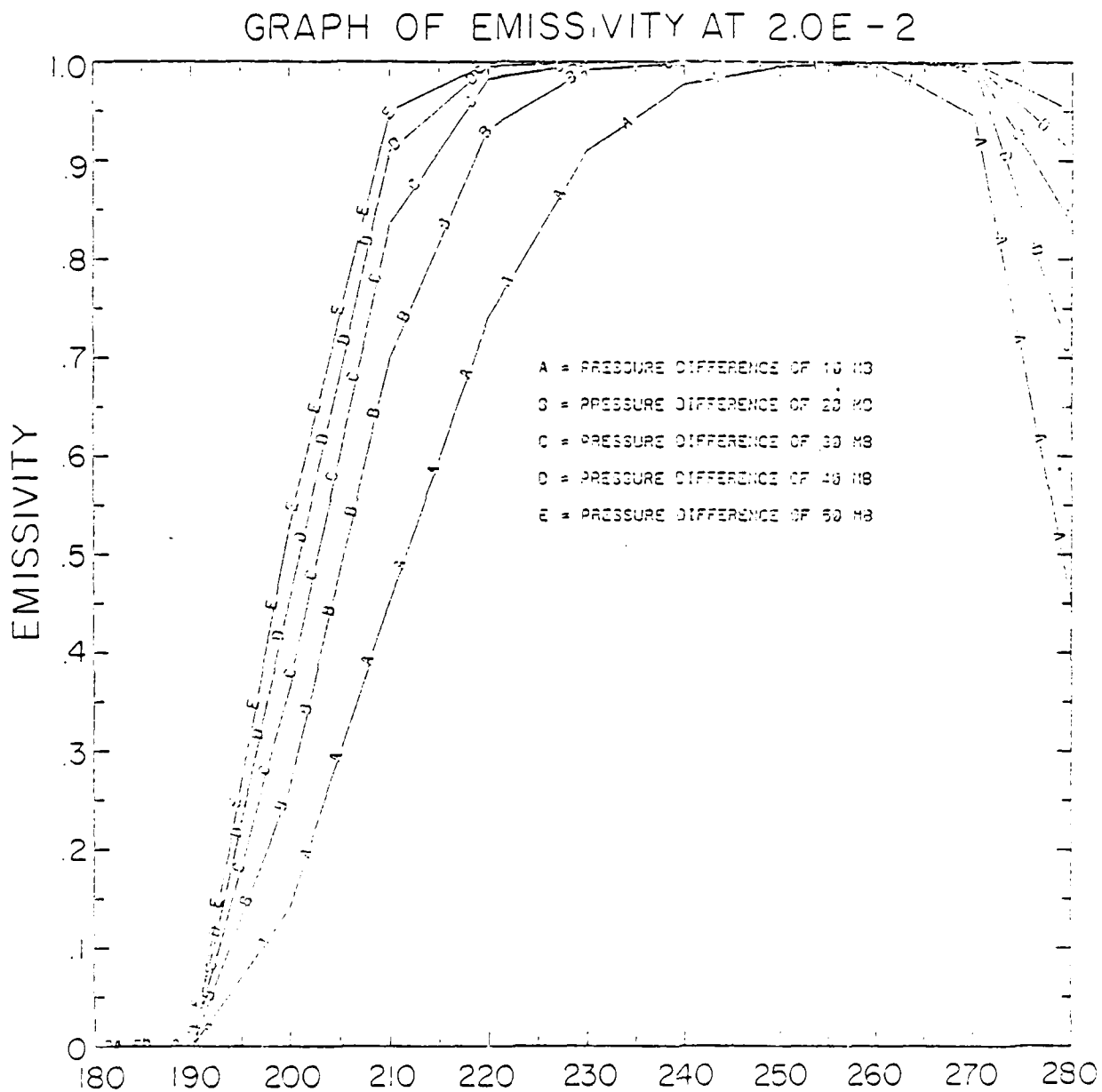


Figure 3.2a The emittance of clouds as a function of temperature and pressure thickness (10 mb through 50 mb).

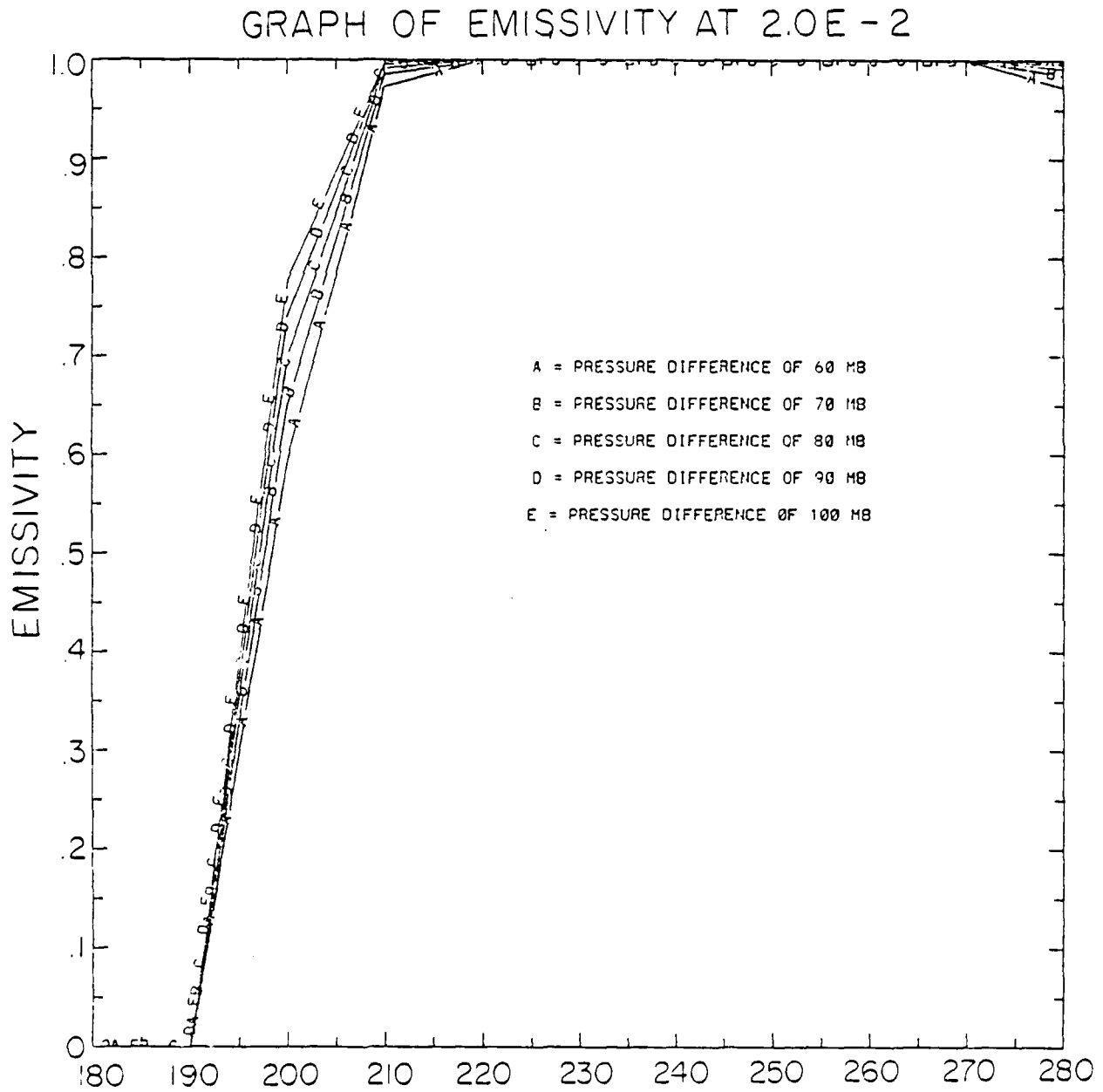


Figure 3.2b The emittance of clouds as a function of temperature and pressure thickness (60 mb through 100 mb).

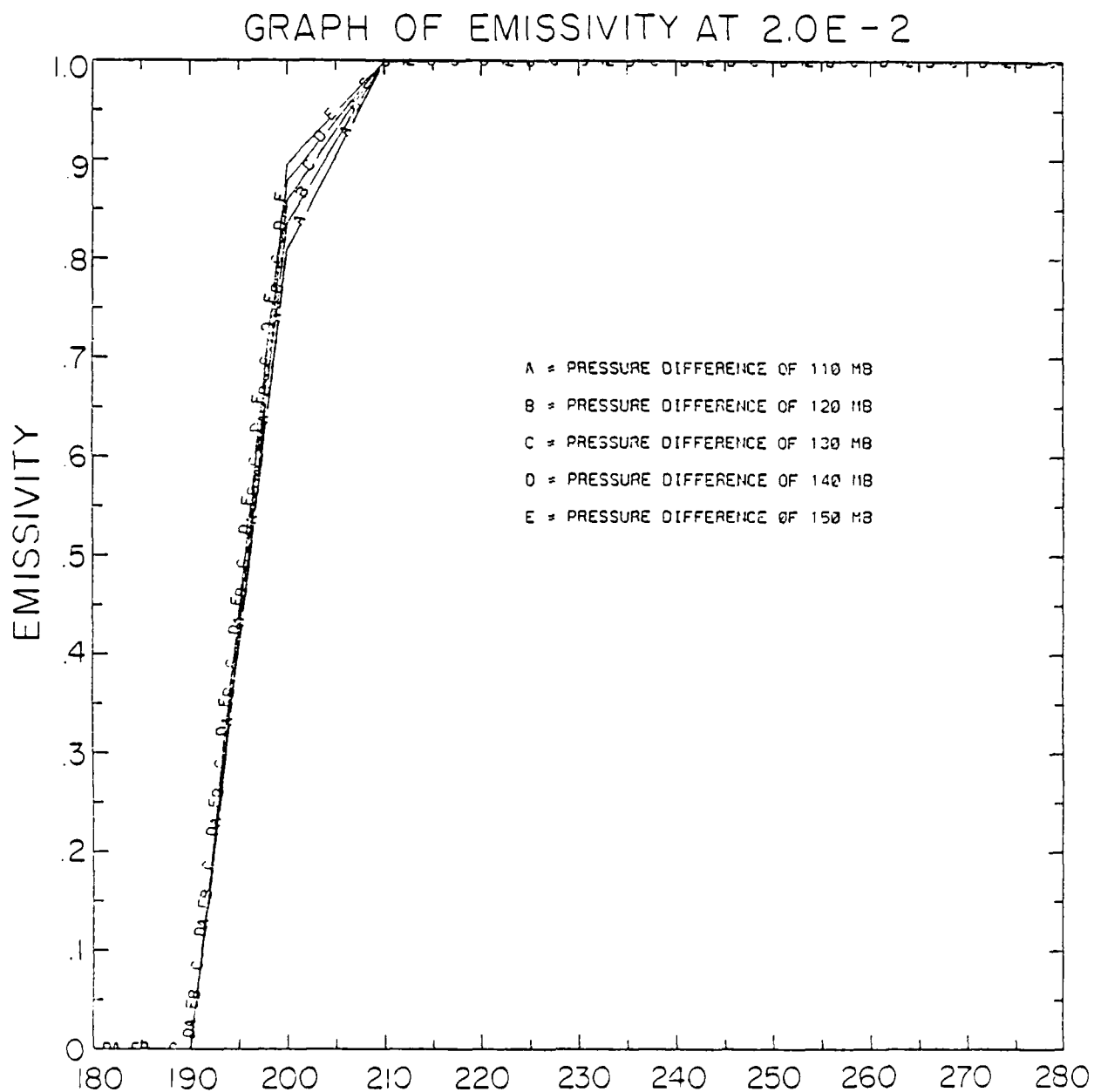


Figure 3.2c The emittance of clouds as a function of temperature and pressure thickness (110 mb through 150 mb).

### 3.3.1 ISCCP clouds

The cloud data used are from the ISCCP cloud data set obtained from operational weather satellites (METEOSAT, GOES (EAST), GOES (WEST), GMS, and TIROS-N). The onboard radiometers used the 0.6 and the 11  $\mu\text{m}$  narrow bands to receive radiance data. Pixels ranged in size from 4 to 8 km and were grouped into grids of 250 km<sup>2</sup>. A sample of ISCCP data is shown in figure 3.3. The clouds depicted in this figure are fractions of the cloud tops as seen by the satellite. The total cloud fraction is the sum of the other cloud top categories.

The cloudy versus clear sky decision algorithms are described in detail by Rossow *et al.* (1988) and summarized by Krishnamurti *et al.* (1988). Several tests and statistical calculations are used to identify clear skies. For the longwave radiances, spatial and temporal tests are made. In the spatial test, all pixels exceeding a relative threshold value (3.5 K over the ocean or 6.5 K over the land colder than the warmest pixel) are considered cloudy. All other pixels are considered undecided. In the temporal tests, the same geographic pixel is considered for a 3 day sequence (day 1 and the previous day, and day 1 and the following day). Those pixels exceeding a relative threshold (3.5 K over oceans or 8.0 K over land colder than the warmest pixel) on either the first half of the sequence and/or the second half of the sequence are considered cloudy. Those pixels which do not vary by more than either 1.1 K (over ocean) or 2.5 K (over land) for the first half and/or the second half are considered clear. The pixels not meeting either criteria are labeled undecided. Because of the first half/second half option, it is possible that a pixel could be labeled clear in one half and cloudy in the other half. In these instances, the pixel is considered mixed. All other pixels are labeled undecided. The spatial and temporal tests results are finally combined by the decision algorithm in Table 3.3. For the shortwave radiances, spatial

and temporal tests are also conducted. Visible radiances are not measured as absolute values, but as percentages of the instrument response obtained when measuring the full solar flux. Variations in space and time (from the minimum 5 day value) exceeding a threshold (3.0% over oceans and 6.0% over land) are considered cloudy.

Finally, a bispectral test determines if the pixel is cloudy or clear (an IR only test is performed at night). All pixels which exceed the threshold test in either the longwave or the shortwave test are considered cloudy. All pixels which were not considered cloudy in either test, but may have been considered mixed in at least one test, are also considered cloudy. All remaining pixels are considered clear. There are no undecided pixels. The percent cloudiness is then the number of pixels considered cloudy divided by the total pixels in the grid box.

### 3.3.2 Clouds in a column

The ISCCP cloud data produces the amount of cloud tops in a layer, not the amount of clouds in a layer. To convert the cloud top information to cloud amount information a random overlap of clouds is assumed. The formulation for the clouds in a column is:

$$C_n = \frac{C_{sn}}{\prod_{i=1}^{n-1} (1.0 - C_i)} \quad (3.8)$$

where:

$C_n$  = actual cloudiness at level n

$C_{sn}$  = cloud top cloudiness, as measured by the satellite

$C_i$  = actual cloudiness at a level above n

A similar method is used by Saito and Baba (1988) in a recent study of satellite

observed clouds. After this conversion, the satellite clouds can be compared to the numerical model clouds at the same levels.

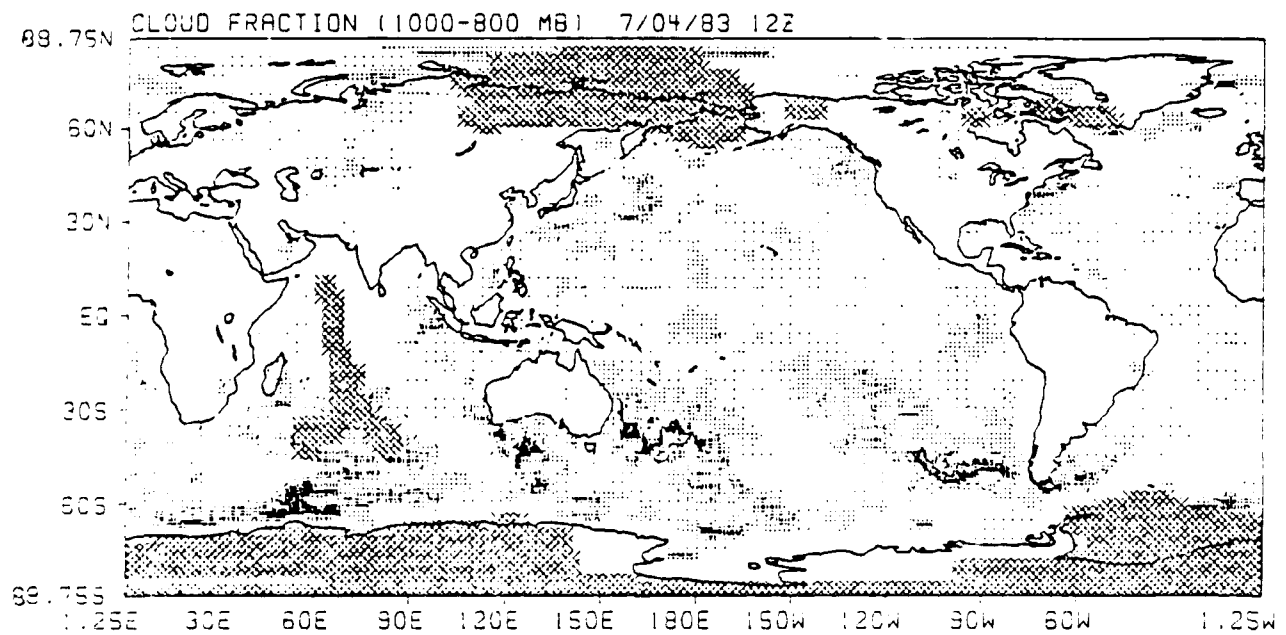
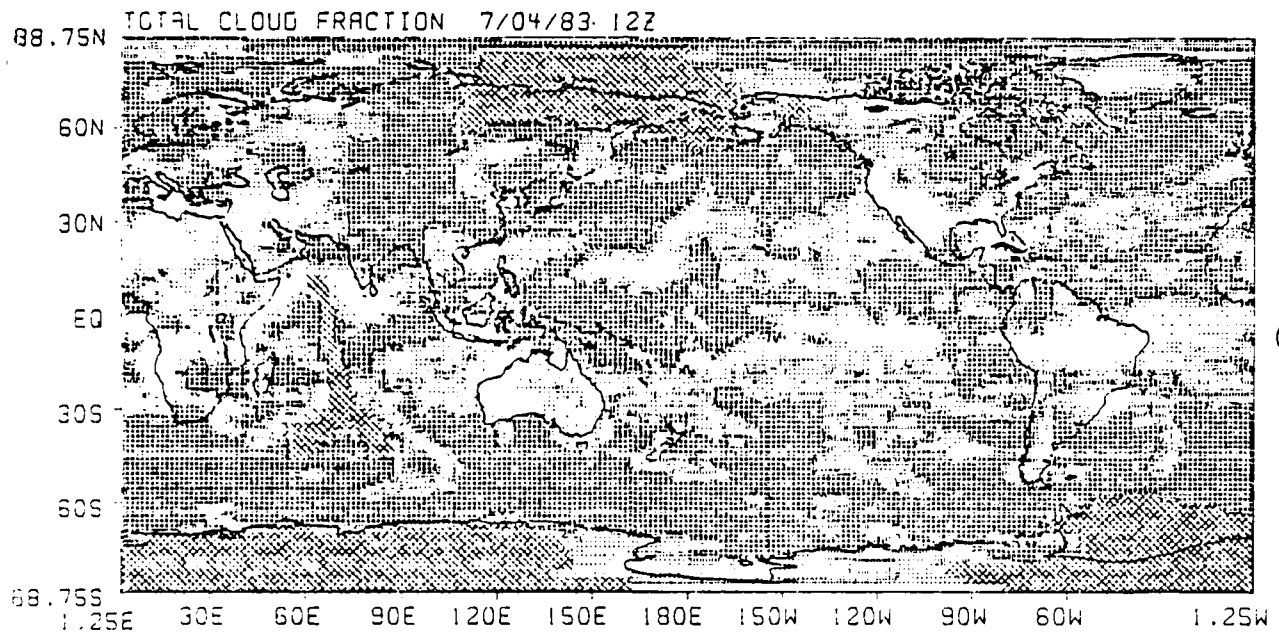


Figure 3.3a ISCCP total cloud fraction for July 4, 1983, 12GMT (legend in figure 3.3g)

Figure 3.3b ISCCP 1000 mb through 800 mb cloud fraction for July 4, 1983, 12GMT (legend in figure 3.3g)

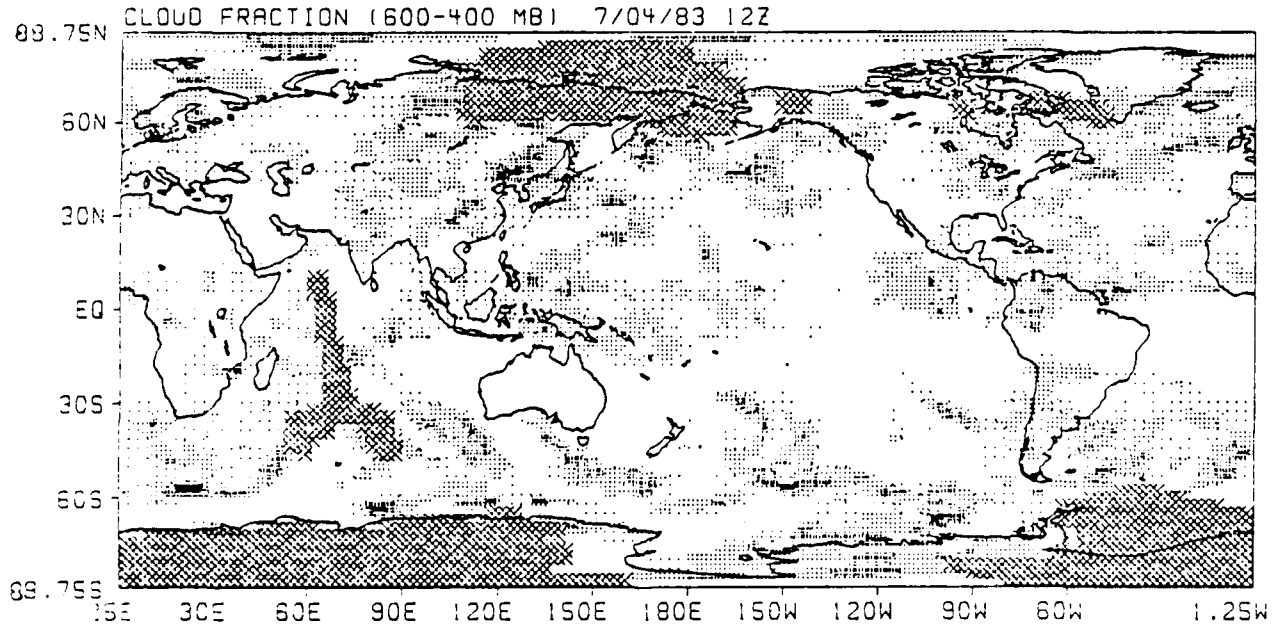
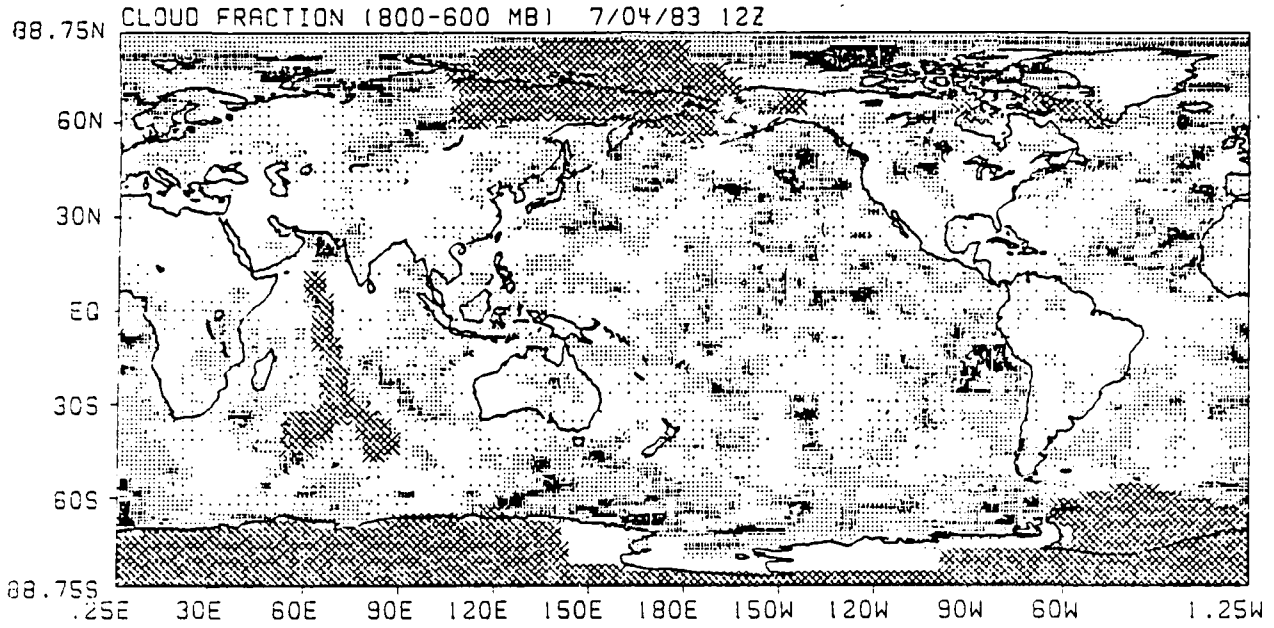


Figure 3.3c ISCCP 800 mb through 600 mb cloud fraction for July 4, 1983, 12GMT (legend in figure 3.3g)

Figure 3.3d ISCCP 600 mb through 400 mb cloud fraction for July 4, 1983, 12GMT (legend in figure 3.3g)

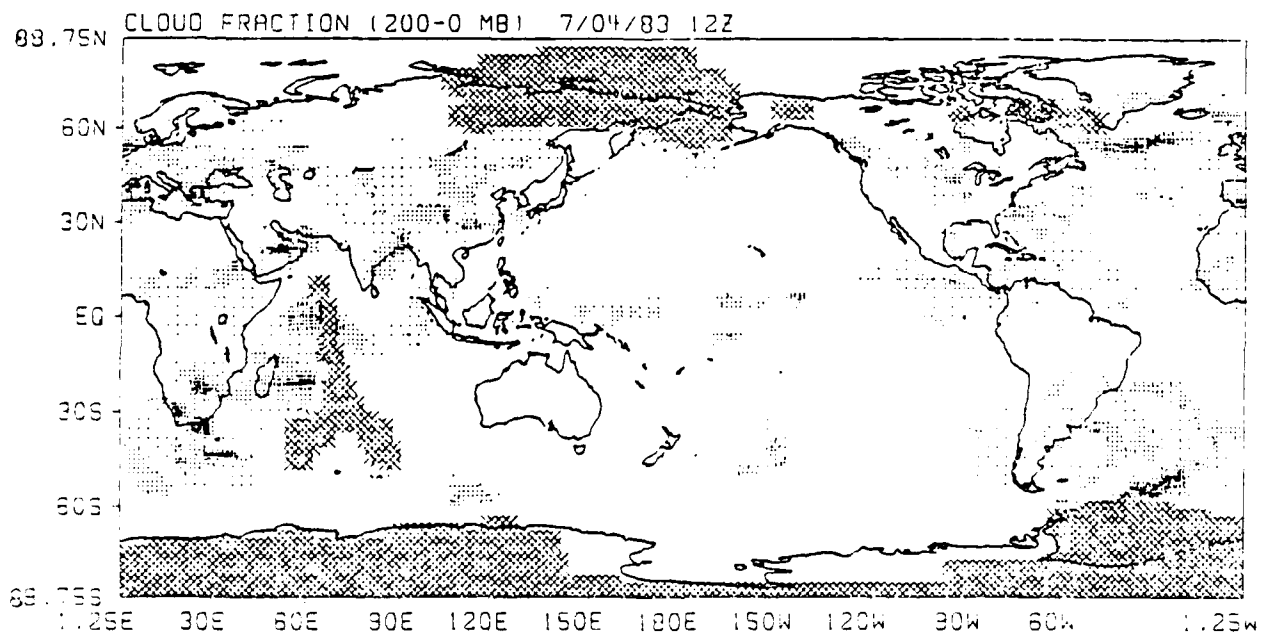
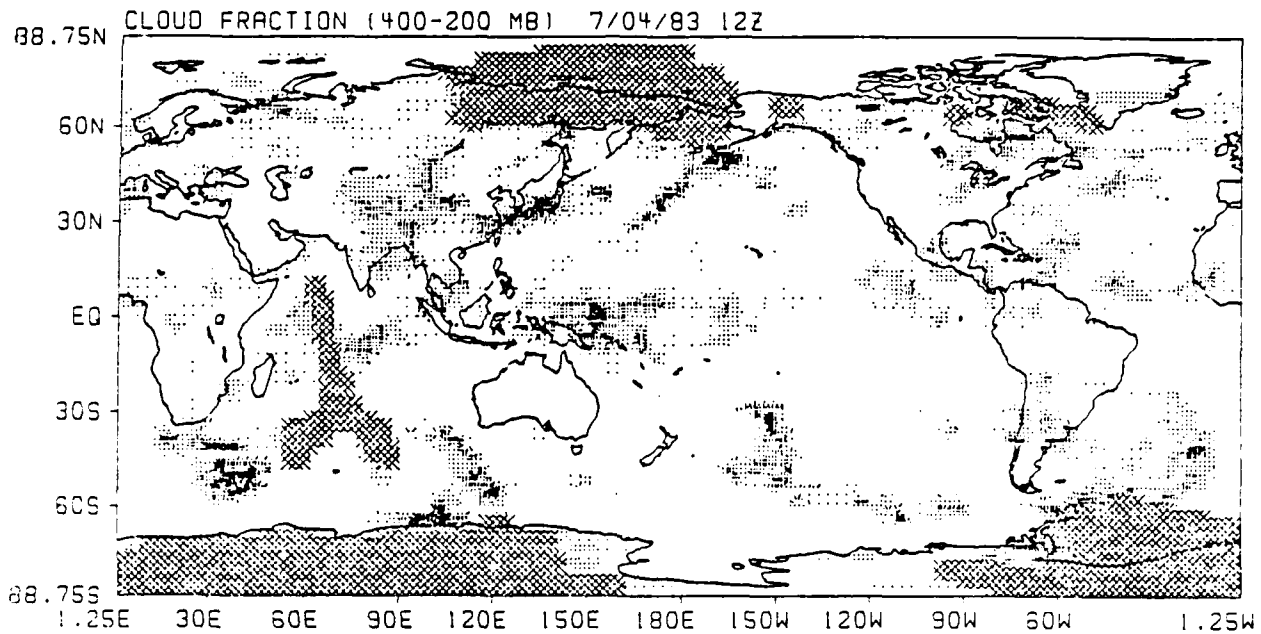


Figure 3.3e ISCCP 400 mb through 200 mb cloud fraction for July 4, 1983, 12GMT (legend in figure 3.3g)

Figure 3.3f ISCCP 200 mb through 000 mb cloud fraction for July 4, 1983, 12GMT (legend in figure 3.3g)

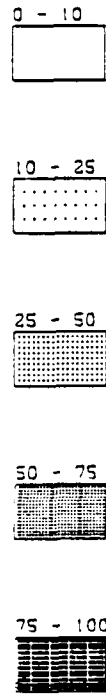


Figure 3.3g Cloud fraction legend for ISCCP data.

Table 3.3 Decision algorithm for the space and time, cloud versus clear test.

---



---

<u>SPACE TEST</u>		
	CLOUDY	UNDECIDED
<hr/>		
<u>TIME TEST</u>		
CLOUDY	CLOUDY	CLOUDY
UNDECIDED	CLOUDY	UNDECIDED
MIXED	MIXED	MIXED
CLEAR	MIXED	CLEAR

---



---

## CHAPTER IV

### INITIALIZATION METHODS

Three methods of initialization are used. Method A is a single parameter OLR initialization. Method B is a six-parameter initialization utilizing random moisture deviations. Method C is a six-parameter initialization which uses an iteration scheme similar to Method A.

#### 4.1 Method A – Single parameter initialization

The single parameter initialization method utilizes only the satellite observed Outgoing Longwave Radiation (OLR). The moisture data is varied until the model computed OLR has converged to the satellite measured OLR. The criteria for satisfactory convergence is a difference of less than  $\pm 10\text{W/M}^2$  between the observed and computed OLR.

Three iteration methods were used for the single parameter initialization method. They were:

1. False position
2. Secant

### 3. Bisection

The false position (or *regula falsa*) and secant methods required more computing time to converge than the bisection method. The bisection method converged quickly, usually in less than five iterations.

#### 4.1.1 The false position method

One method to find the root of a function is the false position (*regula falsa*) method. According to Press *et al.* (1989), this method will converge faster than the bisection method. Unfortunately, this is only true if the function being solved is approximately linear in the region of investigation.

The assumptions of the false position method are: Let  $y = f(x)$  be defined in  $J_x$ ;  $x_1, x_2 \in J_x$ ;  $x_1 \neq x_2$ ; and  $x_1$  and  $x_2$  bracket the root. Also,  $f(x_1) = y_1$  and  $f(x_2) = y_2$ , with  $y_1 \neq y_2$  and  $y_1 y_2 \neq 0$ . The  $f(x)$  is approximated by a linear function  $L(x)$ , which also assumes the values of  $y_1$  and  $y_2$  in  $x_1$  and  $x_2$ . Using the standard linear relation  $y = mx + B$ , we may write:

$$f(x) \cong L(x) = \frac{(x - x_1)y_2 - (x - x_2)y_1}{x_2 - x_1} \quad (4.1)$$

At the root  $f(x) = 0$  and  $L(x) = 0$ . Solving in terms of  $x$  at  $L(x) = 0$ :

$$x = \frac{x_1 y_2 - x_2 y_1}{y_2 - y_1} \quad (4.2)$$

This is called the *regula falsa* equation (A. M. Ostrowski, 1966).

Figure 4.1 (after Press *et al.*, 1989) shows that when certain non-linear functions are operated upon by the false position method, convergence will be

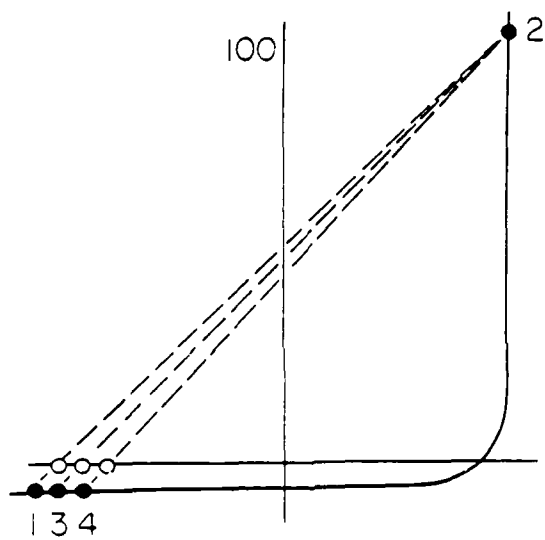


Figure 4.1 Demonstration of situation where the false position method is slow to converge.

extremely slow. The function in figure 4.1 is similar to what is encountered in the moisture initialization scheme. The modification of the moisture causes a small change in the OLR until the critical relative humidity for cloud formation has been exceeded. At that point, small moisture modifications will lead to locally large changes in OLR.

#### 4.1.2 The secant method

This method is very similar to the false position method. Moursund and Durns (1967) define the equation for the secant method as:

$$x = \frac{x_1 y_2 - x_2 y_1}{y_2 - y_1} \quad (4.3)$$

This is exactly the same equation that defines the false position equation. However, the secant method does not assume the root is bracketed by  $x_1$  and  $x_2$ . Because the secant and false position methods are based on the same equation, they are both subject to the same problem: they converge very slowly in regions such as those shown in figure 4.1.

#### 4.1.3 The bisection method

The bisection method is based on the Intermediate Value Theorem (Burden and Faires, 1985). This theorem states that if  $f(x) \in C[x_1, x_2]$  and  $y$  is any number between  $f(x_1)$  and  $f(x_2)$ , then there exists  $x_3$  in  $(x_1, x_2)$  for which  $f(x_3) = y$ . In this method, the interval between  $x_1$  and  $x_2$  is repeatedly halved until it satisfies the convergence criteria.

In the first step of this method, the midpoint,  $x_3$ , of the interval  $x_1$  to  $x_2$  is calculated. If  $f(x_3)$  has the same sign as  $f(x_1)$ , then  $y \in (x_3, x_2)$ , and the next iteration is

set as  $x_1' = x_3$  and  $x_2' = x_2$ . If  $f(x_3)$  has the same sign as  $f(x_2)$ , then  $y \in (x_1, x_3)$ , and the next iteration is set as  $x_1' = x_1$  and  $x_2' = x_3$ . The procedure is repeated until convergence is satisfied.

The advantage of this method is that there is no assumption of linearity. This method will not suffer from slow convergence in the situation that exists in figure 4.1. Therefore, it is the best iteration method to use for the single parameter moisture initialization method.

To start the bisection method, the root must be bracketed. One way to ensure the root is bracketed is to choose a completely dry profile for  $x_1$  (relative humidity set at 0.0%) and a completely saturated profile for  $x_2$  (relative humidity set at 100%). However, since all moisture profiles produced by these starting points would be unrealistic (the vertical distribution of relative humidity in the atmosphere would be a constant value), they should not be used as brackets. Therefore, the value of  $x_1$  is the original analyzed moisture profile. The value of  $x_2 = x_1 * F_n$ , where  $F_n$  is an iteration factor which may vary from 0.0 to 2.0. To test whether  $x_1$  and  $x_2$  bracket the root, the arithmetic sign of  $f(x_1) * f(x_2)$  is determined (where  $f(x_n) = OLR_n - OLR_{SAT}$ ). If the arithmetic sign is less than zero, then the root is bracketed and the bisection method is used to find the root. If the arithmetic sign is greater than zero, then the root is not bracketed and the procedure is repeated using  $x_1' = \text{MIN}\{\text{ABS}[f(x_1)], \text{ABS}[f(x_2)]\}$  and  $x_2' = x_1' * F_n$ . This is repeated until bracketing is achieved, then the bisection method is used. A possible source of error involves multiple roots. If the function has multiple roots, then the bisection method may converge to either root.

In figures 4.2 and 4.3 an example of the original and resultant moisture profiles due to single parameter initialization is shown. In figure 4.2, a large moisture change was necessary for convergence, but in Figure 4.3, only a small change was required.

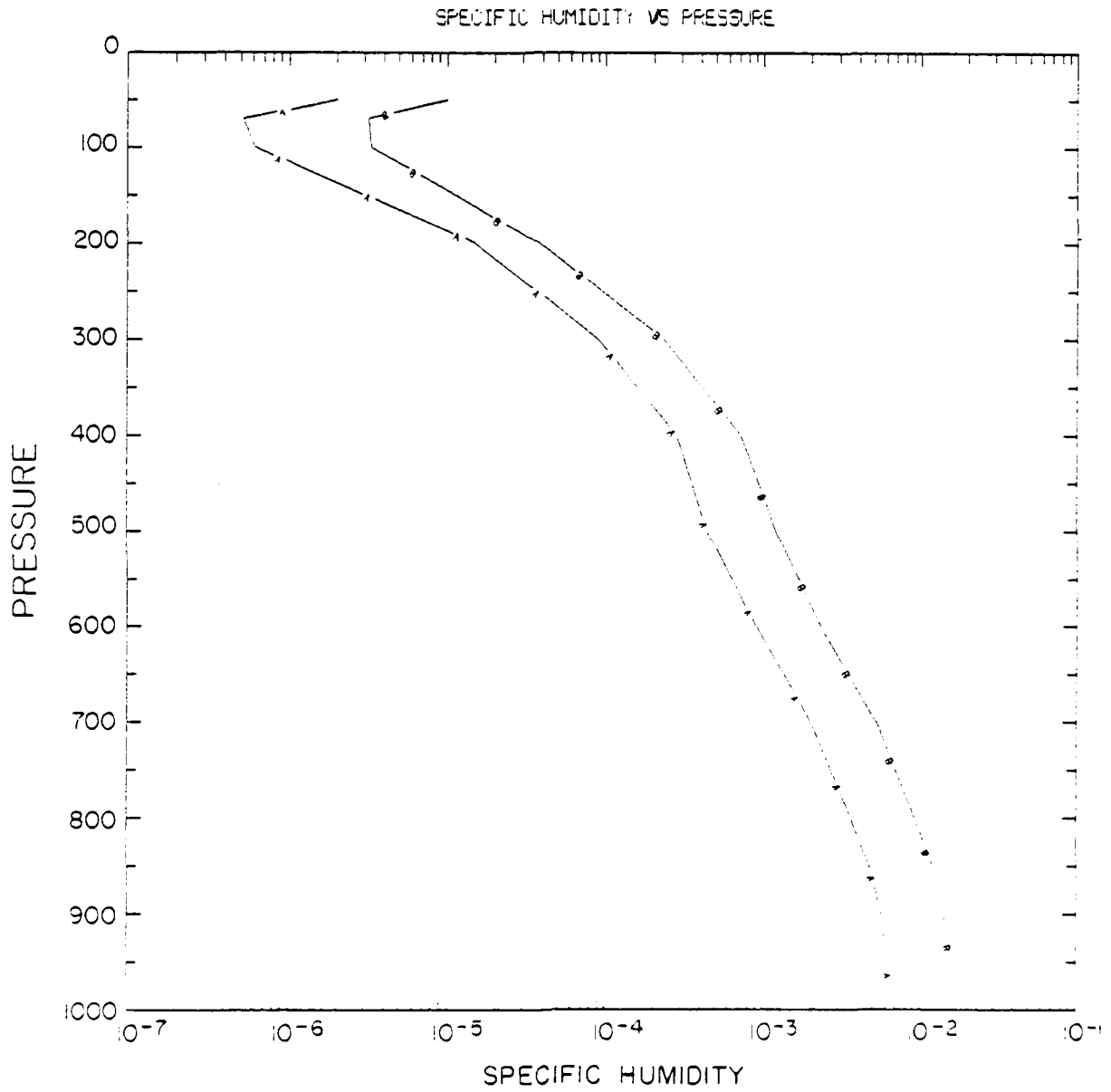


Figure 4.2 Example of the original and resultant moisture profiles due to the single parameter initialization scheme.

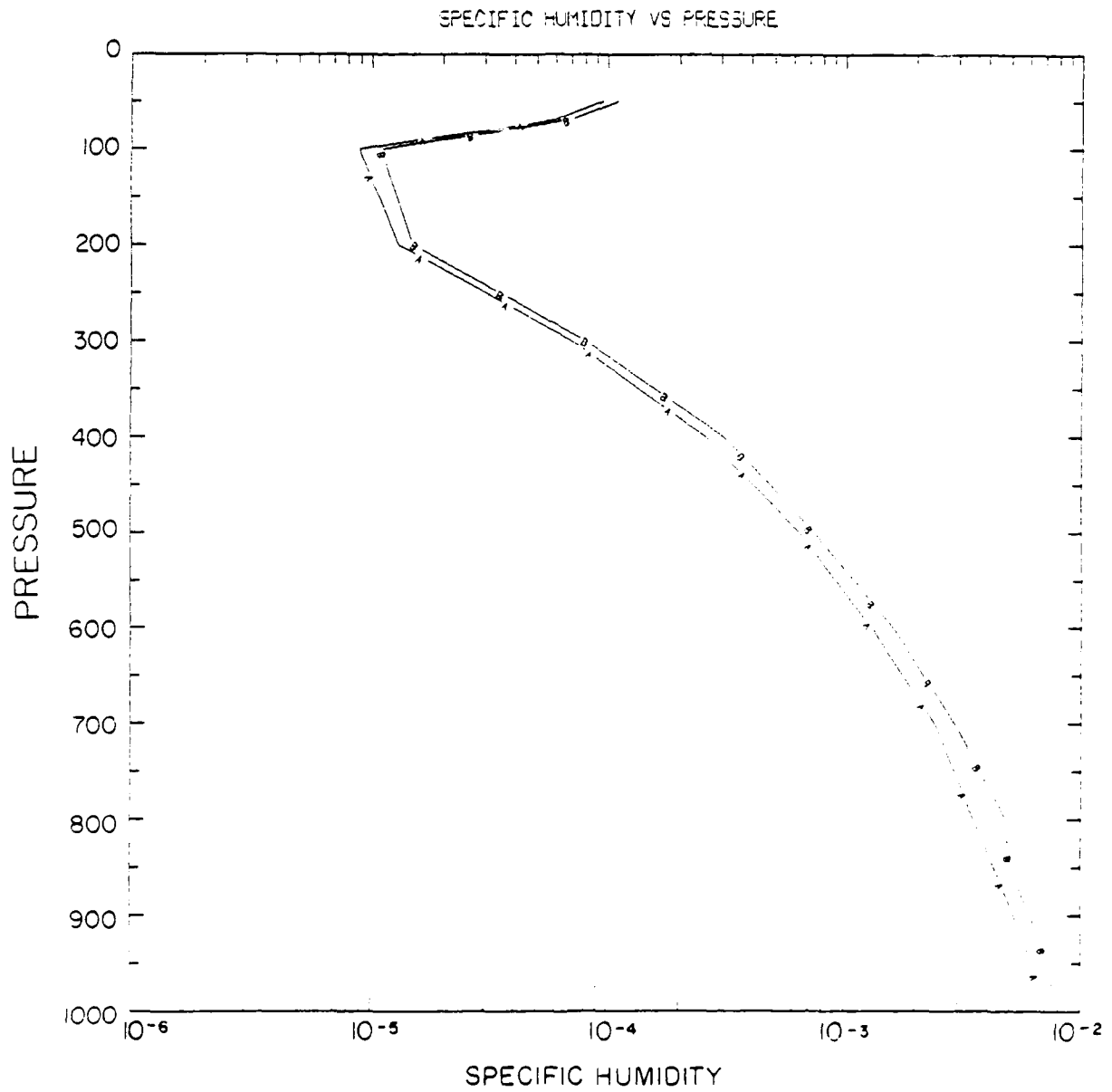


Figure 4.3 Example of the original and resultant moisture profiles due to the single parameter initialization scheme.

#### 4.2 Method B – Six parameter initialization utilizing random moisture deviations

This method utilizes six parameters for convergence. The first parameter is the OLR. Parameters two through six are the clouds of the ISCCP data set (described in Chapter III). The initial moisture analysis, which defines the six parameters, is assumed to contain small errors. A set of random moisture deviations are generated to compensate for the analysis errors. The adjusted profile is considered correct if the computed OLR and clouds have errors smaller than that of the analysis.

The random numbers generated by the computer are in a rectangular (uniform) distribution (figure 4.4). Because the errors in the moisture profile are assumed to be normally distributed, this type of random number distribution is unsuitable for use. The Central Limit Theorem provides a means for modifying the rectangular distribution into a normal distribution. This theorem, as given by Harnet and Murphy (1980), states that "regardless of the distribution of the parent population (as long as it has a finite mean  $\mu$  and variance  $\sigma^2$ ), the distribution of the means of random samples will approach a normal distribution with mean  $\mu$  and variance  $\sigma^2/n$  as the sample size approaches infinity". Using this theorem, the distribution of random numbers was normalized. Figure 4.4 shows the set of random numbers in the rectangular distribution and the normalized distribution.

A different set of random numbers was generated for each level in the moisture profile. This enables the value at each level to deviate from the analysis, by a small amount, independent of the other levels. Because of the properties of a normal distribution, most of deviations are small, although a few larger deviations may occur. The new moisture values at each level would then be:

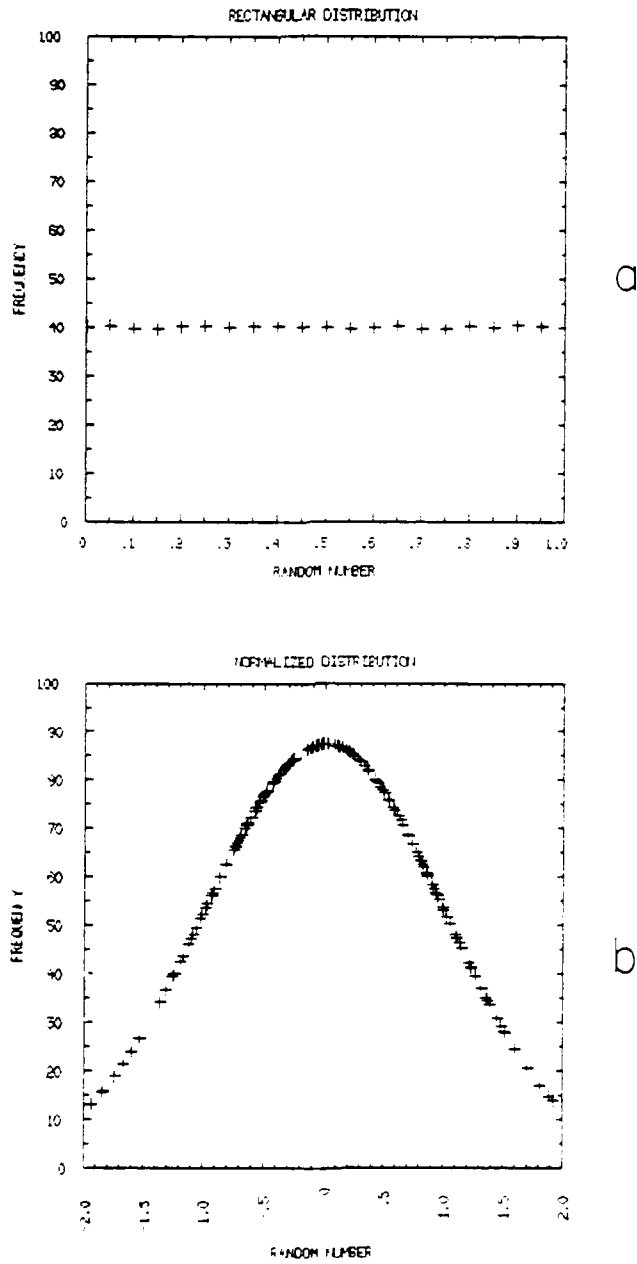


Figure 4.4 Conversion of random numbers from a rectangular distribution (a) to a gaussian distribution (b).

$$Q' = Q^{\circ} + Q^{\circ} * R \quad (4.4)$$

where:

$Q'$  = modified moisture value

$Q^{\circ}$  = analyzed moisture value

$R$  = normalized random number

This scheme is repeated 500 times for each grid point, calculating the OLR, clouds, and errors on each iteration. After the 500 iterations are completed, the moisture profile with the smallest error replaces the original profile. In several instances, the profile chosen was from an iteration greater than 450, implying that 500 iterations are necessary to achieve the best profile.

The computer time used by this method was more than two orders of magnitude greater than that used by methods A or C. This made global initialization impossible and only one latitude band was initialized by this method. Further evaluation of this method is dependent on the development of faster supercomputers. In addition, without global initialization, the moisture profiles generated could not be evaluated, because the evaluation procedure involves the use of the FSUGSM, which requires a global data base.

#### 4.3 Method C – Six parameter initialization

The six parameter initialization method utilizes the OLR and five layers of clouds observed by the satellite. This method uses the bisection method used in Method A. In addition, just as in Methods A and B, only the moisture is varied. The variation of the moisture leads to diagnostic variations in the computed OLR and cloud

amounts. The convergence criteria in this method is twofold, being a function of both the OLR deviation and the average cloud deviation in the column. The specific criteria for convergence are  $\pm 25\text{W/M}^2$  and  $\pm 20\%$  in average OLR and cloud deviation.

To start the bisection method, the root must be bracketed. In the first iteration the value  $x_1$  is the original analyzed moisture profile. The value of  $x_2 = x_1 * F_n$ , where  $F_n$  is an iteration factor which may vary from 0.0 to 2.0. To test whether  $x_1$  and  $x_2$  bracket the root, the arithmetic sign of  $f(x_1) * f(x_2)$  is determined (where  $f(x_n)$  is a function of both the OLR error and the average cloud error through the column). If the arithmetic sign of  $f(x_1) * f(x_2)$  is less than zero, then the root is bracketed and the bisection method is used to find the root. If the arithmetic sign is greater than zero, then the root is not bracketed. In this case the procedure is repeated using  $x_1' = \text{MIN}\{\text{ABS}[f(x_1)], \text{ABS}[f(x_2)]\}$  and  $x_2' = x_1' * F_n$ . This is repeated until bracketing is achieved, and then the bisection method is used.

## CHAPTER V

### INITIALIZATION RESULTS

#### 5.1 Introduction

This chapter discusses the results of moisture initialization experiments. The experiments in section 5.2 use OLR as the sole criterion for initialization. A dramatic improvement in the OLR forecast is made in this experiment. Figure 5.1 shows the verification of the control and moisture initialization experiment. When the integration begins, the moisture initialization experiment verified 38 percent better than the control experiment. After five days of integration, the moisture initialization experiment verified more than 30 percent better than the control experiment. The OLR of the five day moisture initialized experiment has approximately the same verification score as the control experiment before the integration begins. This gives the moisture initialization experiment a five day advantage in forecasting the OLR. In section 5.2, the ISCCP cloud data set and the OLR are the criteria for initialization.

## OLR PER CENT CORRECT VS FCST DAY

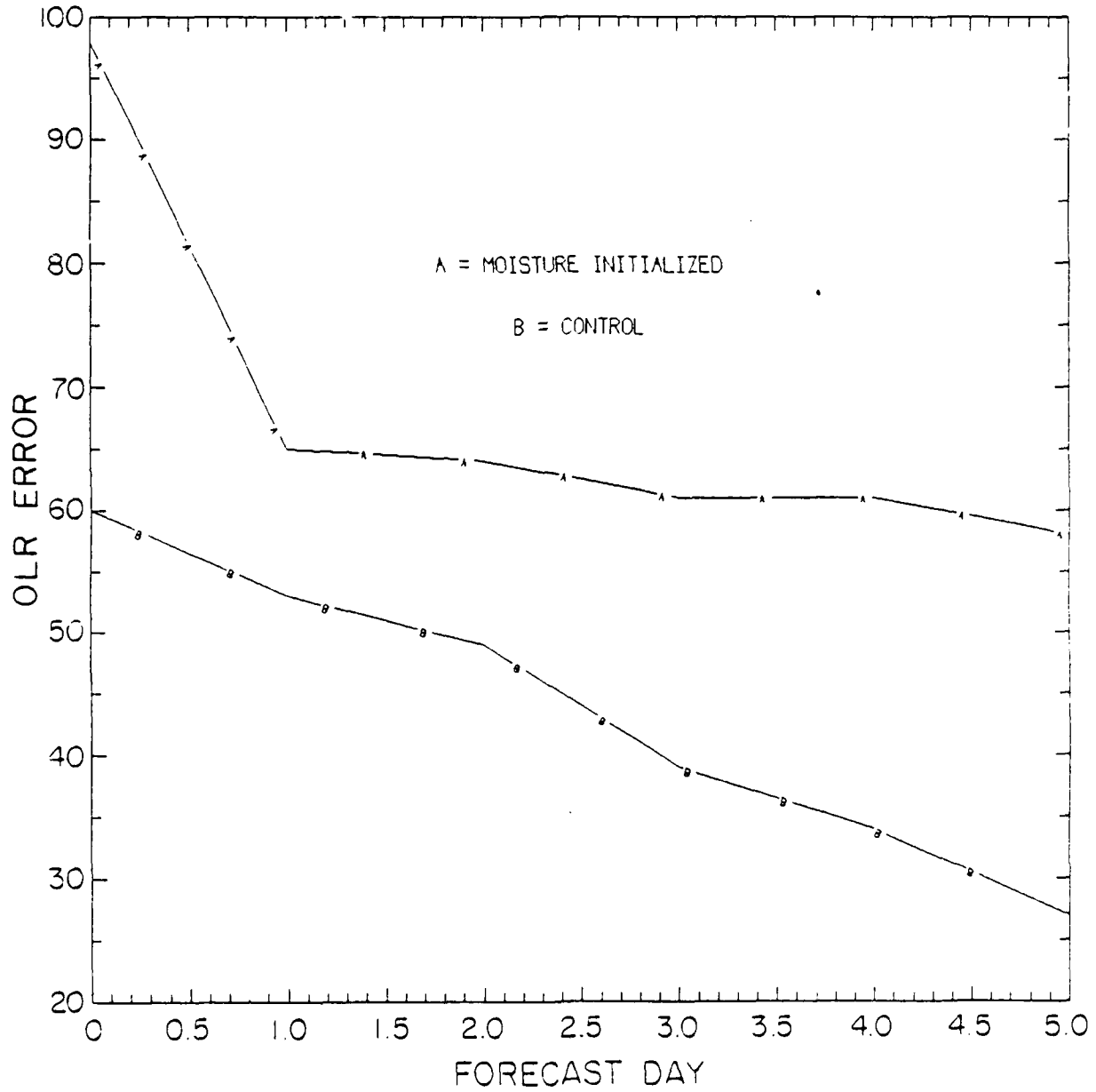


Figure 5.1 Verification of the control and moisture initialization experiments as a function of time.

## 5.2 Moisture initialization using OLR

The moisture initialization of this experiment was accomplished by the single parameter method described in section 4.1. The computed OLR is determined from the analysis fields of moisture, temperature, and pressure. If the absolute difference between the calculated and satellite observed OLR is more than  $10 \text{ Wm}^{-2}$ , the moisture values are varied until convergence is achieved. The type of iteration scheme used to achieve convergence is bisection. In this scheme, the interval between the last two iterated values is constantly halved until the convergence criterion is satisfied. Convergence was usually achieved in less than five iterations. After initialization, the data was integrated for five days with the T42 FSUGSM. The control experiment did not initialize the moisture data; the analysis fields were used unmodified to start the integration. Verification of the resultant OLR of the control and the initialized data was made by comparison to satellite-observed OLR. Those grid points within a specified absolute difference are considered correct; those greater than the absolute difference are considered incorrect. The verification is reported as the percent correct.

### 5.2.1 Discussion of the satellite observed OLR

Figure 5.2 shows the satellite observed OLR for the period 12 GMT July 27, 1979 through 12 GMT August 1, 1979. The shading indicates areas of OLR less than  $240 \text{ Wm}^{-2}$ . There are several areas that are particularly noteworthy in this figure. The ITCZ is evident across the Atlantic and Pacific Oceans as an area of OLR less than  $280 \text{ Wm}^{-2}$ . This is due to the fact that the cloud tops in the ITCZ radiate at lower temperatures than the surrounding ocean regions. The shaded regions of the ITCZ, where the OLR is less than  $240 \text{ Wm}^{-2}$ , stand out to demarcate the stronger, more vigorous areas of active convection. The large values of OLR over the North African

and Saudi Arabian deserts are in contrast to these low tropical OLR observations. The arid desert areas have no cloud cover and little atmospheric moisture. Because of this, the surface radiation traverses the atmosphere unimpeded, yielding OLR values in excess of  $320 \text{ Wm}^{-2}$ .

Two synoptic features with OLR signatures due to their cloud cover are the monsoon and Typhoon Hope. The cloud cover of the monsoon is evident as a large shaded area from the Arabian Sea to the Bay of Bengal, including India. There are also strong areas of convection in the Arabian Sea and the Bay of Bengal, with satellite OLR observations of less than  $160 \text{ Wm}^{-2}$ . Typhoon Hope was active during this period, and its signature is evident in the OLR observations. At 12 GMT July 27, 1979, Typhoon Hope was a tropical depression, located at  $15^\circ$  North and  $139^\circ$  East. At this location, there is a small area with observed OLR values of  $120 \text{ Wm}^{-2}$ . Although this small OLR is not maintained throughout the lifecycle, the  $120 \text{ Wm}^{-2}$  radiation of the Typhoon Hope cloud tops is observed again in the 12 GMT August 1, 1979 OLR panel just south of Taiwan.

A constant OLR feature seen in all of the panels of figure 5.2 is the  $280 \text{ Wm}^{-2}$  contour extending from western South America to  $100^\circ$  West. It can be attributed to several synoptic features. The cold waters of the Peruvian Current keep the sea surface temperatures cool in this area. The Andes Mountain chain also has cool surface temperatures due to its high elevation. Additionally, there is a high pressure system at  $120^\circ$  West and  $25^\circ$  South, with a counterclockwise circulation (Southern Hemisphere). This circulation causes a southerly wind to advect cool air along the coast of western South America. These three features cause the local surface temperatures to be cooler than the surrounding areas, resulting in lower observed OLR values.

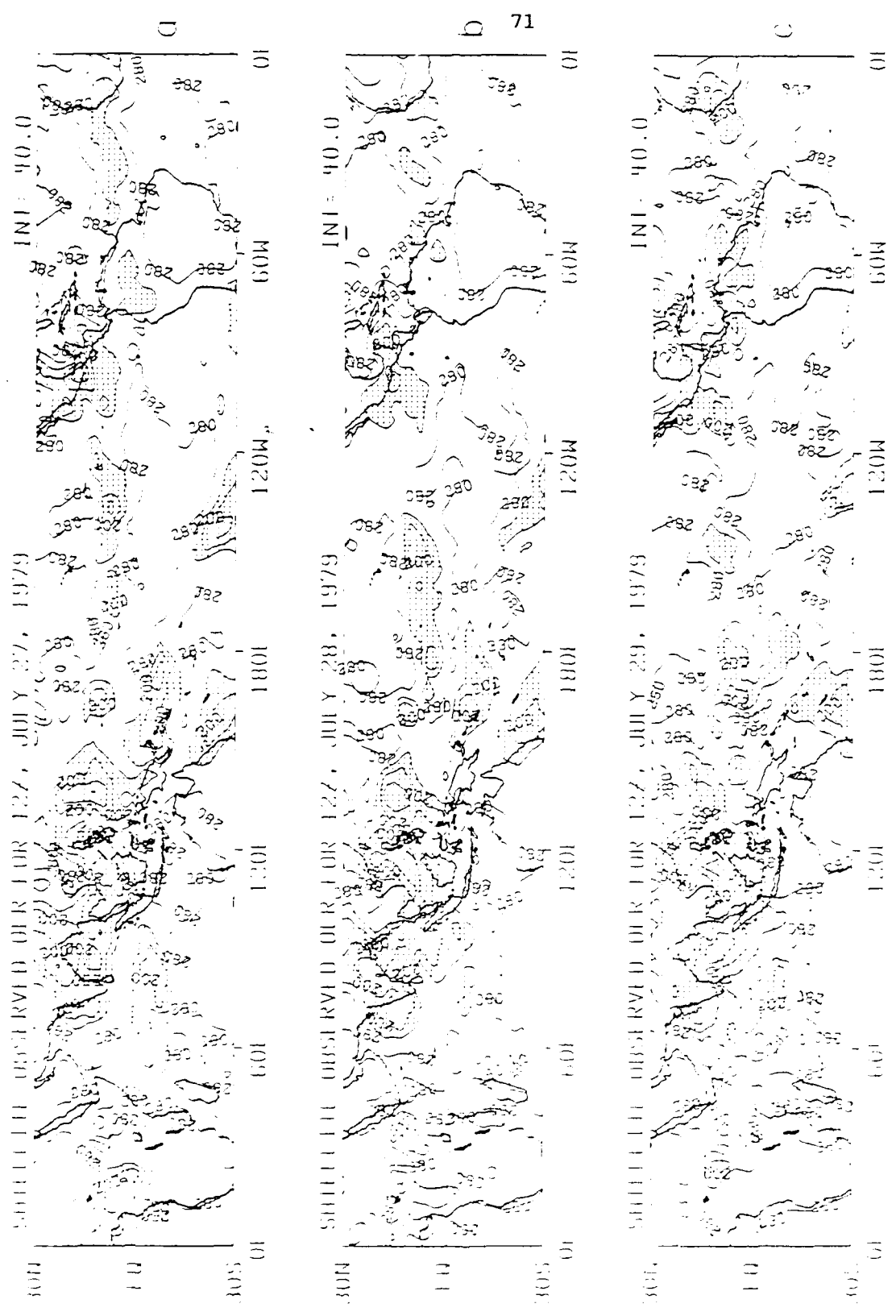
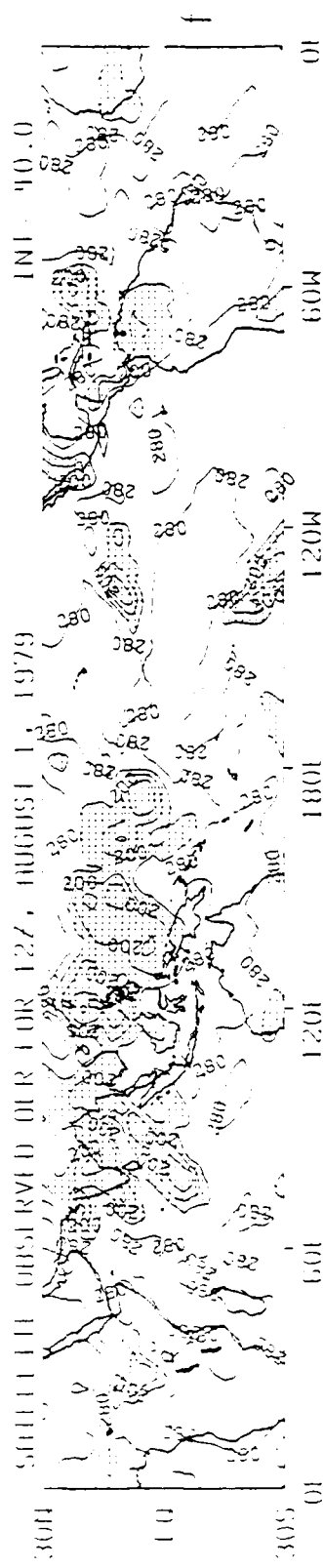
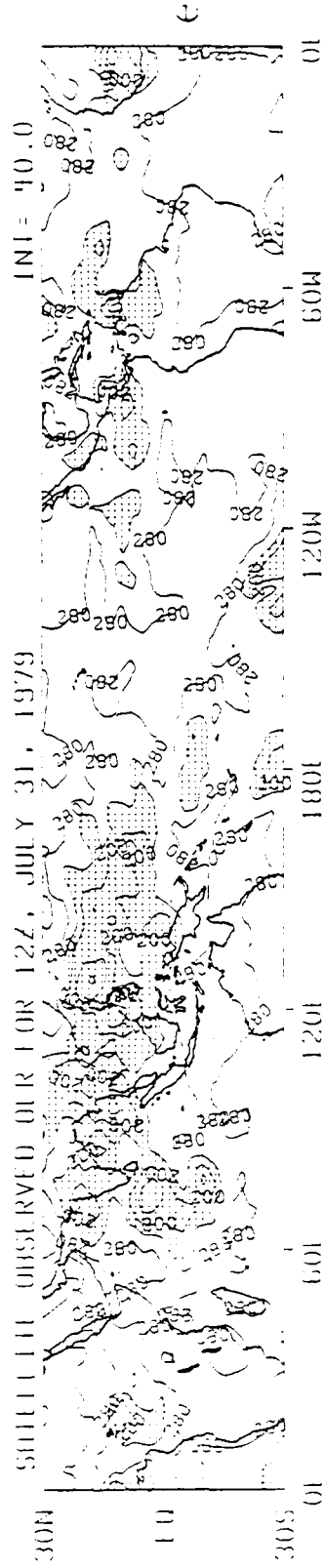
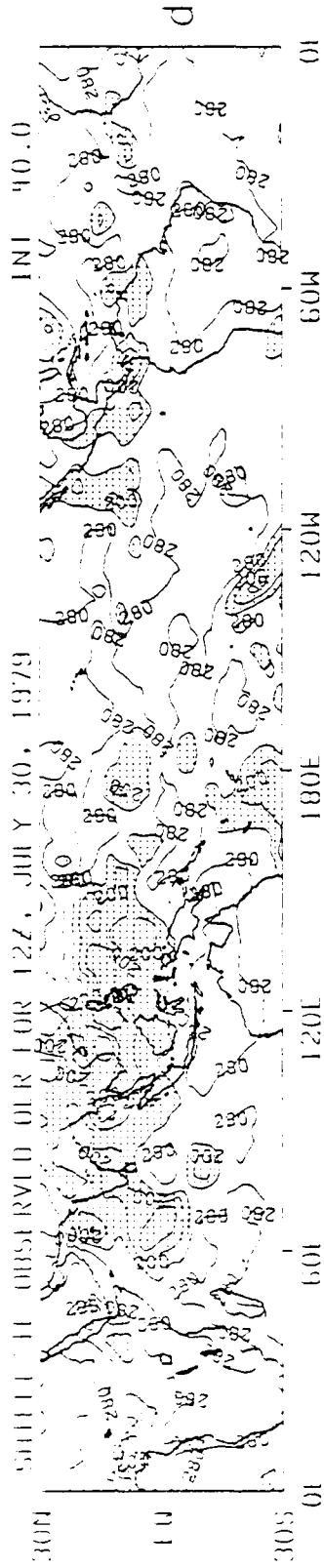


Figure 5.2a through f Satellite observed OLR for the period 12 GMT July 27, 1979 through 12 GMT August 1, 1979. (Shading indicates areas of OLR less than  $240 \text{ Wm}^{-2}$ ).



### 5.2.2 Discussion of the control experiment OLR

Figure 5.3 shows the OLR results of the control experiment. It is immediately obvious that the OLR values are larger than observed across the tropics and that the gradient of OLR is very small. This is due to the poor moisture analysis. It can also be seen that the OLR values increase with time. The FSUGSM has a systematic error with moisture loss. The decrease in moisture means that there are less clouds. With fewer clouds, the surface radiation will escape to the top of the atmosphere, resulting in a larger diagnosed OLR. This can be seen in the control experiment by comparing the 12 GMT July 27, 1979 panel with the 12 GMT August 1, 1979 panel. The ITCZ of the Atlantic and Pacific Oceans is much weaker in the first panel of figure 5.3 than in the first panel of the satellite observed OLR of figure 5.2. As time progresses, the ITCZ signature virtually disappears from the control experiment, due to the drying of the upper levels. Generally, by the end of the integration, the only OLR values less than  $280 \text{ Wm}^{-2}$  are those associated with convective cells; small regions where the moisture is continuously being transported from the lower to the upper levels. There are very few areas of large scale OLR less than  $280 \text{ Wm}^{-2}$ . The drying of the atmosphere is not only noticeable in the convective regions of the ITCZ, but also in the deserts of North Africa and Saudi Arabia. At the analysis time, North Africa and Saudi Arabia have been correctly diagnosed with an OLR value of  $320 \text{ Wm}^{-2}$ . As the atmosphere dries in the panels that follow, more of longwave surface radiation will reach the top of the atmosphere. The OLR grows until it finally reaches values in excess of  $360 \text{ Wm}^{-2}$ . This is an error of more than  $40 \text{ Wm}^{-2}$ .

The OLR values in the regions of the monsoonal trough and Typhoon Hope also increase with time. The OLR in the monsoon region of the control experiment is generally greater than in the satellite observed panels. This shows the atmosphere is

drying. By the fifth day of the integration, the Bay of Bengal contains little upper level cloudiness (large OLR) and only small areas of convection in the Arabian Sea and India. The movement of Typhoon Hope can be seen easily in the last few panels. The convective nature of Typhoon Hope builds clouds in the upper levels and decreases the OLR values throughout the forecast. By the end of the model integrations, there is a local maxima over Taiwan due to the convective activity in Typhoon Hope.

One of the few features that persists through all of the integrations is the  $280 \text{ Wm}^{-2}$  OLR over the Andes Mountain range. The model diagnoses this higher mountain region, with colder surface temperatures, as an area of lower OLR.

### 5.2.3 Discussion of the moisture initialization experiment OLR

The resultant OLR fields of the initialization experiment are shown in figure 5.4. After moisture initialization the data were integrated for 120 hours using the T42 FSUGSM. In this experiment, the FSUGSM was modified to prevent atmospheric drying by invoking constraints to conserve the first- and second-order global average of moisture throughout the forecast. This ensures that the OLR will not increase over the tropics and that the average of the tropical cloud amounts will stay constant.

The differences between the observed OLR and the moisture initialized OLR (12 GMT July 27, 1979) are minimal. In both panels the OLR values and the gradients are comparable throughout the tropics. The initial panel of figure 5.4 shows an active, vigorous ITCZ in the Atlantic and Pacific Oceans. The ITCZs persist throughout the five days of integration. This is in sharp contrast to the control experiment, which had

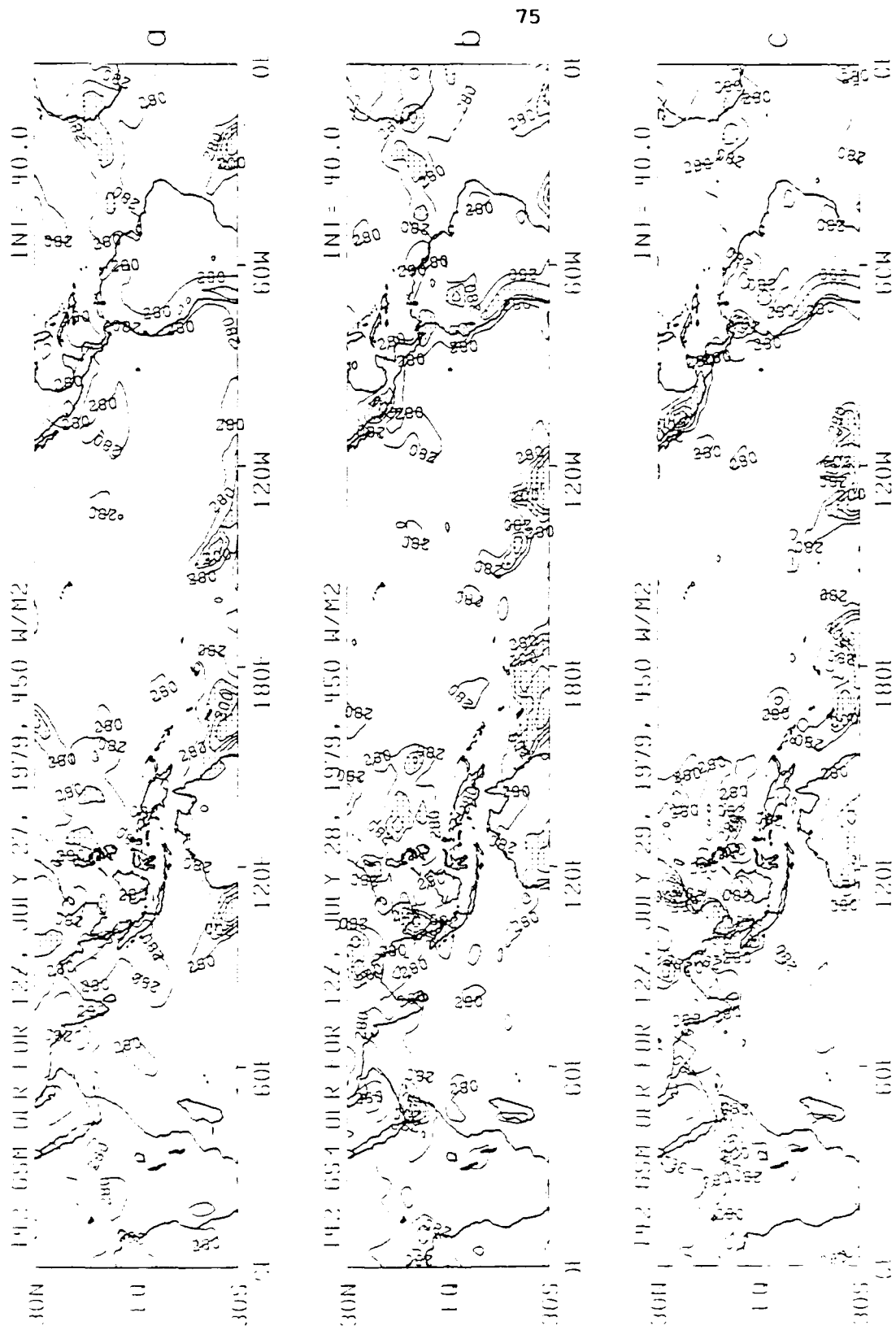
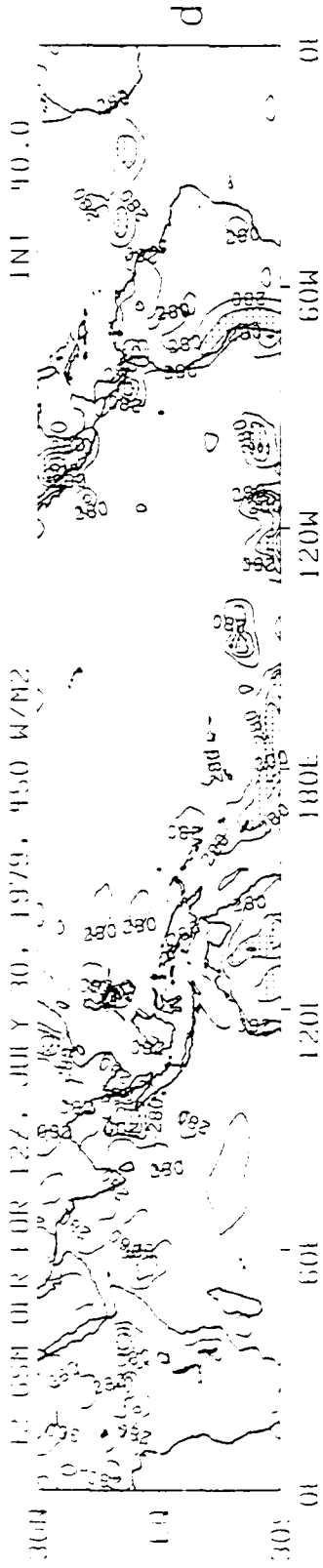
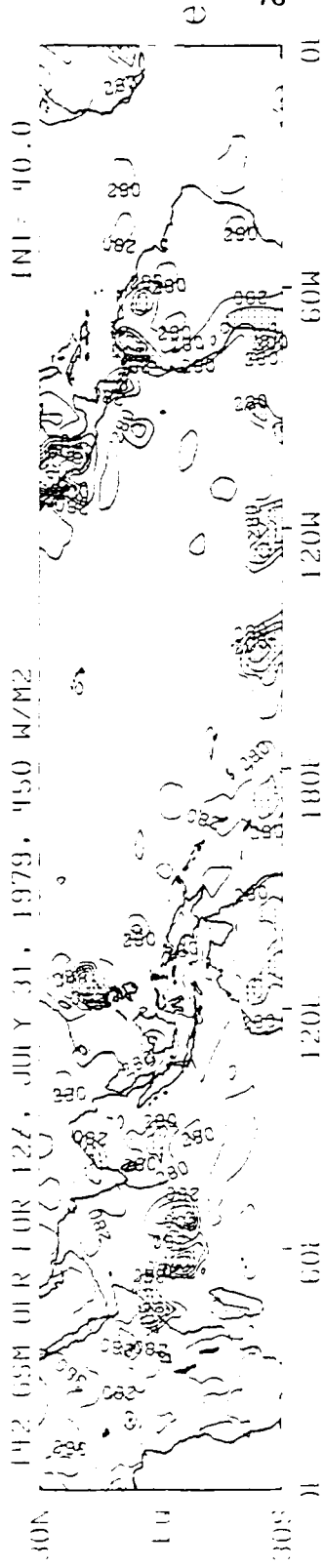


Figure 5.3a through 5.3c are contour plots of OLR for the period 12 GMT July 27, 1979 through 12 GMT August 1, 1979. (Shading indicates areas of OLR less than 240  $Wm^{-2}$ ).

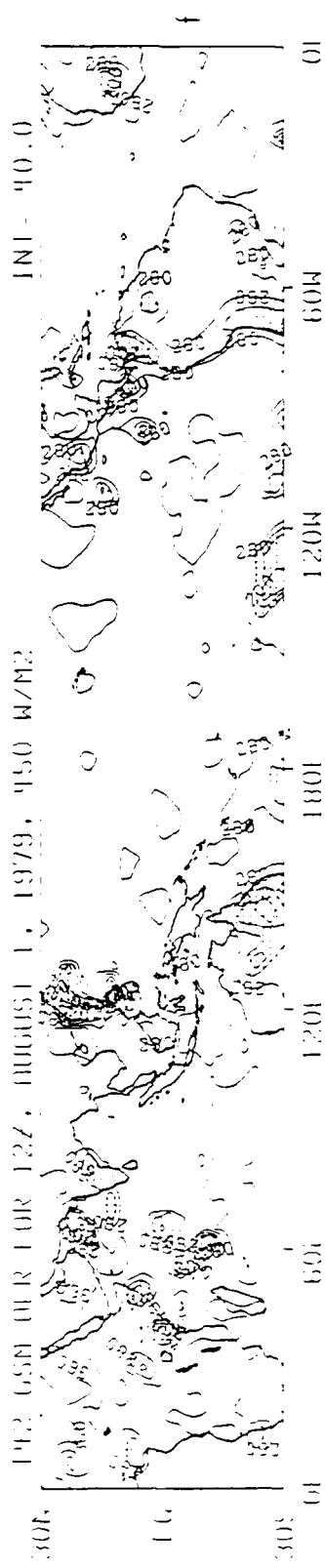
12. GSM OLR FOR 127, JULY 30, 1979, 450 W/M2



142. GSM OLR FOR 127, JULY 31, 1979, 450 W/M2



143. GSM OLR FOR 127, AUGUST 1, 1979, 450 W/M2



no initial Pacific Ocean ITCZ signature in the OLR fields, and completely lost the Atlantic ITCZ by the fifth day of integration. The dry deserts of North Africa and Saudi Arabia have a OLR signature just as distinct as the ITCZ. The desert of North Africa correctly remains at  $320 \text{ Wm}^{-2}$  throughout the integration, while portions of Saudi Arabia show a decrease below  $320 \text{ Wm}^{-2}$ . This is an improvement from the control experiment, which continued to dry throughout the integrations and achieved a final OLR error of  $40 \text{ Wm}^{-2}$  too large.

The synoptic features of the monsoon and Typhoon Hope are also evident in the OLR charts. The OLR of the monsoon in the initial panel of figure 5.4 is in close agreement with the satellite observed OLR. Although the intensity of the OLR is not maintained for five days, the area of the monsoon is correct. At the end of the integration, a band of low OLR values extends westward across equatorial Africa, and then across the Arabian Sea, India, and the Bay of Bengal. The control experiment had only isolated areas of convection by the end of the integration in these areas. The OLR signature of Typhoon Hope can be followed through the entire forecast. At the end of the forecast, it is an area of OLR minima to the southwest of Taiwan.

The constant feature of the low OLR over the Andes mountain chain is in 11 panels of figure 5.4. This feature is a result of higher elevations of terrain with colder surface temperatures.

#### 5.2.4 Verification and comparison

In the previous section, it was qualitatively noted that the moisture initialized experiment performed better than the control experiment. This section will quantify those results. Figure 5.1 is a comparison of the verification of the two experiments. The percentage of correct points is shown as a function of the forecast day. Data

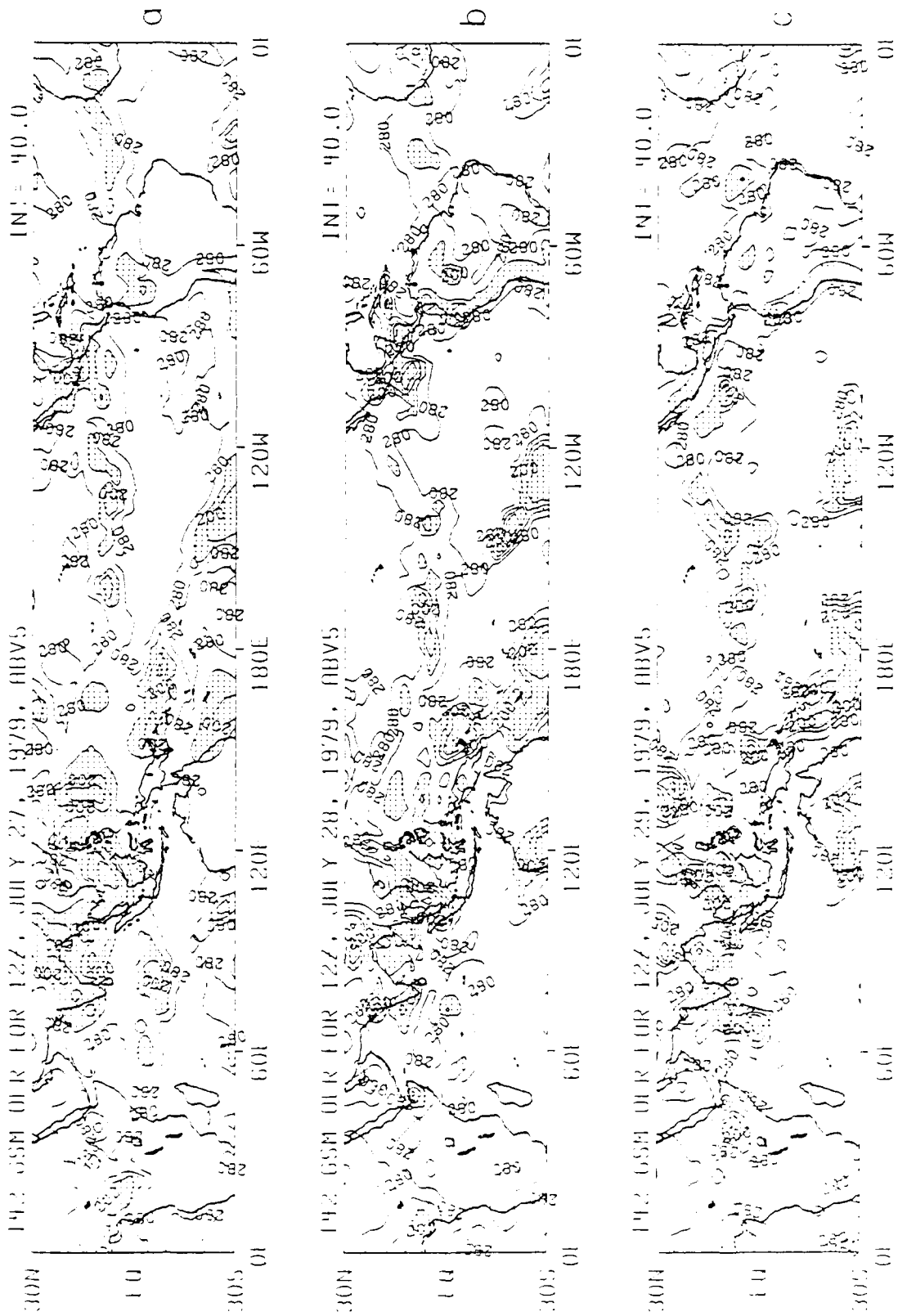
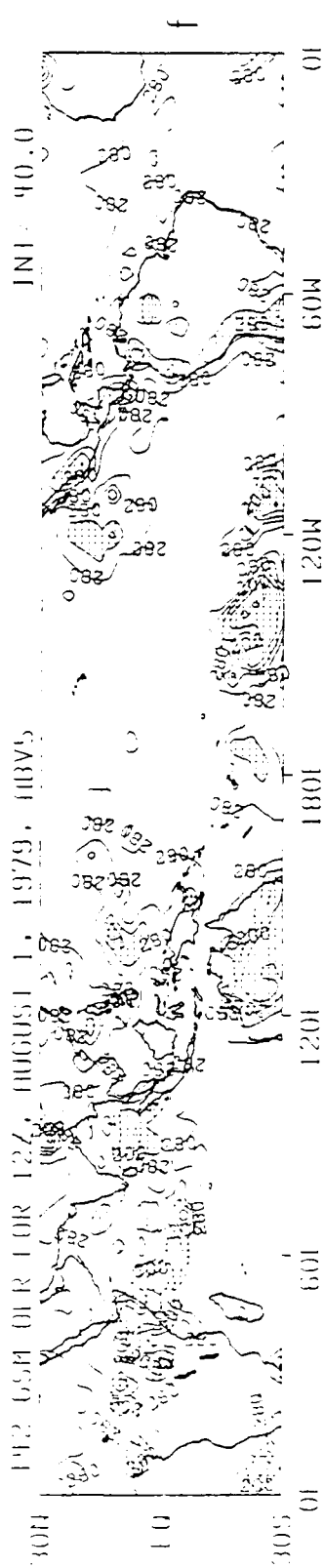
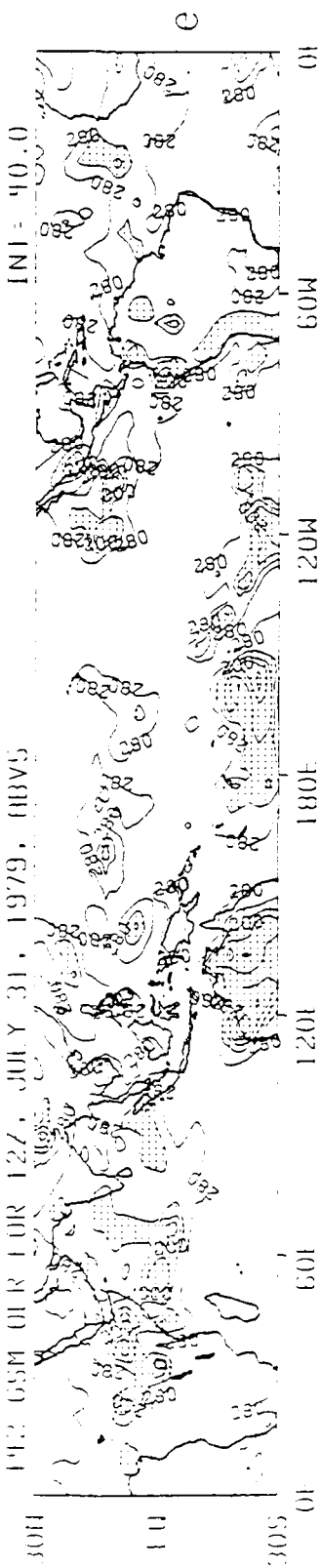
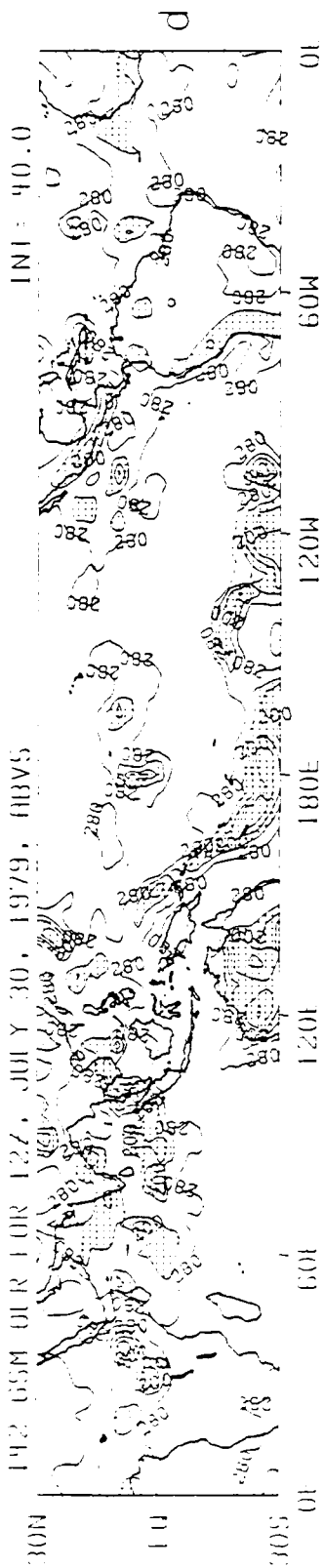


Figure 5.4a through f. OLR of the moisture initialization experiment for the period 12 GMT July 27, 1979 through 12 GMT August 1, 1979. (Shading indicates areas of OLR less than 240 Wm<sup>-2</sup>).



values are considered "correct" if the forecast OLR values are within  $\pm 20 \text{ Wm}^{-2}$  of the observed OLR values. There is a notable difference between the two experiments at the beginning of the forecast when the moisture initialization experiment has verified 38 % better than the control experiment. After one forecast day, the moisture initialization experiment has verified 12 % better than the control experiment. The difference is 15 %, 22 %, 27 %, and 31 % on the second, third, fourth, and fifth days, respectively. The decrease in the OLR verification of the control experiment already has been attributed to a systematic error of the FSUGSM that decreases the moisture as integration proceeds. To demonstrate this, the diagnosed cloud charts corresponding to each of the OLR figures are shown in figures 5.5 through 5.10. There is a set of charts for the control experiment and a set of charts for the moisture initialization experiment. Each set of charts contain high, middle, and low clouds. The overall tropical cloud patterns of the control experiment are weak and barely discernible, compared to the initialized experiment that begins with cloud patterns which are easily recognizable as tropical synoptic conditions. This implies that the cloud and radiative initialization favorably affects the FSUGSM producing forecasts of clouds (high, middle, and low) and radiation (OLR) that are clearly superior to the control experiment.

The high cloud charts of the control experiment (figure 5.5) show few clouds throughout the integrations. There are almost no clouds in the initial panel. The convective processes of the ITCZ succeed in bringing enough moisture to the upper levels to form clouds in only a few portions of the eastern Pacific Ocean. All other areas of the ITCZ have no high clouds. The monsoon area begins with no high clouds from the Arabian Sea to the Bay of Bengal. By the end of the integration, there are a few small convective cloud areas in the region of the monsoon. Typhoon Hope can be seen as a small band of clouds on the third day of the integration. At the end of the

forecast, the convective activity of Typhoon Hope has brought enough moisture from the lower levels to produce 100 % high clouds over Taiwan. The overall tropical high cloud production by the control experiment was minimal. This can be attributed to a lack of moisture in the initial analysis and the systematic drying of the FSUGSM.

The high cloud chart of the moisture initialization experiment for 12 GMT July 27, 1979 (figure 5.6) has more clouds than the corresponding chart for the control experiment. The high clouds of the Pacific ITCZ are well defined at the start of the forecast, but fragment and dry with time. The Atlantic ITCZ is fragmented throughout the integration. The high clouds of the monsoon area are initially well represented. The Arabian Sea initially has no high clouds, except along the coast of India. The central region of India has scattered high clouds, and the eastern coast and the Bay of Bengal are covered with clouds. This agrees with the overall satellite observed OLR pattern for the monsoon region. As time proceeds, the high clouds move south into the Indian Ocean and the southern Bay of Bengal. Typhoon Hope is located to the south of Taiwan in the final panel. The difference in the initial high cloud depictions of the control and the initialization experiments is the increase in moisture after initialization.

The middle cloud charts of the control experiment (figure 5.7) contain slightly more cloud than the high cloud charts throughout the tropics. The Atlantic Ocean ITCZ initially shows some activity in the middle levels but decreases to almost zero cloud by the end of the forecast. The Pacific Ocean ITCZ has a small amount of convective middle clouds in its eastern and western regions; however, the bulk of the tropical Pacific Ocean is devoid of middle clouds throughout the forecast. The cloud signature of the monsoon area shows some convective activity in the middle clouds, although this activity is much less than is usually associated with the monsoon. Typhoon Hope is discernible in all panels. As with the high clouds, the lack of tropical

middle cloud production can be attributed to a lack of moisture in the initial analysis and the systematic drying of the FSUGSM.

The middle cloud charts of the moisture initialized experiment (figure 5.8) show more cloud than the control experiment. The middle clouds of the Atlantic ITCZ are well represented for the first four days. By the end of the fifth day of integration they begin to dissipate due to the systematic drying of the FSUGSM. The middle clouds of the Pacific ITCZ are intermittent throughout the integration. The monsoon region initially has clouds from the Arabian Sea to the Bay of Bengal. By the fifth day of the integration, there are still clouds throughout the monsoon area, although the quantity is less than in the initial panel. The African rainbelts also are evident in this experiment through the persistence of middle clouds for the entire forecast period. The large initial differences in middle clouds of the two experiments is due to the increase in moisture after initialization.

The control experiment has considerably more low clouds (figure 5.9) than middle or high clouds. The monsoon is initially underrepresented by cloud amount, but then develops slightly more clouds. By the fifth day, the monsoon has again dried and is underrepresented. The Pacific ITCZ also develops more clouds over the first day, and then begins to dry to small convective areas. The Atlantic Ocean ITCZ is initially represented well, extending from Africa to South America. This is true for most of the integration, but some drying has occurred by the end of the integration, when the ITCZ is discontinuous across the ocean. Typhoon Hope is easily followed in all of the panels.

The 12 GMT July 27, 1979 low clouds of the moisture initialization experiment (figure 5.10) are similar to the low clouds of the control experiment. The Atlantic Ocean ITCZ is well represented throughout the integrations, with low clouds extending

from South America to Africa, even at the end of the five day day integration. The Pacific low cloud amount is initially underrepresented by low cloud amount, but significant activity is indicated by the end of the integration across the Pacific Ocean. The monsoon region is also initially underrepresented, but then develops low cloud activity over most of the area. By the end of the integration India is covered by clouds with accompanying clouds in the Bay of Bengal and the Arabian Sea. The low clouds of Typhoon Hope can be followed throughout the integrations.

#### 5.2.5 Discussion

The control experiment suffered from a poor moisture analysis and a systematic drying in the FSUGSM. The moisture initialization experiment, using OLR as a convergence criterion, corrected both of these deficiencies and produced more realistic OLR and cloud patterns than the control experiment. The moisture initialization data verified almost 40 % better than the control data for the zero hour forecast. After five days of integration, the moisture initialization data had approximately the same verification as the zero hour data. This effectively gives a five day advantage when forecasting OLR. Since the OLR is dependent on the cloud distributions, it can also be inferred that the cloud forecast is equally improved, and that this method has an advantage in forecasting clouds.

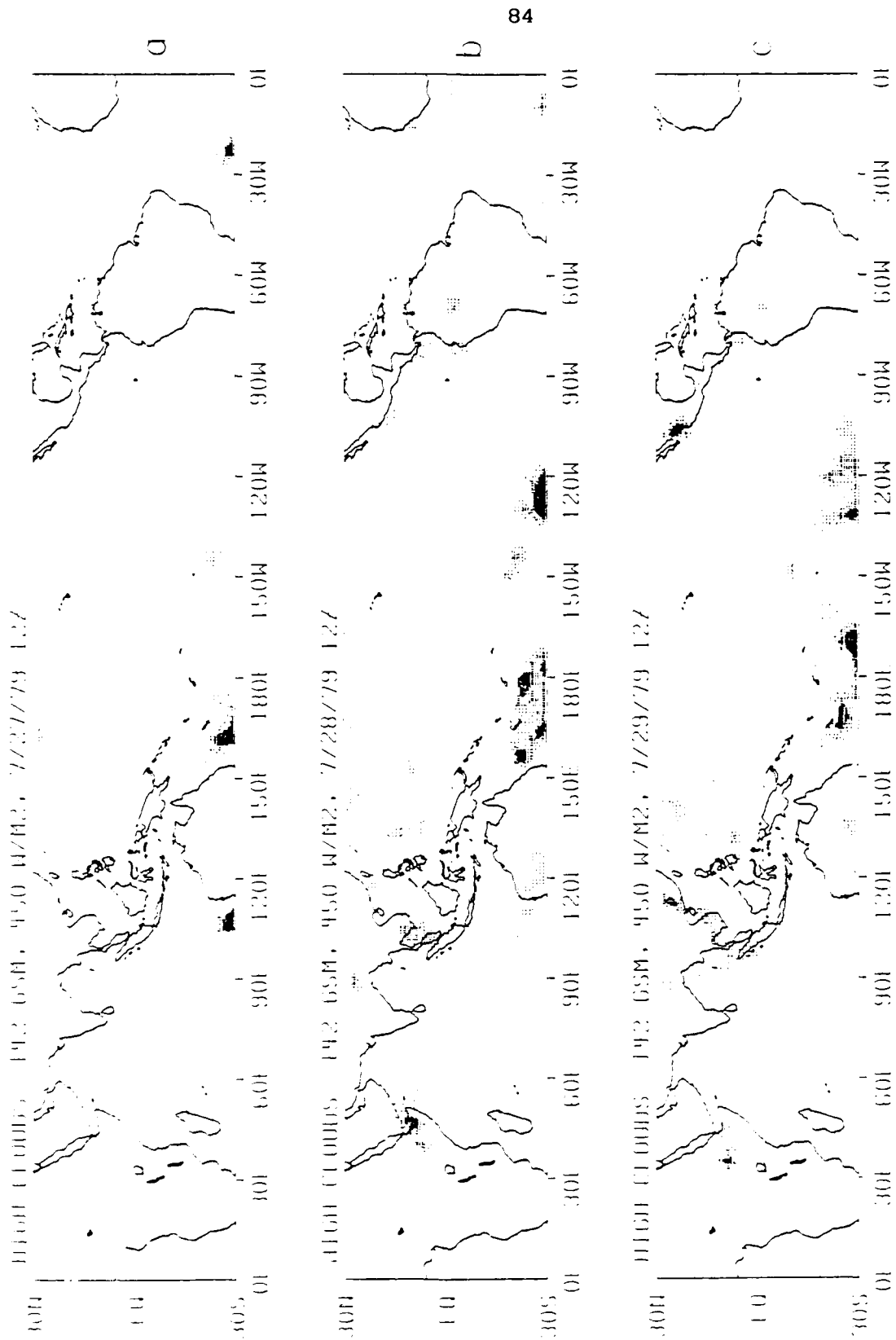
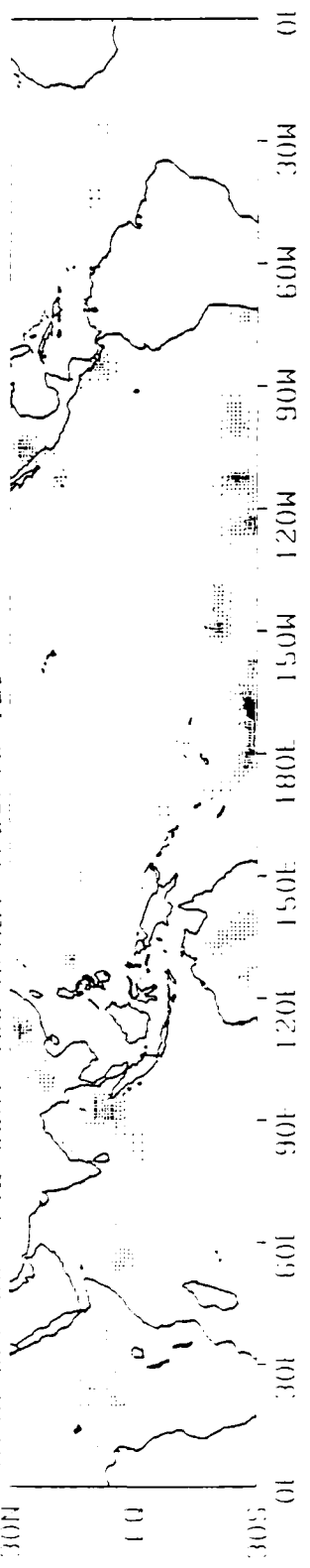
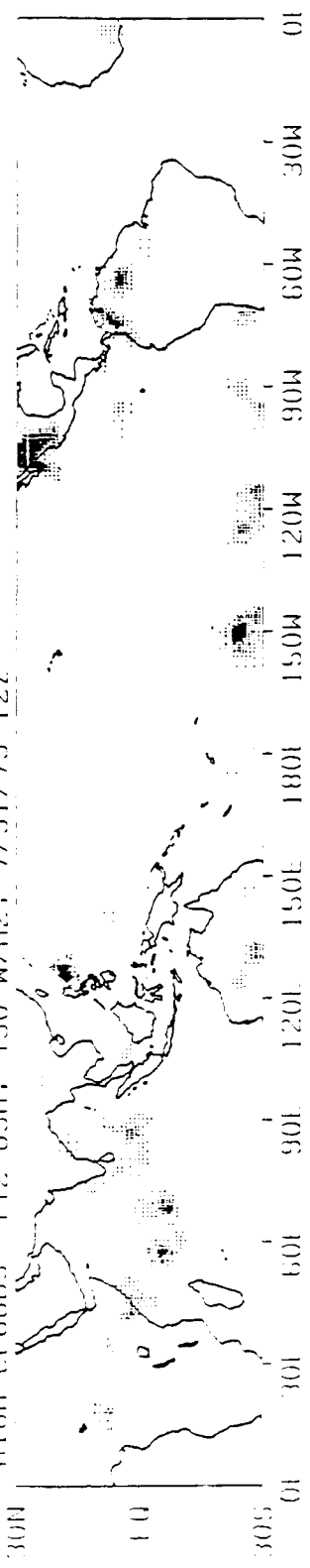


Figure 5.5a through g High clouds of the control experiment for the period 12 GMT July 27, 1979 through 12 GMT August 1, 1979. (Cloud legend in figure 5.5g)

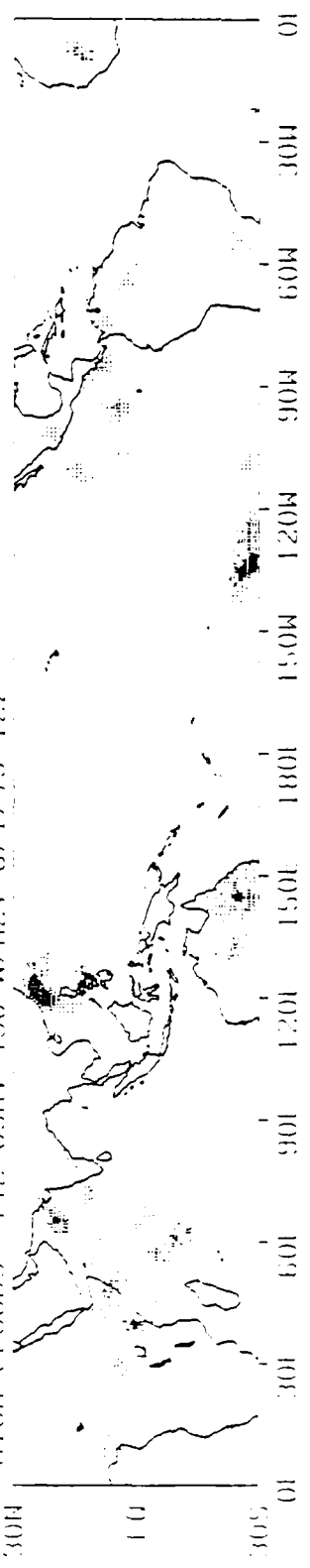
HIGH CLOUDS 142 GSM, 450 W/M2, 7/30/79 12Z



HIGH CLOUDS 142 GSM, 450 W/M2, 7/31/79 12Z



HIGH CLOUDS 142 GSM, 450 W/M2, 8/1/79 12Z



0 - 10

10 - 25

25 - 50

50 - 75

75 - 100

G

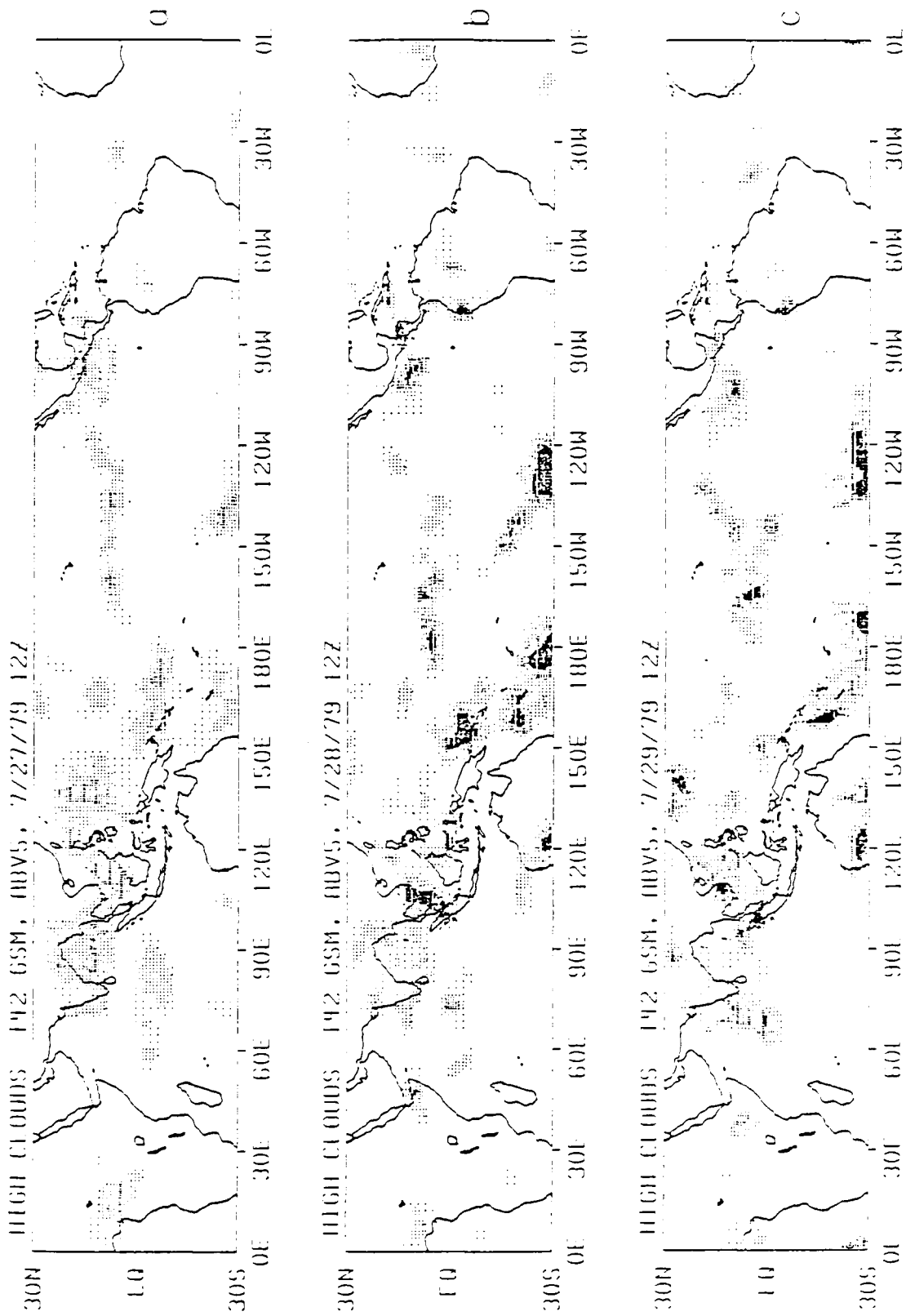
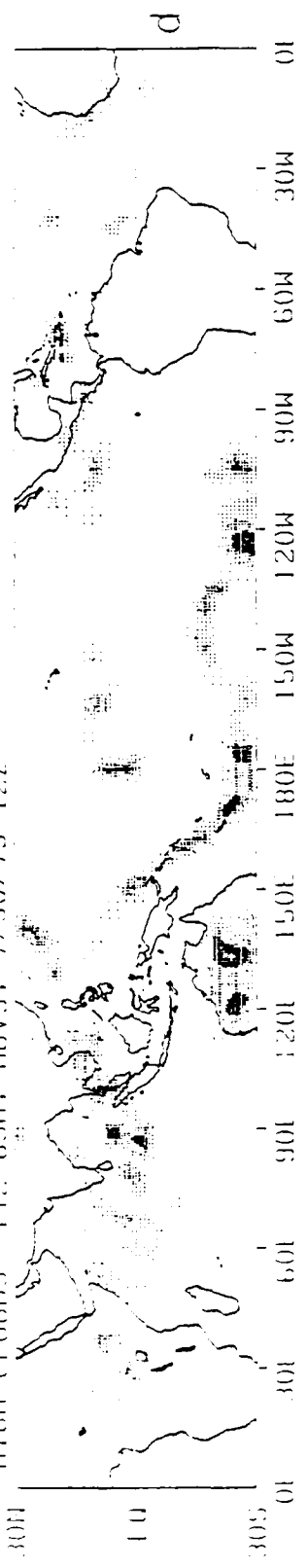
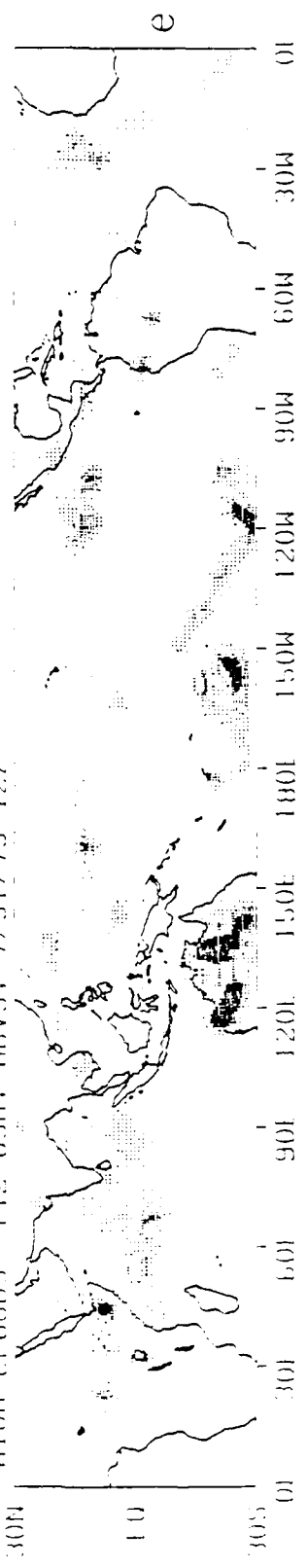


Figure 5.6a through f High clouds of the moisture initialization experiment for the period 12 GMT July 27, 1979 through 12 GMT August 1, 1979. (Cloud legend in figure 5.5g)

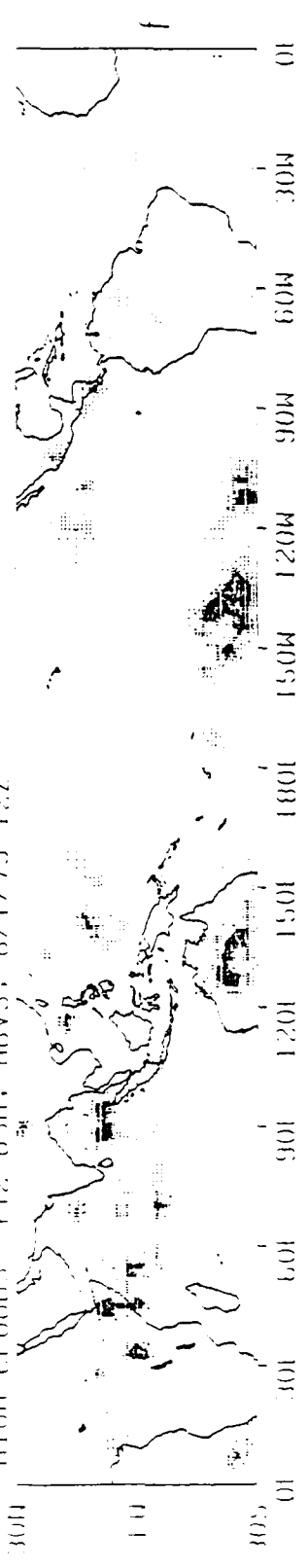
HIGH CLOUDS 142 65M, HBVS, 7/30/79 12Z



HIGH CLOUDS 142 65M, HBVS, 7/31/79 12Z



HIGH CLOUDS 142 65M, HBVS, 8/17/79 12Z



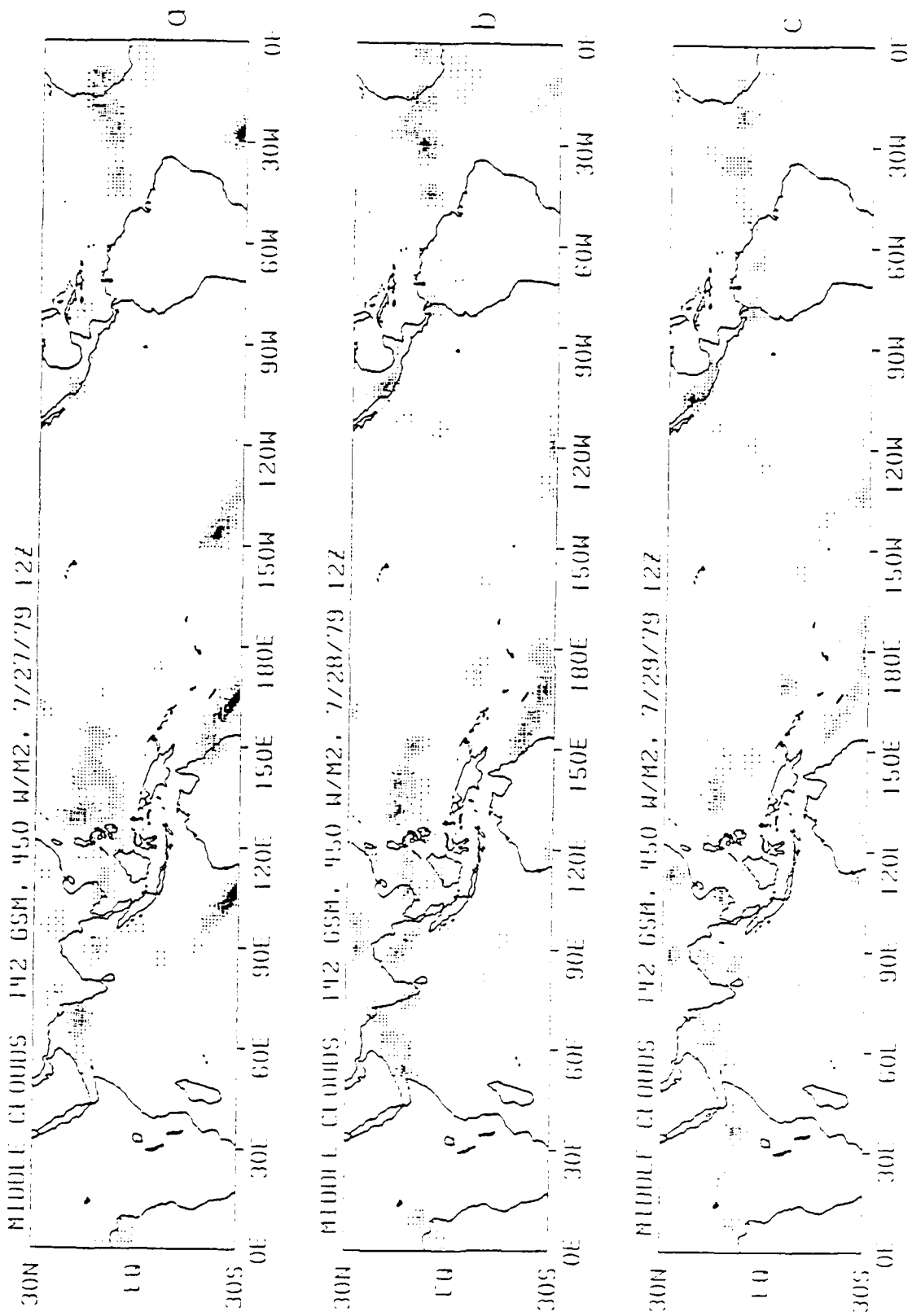
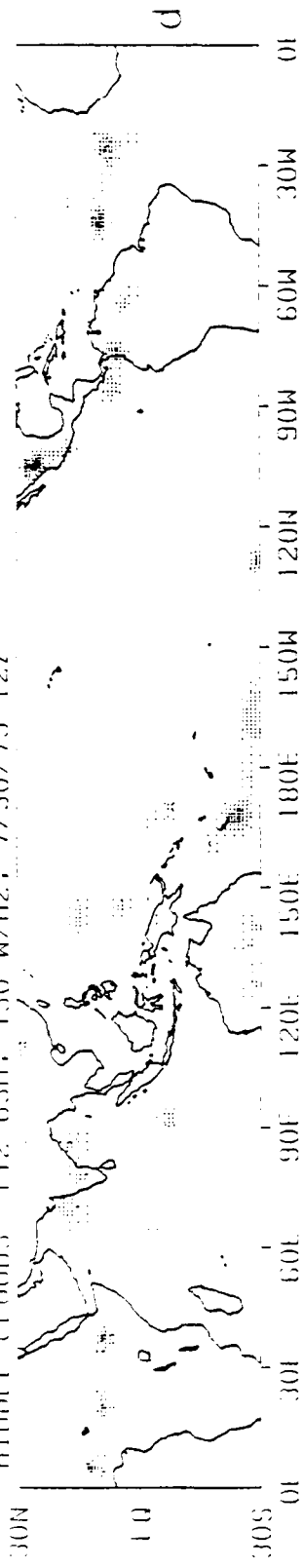
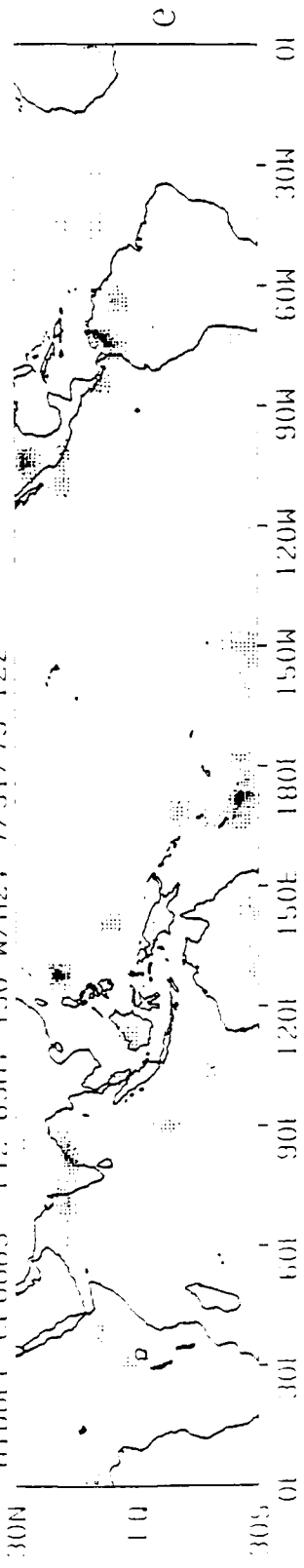


Figure 5.7a through f Middle clouds of the control experiment for the period 12 GMT July 27, 1979 through 12 GMT August 1, 1979. (Cloud legend in figure 5.5g)

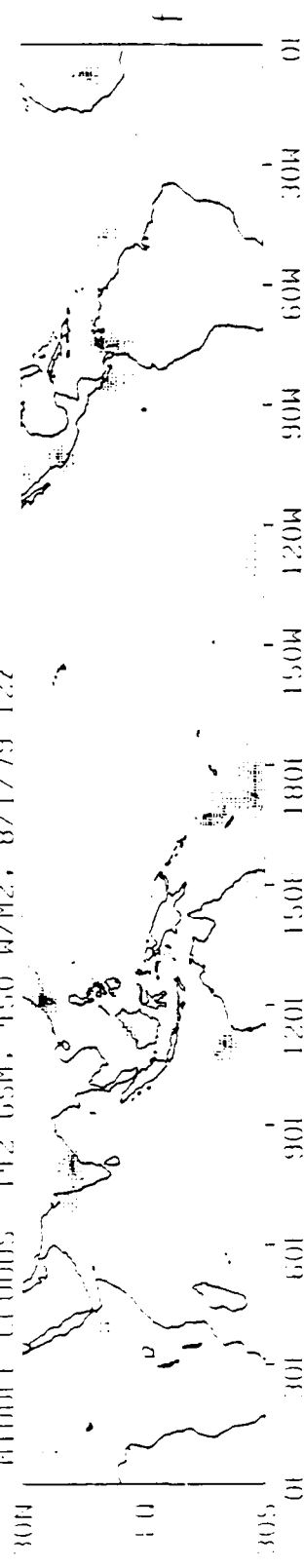
MIDDLE CLOUDS 142 GSM, 450 W/M2, 7/30/79 12Z



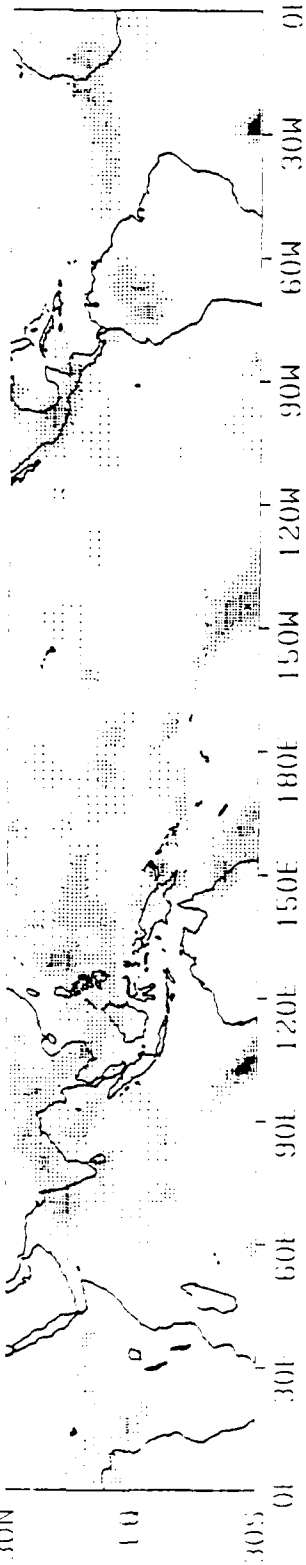
MIDDLE CLOUDS 142 GSM, 450 W/M2, 7/31/79 12Z



MIDDLE CLOUDS 142 GSM, 450 W/M2, 8/1/79 12Z



MIDDLE CLOUDS 142 65M, FBV5, 7/27/79 12Z



MIDDLE CLOUDS 142 65M, FBV5, 7/28/79 12Z

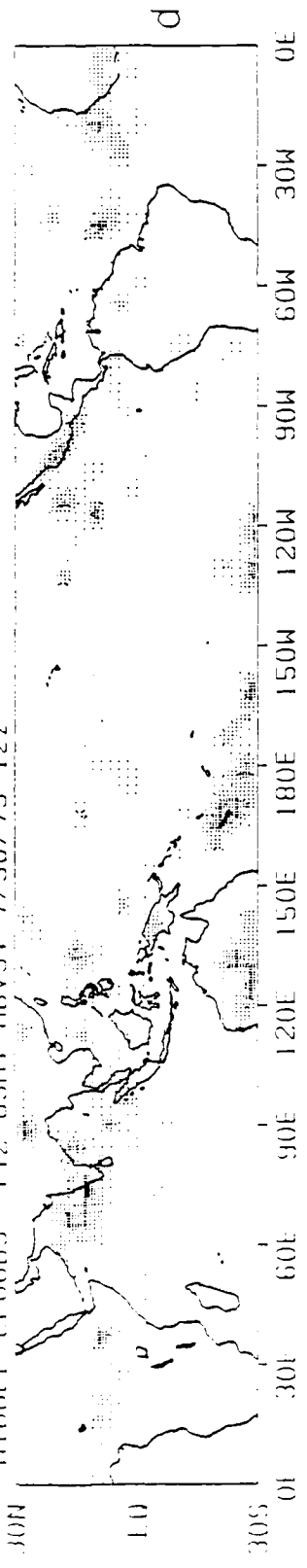


MIDDLE CLOUDS 142 65M, FBV5, 7/29/79 12Z

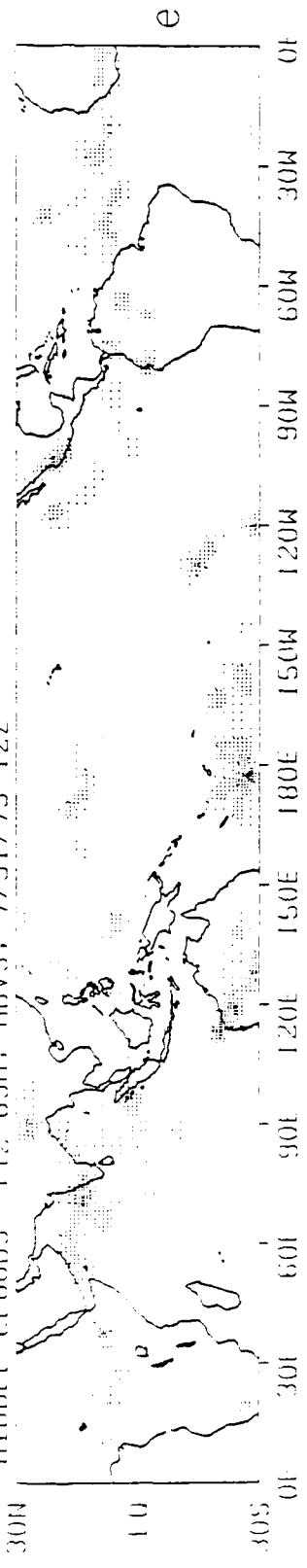


Figure 5.8a through f Middle clouds of the moisture initialization experiment for the through 12 GMT August 1, 1979. (Cloud legend in figure 5.5g)

MIDDLE CLOUDS 142 GSM, HRV5, 7/30/79 12Z



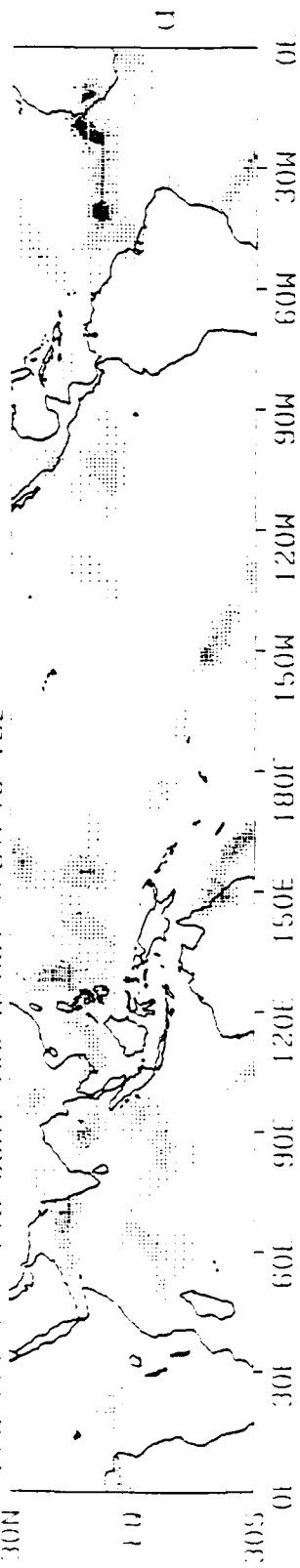
MIDDLE CLOUDS 142 GSM, HRV5, 7/31/79 12Z



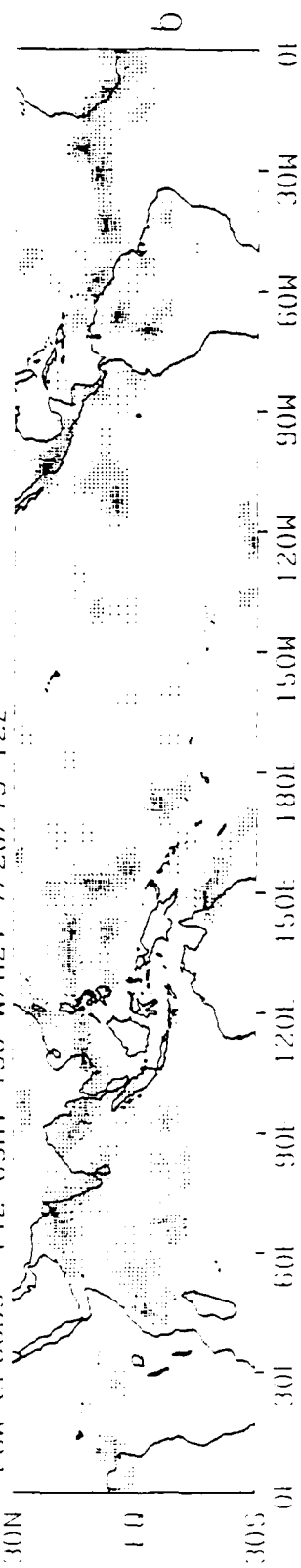
MIDDLE CLOUDS 142 GSM, HRV5, 8/1/79 12Z



LOW CLOUDS 142 G5M, 450 W/M2, 7/27/79 12Z



LOW CLOUDS 142 G5M, 450 W/M2, 7/28/79 12Z



LOW CLOUDS 142 G5M, 450 W/M2, 7/29/79 12Z

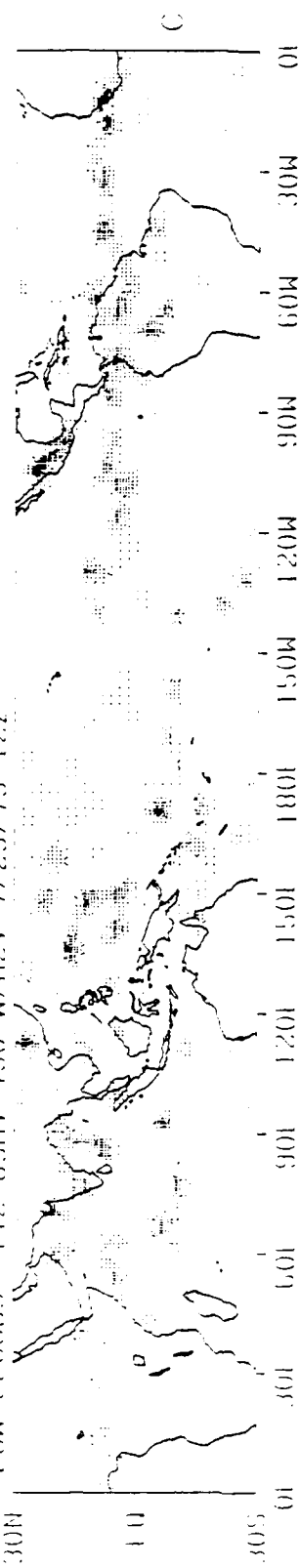
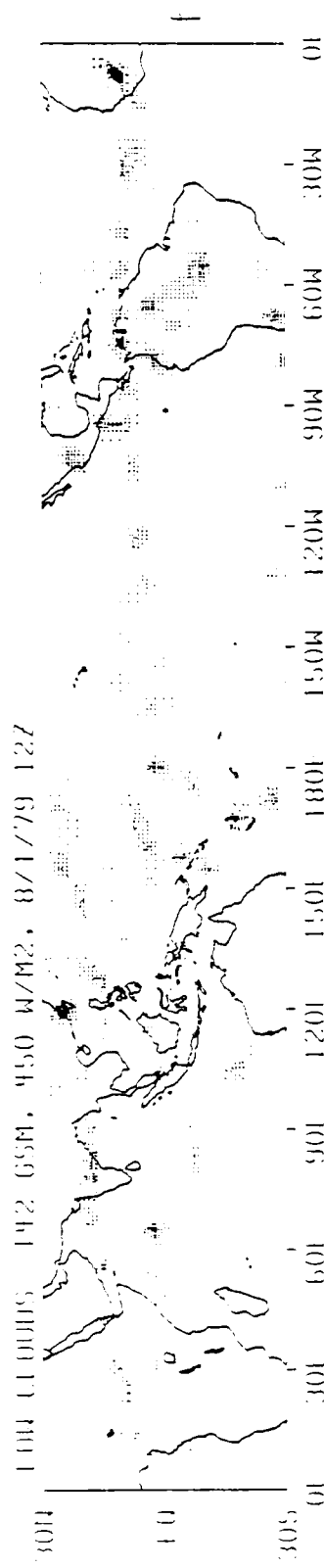
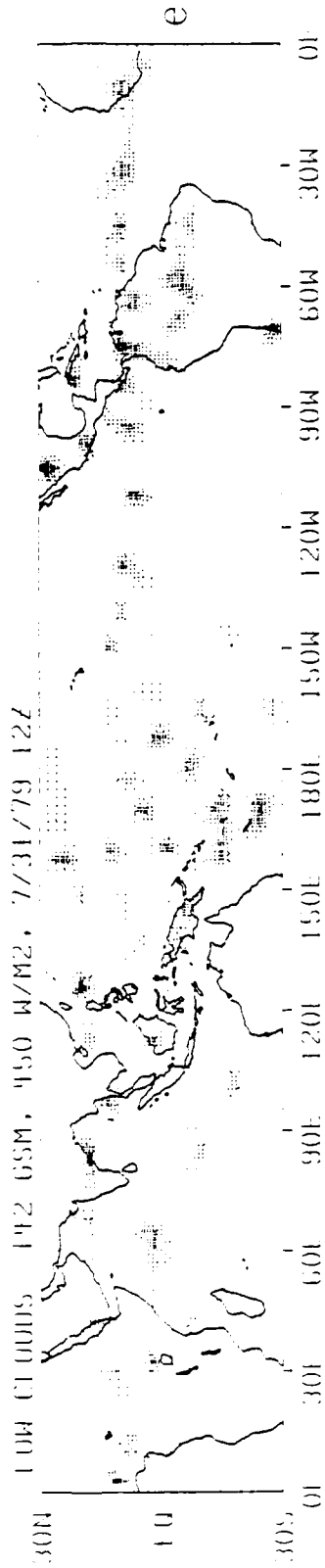


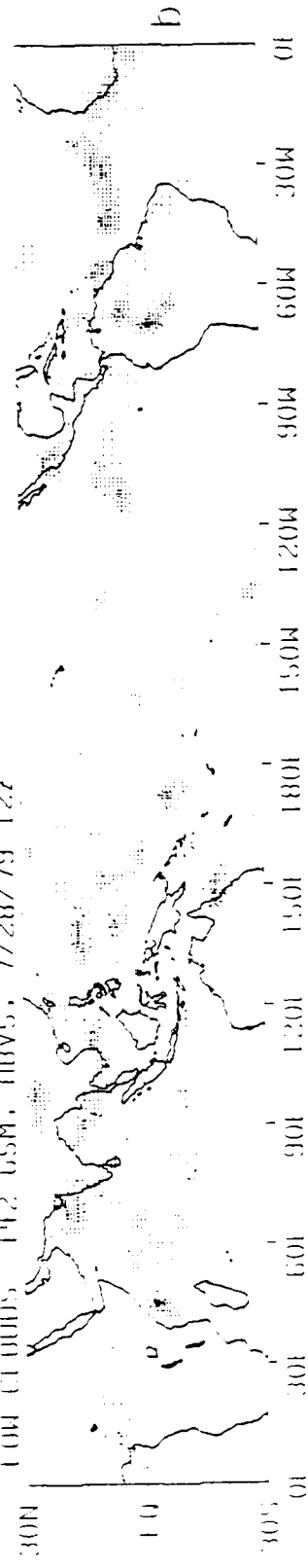
Figure 5.9a through f Low clouds of the control experiment for the period 12 GMT July 27, 1979 through 12 GMT August 1, 1979. (Cloud legend in figure 5.5g)



LOW CLOUDS 142 65M, HBV5, 7/27/79 12Z



LOW CLOUDS 142 65M, HBV5, 7/28/79 12Z



LOW CLOUDS 142 65M, HBV5, 7/29/79 12Z

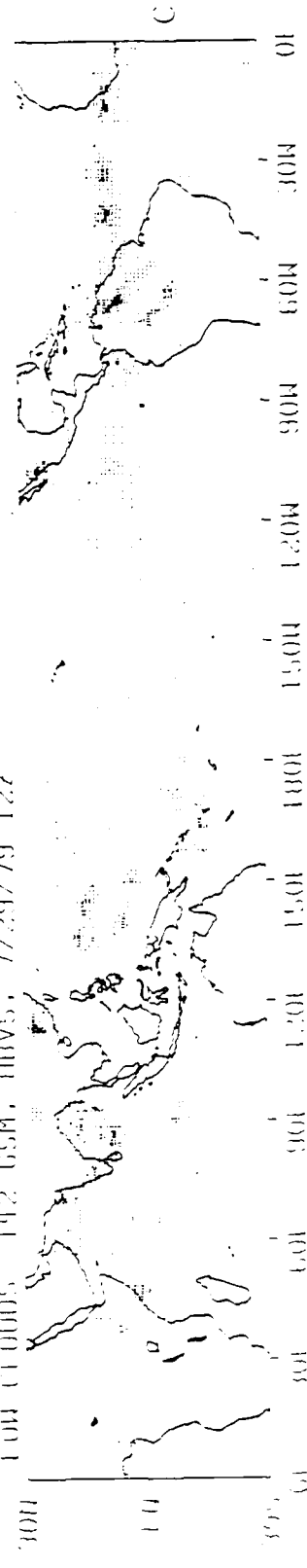
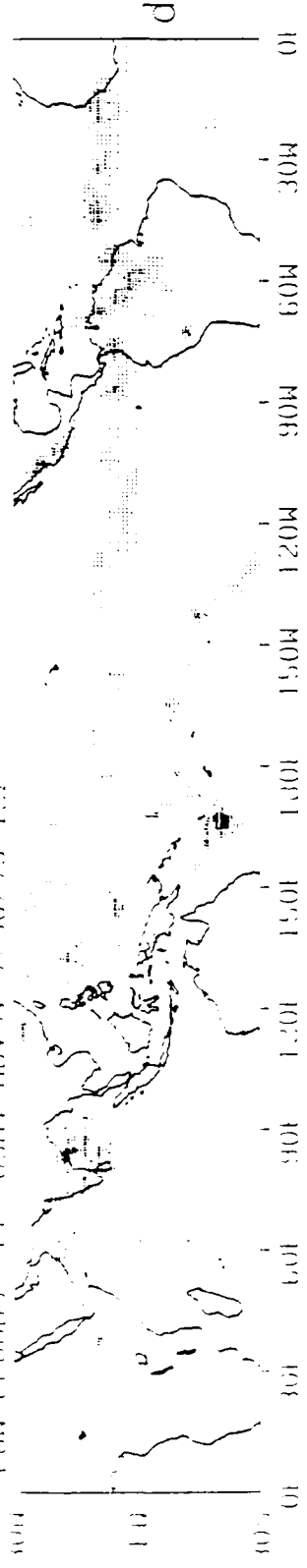
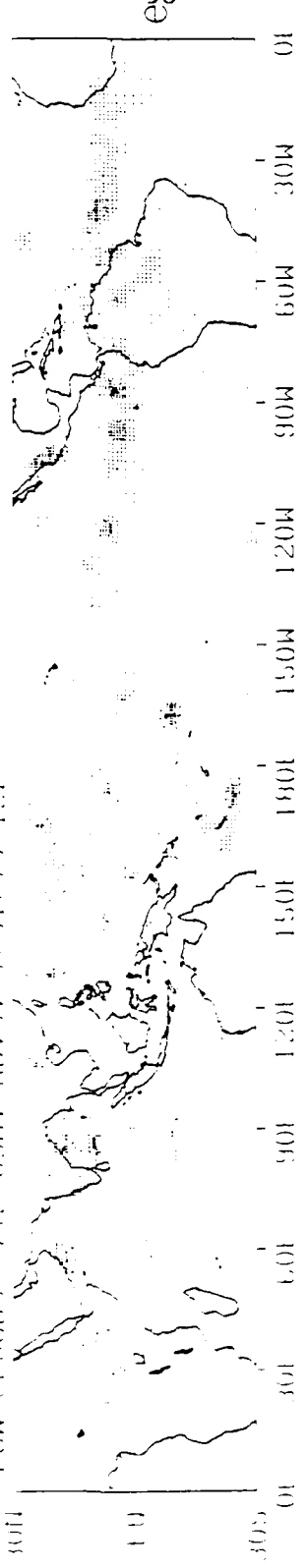


Figure 5.10a through f Low clouds of the moisture initialization experiment for the period 12 GMT July 27, 1979 through 12 GMT August 1, 1979. (Cloud legend in figure 5.5g)

FOR CLOUDS, 1976-79, HBVS, 7/30/79 1.27



FOR CLOUDS, 1976-79, HBVS, 7/31/79 1.27



FOR CLOUDS, 1976-79, HBVS, 8/1/79 1.27



### 5.3 Moisture initialization using clouds and OLR

The moisture initialization of this experiment was accomplished by the method described in section 4.3. After initialization, the data were integrated for three days with the T42 FSUGSM. The control experiment did not initialize the moisture before the integration. Verification of the resultant OLR by the control and the initialized data was accomplished through comparison with the ISCCP data set.

#### 5.3.1 Results

This initialization scheme used the OLR and cloud data of the ISCCP data set for initialization. This data set was described in section 3.1. Case studies of this data have been previously made with the FSUGSM (Krishnamurti *et al*, 1988). This study concluded that the FSUGSM underestimates the low clouds, but predicts middle and high clouds reasonably well. This is in agreement with the present research. The initialization of the data was verified against the ISCCP data set. The results of the verification are presented in figure 5.11. The initialized and control data performed well in the upper and lower levels. The lowest level had the poorest verification in both experiments. A notable point is that the control data had a better verification at the 600 to 800 mb level than the initialized data (69 % versus 54 %).

Both the control and initialization experiments had a tendency to underforecast the clouds. Figure 5.12 shows the cloud verification of the control and initialized forecasts. The bottom two levels of the ISCCP data were poorly forecast in both cases, with the upper and middle levels being forecast much better. There was no significant difference between the upper and middle level verification of either forecast. At the 600 to 800 mb level the initialized cloud forecast verified better than the control cloud forecast. This is opposite of the zero hour verification. The OLR verification shows

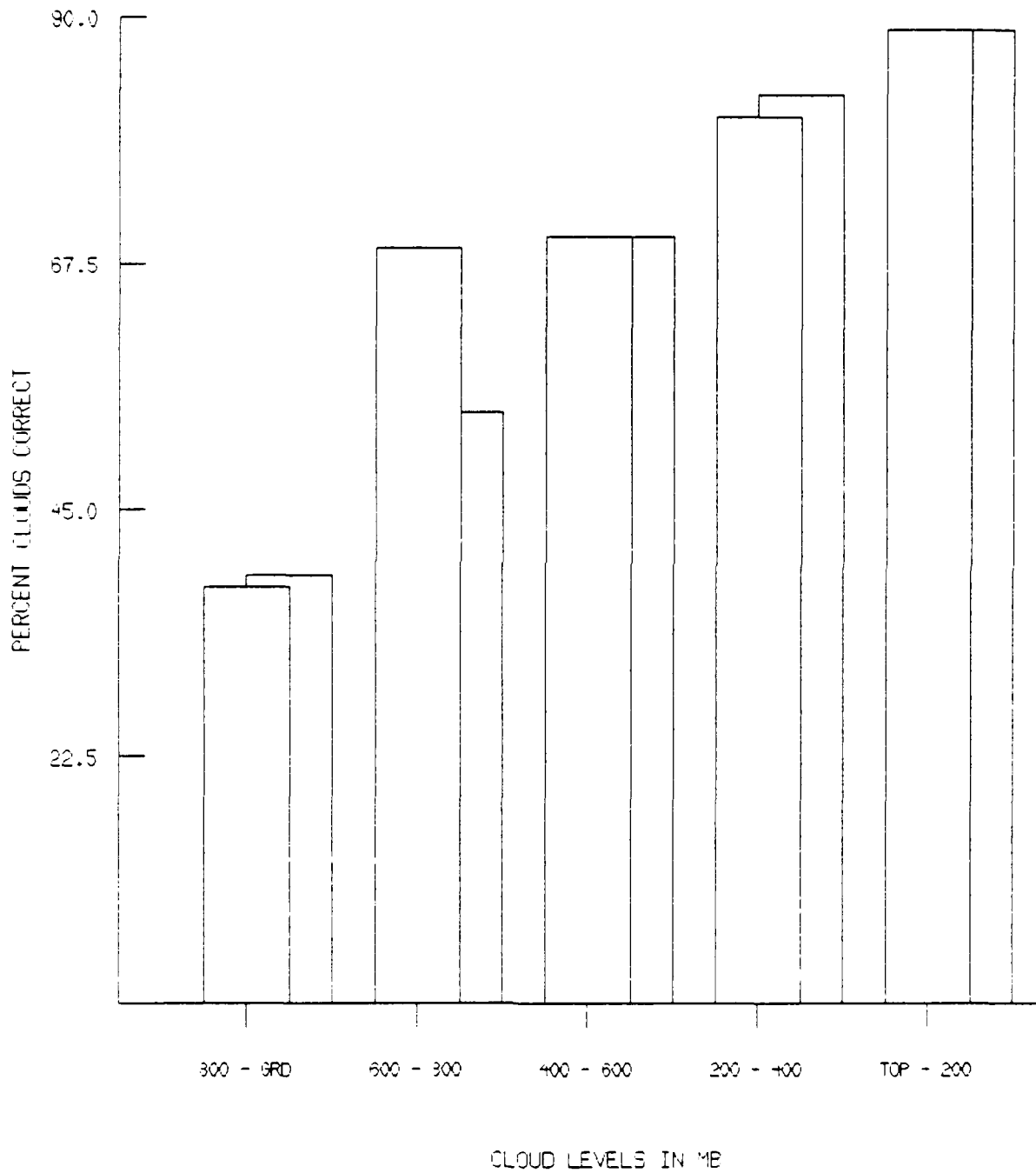


Figure 5.11 Histogram of cloud verification for the ISCCP initialization. The control experiment is in the foreground and the moisture initialization experiment is in the background.

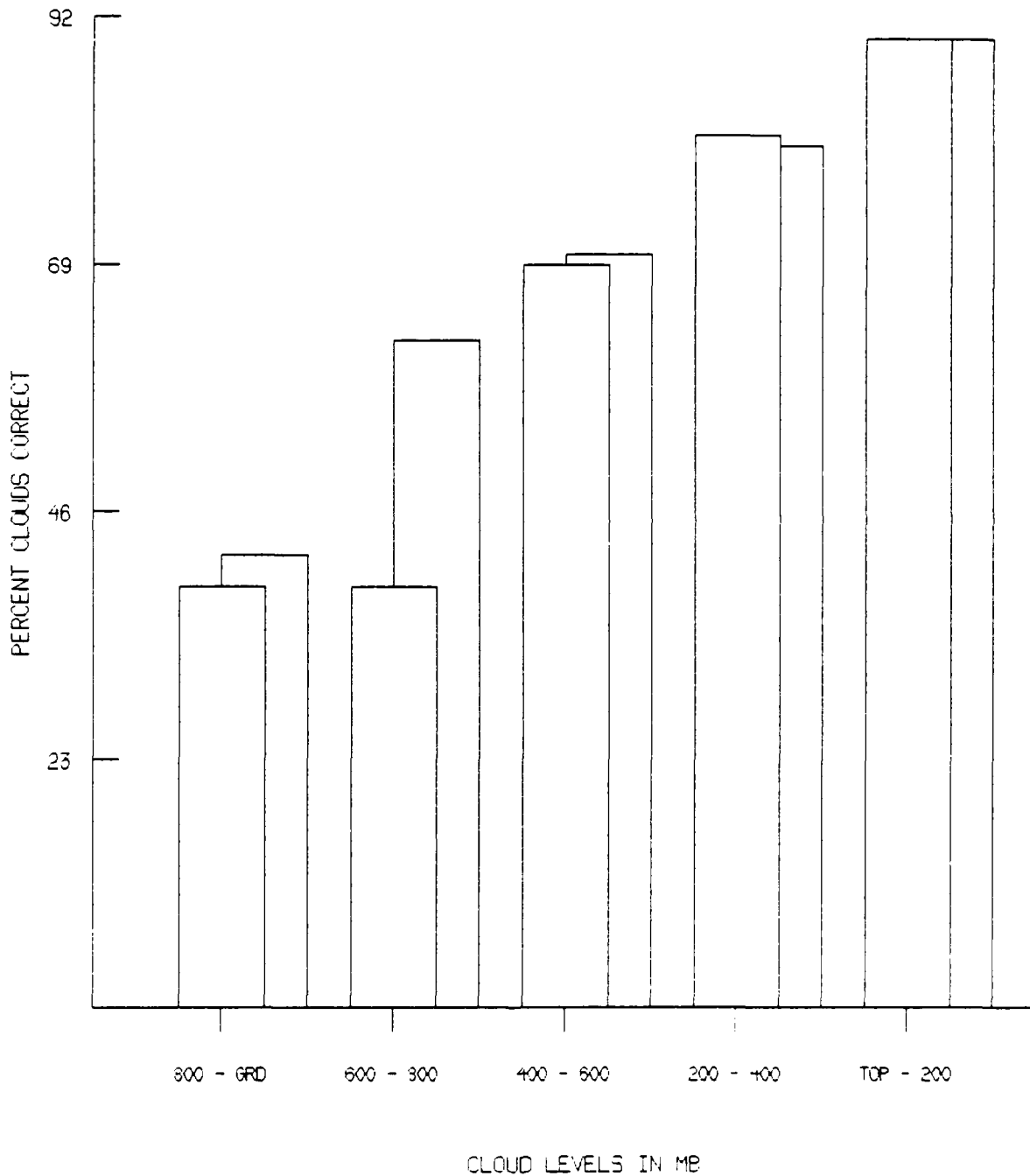


Figure 5.12 Histogram of cloud verification for the ISCCP forecast. The control experiment is in the foreground and the moisture initialization experiment is in the background.

that the OLR of the initialized data approached that of the control within 24 hours, with no significant difference thereafter.

### 5.3.2 Discussion

The results show that when the ISCCP cloud data are incorporated into the initialization scheme, there is no significant improvement in the analysis or forecast versus when the initialization uses only OLR data. The analysis showed no significant difference at any level after the initialization, except at the 600 to 800 mb level, where it had a worse verification (figure 5.11). Using this initialization scheme, the forecast only saw improvement at one level (figure 5.12). There was no difference at the other levels.

## 5.4 Summary of the moisture initializations

Two different methods of moisture initialization were studied. The first method used OLR differences as a convergence criteria and the second method used OLR and cloud differences as convergence criteria. The first method produced OLR values that were in close agreement with the satellite observed OLR. The second method also produced initial OLR fields with small errors, but could not match the observed cloud values in the lower levels. As the integration proceeded, there was no difference in the diagnosed clouds of the control and moisture initialized experiment.

Moisture initialization using OLR without clouds is the best moisture initialization method. This is not inferring that clouds cannot be used for moisture initialization, but that clouds are not yet fully understood. Krishnamurti *et al* (1988) stated that some deficiencies may be due to an inability to translate the ISCCP clouds to those inferred from the model. They cited several areas needing further research,

such as definition of clouds, relation of satellite viewed cloud top to cloud amount, relationship of cloud depth and temperature to emissivity, how to distinguish between cloud types in the model, and what feedback mechanisms exist between clouds and atmospheric warming/cooling. After these areas have been studied more extensively, moisture initialization using satellite observed clouds and OLR should be revisited.

CHAPTER VI  
THE LONGWAVE RADIATIVE TRANSFER FORMULATION

6.1 The longwave radiation model – overview

The longwave radiation scheme of the FSUGSM was originally an emissivity model as described by Chang (1980). It was recently changed to a band model, based on the radiation scheme of the UCLA/GLAS GCM (Harshvardhan and Corsetti (1984)).

The basic equations for the upward and downward flux are:

$$F_{cIr\uparrow}(p) = \int_{\Delta\nu} d\nu [B_{\nu}(T_s)\tau_{\nu}(p,p_s) + \int_{p_s}^p B_{\nu}(T(p')) \frac{d\tau_{\nu}(p,p')}{dp'} dp'] \quad (6.1a)$$

$$F_{cIr\downarrow}(p) = \int_{\Delta\nu} d\nu [\int_{p_t}^p B_{\nu}(T(p')) \frac{d\tau_{\nu}(p,p')}{dp'} dp'] \quad (6.1b)$$

These equations are for a clear sky case, integrated over the spectral range  $\Delta\nu$ . Here the individual variables are:

where:

$B_{\nu}(T_s)$  = blackbody flux at the surface temperature  $T_s$

$p_s$  = pressure at the bottom of the atmosphere

$p_t$  = pressure at the top of the atmosphere

$T_s$  = surface temperature

$T(p')$  = air temperature at pressure  $p'$

$t$  = top of the atmosphere

$\tau_v(p,p')$  = diffuse transmittance between the levels  $p$  and  $p'$

$\nu$  = spectral wavenumber

Integration of equations 1a and 1b gives:

$$F_{c\text{ir}\uparrow}(p) = B(T(p)) + G(p,p_s,T_s) - G(p,p_s,T(p_s)) + \int_{T(p)}^{T(p_s)} \frac{\partial G(p,p',T(p'))}{\partial T} dT(p') \quad (6.2a)$$

$$F_{c\text{ir}\downarrow}(p) = B(T(p)) - G(p,p_s,T(p_s)) + \int_{T(p)}^{T(p_s)} \frac{\partial G(p,p',T(p'))}{\partial T} dT(p') \quad (6.2b)$$

$$G(p,p',T) = \int_{\Delta\nu} \tau_v(p,p') B_v(T) d\nu \quad (6.2c)$$

$$\frac{\partial G(p,p',T)}{\partial T} = \int_{\Delta\nu} \tau_v(p,p') \frac{\partial B_v(T)}{\partial T} d\nu \quad (6.2d)$$

The spectral width of the 9.6  $\mu\text{m}$  and 15  $\mu\text{m}$  bands are narrow enough to use a mean value of the Planck function. The equation for  $G$  then becomes:

$$G(p,p',T) = \int_{\Delta\nu} \tau_v(p,p') \frac{d\nu}{\Delta\nu} * \int_{\Delta\nu} B_v(T) d\nu \quad (6.3)$$

The radiative cooling rate, or the divergence of net flux, is the final output of the model. It is given by:

$$-\frac{dT}{dt} = \frac{g}{C_p} \frac{d(F\downarrow - F\uparrow)}{dp} \quad (6.4)$$

The model uses the equations above to calculate the longwave flux of the atmosphere. Special considerations are given for overcast or partial cloud cover. The surface flux is also calculated. The methods of solving for the fluxes vary slightly for each type of radiatively active atmospheric constituent. The water vapor flux is solved by the methods of Chou and Arking (1980) and Chou (1984). The carbon dioxide flux is solved by the method of Chou and Peng (1983). The ozone flux is solved by the method of Rodgers (1968). The method used to compute each band is described in detail below.

#### 6.1.1 Water vapor bands

The IR spectrum is divided into the water vapor bands, the 15 m band, and the 9.6  $\mu\text{m}$  band. The spectral ranges for the water vapor band centers and wings are listed in Table 6.1. According to Chou and Arking (1980), the diffuse transmittance associated with molecular line absorption at wavenumber  $\nu$  is:

$$\tau_{\nu}(p_1, p_2) = 2 \int_0^1 \exp[-k_{\nu}(p_r, T_r)w(p_1, p_2)/\mu] \mu d\mu \quad (6.5)$$

where:

$k$  = molecular line absorption coefficient

$T$  = temperature

$\mu$  = cosine of the zenith angle

$p$  = pressure

$p_r$  = reference pressure, listed in Table 6.1

$T_r$  = reference temperature, listed in Table 6.2

w = scaled water vapor amount and is given by:

$$w(p_1, p_2) = \int_{p_1}^{p_2} (p/p_r) R[T(p)] q(p) dp/g \quad (6.6)$$

where:

g = gravity

q = water vapor mixing ratio

R(T) = temperature scaling factor and is given by:

$$R(T) = \exp[r(T - T_r)] \quad (6.7)$$

where:

r = factor from Chou (1980), listed in Table 6.1

The diffuse transmittance associated with e-type absorption is:

$$\tau_v(p_1, p_2) = 2 \int_0^1 \exp[-\sigma (T_0) u(p_1, p_2) / \mu] \mu d\mu \quad (6.8)$$

where:

$\sigma$  = e-type absorption coefficient

$T_0 = 296K$

u = scaled water vapor amount and is given by:

$$u(p_1, p_2) = \int_{p_1}^{p_2} e(p) \exp\{1800[1/T(p) - 1/T_0]\} q(p) dp/g \quad (6.9)$$

where:

e(p) = water vapor pressure in atmospheres

$$T_0 = 296 \text{ K}$$

1800 = 1800 K, a temperature dependence constant. Roberts (1976) states that "this is in accord with the fact that the hydrogen bond between two water molecules is in the neighborhood of 3–4 kcal, which leads to  $\cong 1800 \text{ K}$ ."

Broad transmission functions can be derived by averaging equations 6.5 and 6.8 over wide spectral intervals. In the water vapor bands, the "Planck weighted" transmission function is:

$$\tau(w,u;T) = \int B_v(T)\tau_v(w)\tau_v(u)dv/B(T) \quad (6.10)$$

where:

$B(T)$  = the spectrally integrated Planck flux

$B_v(T)$  = the Planck flux

$\tau_v(w)$  = the transmittance given by equation 6.5

$\tau_v(u)$  = the transmittance given by equation 6.8

Since  $\tau_v(w,u;T)$  is a slowly varying function of temperature, it can be fitted by the quadratic function (Chou (1984)):

$$\tau_v(w,u;T) = \tau(w,u;250)[1 + \alpha(w,u)(T-250) + \beta(w,u)(T-250)^2] \quad (6.11)$$

where:

$\alpha(w,u)$  = regression coefficient, given by Chou (1984)

$\beta(w,u)$  = regression coefficient, given by Chou (1984)

$\tau(w,u,250)$  = standardized transmission function, given by Chou (1984)

The band center region absorption can be neglected because it is dominated by molecular lines and the effect due to e-type absorption is small. Therefore, in the tables of Chou (1984) the last column shows  $\tau$ ,  $\alpha$ , and  $\beta$  as a function of  $w$  only. Equation 6.11 gives the Planck weighted transmission function to be within an error of less than .002.

For the 15  $\mu\text{m}$  region, Chou (1984) has fit the diffuse transmission function averaged over the entire band as:

$$\tau(w) = \exp[-6.7w/(1+16w^{0.6})] \quad (6.12)$$

$$\tau(u) = \exp[-27u^{0.83}] \quad (6.13)$$

Because the molecular line absorption is weak in the 9.6  $\mu\text{m}$  region, only the e-type absorption is considered. Chou (1984) has also fit the diffuse transmission associated with the e-type absorption in this region as:

$$\tau(u) = \exp(-9.79u) \quad (6.14)$$

The difference between the transmission functions using equations 6.12, 6.13, and 6.14 and those derived from equations 6.5 and 6.8 is less than .015 (less than 5% of the mean absorption).

Table 6.1 Water vapor absorption parameters (from Chou, 1984).

	H <sub>2</sub> O band-center	H <sub>2</sub> O band-wing	15 μm band	9.6 μm band
Spectral Range (cm <sup>-1</sup> )	0-340 1380-1900	340-540 800-980 1100-1380 1900-3000	540-800	980-1100
p <sub>r</sub> (mb)	275	550	550	—
T <sub>r</sub> (K)	225	256	256	—
r (K <sup>-1</sup> )	0.005	0.016	0.016	—

### 6.1.2 CO<sub>2</sub> bands

The spectral thermal radiative flux, in a non-scattering atmosphere, can be found by integrating the Schwarzschild equation:

$$F_{\nu}(p)\downarrow = \int_0^p B_{\nu}[T(p')][d\tau_{\nu}(p,p')/dp']dp' \quad (6.15)$$

where:

$\tau_{\nu}(p,p')$  = the transmittance averaged over zenith angles,  $\theta$ , and is given

by:

$$\tau_{\nu}(p,p') = 2 \int_0^1 \exp[-u_{\nu}(p,p')/\mu] \mu d\mu \quad (6.16)$$

where:

$u_{\nu}(p,p')$  = optical thickness and is given by:

$$u_{\nu}(p,p') = \int_{p'}^p c(p'')k_{\nu}[p'',T(p'')]dp''/g \quad (6.17)$$

where:

$c(p'')$  = CO<sub>2</sub> concentration

$k_{\nu}[p'',T(p'')] =$  absorption coefficient

For a small enough spectral interval,  $\Delta\nu_i$ , integration of equation 15 gives:

$$F_{\nu_i}(p)\downarrow = \int_0^p B_i[T(p')][d\tau_{\nu_i}(p,p')/dp']dp' \quad (6.18)$$

where:

$B_i [T(p')] =$  spectrally integrated Planck flux

$\tau_i (p, p') =$  spectrally averaged diffuse transmittance and is given by:

$$\tau_i(p, p') = \int_{\Delta v_i} \tau_v(p, p') dv / \Delta v_i \quad (6.19)$$

We now have equation 6.19, where the spectrally averaged diffuse transmittance depends on the transmittance at a single wavenumber,  $\tau_v$ . However, we see from equations 6.16 and 6.17 that  $\tau_v$  is dependent on the absorption coefficient, which is a function of wavenumber, temperature, and pressure. Therefore,  $\tau_v$  requires computations at numerous points in the spectral interval for each atmospheric situation in order to find the mean diffuse transmittance. Fortunately the computations can be simplified by relating the absorption coefficient to a reference pressure,  $p_r$ , and a reference temperature,  $T_r$ , through a scaling function  $f(p, T)$  as shown:

$$k_v(p, T) = k_v(p_r, T_r) f(p, T) \quad (6.20)$$

We may now combine and rewrite equations 6.16 and 6.17 as follows:

$$\tau_v(p, p') = 2 \int_0^1 \exp[-k_v(p_r, T_r) w(p, p') / \mu] \mu d\mu \quad (6.21)$$

where:

$w(p, p') =$  scaled  $\text{CO}_2$  amount and is given by:

$$w(p, p') = \int_{p'}^p c(p'') f(p'', T(p'')) dp'' / g \quad (6.22)$$

Equation 6.21 treats an inhomogeneous atmosphere as a homogeneous atmosphere, with a constant pressure and temperature of  $p_r$  and  $T_r$ . This is possible because equation 6.22 scales the  $\text{CO}_2$  concentration to simulate the absorption in an inhomogeneous atmosphere.

Equation 6.20 separated the absorption coefficient from the pressure and temperature variables. We may now rewrite equation 6.19 to express the mean transmittance averaged over the spectral interval,  $\Delta v$ , as a function only of the scaled absorber amount,  $w$ :

$$\tau_v(w) = \int_{\Delta v_i} \tau_v(w) dv / \Delta v_i \quad (6.23)$$

We may accurately precompute  $\tau_i$  as function of  $w$ , with  $k_v(p_r, T_r)$  obtained from accurate line by line calculations and then stored it in a look-up table for quick and efficient use. Chou and Peng (1983) have shown that the spectrally averaged diffuse transmittance,  $\tau_i$ , can be accurately precomputed from the analytical function:

$$\tau_i(w) = \exp[-aw/(1 + bw^n)] \quad (6.24)$$

where  $a$ ,  $b$ , and  $n$  are chosen for individual spectral intervals such that the computed rms error in  $\tau_i(w)$  is minimized. Chou and Peng (1983) have computed values for  $a$ ,  $b$ , and  $n$ . They are shown in Table 6.2.

The absorption coefficients at the selected reference levels are accurately computed using line-by-line methods. Radiative transfer in the regions close to the reference levels will also be accurately computed. Therefore, the values of  $p_r$  and  $T_r$  should be chosen close to the regions where accurate computations of radiative transfer

are important. One important region is the stratosphere, where radiative cooling due to CO<sub>2</sub> emission is a dominant factor. Another important region is the lower troposphere, where downward radiative flux at the surface is an important component affecting the surface temperature. The cooling of the stratosphere is mostly due to the absorption band center. Cooling in the lower troposphere is mostly due to the absorption band wings. Therefore, when we are considering the band centers, we choose a  $p_r$  to be representative of the stratosphere, and when we are considering the band wings, we choose a  $p_r$  representative of the lower troposphere. Chou and Peng (1983) state that the temperature is less critical to the equations and choose a value of 240 K, which they consider to be an intermediate value for both the stratosphere and the troposphere.

The scaling function used in equation 6.20 is that of Chou and Arking (1980 and 1981):

$$f(p,T) = (p/p_r)^m R(T,T_r) \quad (6.25)$$

where:

$m$  = parameter for correcting the error arising from the assumption of linear dependence of the absorption coefficient on pressure.

$R(T,T_r)$  = temperature scaling factor and is given by:

$$R(T,T_r) = \exp[r(T - T_r)] \quad (6.26)$$

where:

$r = .0089$  for the band center and  $.025$  for the band wings

$T_r = 240$  K for both the band center and the band wings

Table 6.2 15  $\mu\text{m}$  band parameters (from Chou and Peng, 1983)

	Band Center	Band Wings	
		Narrow	Wide
$\Delta\nu$ ( $\text{cm}^{-1}$ )	620–720	580–620 720–760	540–620 720–800
$p_r$ (mb)	30	300	300
$p_c$ (mb)	1	1	1
m	0.85	0.85	0.50
n	0.56	0.55	0.57
a	3.1	0.08	0.04
b	15.1	0.9	0.9
$T_r$ (K)	240	240	240
$R(T, T_r)$	0.0089	0.025	0.025

The pressure scaling in equation 6.25 assumes that the absorption coefficient follows the Lorentz function. This assumption is not valid at low pressures where broadening of absorption lines due to Doppler shift is important. In the 15  $\mu\text{m}$  spectral region, the height where line broadening due to molecular collision and Doppler shift are equally important is approximately 10 mb. For a Doppler line function, the absorption is independent of pressure. To account for the Doppler effect, we define a critical pressure level,  $p_c$ . At pressures higher than this critical pressure, the absorption coefficient is independent of pressure. We may now rewrite equation 6.25 as:

$$f(p,T) = (p/p_r)^m R(T,T_r), \text{ for } p < p_c \quad (6.27)$$

where the values for  $p_r$ ,  $T_r$ ,  $p_c$ , and  $m$  were obtained empirically by Chou and Peng (1983) and are listed in Table 6.2.

### 6.1.3 Ozone bands

Rodgers (1968) defines a transmission function for a Lorentz line shape as:

$$T(k_i, m, p) = \exp \left[ - \frac{\pi \alpha p}{2 \delta} \left[ \left[ 1 + \frac{4 k m}{\pi \alpha p} \right]^{0.5} - 1 \right] \right] \quad (6.28)$$

where:

$\alpha$  = line width at one atmosphere

$\delta$  = spectral interval

Table 6.3 Ozone coefficients (from Rodgers, 1968).

$k$ ( $\text{cm g}^{-1}$ )	$a$ ( $\text{cm}^{-1}$ )	$\alpha$ ( $\text{cm}^{-1}$ )	$\delta$ ( $\text{cm}^{-1}$ )
208	81.21	0.28	0.1

$k$  = line strength

$m$  = ozone concentration

Rodgers (1968) used this transmission function to find the 9.6  $\mu\text{m}$  ozone band absorption. The absorption equation is:

$$A(m,p) \cong \sum_i a_i (1 - T(k_i, m, p)) \quad (6.29)$$

where:

$a_i$  = line strength

The values of the coefficients were chosen empirically by Rodgers (1968) and are listed in Table 6.3. Since transmission can be defined as one minus the absorption, Harshvardhan and Corsetti (1984) subtracted equation 29 from 1.0 to find the ozone transmission through the atmosphere.

#### 6.1.4 Treatment of clouds

Consider a simple five layer atmosphere with only one cloud layer. The fractional cloud cover in that layer is defined as  $N$ . Equation 6.2b, for a level below the cloud, may then be rewritten as:

$$F_{\text{cl}\downarrow}(p) = B(T(p)) - (1 - N)G(p, p_b, T(p)) +$$

$$(1 - N) \int_{T(p)}^{T(p_c)} \frac{\partial G(p, p', t(p'))}{\partial T} dT(p') +$$

$$N \int_{T(p)}^{T(p_{cb})} \frac{\partial G(p, p', T(p'))}{\partial T} dT(p') \quad (6.30)$$

where:

cb = cloud base

t = top of the atmosphere

N = fractional cloud cover in layer

1 - N = probability of clear line of sight from p to p

By splitting the limits of integration, equation 6.30 may be rewritten as:

$$F_{cld\downarrow}(p) = B(T(p)) - (1 - N)G(p, p, T(p)) +$$

$$(1 - N) \int_{T(p_{cb})}^{T(p)} \frac{\partial G(p, p', T(p'))}{\partial T} dT +$$

$$\int_{T(p)}^{T(p_{cb})} \frac{\partial G(p, p', T(p'))}{\partial T} dT(p') \quad (6.31)$$

The probability of a clear line of sight between any two levels will always be in the range from zero to one. That is to say:

<u>Probability</u>	<u>Levels</u>
1 - N	p to p
1 - N	p to p' (where p' is between p and p)
1.0	p to p' (where p' is between p and p)

Equation 6.31 may now be rewritten:

$$F_{\text{clid}}\downarrow(p) = B(T(p)) - C(p, p_s)G(p, p_s, T(p)) +$$

$$\int_{T(p)}^{T(p_s)} C(p, p') \frac{\partial G(p, p', T(p'))}{\partial T} dT(p')$$

(6.32)

where:

$C(p, p')$  = probability of a clear line of sight from  $p$  to  $p'$

Equation 6.2a may be manipulated in the same way to yield:

$$F_{\text{clid}}\uparrow(p) = B(T(p)) + C(p, p_s)[G(p, p_s, T_s) - G(p, p_s, T(p_s))] +$$

$$\int_{T(p)}^{T(p_s)} C(p, p') \frac{\partial G(p, p', T(p'))}{\partial T} dT(p')$$

(6.33)

Equations 6.32 and 6.33 are still valid even when there is more than one cloud layer. The longwave parameterization utilizes a random overlap of clouds, which is equal to the product of all fractional cloud amounts for all levels that have clouds (*i.e.*,  $N(3)*N(4)*etc.$ ). Note that the minimum cloud free line of sight for a random overlap atmosphere is  $(1-N(3))*(1-N(4))*etc.$

## 6.2 Column model results

The UCLA/GLAS radiation algorithm was verified against line by line calculations using standard atmosphere profiles. The FSUGSM algorithm was verified using the same standard atmosphere profiles. The error in cooling was less than five percent at all tropospheric levels, except the boundary layer where the surface temperature was calculated differently.

Figure 6.1 shows column model results of the newer band model versus the older emissivity model for a standard tropical atmosphere. The largest difference between the two models is the stronger cooling of the troposphere in the band model. Figure 6.2 shows the same atmospheric profile, except the moisture in the lower layers has been modified to produce clouds. The maximum cooling for the band model is at the cloud tops. The maximum cooling in the emissivity model is several layers above the cloud tops. In addition, the band model shows stronger cooling than the emissivity model. This strong radiative cooling plays an important role in many tropical processes. Krishnamurti *et al* (1990) recently demonstrated the effect of these two radiation schemes on the life cycle of Typhoon Hope. The emissivity method, with smaller cooling at the cloud top levels, could not maintain the adequate radiative destabilization for the typhoon to continue development. On the other hand, the band model contributed to a stronger typhoon.

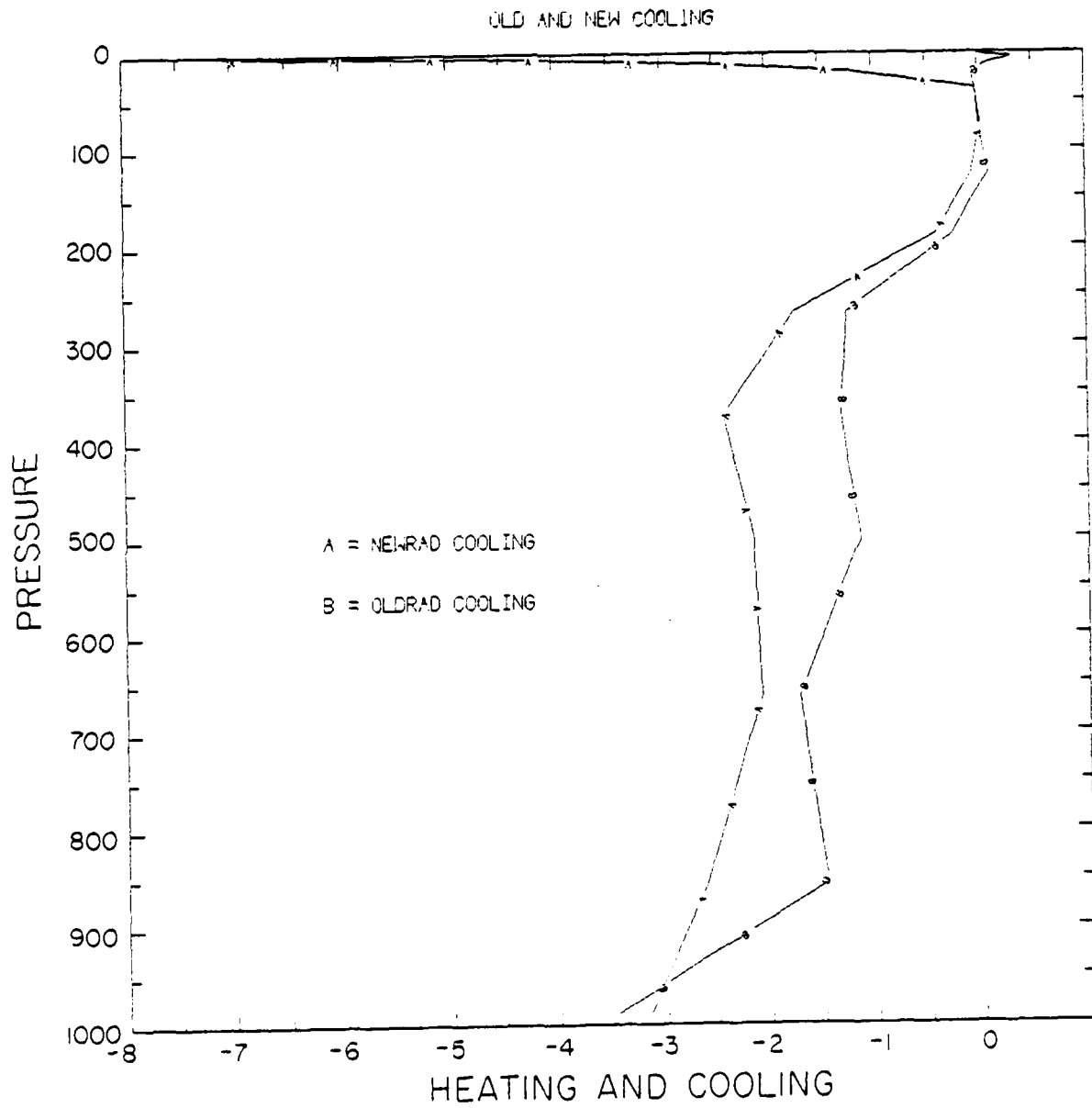


Figure 6.1 Column model results for a standard tropical atmosphere with the old and new radiation models

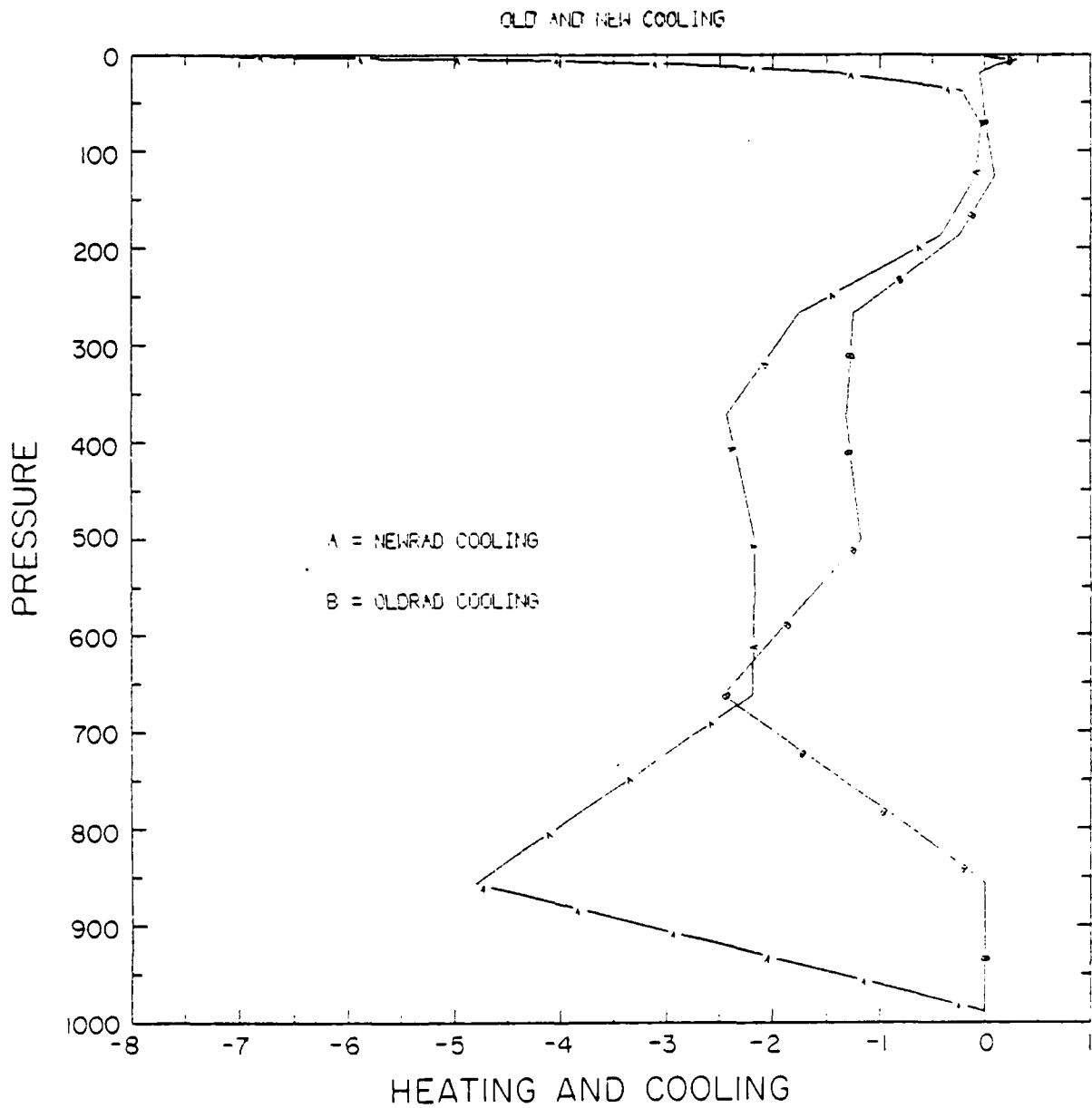


Figure 6.2 Column model results for a standard tropical atmosphere with the old and new radiation models. The moisture of the lower levels has been modified to produce clouds.

## Chapter VII

### Moist Static Stability

#### 7.1 Introduction

Atmospheric stability can be determined from the equivalent potential temperature profile. The stability can also be inferred from the moist static energy profile. This chapter will show that the equivalent potential temperature and the moist static energy profiles can be used interchangeably to infer the instability. In addition, the equation for the moist static stability tendency will be derived, both in its classical form and in terms of the apparent heat source and apparent moisture sink. These equations will be used to demonstrate the effects of moisture initialization on the FSUGSM forecasts. It is shown that the moisture initialization procedure improved the model's forecast ability, as demonstrated by the five day model forecast.

#### 7.2 Stability

The classical definition of conditional instability is:

$$\gamma_d > \gamma > \gamma_m \quad (7.1)$$

where:

$\gamma_d$  = dry adiabatic lapse rate

$\gamma$  = atmospheric lapse rate

$\gamma_m$  = moist pseudo – adiabatic lapse rate

Conditional instability can also be expressed by:

$$-\frac{\partial\theta}{\partial p} > 0 ; -\frac{\partial\theta_e^*}{\partial p} < 0 \quad (7.2)$$

where:

$\theta$  = potential temperature

$\theta_e^*$  = equivalent potential temperature of a saturated atmosphere

However, the equivalent potential temperature is often used in place of  $\theta_e^*$ :

$$-\frac{\partial\theta}{\partial p} > 0 ; -\frac{\partial\theta_e}{\partial p} < 0 \quad (7.3)$$

or:

$$-\frac{\partial}{\partial p} (gz + C_p T) > 0 ; -\frac{\partial}{\partial p} (gz + C_p T + Lq) < 0 \quad (7.4)$$

where:

$\theta_e$  = equivalent potential temperature

In the following section we will show that the equivalent potential temperature and the moist static energy both come from the same basic equation and their profiles may be used interchangeably when referring to stability.

### 7.3 Equivalent Potential Temperature versus the Moist Static Stability

The First Law of Thermodynamics may be expressed as:

$$C_{pm} \frac{dT}{T} - \alpha_m \frac{dp}{T} = -\frac{L}{T} \frac{dm_v}{m_d + m_v} \quad (7.5)$$

where:

$C_{pm}$  = specific heat of moist air

$T$  = temperature

$\alpha_m$  = specific volume of moist air

$p$  = pressure

$L$  = latent heat of condensation

$m_v$  = mass of water vapor

$m_d$  = mass of dry air

Approximating  $C_{pm} = C_p$ ,  $\frac{\alpha_m}{T} = \frac{R_d}{p}$ , and  $\frac{dm_v}{m_d + m_v} = dr$ :

$$C_p \frac{dT}{T} - R_d \frac{dp}{p} = -\frac{L}{T} dr = -d \left[ \frac{Lr}{T} \right] - \frac{Lr}{T^2} dT \quad (7.6)$$

where:

$r$  = mixing ratio

$R_d$  = gas constant for dry air

collecting terms:

$$\left(C_p + \frac{Lr}{T}\right) \frac{dT}{T} - R_d \frac{dp}{p} + d\left[\frac{Lr}{T}\right] = 0 \quad (7.7)$$

But  $C_p$  is an order of magnitude greater than  $\frac{Lr}{T}$ :

$$C_p \frac{dT}{T} - R_d \frac{dp}{p} + d\left[\frac{Lr}{T}\right] = 0 \quad (7.8)$$

Both the equivalent potential temperature and the moist static energy may be derived from this one equation.

To find the equivalent potential temperature, integrate the above equation:

$$C_p \ln \frac{T}{T_o} - R_d \ln \frac{p}{p_o} + \frac{Lr}{T} - \left[\frac{Lr}{T}\right]_o = 0 \quad (7.9)$$

Dividing by  $-C_p$  and rearranging:

$$\ln \frac{T}{T_o} + \frac{R_d}{C_p} \ln \frac{p}{p_o} = \frac{Lr}{C_p T} - \left[\frac{Lr}{C_p T}\right]_o \quad (7.10)$$

Taking the exponential:

$$\frac{T}{T_o} \left[\frac{p}{p_o}\right]^{R/C_p} = \exp\left[\frac{Lr}{C_p T} - \left[\frac{Lr}{C_p T}\right]_o\right] \quad (7.11)$$

Rearranging:

$$T_o = T \left[ \frac{p_o}{p} \right]^{R/C_p} \exp \left[ \frac{Lr}{C_p T} - \left[ \frac{Lr}{C_p T} \right]_o \right] \quad (7.12)$$

But  $\theta = T \left[ \frac{p_o}{p} \right]^{R/C_p}$ :

$$T_o = \theta \exp \left[ \frac{Lr}{C_p T} - \left[ \frac{Lr}{C_p T} \right]_o \right] \quad (7.13)$$

The equivalent potential temperature assumes that the parcel has been lifted pseudo – adiabatically until all its water vapor has condensed and the parcel is completely dry. It is then brought isentropically to 1000 mb. Because the parcel is dry at the end of the process,  $r = 0$  and:

$$\theta_e = \theta \exp \left[ \frac{Lr}{T} \right] \quad (7.14)$$

where:

$\theta_e =$  equivalent potential temperature

Madden and Robitaille (1970) have shown that the moist static energy may be derived from the same basic equation (7.8):

$$C_p \frac{dT}{T} - R_d \frac{dp_d}{p_d} + d \left[ \frac{Lr}{T} \right] = 0 \quad (7.15)$$

Expanding the last term:

$$C_p \frac{dT}{T} - R_d \frac{dp_d}{p_d} + \frac{1}{T} d(Lr) - \frac{Lr}{T^2} dT = 0 \quad (7.16)$$

Next an appropriate substitute for  $dp_d$  must be found. Start with the equation for vertical velocity:

$$\frac{dw}{dt} = -\frac{1}{\rho} \frac{\partial p}{\partial z} - g \quad (7.17)$$

where:

$w$  = vertical velocity

$t$  = time

$\rho$  = density of moist air

$p$  = pressure of moist air

$z$  = height

$g$  = gravity

If we assume that the sum of the local and horizontal pressure changes are zero, then the equation for the total derivative of pressure goes from:

$$\frac{dp}{dt} = \frac{\partial p}{\partial t} + u \frac{\partial p}{\partial x} + v \frac{\partial p}{\partial y} + w \frac{\partial p}{\partial z} \quad (7.18)$$

to:

$$\frac{dp}{dt} = w \frac{\partial p}{\partial z} \quad (7.19)$$

or:

$$\frac{\partial p}{\partial z} = \frac{1}{w} \frac{dp}{dt} \quad (7.20)$$

Substituting:

$$\frac{dw}{dt} = -\frac{1}{w\rho} \frac{dp}{dt} - g \quad (7.21)$$

Multiplying by wdt:

$$wdw = -\frac{1}{\rho} dp - gw dt \quad (7.22)$$

but  $w = \frac{dz}{dt}$ :

$$wdw + \frac{dp}{\rho} + gdz = 0 \quad (7.23)$$

The total pressure,  $p$ , may be broken into the dry air pressure and the water vapor partial pressure as:  $dp = dp_d + de_s$ . The Clausius-Clapeyron equation states that  $de_s = e_s L dT / (R_v T^2)$ . Substituting:

$$wdw + \frac{dp_d}{\rho} + \frac{e_s L dT}{\rho R_v T^2} + gdz = 0 \quad (7.24)$$

where:

$e_s$  = partial pressure due to water vapor

$L$  = latent heat of vaporization

$R_v$  = gas constant for water vapor

The Ideal Gas Law states that  $e_s = \rho_v R_v T$ :

$$wdw + \frac{dp_d}{\rho} + \frac{\rho_v L dT}{\rho T} + gdz = 0 \quad (7.25)$$

Solving for  $dp_d$ :

$$dp_d = -\rho w dw - \frac{\rho_v L dT}{T} - \rho g dz \quad (7.26)$$

Substituting back into equation 7.16:

$$C_p T \frac{dT}{T} - \frac{R_d}{p_d} \left[ -\rho w dw - \frac{\rho_v L dT}{T} - \rho g dz \right] + \frac{1}{T} d(Lr) - \frac{Lr}{T^2} dT = 0 \quad (7.27)$$

Using  $\frac{R_d}{p_d} = \frac{1}{\rho_d T}$  from the Ideal Gas Law:

$$C_p \frac{dT}{T} + \frac{\rho w dw}{\rho_d T} + \frac{\rho_v L dT}{\rho_d T^2} + \frac{\rho g dz}{\rho_d T} + \frac{1}{T} d(Lr) - \frac{Lr}{T^2} dT = 0 \quad (7.28)$$

Since  $\rho_v/\rho_d = r$ , the third and last terms cancel. Also  $\rho = \rho_v + \rho_d$ :

$$C_p \frac{dT}{T} + (r+1) \frac{w dw}{T} + (r+1) \frac{g dz}{T} + \frac{1}{T} d(Lr) = 0 \quad (7.29)$$

But  $r \ll 1$  and may be neglected in the  $(r+1)$  terms:

$$C_p \frac{dT}{T} + \frac{w dw}{T} + \frac{g dz}{T} + \frac{1}{T} d(Lr) = 0 \quad (7.30)$$

Multiplying by  $T$ :

$$C_p dT + w dw + g dz + d(Lr) = 0 \quad (7.31)$$

Integrating:

$$C_p T + \frac{w^2}{2} + gz + Lr = \text{constant} \quad (7.32)$$

Rearranging:

$$C_p T + gz + Lr = \frac{w^2}{2} + \text{constant} \quad (7.33)$$

where:

$$C_p T + gz + Lr = \text{moist static energy}$$

$$\frac{w^2}{2} = \text{vertical kinetic energy per unit mass}$$

This equation states that under certain conditions (*i.e.*, steady state, no horizontal pressure changes, neglecting the contribution of water vapor to the changing kinetic and potential energy of the parcel, and approximating the available latent heat by  $Lr$ ) the moist static energy is equal to a constant plus the vertical kinetic energy per unit mass as the parcel moves from one thermodynamic state to another through pseudo-adiabatic processes. Madden and Robitaille (1970) have estimated the moist static energy to be two orders of magnitude larger than the vertical kinetic energy per unit mass. As a result, the moist static energy is usually considered to be a conservative quantity.

It can now be seen that both the equivalent potential temperature and the moist static energy come from the same basic equation (7.8). The equivalent potential temperature was related to the 1000 mb level through a definite integration from the LCL. The moist static energy was based on an indefinite integration and related to the 1000 mb level by choosing it as a reference level and allowing  $z$  to be the height above

it. Madden and Robitaille (1970) have shown an example of how the profiles of the equivalent potential temperature and the moist static energy are very much alike. The major difference in the profiles of their example is the limit of convection. After going through a layer of the atmosphere more than 800 mb thick, the difference in the limit of convection between the two profiles is only 9 mb. With a difference this small, the two profiles may be considered the identical, with the exception of the proportionality.

#### 7.4 Derivation of Moist Static Stability Tendency

The equivalent potential temperature may be written:

$$\theta_e = \theta \exp \left[ \frac{Lq}{C_p T} \right] \quad (7.34)$$

where.

$\theta_e$  = equivalent potential temperature

$\theta$  = potential temperature =  $T \left[ \frac{p_0}{p} \right]^{R/C_p}$

T = temperature

$p_0$  = 1000 mb

p = pressure

R = universal gas constant for dry air

$C_p$  = specific heat of dry air at constant pressure

L = latent heat of vaporization at temperature T

q = mixing ratio of water vapor to dry air

Substituting the potential temperature:

$$\theta_e = T \left[ \frac{p_0}{p} \right]^{R/C_p} \exp \left[ \frac{Lq}{C_p T} \right] \quad (7.35)$$

Taking the natural log:

$$\ln \theta_e = \ln T + \frac{R}{C_p} \ln p_0 - \frac{R}{C_p} \ln p + \frac{Lq}{C_p T} \quad (7.36)$$

Differentiating with respect to time:

$$\frac{1}{\theta_e} \frac{d\theta_e}{dt} = \frac{1}{T} \frac{dT}{dt} - \frac{R}{C_p p} \frac{dp}{dt} + \frac{L}{C_p T} \frac{dq}{dt} - \frac{Lq}{C_p T^2} \frac{dT}{dt} \quad (7.37)$$

Multiply by  $C_p T$ :

$$\frac{C_p T}{\theta_e} \frac{d\theta_e}{dt} = C_p \frac{dT}{dt} - \frac{RT}{p} \frac{dp}{dt} + L \frac{dq}{dt} - \frac{Lq}{T} \frac{dT}{dt} \quad (7.38)$$

By scale analysis, the last term on the right hand side is much smaller than the other terms and may be disregarded. Using the hydrostatic equation and the ideal gas law:

$$\frac{C_p T}{\theta_e} \frac{d\theta_e}{dt} = C_p \frac{dT}{dt} + g \frac{dz}{dt} + L \frac{dq}{dt} \quad (7.39)$$

or:

$$\frac{C_p T}{\theta_e} \frac{d\theta_e}{dt} = \frac{d}{dt} [C_p T + gz + Lq] \quad (7.40)$$

The terms in the brackets are known as the moist static energy. They will be abbreviated in the following discussions as  $E_m$ . The term on the left is known as the heat source/sink term. It is abbreviated as:

$$\frac{C_p T}{\theta_e} \frac{d\theta_e}{dt} = LE_O + H_R + S_O = \Sigma H_m \quad (7.41)$$

where:

$LE_O$  = evaporative heat energy

$H_R$  = radiative energy

$S_O$  = sensible heat energy

The equation may now be expressed as:

$$\frac{dE_m}{dt} = \Sigma H_m \quad (7.42)$$

Expanding the total derivative:

$$\frac{\partial E_m}{\partial t} = -\mathbf{V} \cdot \nabla E_m - w \frac{\partial E_m}{\partial z} + \Sigma H_m \quad (7.43)$$

Transforming  $w$  to  $\omega$ :

$$\frac{\partial E_m}{\partial t} = -\mathbf{V} \cdot \nabla E_m - \omega \frac{\partial E_m}{\partial p} + \Sigma H_m \quad (7.44)$$

Expanding:

$$\frac{\partial \mathbf{E}_m}{\partial t} = -\nabla \cdot \mathbf{E}_m \mathbf{V} + \mathbf{E}_m \nabla \cdot \mathbf{V} - \frac{\partial \mathbf{E}_m \omega}{\partial p} + \mathbf{E}_m \frac{\partial \omega}{\partial p} + \Sigma H_m \quad (7.45)$$

or:

$$\frac{\partial \mathbf{E}_m}{\partial t} = -\nabla \cdot \mathbf{E}_m \mathbf{V} - \frac{\partial \mathbf{E}_m \omega}{\partial p} + \mathbf{E}_m (\nabla \cdot \mathbf{V} + \frac{\partial \omega}{\partial p}) + \Sigma H_m \quad (7.46)$$

The continuity equation states that  $\nabla \cdot \mathbf{V} + \frac{\partial \omega}{\partial p} = 0$ :

$$\frac{\partial \mathbf{E}_m}{\partial t} = -\nabla \cdot \mathbf{E}_m \mathbf{V} - \frac{\partial \mathbf{E}_m \omega}{\partial p} + \Sigma H_m \quad (7.47)$$

Using  $\overline{AB} = \overline{A} \overline{B} + \overline{A'B'}$  to average the terms:

$$\overline{\frac{\partial \mathbf{E}_m}{\partial t}} = -\nabla \cdot (\overline{\mathbf{E}_m \mathbf{V}} + \overline{\mathbf{E}_m' \mathbf{V}'}) - \frac{\partial}{\partial p} (\overline{\mathbf{E}_m \omega} + \overline{\mathbf{E}_m' \omega'}) + \overline{\Sigma H_m} \quad (7.48)$$

or:

$$\overline{\frac{\partial \mathbf{E}_m}{\partial t}} = -\nabla \cdot \overline{\mathbf{E}_m \mathbf{V}} - \nabla \cdot \overline{\mathbf{E}_m' \mathbf{V}'} - \frac{\partial}{\partial p} \overline{\mathbf{E}_m \omega} - \frac{\partial}{\partial p} \overline{\mathbf{E}_m' \omega'} + \overline{\Sigma H_m} \quad (7.49)$$

Scale analysis shows that the second term on the right hand side is small and may be neglected. Expanding:

$$\frac{\partial \overline{E_m}}{\partial t} = -\overline{E_m} \nabla \cdot \overline{V} - \overline{V} \cdot \nabla \overline{E_m} - \overline{E_m} \frac{\partial \overline{\omega}}{\partial p} - \overline{\omega} \frac{\partial \overline{E_m}}{\partial p} - \frac{\partial}{\partial p} (\overline{E_m}' \overline{\omega}') + \overline{\Sigma H_m} \quad (7.50)$$

or:

$$\frac{\partial \overline{E_m}}{\partial t} = -\overline{E_m} (\nabla \cdot \overline{V} + \frac{\partial \overline{\omega}}{\partial p}) - \overline{V} \cdot \nabla \overline{E_m} - \overline{\omega} \frac{\partial \overline{E_m}}{\partial p} - \frac{\partial}{\partial p} (\overline{E_m}' \overline{\omega}') + \overline{\Sigma H_m} \quad (7.51)$$

The continuity equation states  $\nabla \cdot \overline{V} + \frac{\partial \overline{\omega}}{\partial p} = 0$ . Differentiating with respect to  $p$ :

$$-\frac{\partial^2 \overline{E_m}}{\partial t \partial p} = \overline{V} \cdot \nabla \frac{\partial \overline{E_m}}{\partial p} + \frac{\partial \overline{\omega}}{\partial p} \frac{\partial \overline{E_m}}{\partial p} + \overline{\omega} \frac{\partial^2 \overline{E_m}}{\partial p^2} + \frac{\partial^2}{\partial p^2} (\overline{E_m}' \overline{\omega}') - \frac{\partial}{\partial p} \overline{\Sigma H_m} \quad (7.52)$$

However, the moist static stability is defined as  $\Gamma_m \equiv -\frac{\partial \overline{E_m}}{\partial p}$ :

$$\frac{\partial \overline{\Gamma_m}}{\partial t} = -\overline{V} \cdot \nabla \overline{\Gamma_m} - \overline{\Gamma_m} \frac{\partial \overline{\omega}}{\partial p} - \overline{\omega} \frac{\partial \overline{\Gamma_m}}{\partial p} + \frac{\partial^2}{\partial p^2} (\overline{E_m}' \overline{\omega}') - \frac{\partial}{\partial p} (\overline{L E_O} + \overline{H_R} + \overline{S_O}) \quad (7.53)$$

where:

$\frac{\partial \overline{\Gamma_m}}{\partial t}$  = rate of change of moist static stability

$-\overline{V} \cdot \nabla \overline{\Gamma_m}$  = horizontal advection of the moist static stability

$-\overline{\omega} \frac{\partial \overline{\Gamma_m}}{\partial p}$  = vertical advection of moist static stability

$\frac{\partial}{\partial p^2} (\overline{E_m}' \overline{\omega}')$  = vertical eddy flux of moist static stability

$$-\overline{\Gamma_m} \frac{\partial \overline{\omega}}{\partial p} = \text{divergence of moist static stability}$$

$-\frac{\partial}{\partial p}(\overline{LE_O} + \overline{H_R} + \overline{S_O}) = \text{stabilization by evaporative, radiative, and sensible heat fluxes}$

### 7.5 Moist Static Stability Tendency in Relation to the Apparent Heat Source and the Apparent Moisture Sink

Equation 7.53 is the classical definition of the moist static stability. It can also be defined in terms of two other meteorological quantities called the apparent heat source ( $Q_1$ ) and the apparent moisture sink ( $Q_2$ ). Yanai *et al.* (1973) have provided a derivation of these quantities. The apparent heat source will be derived first. The equation of heat energy, averaged over a small area is:

$$\frac{\partial \overline{s}}{\partial t} + \overline{\nabla \cdot sV} + \frac{\partial \overline{\omega s}}{\partial p} = Q_R + L(c - e) \quad (7.54)$$

where:

$s = \text{dry static energy} = C_p T + gz$

$Q_R = \text{heating due to radiation}$

$c = \text{rate of condensation per unit mass of air}$

$e = \text{rate of reevaporation of cloud droplets}$

Using  $\overline{AB} = \overline{A} \overline{B} + \overline{A'B'}$  and rearranging:

$$\overline{\frac{\partial s}{\partial t}} + \overline{\nabla \cdot s\mathbf{V}} + \overline{\frac{\partial s}{\partial p} \omega} = Q_R + L(c - e) - \overline{\frac{\partial}{\partial p} s'w'} \quad (7.55)$$

This is the equation for the apparent heat source,  $Q_1$ . The name apparent is used because if only the large scale quantities are known (*i.e.*,  $\overline{s}$ ,  $\overline{s\mathbf{V}}$ , and  $\overline{\omega}$ ), then  $Q_1$  is a measure of the apparent heating on the large scale due to radiation, the release of latent heat by net condensation, and vertical convergence of the vertical eddy transport of sensible heat.

The derivation of the equation for the apparent moisture sink begins with the equation of moisture continuity averaged over a small area:

$$\overline{\frac{\partial q}{\partial t}} + \overline{\nabla \cdot q\mathbf{V}} + \overline{\frac{\partial q\omega}{\partial p}} = e - c \quad (7.56)$$

Using  $\overline{AB} = \overline{A} \overline{B} + \overline{A'B'}$  and rearranging:

$$-\overline{\frac{\partial Lq}{\partial t}} - \overline{\nabla \cdot Lq\mathbf{V}} - \overline{\frac{\partial Lq}{\partial t} \omega} = L(c - e) + L \overline{\frac{\partial}{\partial p} q'\omega'} \quad (7.57)$$

This is the equation for the apparent moisture sink,  $Q_2$ . The name apparent is used because if only the large scale quantities are known (*i.e.*,  $\overline{q}$ ,  $\overline{q\mathbf{V}}$ , and  $\overline{\omega}$ ), then  $Q_2$  is a measure of the apparent moisture loss that the large scale experiences, due to the net condensation and vertical divergence of the eddy transport of moisture.

To achieve a definition of the moist static stability tendency in terms of the apparent heat source and the apparent moisture sink, start with equation 7.44:

$$\frac{\partial E_m}{\partial t} = -\nabla \cdot E_m \mathbf{V} - \frac{\partial E_m \omega}{\partial p} + \Sigma H_m \quad (7.58)$$

or:

$$\frac{\partial E_m}{\partial t} + \nabla \cdot E_m \mathbf{V} + \frac{\partial E_m \omega}{\partial p} = \Sigma H_m \quad (7.59)$$

The definition for the moist static energy was:  $E_m = C_p T + gz + Lq$ . The first two terms of the moist static energy are called the dry static energy:  $s = C_p T + gz$ . The moist static energy then becomes:  $E_m = s + Lq$ . Substituting:

$$\frac{\partial}{\partial t} (s + Lq) + \nabla \cdot (s + Lq) \mathbf{V} + \frac{\partial}{\partial p} (s + Lq) \omega = \Sigma H_m \quad (7.60)$$

or

$$\frac{\partial s}{\partial t} + \frac{\partial Lq}{\partial t} + \nabla \cdot s \mathbf{V} + \nabla \cdot Lq \mathbf{V} + \frac{\partial s \omega}{\partial p} + \frac{\partial Lq \omega}{\partial p} = \Sigma H_m \quad (7.61)$$

Rearranging:

$$\frac{\partial s}{\partial t} + \nabla \cdot s \mathbf{V} + \frac{\partial s \omega}{\partial p} + \frac{\partial Lq}{\partial t} + \nabla \cdot Lq \mathbf{V} + \frac{\partial Lq \omega}{\partial p} = \Sigma H_m \quad (7.62)$$

Taking the average:

$$\overline{\frac{\partial s}{\partial t}} + \nabla \cdot \overline{s \mathbf{V}} + \overline{\frac{\partial s \omega}{\partial p}} + \overline{\frac{\partial Lq}{\partial t}} + \nabla \cdot \overline{Lq \mathbf{V}} + \overline{\frac{\partial Lq \omega}{\partial p}} = \overline{\Sigma H_m} \quad (7.63)$$

Using  $\overline{AB} = \overline{A} \overline{B} + \overline{A'B'}$  for the vertical advection terms:

$$\frac{\partial \bar{s}}{\partial t} + \nabla \cdot \bar{sV} + \frac{\partial}{\partial p} (\bar{s} \bar{\omega} + \bar{s}'\bar{\omega}') + \frac{\partial \bar{Lq}}{\partial t} + \nabla \cdot \bar{LqV} + \frac{\partial}{\partial p} (\bar{Lq} \bar{\omega} + \bar{Lq}'\bar{\omega}') = \bar{\Sigma H}_m \quad (7.64)$$

Rearranging:

$$\frac{\partial \bar{s}}{\partial t} + \nabla \cdot \bar{sV} + \frac{\partial \bar{s}}{\partial p} \bar{\omega} + \frac{\partial \bar{Lq}}{\partial t} + \nabla \cdot \bar{LqV} + \frac{\partial \bar{Lq}}{\partial p} \bar{\omega} = \bar{\Sigma H}_m - \frac{\partial}{\partial p} (\bar{s}'\bar{\omega}' + \bar{Lq}'\bar{\omega}') \quad (7.65)$$

The definitions of  $Q_1$  and  $Q_2$  are:

$$Q_1 \equiv \frac{\partial \bar{s}}{\partial t} + \nabla \cdot \bar{sV} + \frac{\partial \bar{s}}{\partial p} \bar{\omega} \quad (7.66)$$

$$Q_2 \equiv -\frac{\partial \bar{Lq}}{\partial t} - \nabla \cdot \bar{LqV} - \frac{\partial \bar{Lq}}{\partial p} \bar{\omega} \quad (7.67)$$

Substituting 7.66 and 7.67 into 7.65:

$$Q_1 - Q_2 = \frac{\partial \bar{s}}{\partial t} + \nabla \cdot \bar{sV} + \frac{\partial \bar{s}}{\partial p} \bar{\omega} + \frac{\partial \bar{Lq}}{\partial t} + \nabla \cdot \bar{LqV} + \frac{\partial \bar{Lq}}{\partial p} \bar{\omega} \quad (7.68)$$

Recombining  $E_m = s + \bar{Lq}$ :

$$Q_1 - Q_2 = \frac{\partial \bar{E}_m}{\partial t} + \nabla \cdot \bar{E}_m V + \frac{\partial \bar{E}_m}{\partial p} \bar{\omega} \quad (7.69)$$

Rearranging:

$$\overline{\frac{\partial E_m}{\partial t}} = Q_1 - Q_2 - \nabla \cdot \overline{E_m \mathbf{V}} - \frac{\partial \overline{E_m \omega}}{\partial p} \quad (7.70)$$

Differentiating with respect to pressure

$$\overline{\frac{\partial^2 E_m}{\partial t \partial p}} = \frac{\partial Q_1}{\partial p} - \frac{\partial Q_2}{\partial p} - \frac{\partial}{\partial p} (\nabla \cdot \overline{E_m \mathbf{V}}) - \frac{\partial^2 \overline{E_m \omega}}{\partial p^2} \quad (7.71)$$

Using the moist static stability definition,  $\Gamma_m \equiv -\frac{\partial E_m}{\partial p}$

$$\frac{\partial \Gamma_m}{\partial t} = -\frac{\partial Q_1}{\partial p} + \frac{\partial Q_2}{\partial p} + \frac{\partial}{\partial p} (\nabla \cdot \overline{E_m \mathbf{V}}) + \frac{\partial^2 \overline{E_m \omega}}{\partial p^2} \quad (7.72)$$

Expanding the average horizontal advection term:

$$\frac{\partial \Gamma_m}{\partial t} = -\frac{\partial Q_1}{\partial p} + \frac{\partial Q_2}{\partial p} + \frac{\partial}{\partial p} \nabla \cdot \overline{E_m \mathbf{V}} + \frac{\partial}{\partial p} \nabla \cdot \overline{E_m \mathbf{V}'} + \frac{\partial^2 \overline{E_m \omega}}{\partial p^2} \quad (7.73)$$

Yanai (1973) has shown that the fourth term on the right hand side is small and may be neglected. Thus:

$$\frac{\partial \Gamma_m}{\partial t} = -\frac{\partial Q_1}{\partial p} + \frac{\partial Q_2}{\partial p} + \frac{\partial}{\partial p} \nabla \cdot \overline{E_m \mathbf{V}} + \frac{\partial^2 \overline{E_m \omega}}{\partial p^2} \quad (7.74)$$

where the last two terms represent the vertical differential of the three dimensional

advection of moist static energy.

The  $Q_1$  and  $Q_2$  terms are available in the FSUGSM. Bedi and Krishnamurti (1989) have discussed their components and the role they play in the FSUGSM.  $Q_1$  and  $Q_2$  are obtained through residue free heat and moisture budgets of the model at the desired stage of integration and are calculated through the parameterization of the physical processes in the model:

$$Q_1 = \text{Shortwave Radiation} + \text{Longwave Radiation} + \text{Large Scale Precipitation} + \\ \text{Convective Precipitation} + \text{Vertical Fluxes of Sensible Heat} + \\ \text{Latent Heat Flux} \quad (7.75)$$

$$Q_2 = \text{Large Scale Precipitation} + \text{Convective Precipitation} + \text{Latent Heat Flux} \quad (7.76)$$

#### 7.6 Sensitivity of the Moist Static Stability to Moisture Initialization

The moist static stability was derived from the equation for the equivalent potential temperature. This section demonstrates that the moist static stability is sensitive to the initialization as shown by large differences in the two experiments after 96 hours of integration. The effect on the forecast at the 96 hour point is described below for several cases. These cases are:

1. Typhoon Hope
2. monsoon
3. Atlantic ITCZ

Typhoon Hope was tracked by the Joint Typhoon Warning Center from July 25, 1979 (as a tropical disturbance) until August 8, 1979 (as a tropical depression). On 12 GMT July 31, 1979 it was classified as a super typhoon, with a surface wind speed in excess of 130 knots. The forecast initialization began at 12 GMT on 27 July, 1979 when Typhoon Hope became a tropical depression. The 96 hour forecast is valid just after the storm became a super typhoon. Figure 7.1 shows a cross section through the storm at this forecast hour. The cross section is oriented in an east/west direction, extending from 117° East to 137° East, and lies along the 21° North latitude. It extends from 1000 mb to 100 mb. Both cases show a  $\theta_e$  minimum outside the eye of the typhoon. However the profile of  $\theta_e$  for the control experiment is not as steep as the profile of the initialized experiment, implying that it is more stable than the initialized experiment. For the control case, the  $\theta_e$  minimum at 119° East is at 700 mb, yielding a  $\frac{\partial\theta_e}{\partial p}$  of 0.143 K/mb. The minimum at 136° East is at 550 mb, yielding a  $\frac{\partial\theta_e}{\partial p}$  of 0.112 K/mb. The initialized run has  $\theta_e$  minimums at 118° East and 136° East. The minimum at 118° East is at 700 mb, yielding a  $\frac{\partial\theta_e}{\partial p}$  of 0.157 K/mb. The minimum at 136° East is at 600 mb, yielding a  $\frac{\partial\theta_e}{\partial p}$  of 0.120 K/mb. For both storms, the  $\theta_e$  change with height is greater on the west side than on the east side. The direction of movement of the storm is towards the west, and the air with the greatest instability is being advected towards the center from that direction. In addition, the unstable air in the west for the initialized run is more unstable than the control run. This increased instability within the storm is evidenced by the next 24 hour forecast. The next forecast day, the storm has continued to grow in strength for the initialized case, but the control case has slowed its movement and lost some of its strength. This shows that the moist static stability of the tropical storm was sensitive to the initialization process. After 96 hours of integration, the vertical gradient of the equivalent potential temperature was larger

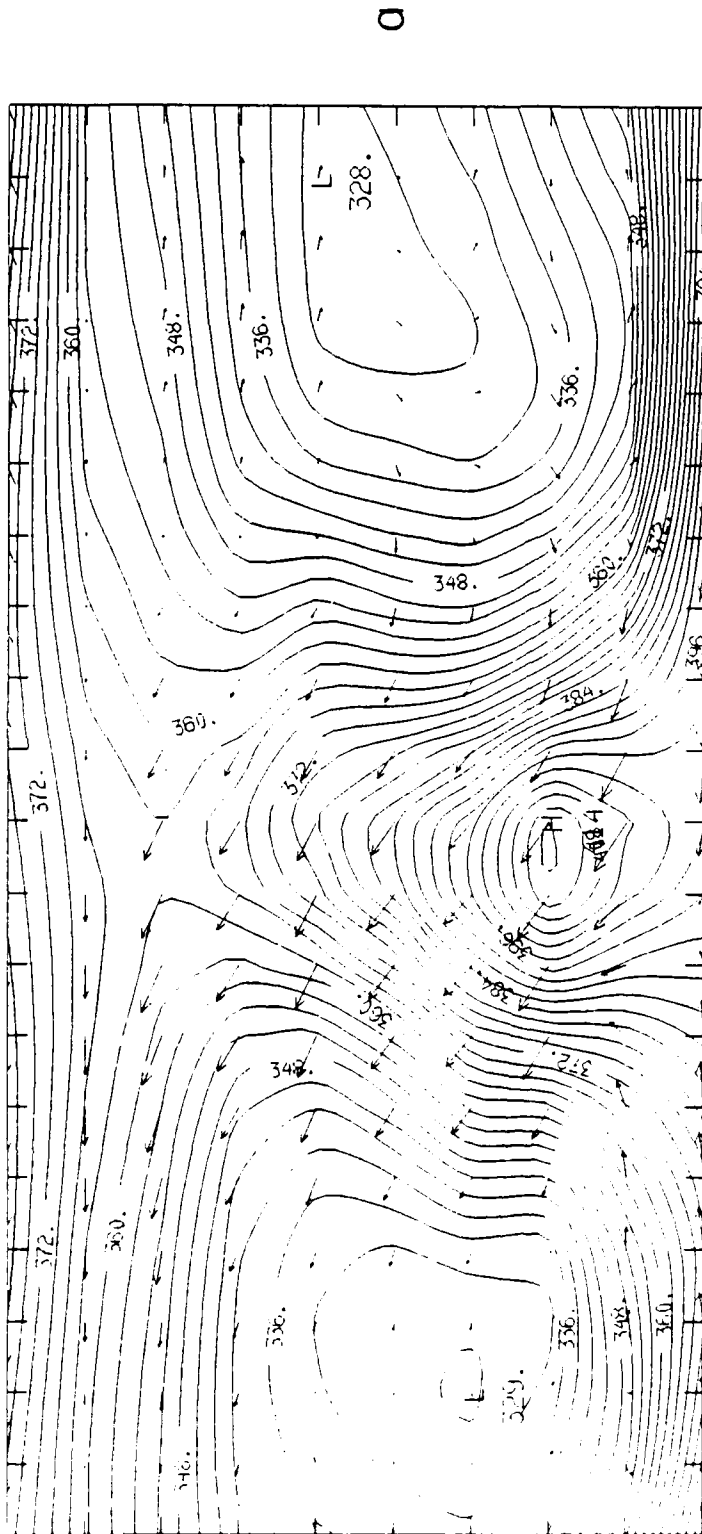
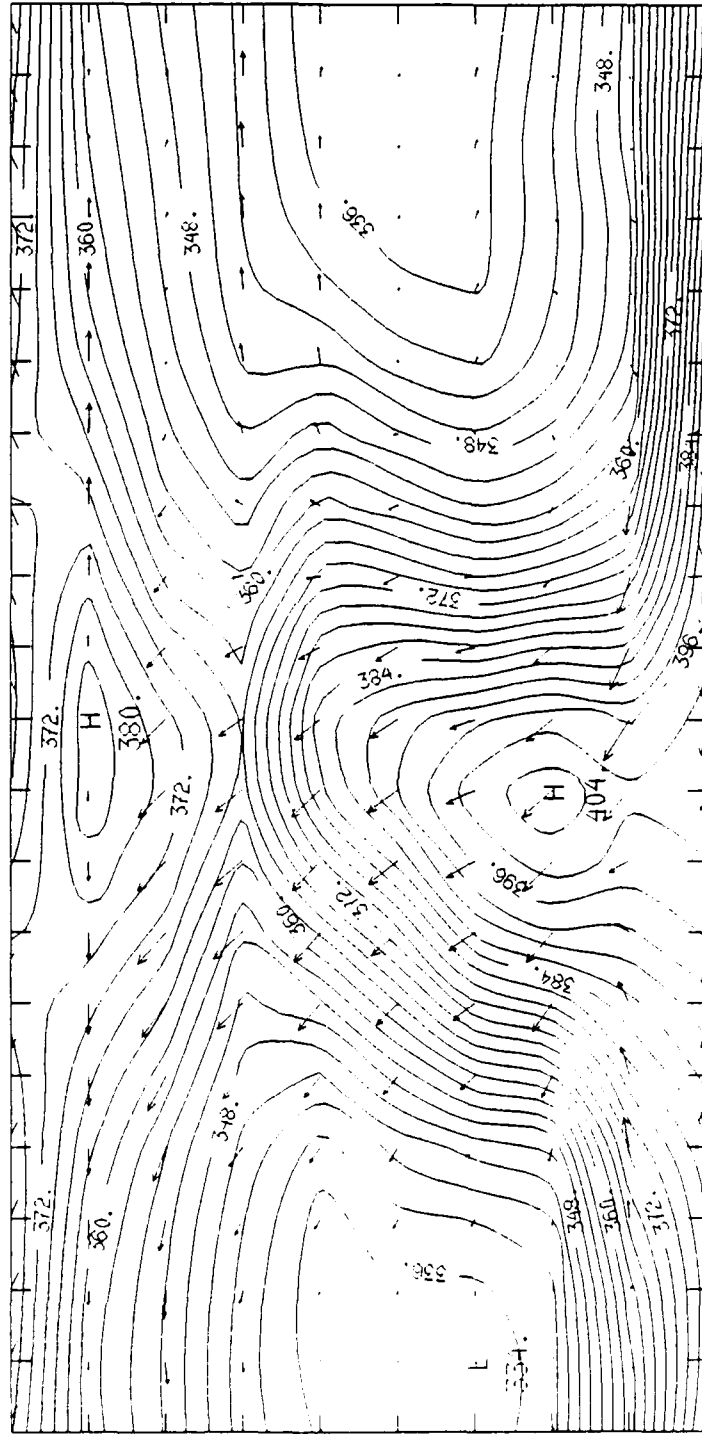


Figure 7.1a and b Cross section of Typhoon Hope showing the  $y/z$  plane, from  $117^\circ$  East to  $137^\circ$  East along the  $21^\circ$  North latitude. The contours are of equivalent potential temperature and the vectors are the  $u-\omega$  wind vectors. Chart a is the control experiment and chart b is the moisture initialization experiment.

b



for the initialized storm than the control storm. Earlier in this chapter, it was shown that the profiles of the equivalent potential temperature and the moist static stability could be considered the the same. The conclusion is that the initialization procedure enhanced the tropical storm by enhancing the profile of moist static stability.

Figure 7.2 is a cross section of the monsoon region. It is oriented in a north/south direction, extending from 0° North to 20° North along the 65° East meridian. In this case, the  $\theta_e$  gradients of both experiments are approximately the same. There are, however, two major differences between the experiments. The area of convection in the control (18° North) has a shallow unstable area (1000 mb to 700 mb), topped by a large constant  $\theta_e$  area (700mb to 400 mb). The initialized run shows the same area of convection, but the instability extends from the surface to almost 400 mb. To the south of this convective area are  $\theta_e$  minimums. The control run has two minimums. The minimum at 10° North is common to both runs, but the minimum at 2° North is found only in the control. Close examination shows that there is a slight downdraft in the control at 500 mb forcing the higher, more stable air into the middle regions and then into the lower levels. This stable air being advected into the lower levels is a likely reason for the double minimum and for the fact that the convective area does not extend very far into the atmosphere. The initialized run is better organized and has an updraft in the area of the control downdraft. The unstable air for the southern regions of the domain can be advected into the convective region without contamination from the more stable air aloft. Thus, even though the profiles of the equivalent potential temperatures were approximately the same, the monsoon of the initialized experiment was stronger due to the effect of the initialization on the organization of the monsoon.

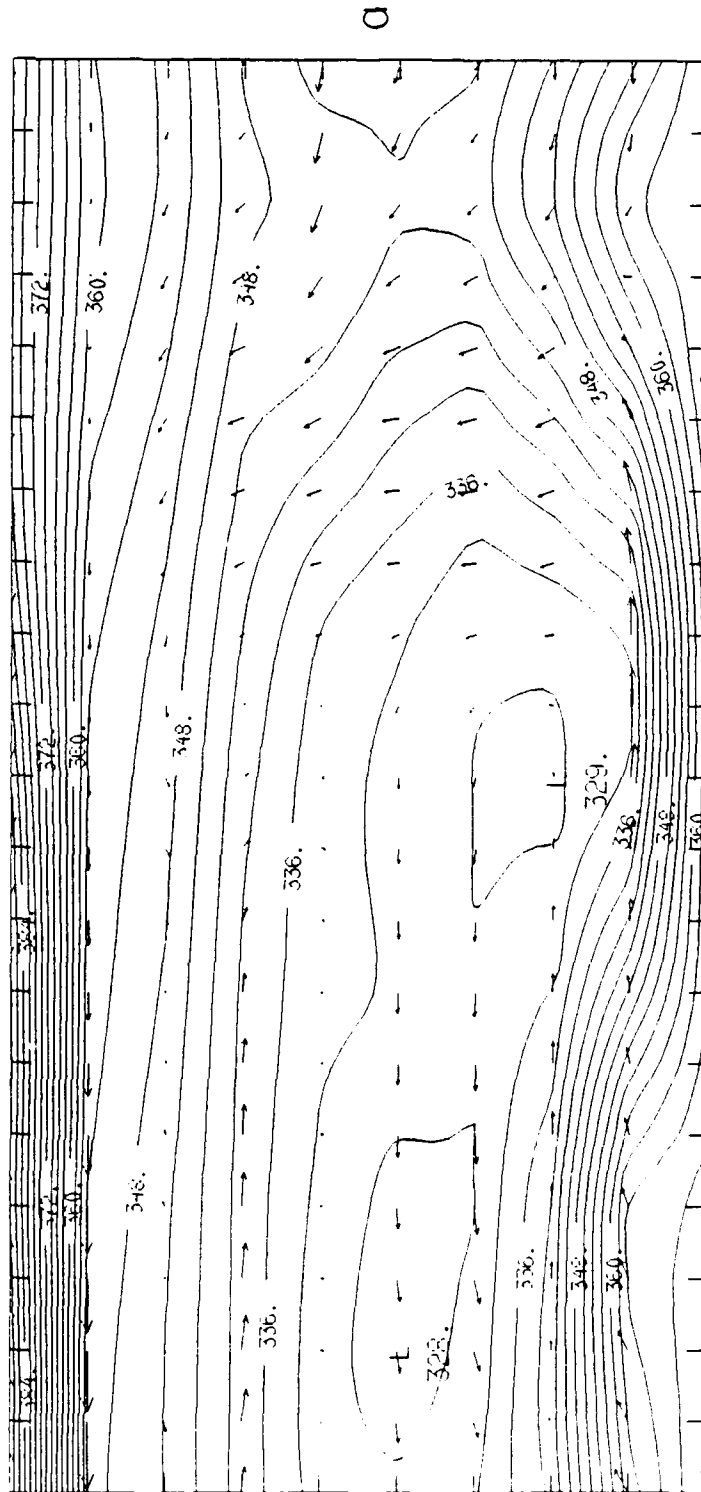
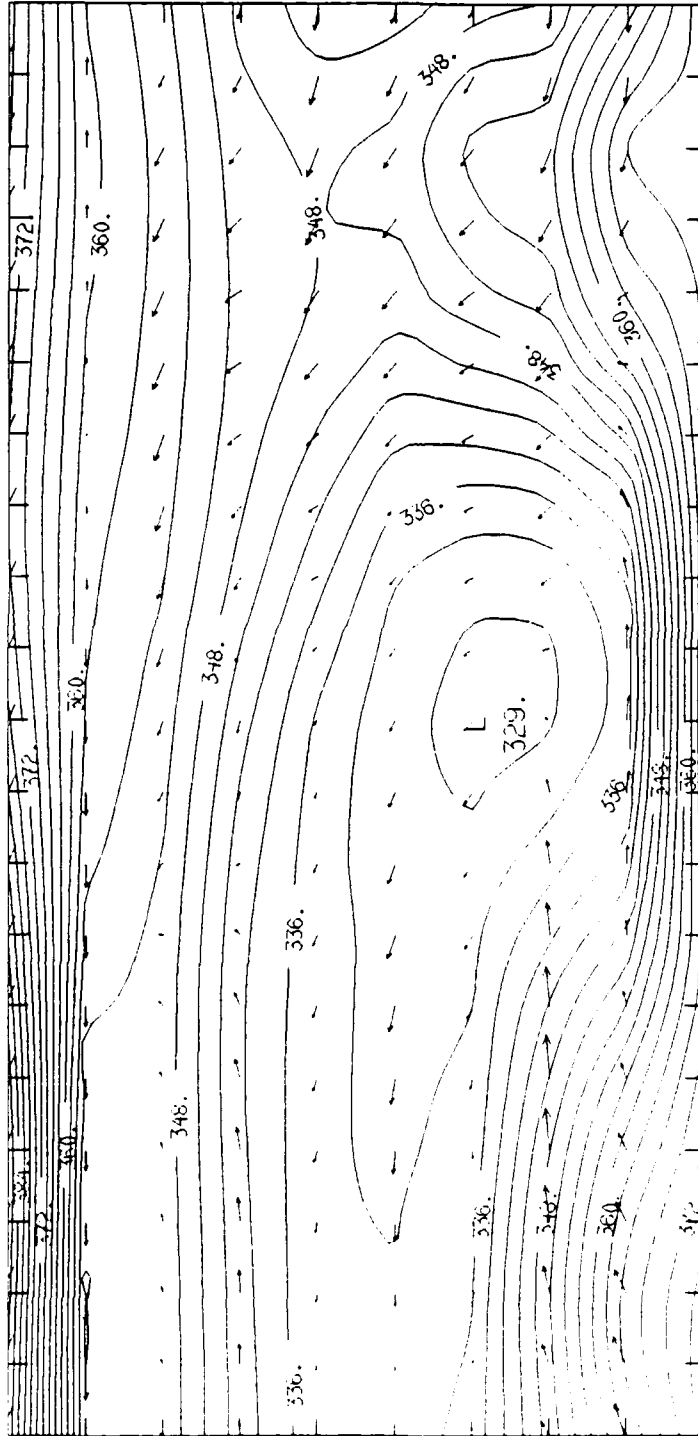


Figure 7.2a and b Cross section of the Indian monsoon, showing the  $x/z$  plane, from  $0^\circ$  North to  $20^\circ$  North along the  $65^\circ$  East meridian. The contours are of equivalent potential temperature and the vectors are the  $v-\omega$  wind vectors. Chart a is the control experiment and chart b is the moisture initialization experiment.

b



0.188E+02  
MAXIMUM VECTOR

CONTOUR FROM 327.00 TO 387.00 CONTOUR INTERVAL OF 3.0000 P.T.(3.3)= 350.68

Figure 7.3 is a cross section of the Atlantic Intertropical Convergence Zone. It is oriented in a north/south direction, extending from 0° North to 20° North along the 25° West meridian. Although the control experiment does not show a stable  $\theta_e$  profile below 600 mb over most of the domain, the vertical component of the wind shows a strong downdraft over most of the troposphere. This prevents any significant convective activity. Additionally, the downdraft prevents the unstable air from the  $\theta_e$  minimum at 2° North from being advected to this area. In the initialized run, there is a small area of updrafts at 9° North. The unstable air from the  $\theta_e$  minimum at 0° North is also being advected into this region. The result is a small convective area extending to the tropopause, even though the unstable profile is shallow (below 700 mb). The initialization did not provide for a deeper unstable profile in this case, but updrafts in the region allowed deep convection in the initialized experiment, while downdrafts in the control experiment prevented any significant convection. Thus, the organization of the Atlantic Ocean ITCZ was improved by the initialization procedure.

### 7.7 Sensitivity of the Moist Static Stability Tendency to Moisture Initialization

The tendency of the moist static stability for the three cases (*i.e.*, Typhoon Hope, the monsoon, and the Atlantic ITCZ) of section 7.6 is shown in figures 7.4 through 7.6. The geographic locations are the same as previously discussed for each of the three cases. In the section 7.6, the moist static stability was shown for an instant in time. In this section, the local rate of change of the moist static stability is presented.

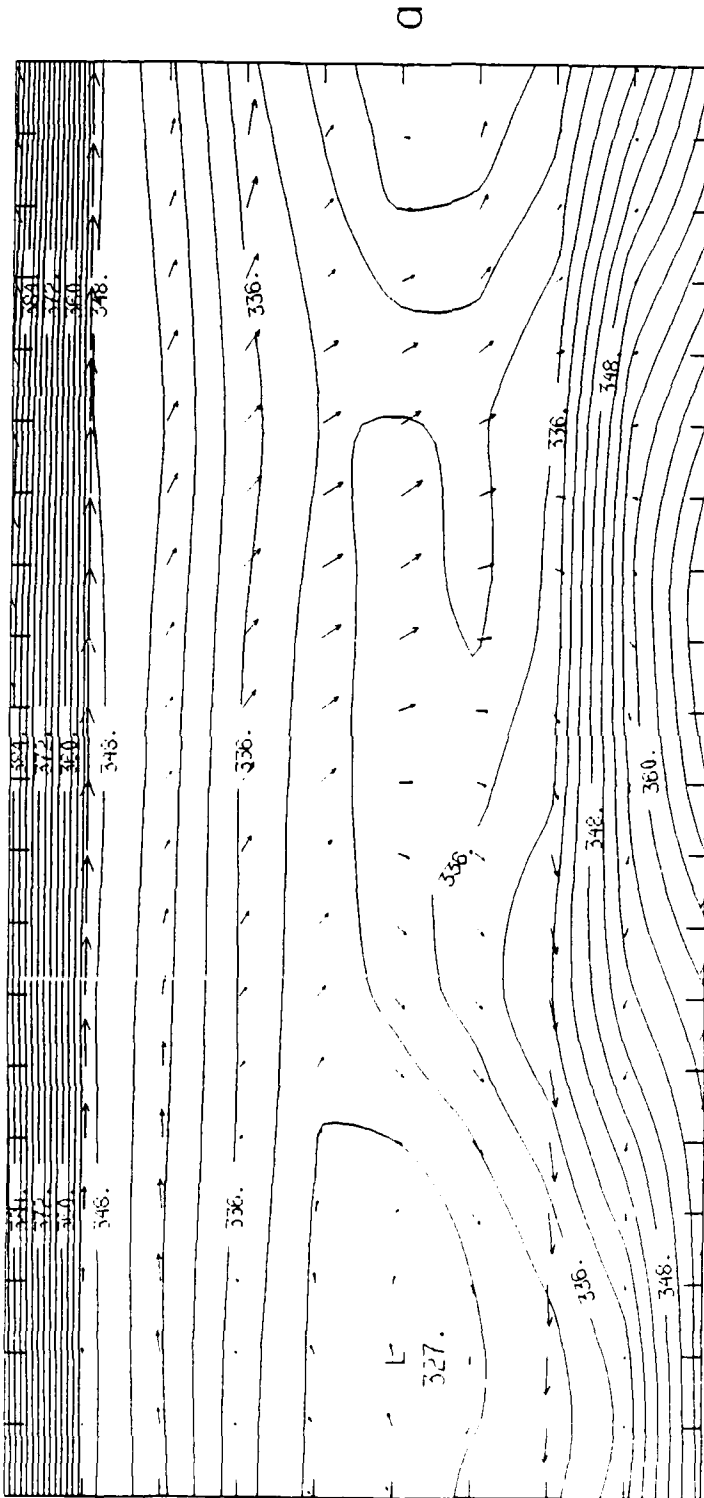
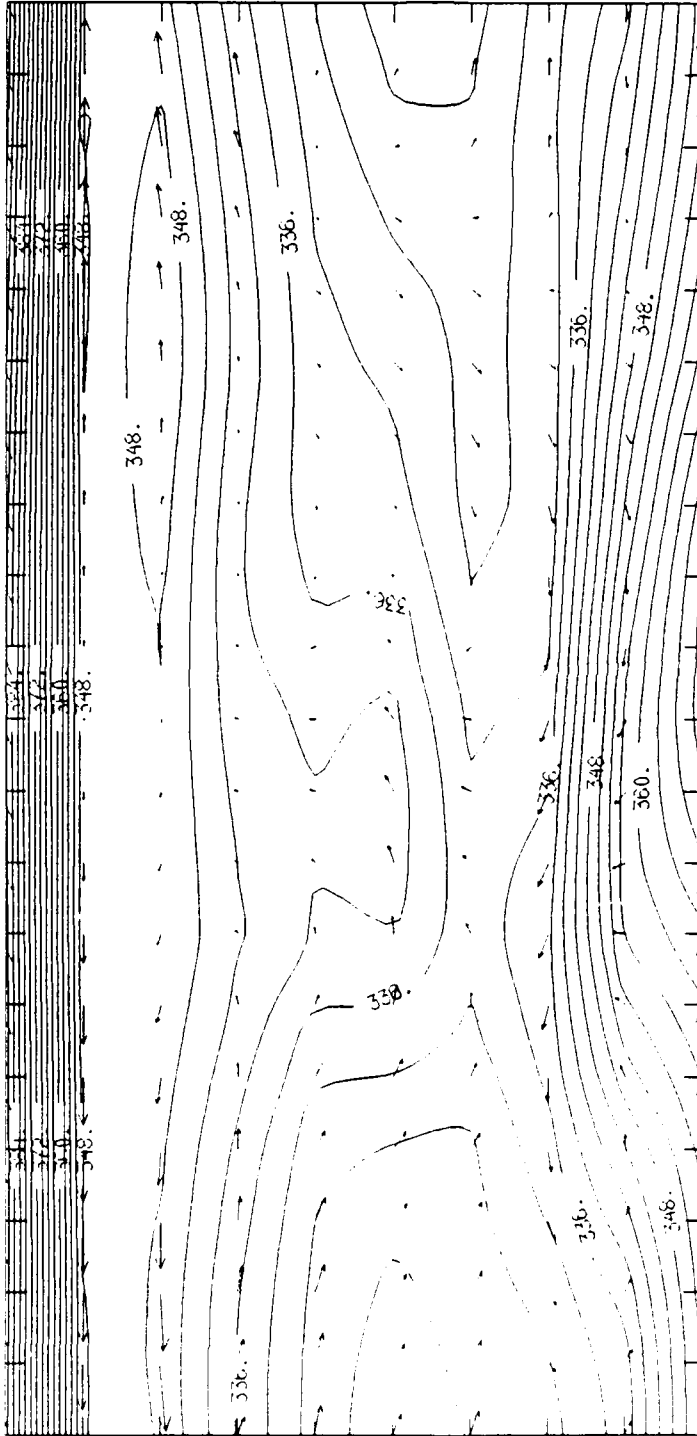


Figure 7.3a and b Cross section of the Atlantic Ocean ITCZ, showing the  $x/z$  plane, from  $0^\circ$  North to  $20^\circ$  North along the  $25^\circ$  West meridian. The contours are of equivalent potential temperature and the vectors are the  $v-w$  wind vectors. Chart a is the control experiment and chart b is the moisture initialization experiment.

b



0.105E+02  
MAXIMUM VECTOR

CONTOUR FROM 324.00 TO 395.00 CONTOUR INTERVAL OF 3.0000 PI(3.3)= 331.09

Figure 7.4 shows the local rate of change of the moist static stability for the case of Typhoon Hope. The area under the eye of Typhoon Hope is strongly positive (tending towards more stability) in both the control and initialized runs. This is in agreement with the classic structure of a typhoon in which the level nearest the surface has a positive stability. Just above this level is an area of negative tendencies. This corresponds to the portion of the eye where the equivalent potential temperature decreases with height. After 96 hours of integration, the initialized typhoon begins to increase translational wind speed, but the control typhoon does not. This is reflected in the moist static stability tendencies. The control typhoon is almost symmetrical about the eye. The tendencies are slightly more negative on the western side, indicating some movement in that direction. The initialized typhoon is not as symmetrical. The eastern side has positive tendencies extending further into the atmosphere while the western side is similar to the control. This indicates that the atmosphere is destabilized ahead of the typhoon and already beginning to stabilize to its east. The vertical differential of the three dimensional moist static energy advection is the dominant term in both of the experiments, followed by the vertical differential of the apparent heat source. The effect of the vertical differential of the apparent moisture sink is small. The effect of the initialization after 96 hours of integration was, therefore, to increase the destabilizing tendencies ahead of the typhoon, causing it to strengthen.

Figure 7.5 shows the moist static stability tendency for the monsoon case. Both experiments show the monsoon as an area of unstable tendencies. The unstable tendency of the initialized case is more than a third stronger than the control case. The unstable area of the initialized experiment is situated just to the north of an area with mildly stable tendencies. To the south of this area is another area of unstable tendencies. The control experiment has the same unstable – stable – unstable pattern.

As the air from the south is advected northward, it passes through the area of stable tendencies. The tendencies of the stable area for the control experiment are almost a factor of three greater than the initialization experiment. Thus, the control experiment will strongly stabilize the atmosphere flowing into the monsoon and the initialized experiment will not modify the unstable air to as great an extent. This permits the initialization experiment to produce a stronger, more vigorous monsoon. In the control case, the vertical differential of the apparent moisture sink and the vertical differential of the three dimensional moist static energy were equally dominant. In the initialized case, the vertical differential of the three dimensional moist static energy advection was the dominant term.

Figure 7.6 shows the moist static stability tendency for the Atlantic ITCZ case. There is a large difference between the control and initialized run. The control run is dominated by downdrafts over most of the region. In agreement with this type of stable situation, the tendencies are also stable for most of the region. The primary stabilizing force over the broadest area is the forcing due to vertical differential of the three dimensional moist static energy advection. The initialized run has downdrafts at both ends of the region and an area of updrafts in the center. This is reflected by a center unstable tendency flanked by regions of stable tendencies. The unstable tendency is enhanced by the forcing due to the vertical differential of the apparent heat source and of the three dimensional advection of the moist static energy. The effect of initialization on this case was to create an area of strongly negative tendencies where the control experiment had weak positive tendencies. Therefore, the initialization experiment was able to produce the deep convection of the Atlantic ITCZ and the control experiment could not.

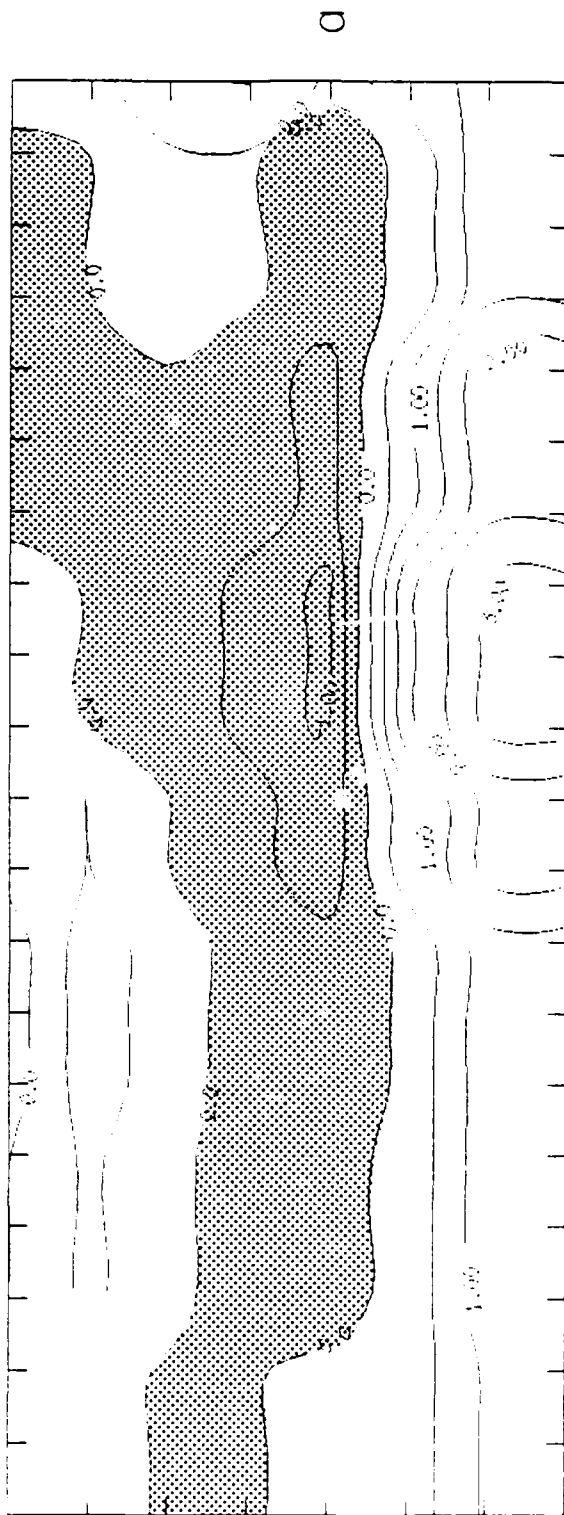
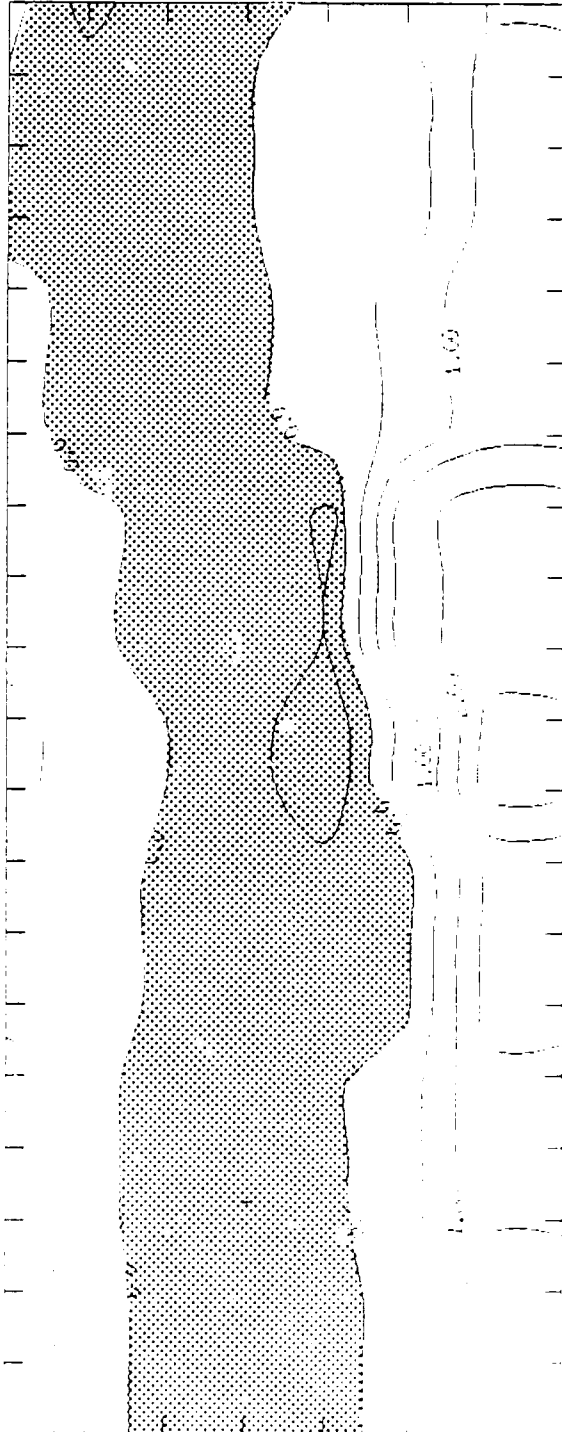


Figure 7.4a and b Cross section of Typhoon Hope showing the  $y/z$  plane, from  $117^{\circ}$  East to  $137^{\circ}$  East along the  $21^{\circ}$  North latitude. Contours are of the moist static stability tendency (negative areas are shaded). Chart a is the control experiment and chart b is the moisture initialization experiment.

b



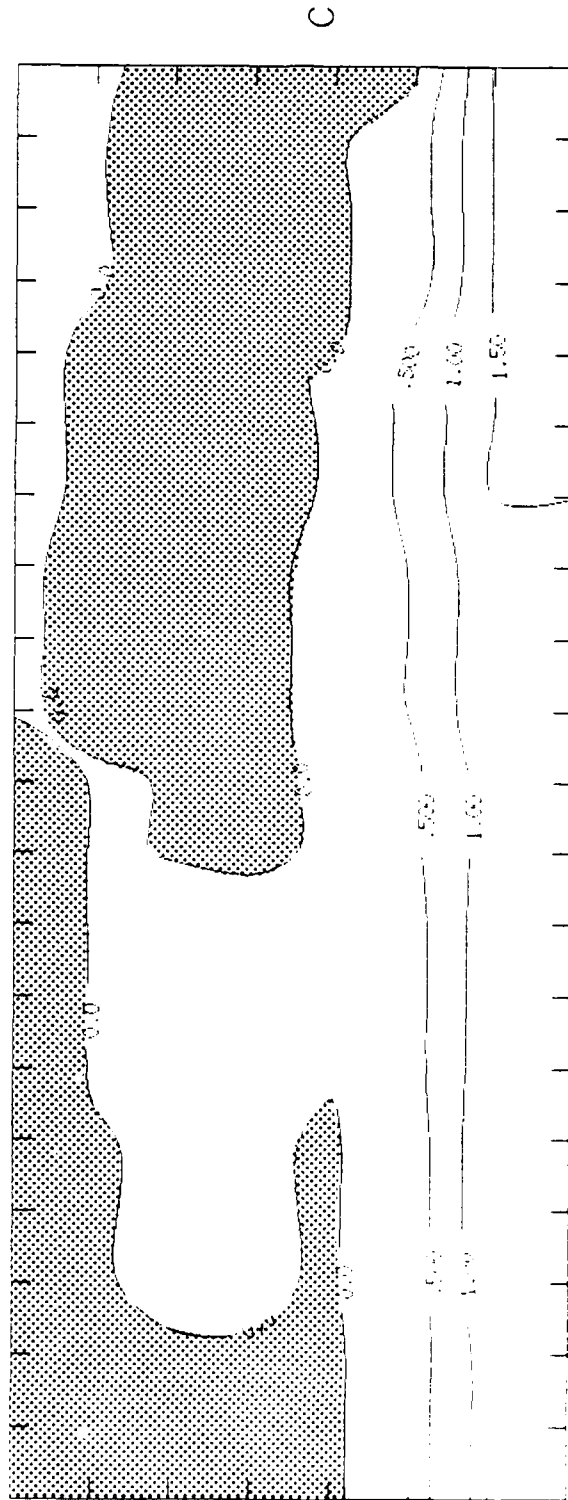


Figure 7.4c and d Cross section of Typhoon Hope showing the  $y/z$  plane, from  $117^{\circ}$  East to  $137^{\circ}$  East along the  $21^{\circ}$  North latitude. Contours are of the vertical differential of the apparent heat source (negative areas are shaded). Chart c is the control experiment and chart d is the moisture initialization experiment.

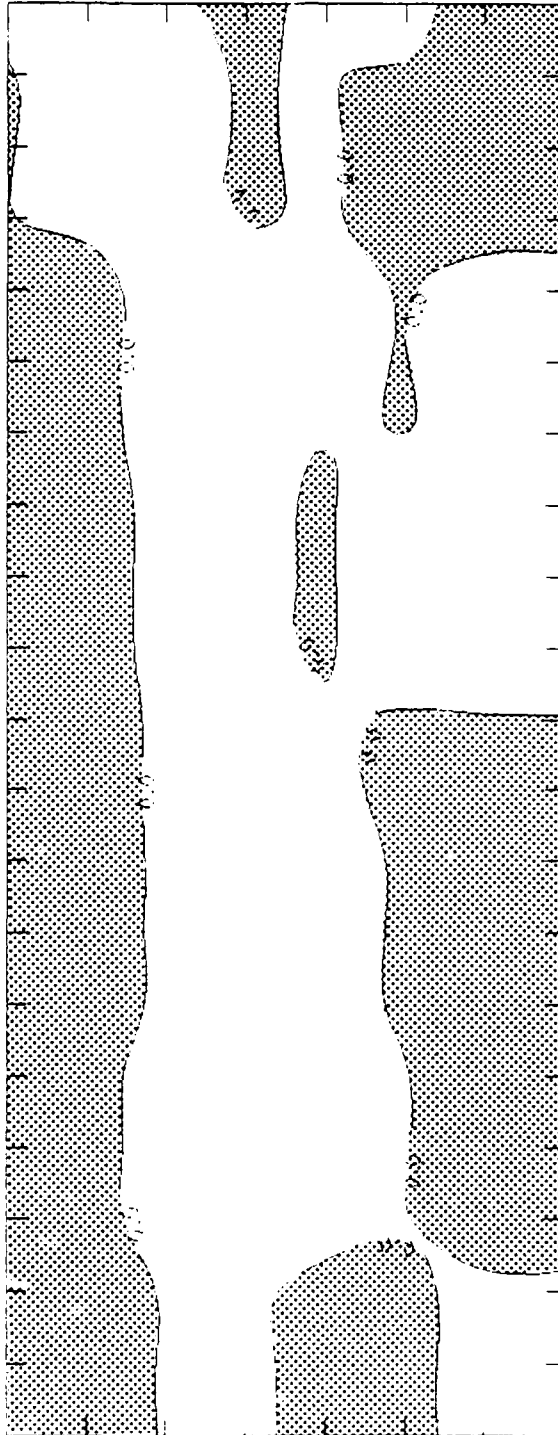
d





Figure 7.4e and f Cross section of Typhoon Hope showing the  $y/z$  plane, from  $117^\circ$  East to  $137^\circ$  East along the  $21^\circ$  North latitude. Contours are of the vertical differential of the apparent moisture sink (negative areas are shaded). Chart e is the control experiment and chart f is the moisture initialization experiment.

f



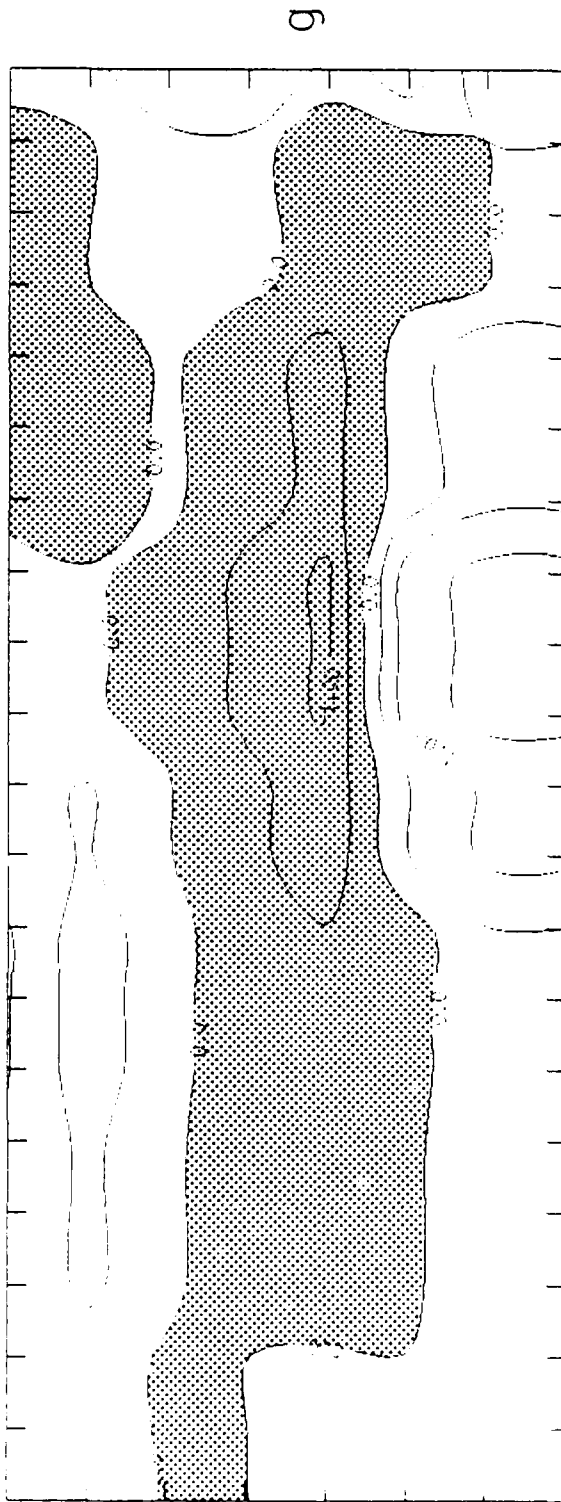
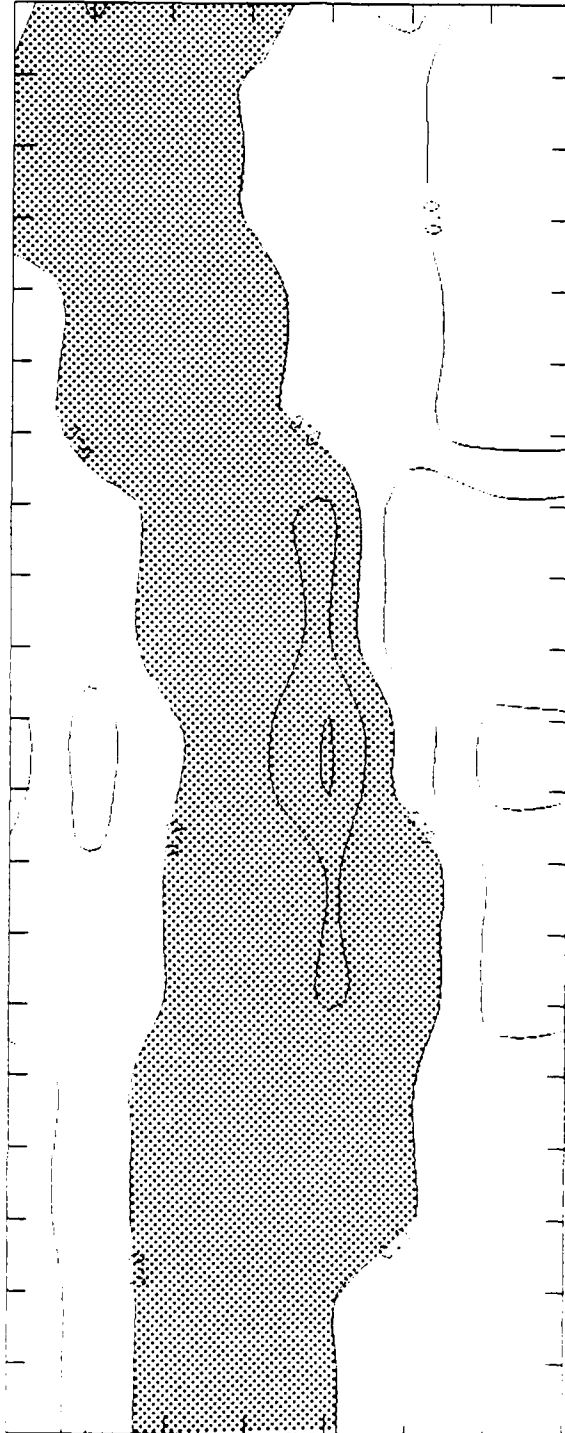


Figure 7.4g and h Cross section of Typhoon Hope showing the  $y/z$  plane, from  $117^\circ$  East to  $137^\circ$  East along the  $21^\circ$  North latitude. Contours are of the vertical differential of the 3 dimensional advection of the moist static energy (negative areas are shaded). Chart g is the control experiment and chart h is the moisture initialization experiment.

h



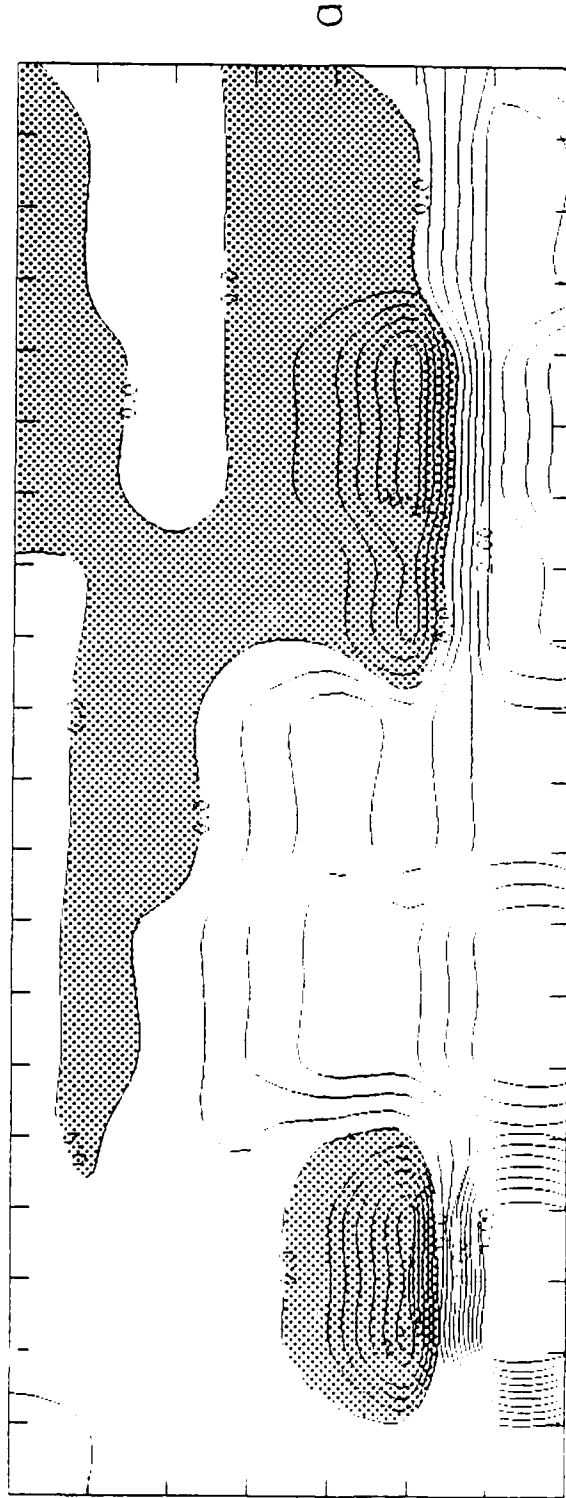
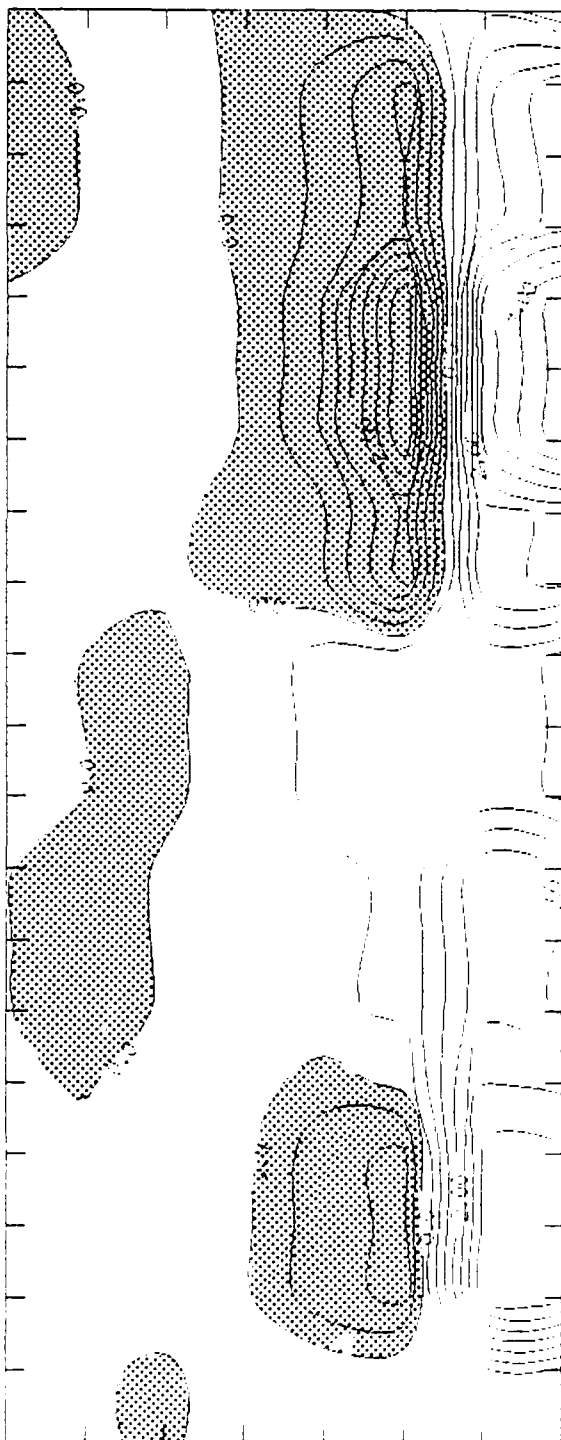


Figure 7.5a and b Cross section of the Indian monsoon, showing the  $x/z$  plane, from  $0^\circ$  North to  $20^\circ$  North along the  $65^\circ$  East meridian. The contours are of moist static stability tendency (negative areas are shaded). Chart a is the control experiment and chart b is the moisture initialization experiment.

b



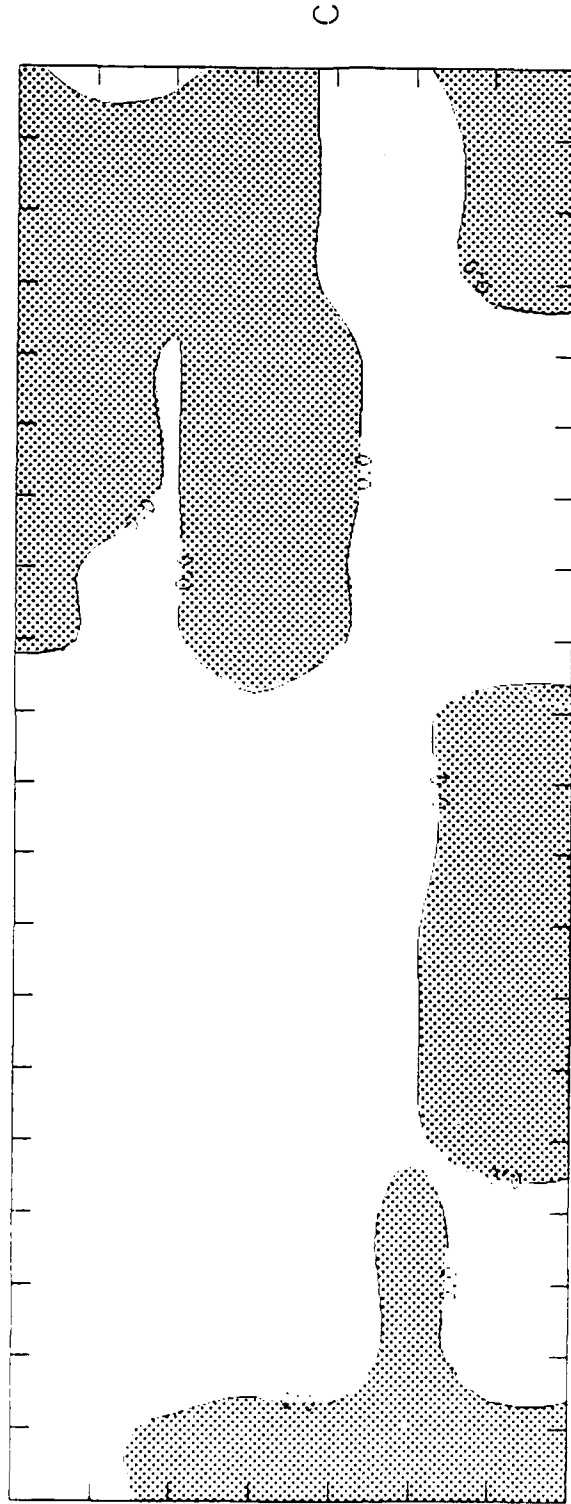


Figure 7.5c and d Cross section of the Indian monsoon, showing the  $x/z$  plane, from  $0^\circ$  North to  $20^\circ$  North along the  $65^\circ$  East meridian. The contours are of the vertical differential of the apparent heat source (negative areas are shaded). Chart c is the control experiment and chart d is the moisture initialization experiment.

p

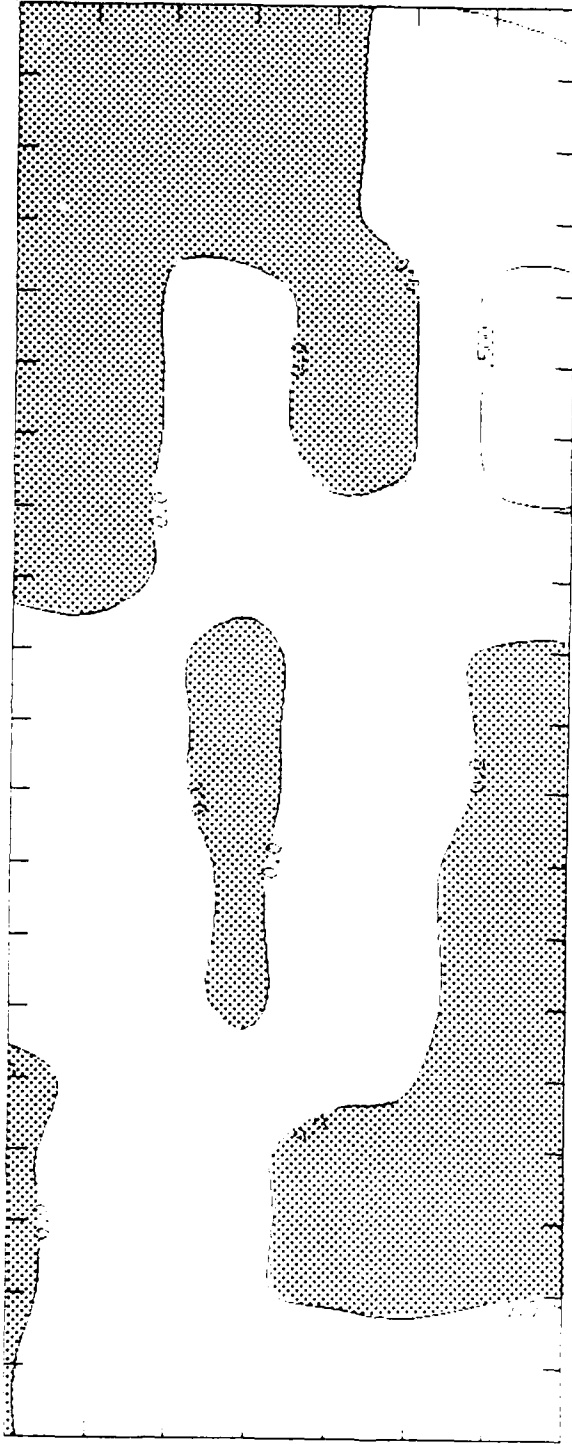
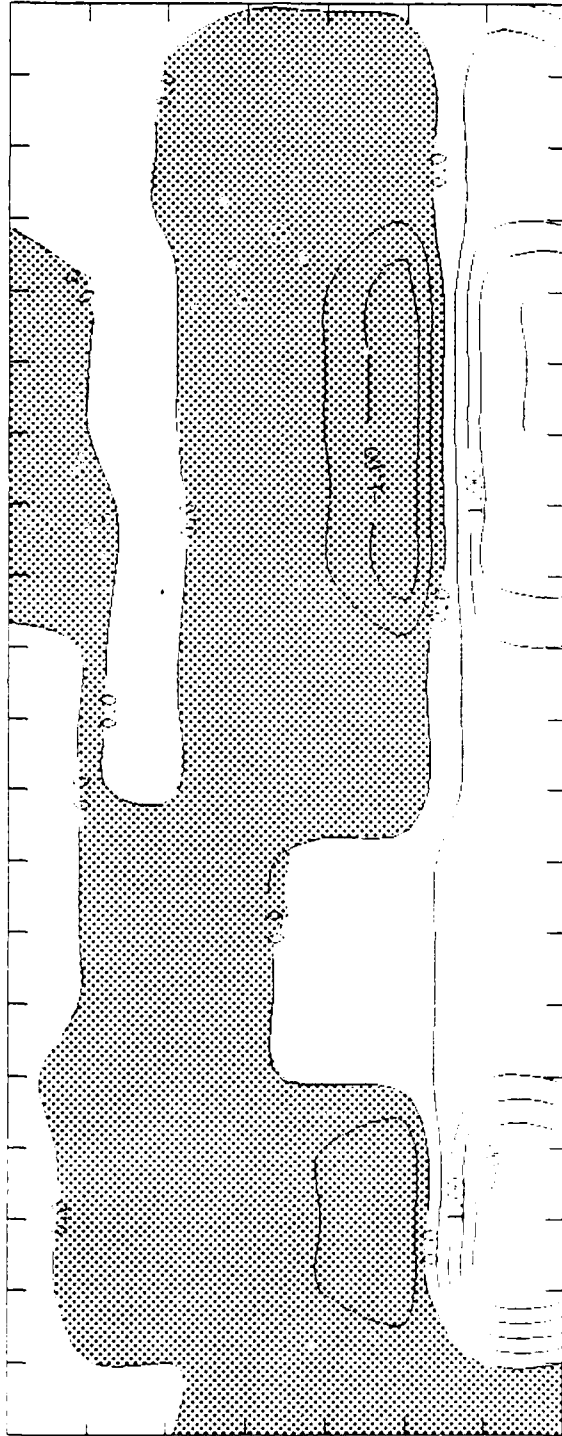




Figure 7.5e and f Cross section of the Indian monsoon, showing the  $x/z$  plane, from  $0^\circ$  North to  $20^\circ$  North along the  $65^\circ$  East meridian. The contours are of the vertical differential of the apparent moisture sink (negative areas are shaded). Chart e is the control experiment and chart f is the moisture initialization experiment.

f



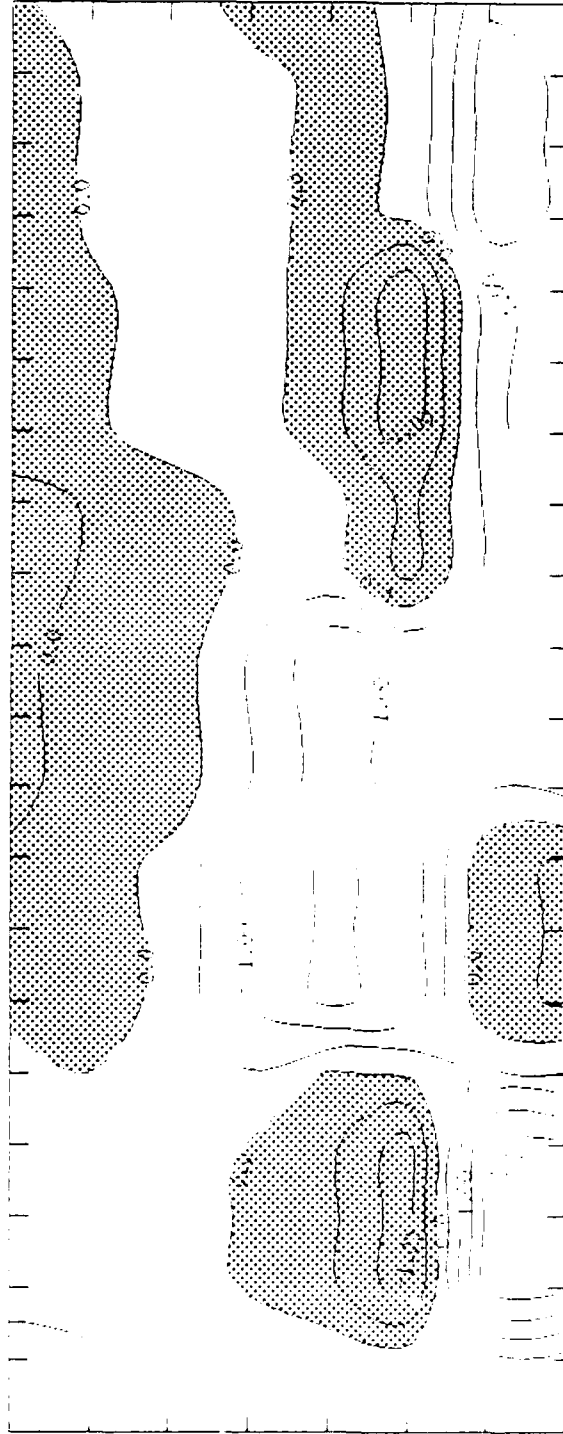
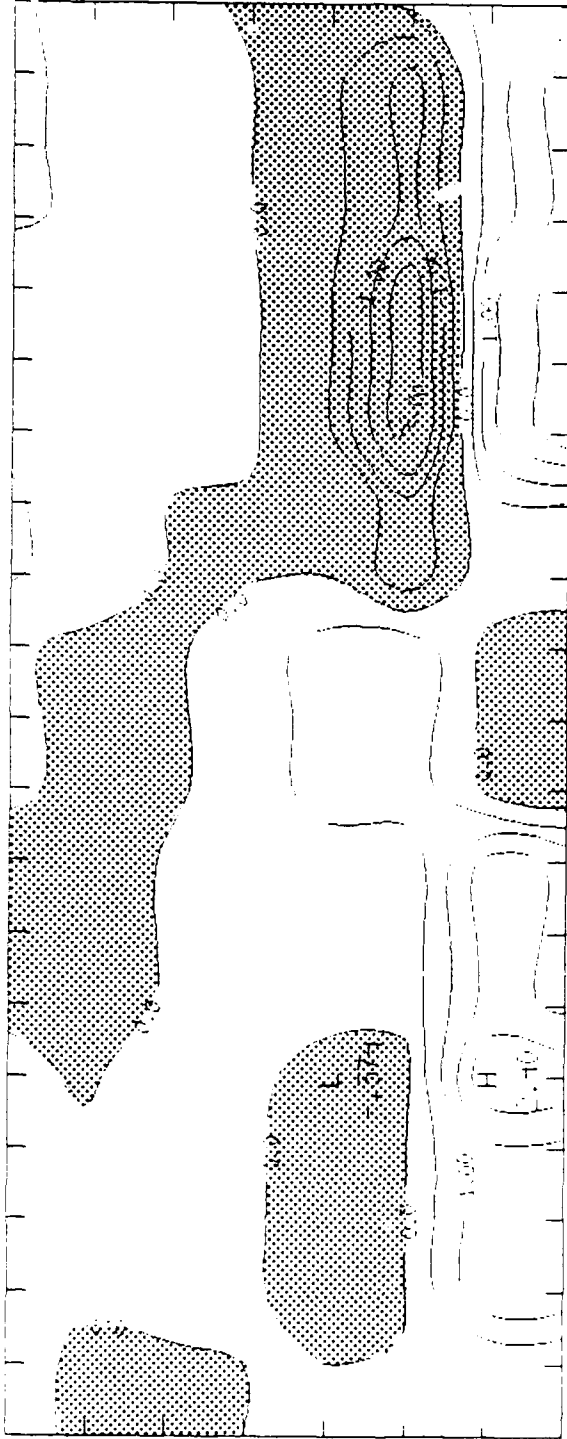


Figure 7.5g and h Cross section of the Indian monsoon, showing the  $x/z$  plane, from  $0^\circ$  North to  $20^\circ$  North along the  $65^\circ$  East meridian. The contours are of the vertical differential of the 3 dimensional advection of the moist static energy (negative areas are shaded). Chart g is the control experiment and chart h is the moisture initialization experiment.

h



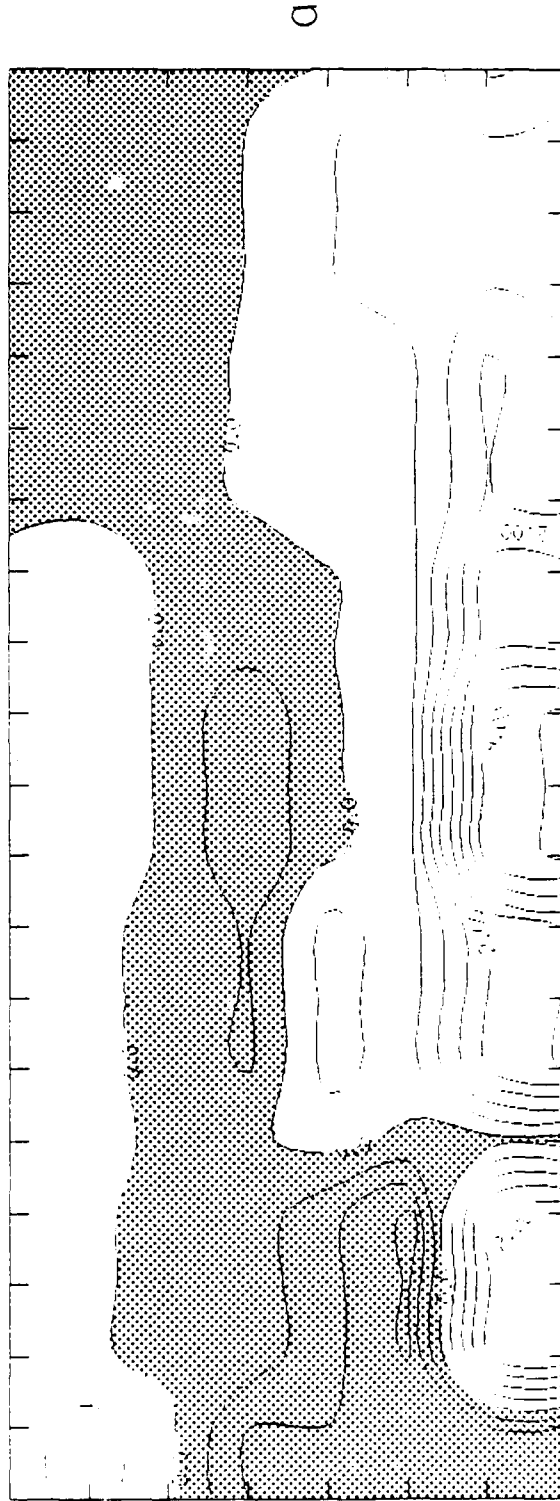
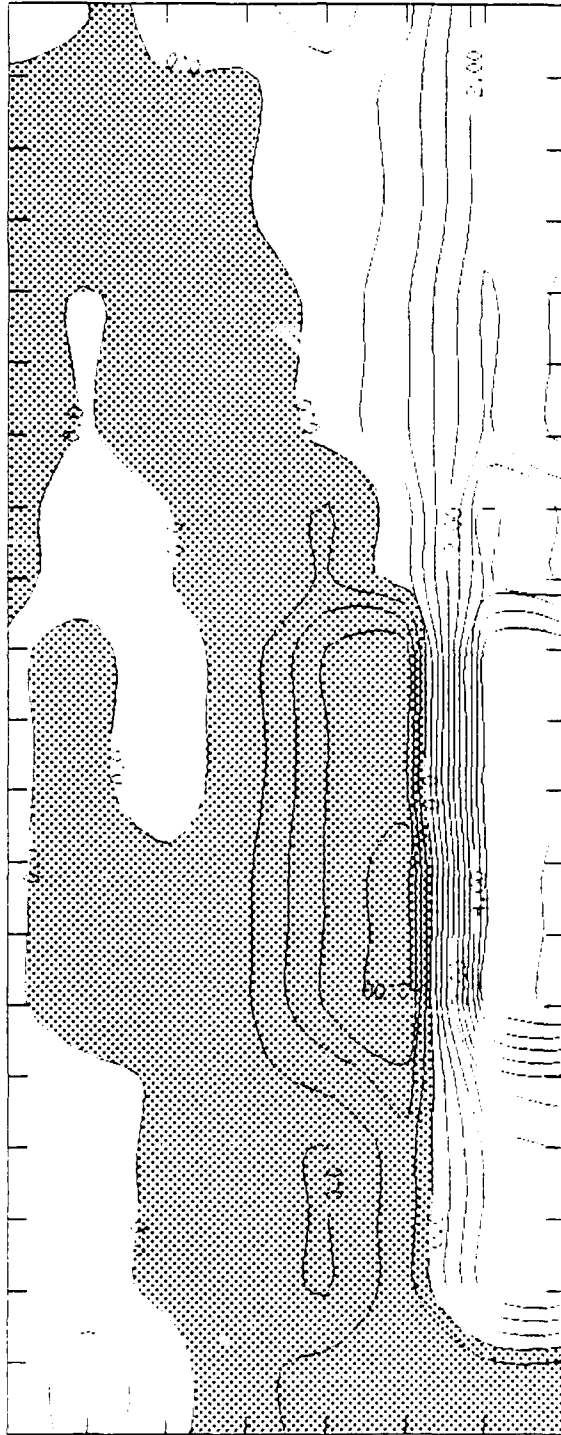


Figure 7.6a and b Cross section of the Atlantic Ocean ITCZ, showing the  $x/z$  plane, from  $0^\circ$  North to  $20^\circ$  North along the  $25^\circ$  West meridian. The contours are of moist static stability tendency (negative areas are shaded). Chart a is the control experiment and chart b is the moisture initialization experiment.

b



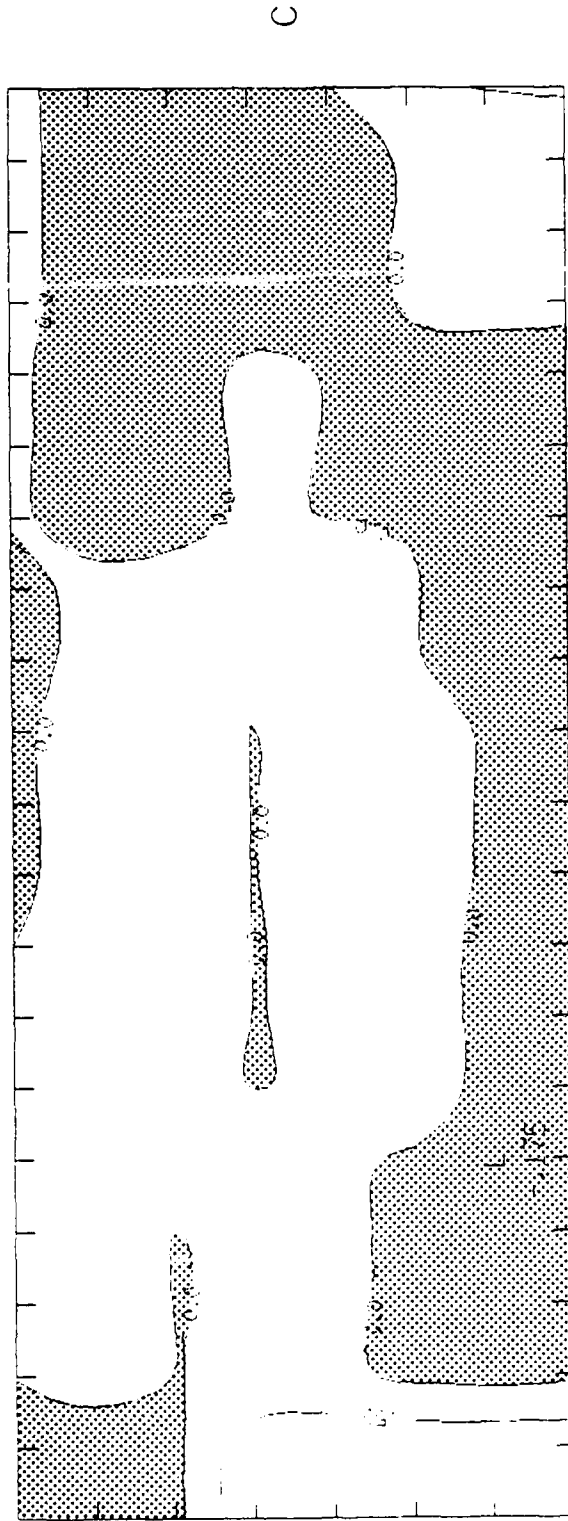
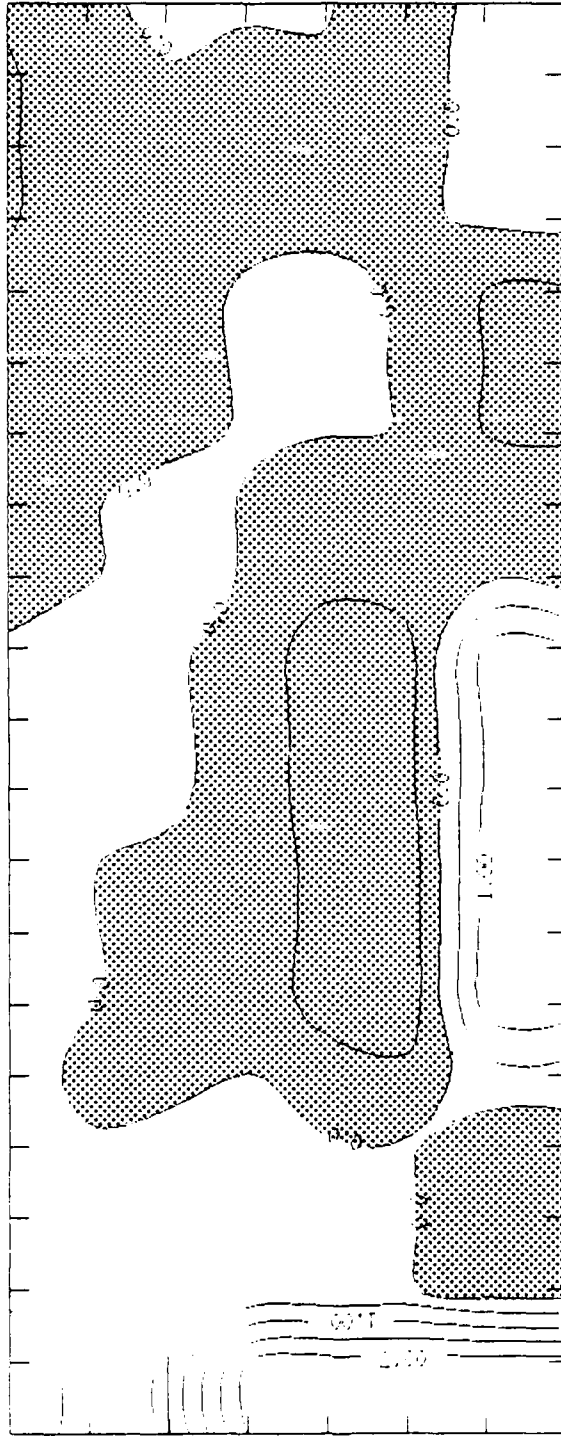


Figure 7.6c and d Cross section of the Atlantic Ocean ITCZ, showing the  $x/z$  plane, from  $0^\circ$  North to  $20^\circ$  North along the  $25^\circ$  West meridian. The contours are of the vertical differential of the apparent heat source (negative areas are shaded). Chart c is the control experiment and chart d is the moisture initialization experiment.

p

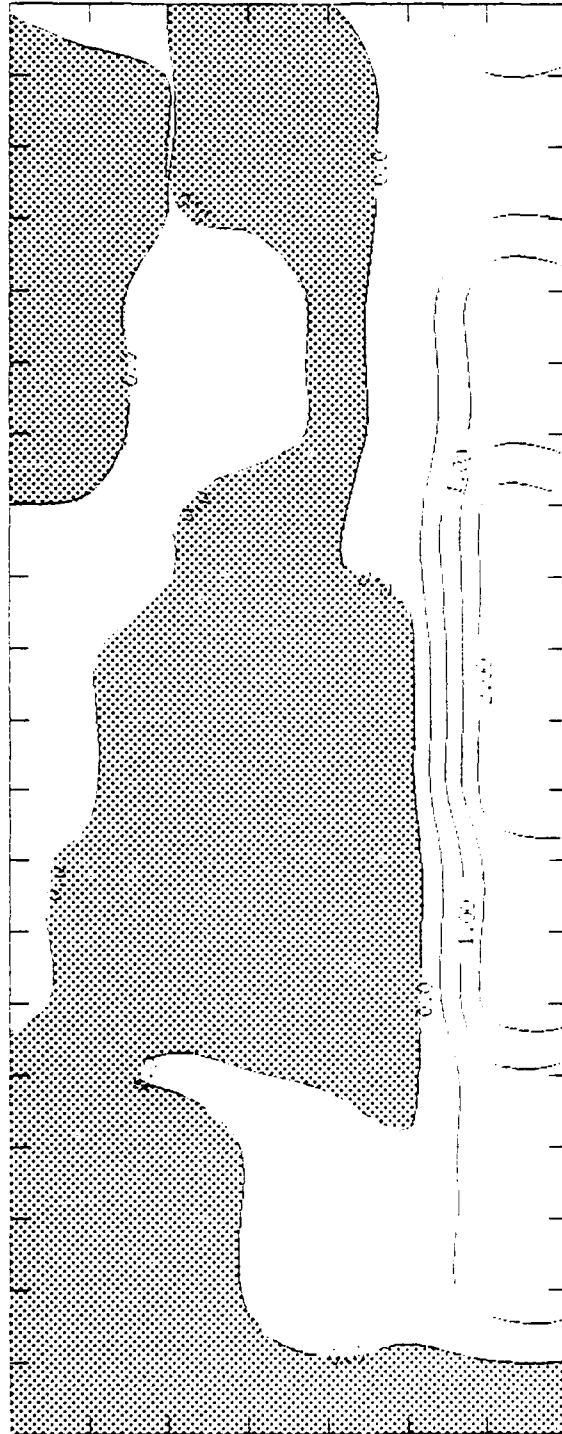


e



Figure 7.6e and f Cross section of the Atlantic Ocean ITCZ, showing the  $x/z$  plane, from  $0^\circ$  North to  $20^\circ$  North along the  $25^\circ$  West meridian. The contours are of the vertical differential of the apparent moisture sink (negative areas are shaded). Chart e is the control experiment and chart f is the moisture initialization experiment.

f



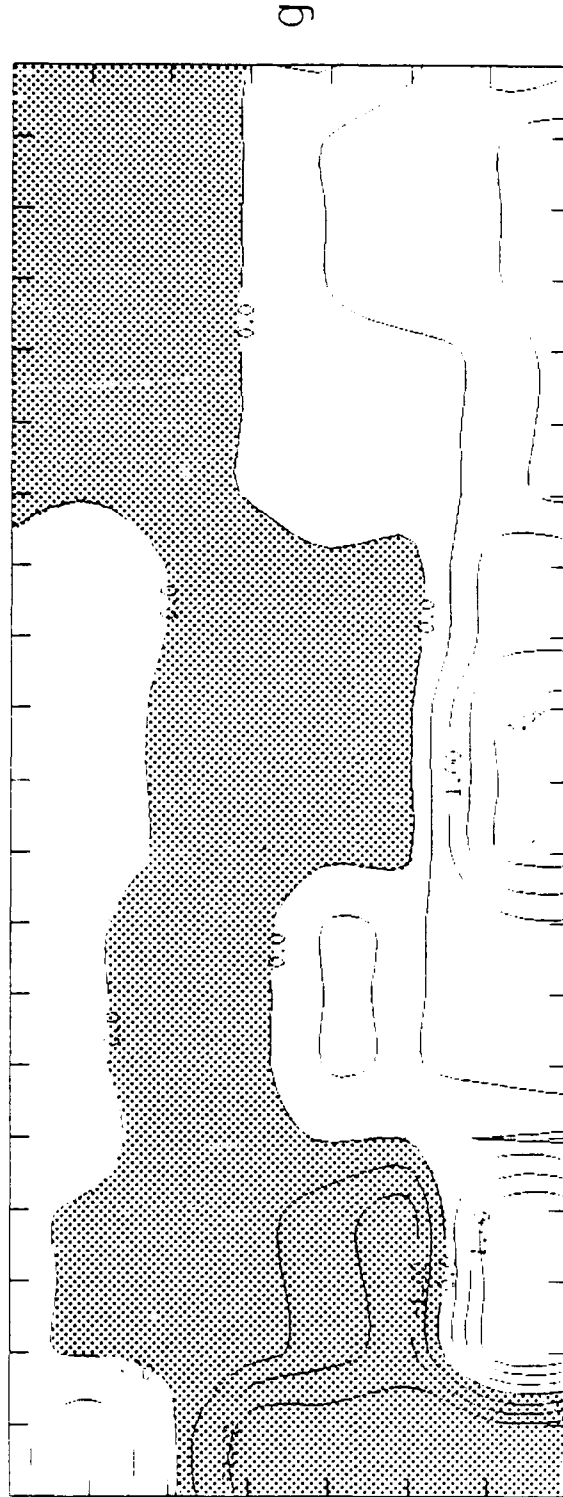
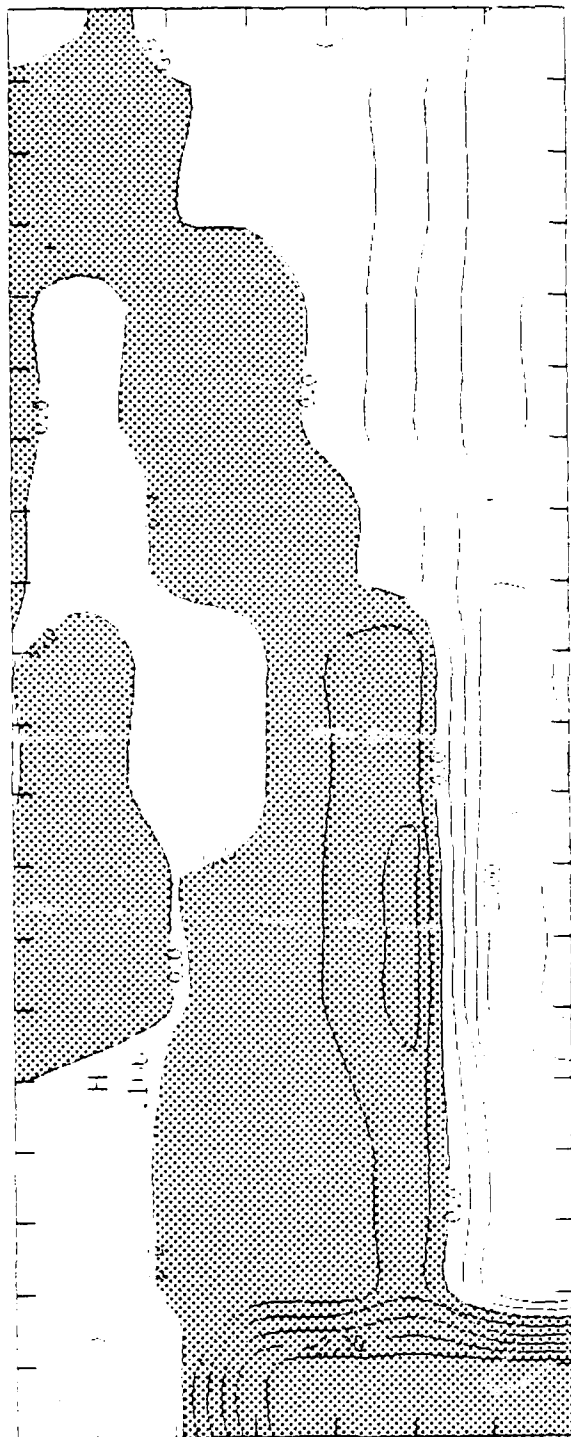


Figure 7.6g and h Cross section of the Atlantic Ocean ITCZ, showing the  $x/z$  plane, from  $0^\circ$  North to  $20^\circ$  North along the  $25^\circ$  West meridian. The contours are of the 3 dimensional advection of the moist static energy (negative areas are shaded). Chart g is the control experiment and chart h is the moisture initialization experiment.

h



### 7.8 Residual free budgets of $Q_1$ and $Q_2$

The apparent heat source ( $Q_1$ ) and the apparent moisture source ( $Q_2$ ) were introduced in section 7.5. They were obtained through residual free heat and moisture budgets of the FSUGSM from parameterization of the physical forcings. As given by equations 7.75 and 7.76, the forcings are:

$$\begin{aligned}
 Q_1 = & \text{Shortwave Radiation} + \text{Longwave Radiation} + \text{Large Scale Precipitation} + \\
 & \text{Convective Precipitation} + \text{Vertical Convergence of Sensible Heat} + \\
 & \text{Latent Heat Flux} \qquad \qquad \qquad (7.77)
 \end{aligned}$$

$$\begin{aligned}
 Q_2 = & \text{Large Scale Precipitation} + \text{Convective Precipitation} + \\
 & \text{Vertical Convergence of Latent Heat} \qquad \qquad \qquad (7.78)
 \end{aligned}$$

The budgets were calculated for an air mass as it entered the Atlantic Ocean ITCZ. Point A refers to the air mass at 18° North and 327° East after 24 hours of integration. Point B refers to the 72 hour slightly modified air mass at 12° North and 316° East. Point C refers to the 120 hour modified air mass at 10° North and 307° East. The control and the moisture initialization results are presented for each point. Another control experiment which uses the older emissivity radiation scheme of Chang, 1980 is also presented because the budgets are sensitive to radiation algorithms. The apparent heat source of the old radiation experiment is presented in figure 7.7. The components of  $Q_1$  are shown in figure 7.8. In this set of charts  $Q_1$  is very shallow. Point A has a small  $Q_1$ , except near the surface, where the flux of sensible heat is large. Points B and C also have a small  $Q_1$ , except where there is a convergence of sensible heat flux centered at 700 mb. At Point C, there is shallow, large scale precipitation contributing

to  $Q_1$ . The apparent heat source of the control experiment is shown in figure 7.9. The components of  $Q_1$  for this experiment are shown in figure 7.10. The  $Q_1$  of Point A is shallow, owing much of its value to convective precipitation at 800 mb. As the parcel moves closer to the ITCZ (point B),  $Q_1$  shows a shallow spike at 800 mb due to a convergence of sensible heat. At the ITCZ (point C),  $Q_1$  is positive throughout the atmosphere. There is a minimum of  $Q_1$  at 800 mb due to weak, large scale and convective precipitation and strong radiative cooling. The  $Q_1$  of the moisture initialization experiment is shown in figure 7.11. The components of  $Q_1$  for this experiment are shown in figure 7.12. At point A,  $Q_1$  is shallow, owing much of its value to convective precipitation below 600 mb. As the parcel moves closer to the ITCZ (point B),  $Q_1$  is strongly positive below 700 mb. This is due to a net convergence of sensible heat at 700 mb and strong contributions from the large scale and convective precipitation heating. At the ITCZ (Point C),  $Q_1$  is positive throughout the column. The 800 mb minimum of the control experiment is not present because the convective precipitation forcing is twice as strong in this experiment. Therefore, the effect of moisture initialization after 120 hours of integration is realized by the increase in the apparent heating at 700 mb due to an increase in convective precipitation.

Krishnamurti *et al.*, 1990 have demonstrated that radiative destabilization due to cloud top cooling plays an important role in the tropical atmosphere. Figures 7.7, 7.9, and 7.11 show the total radiation (shortwave and longwave). Figure 13 shows the longwave radiation of the atmosphere in relation to the cloud amounts of Point C of the moisture initialization experiment. The maximum cooling for this point is at the cloud top of the low clouds. (Note that this area of maximum cooling at the cloud top is also the area of the minimum equivalent potential temperature.) Figure 7.14 shows the radiative destabilization due to the low cloud amounts for three experiments as the

parcels approach the ITCZ. In figure 7.14a (the older emissivity radiation experiment), it is obvious that the lack of low clouds produce no radiative destabilization and an inactive ITCZ. In figure 7.14b (the control experiment), the low clouds produce radiative destabilization and an active ITCZ. The moisture initialization experiment produced the strongest destabilization. After five days of integration, the destabilization is an order of magnitude greater than the control experiment, resulting in a strong and active ITCZ.

The apparent moisture sink of the old radiation experiment is shown in figure 7.15. At Point A, the parcel experiences no net change in moisture above the 600 mb level. This is due to all of the component forcings having a value near zero. Below the 600 mb level, there is an apparent net loss of moisture due to convective precipitation through 800 mb. Below 800 mb, the atmosphere is gaining moisture due to latent heat forcing. As the parcel approaches the ITCZ (Point B), it is gaining moisture at all levels due to the forcing of latent heat. At the ITCZ (Point C), the atmosphere is increasing its apparent moisture at all levels except at 600 to 500 mb. In this layer there is drying due to the fact that the forcing from convective precipitation is stronger than the forcing from latent heat. The control and the moisture initialization experiments produced similar results; therefore, only the moisture initialization experiment will be shown (figure 7.16). At Point A, there is a net loss of moisture throughout the column due to the large scale and convective precipitation. As the parcel nears the ITCZ (Point B), the atmosphere is moistening in the lower levels due to vertical moisture fluxes. In the ITCZ (Point C), the atmosphere is drying due to strong convective precipitation.

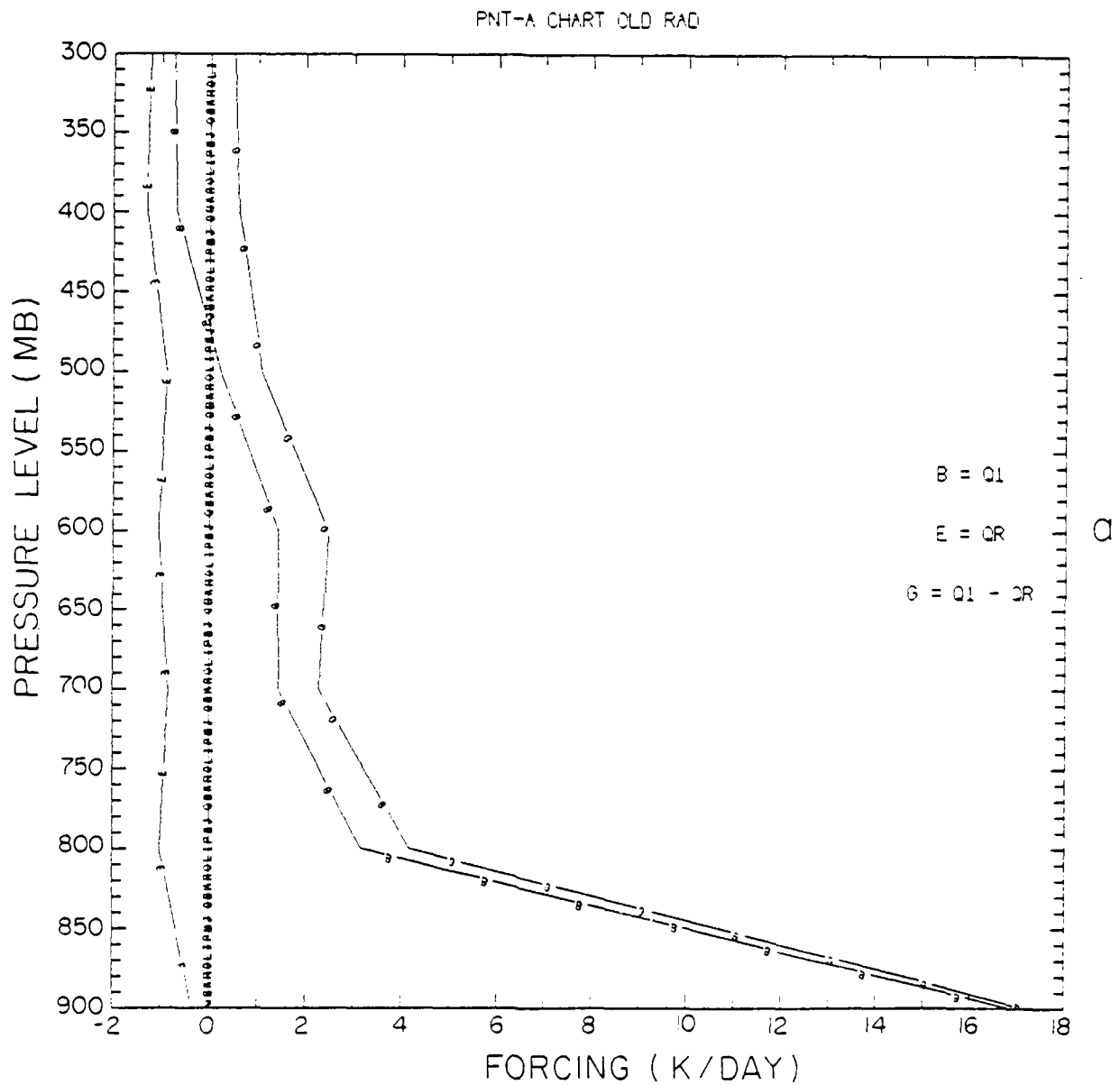
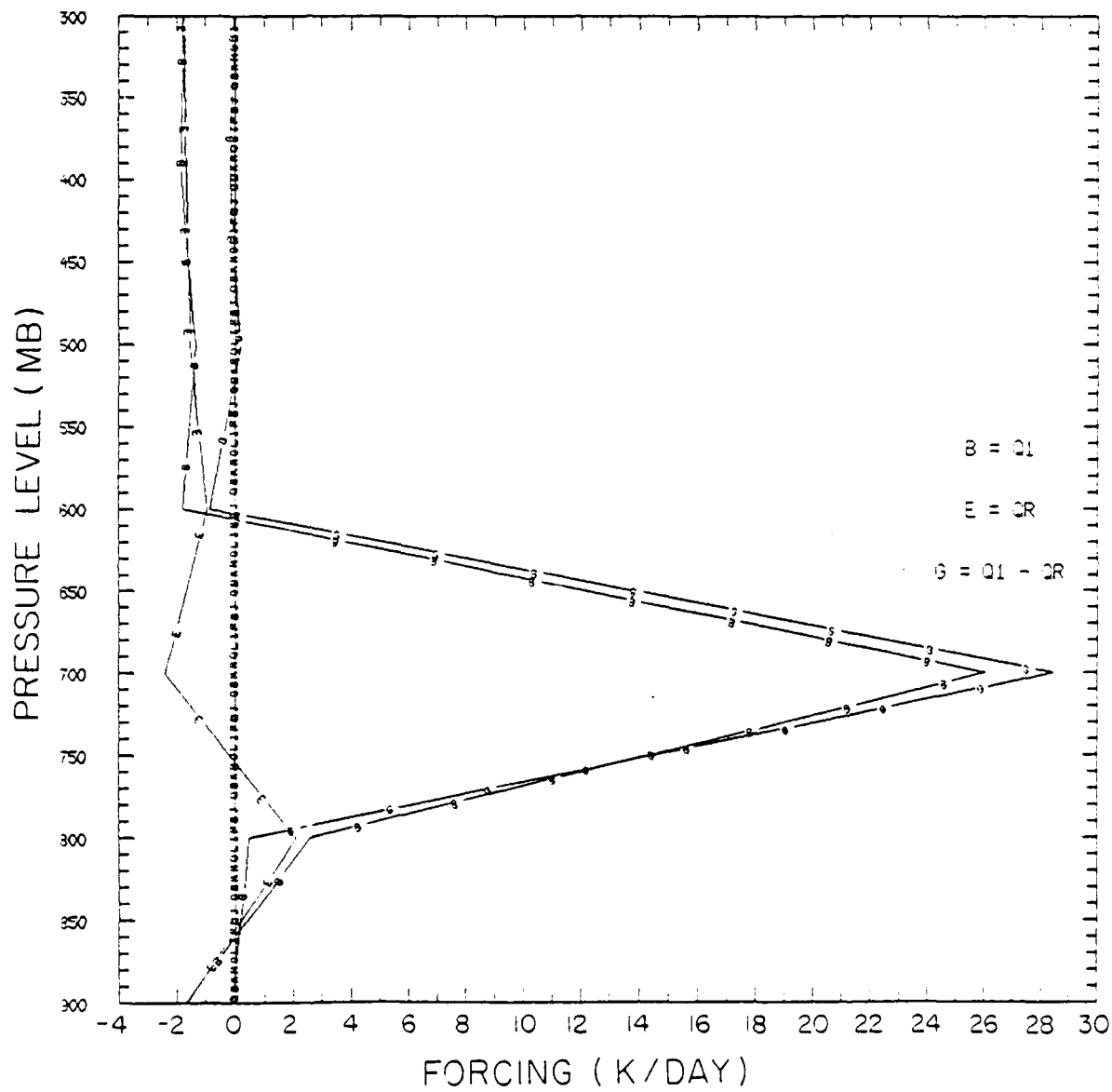


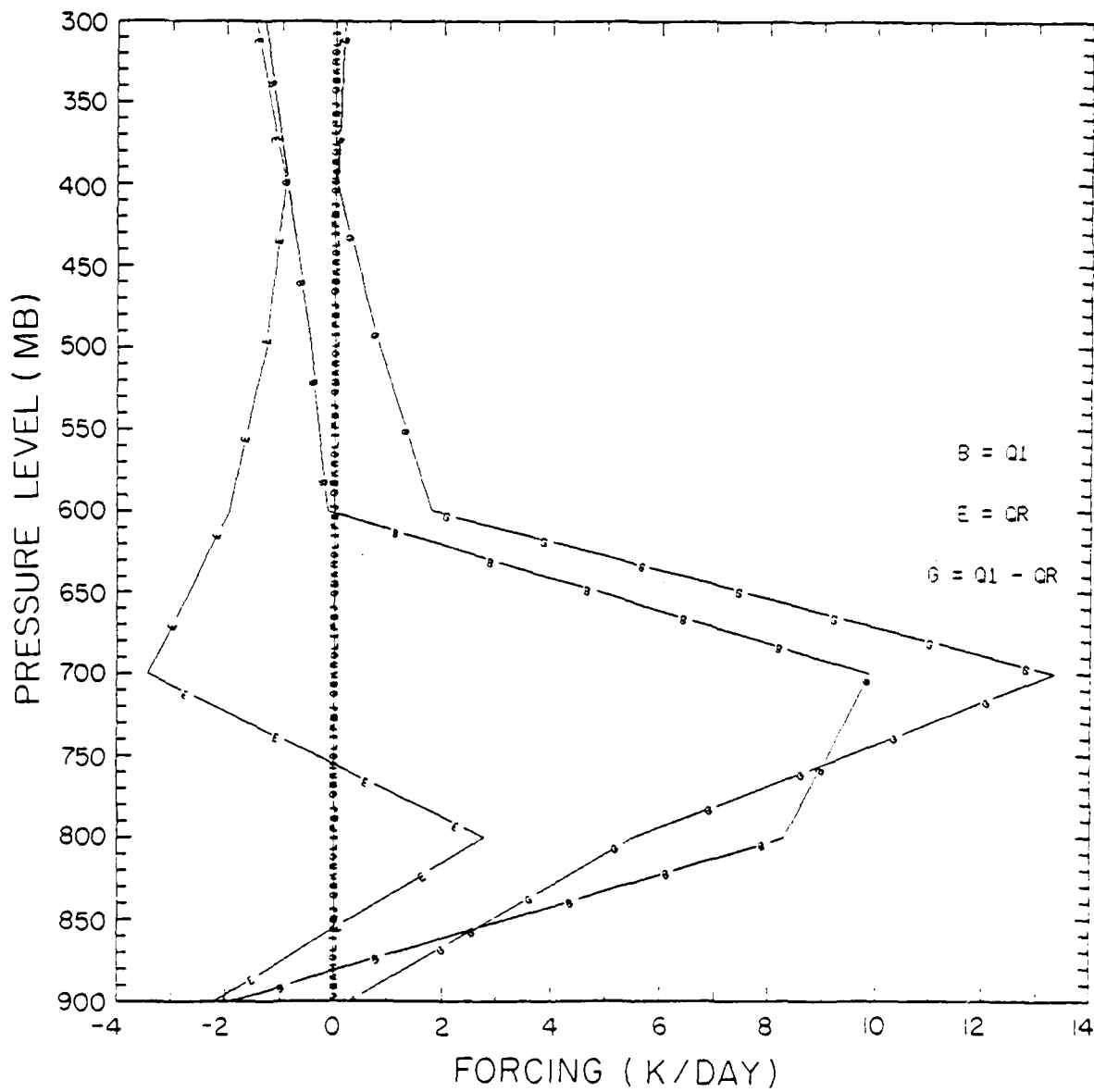
Figure 7.7a, b, and c The apparent heat source as function of pressure level for the old radiation experiment at points A, B, and C. (See text for a description of the points.)

PNT-B CHART OLD RAD



b

PNT-C CHART OLD RAD



C

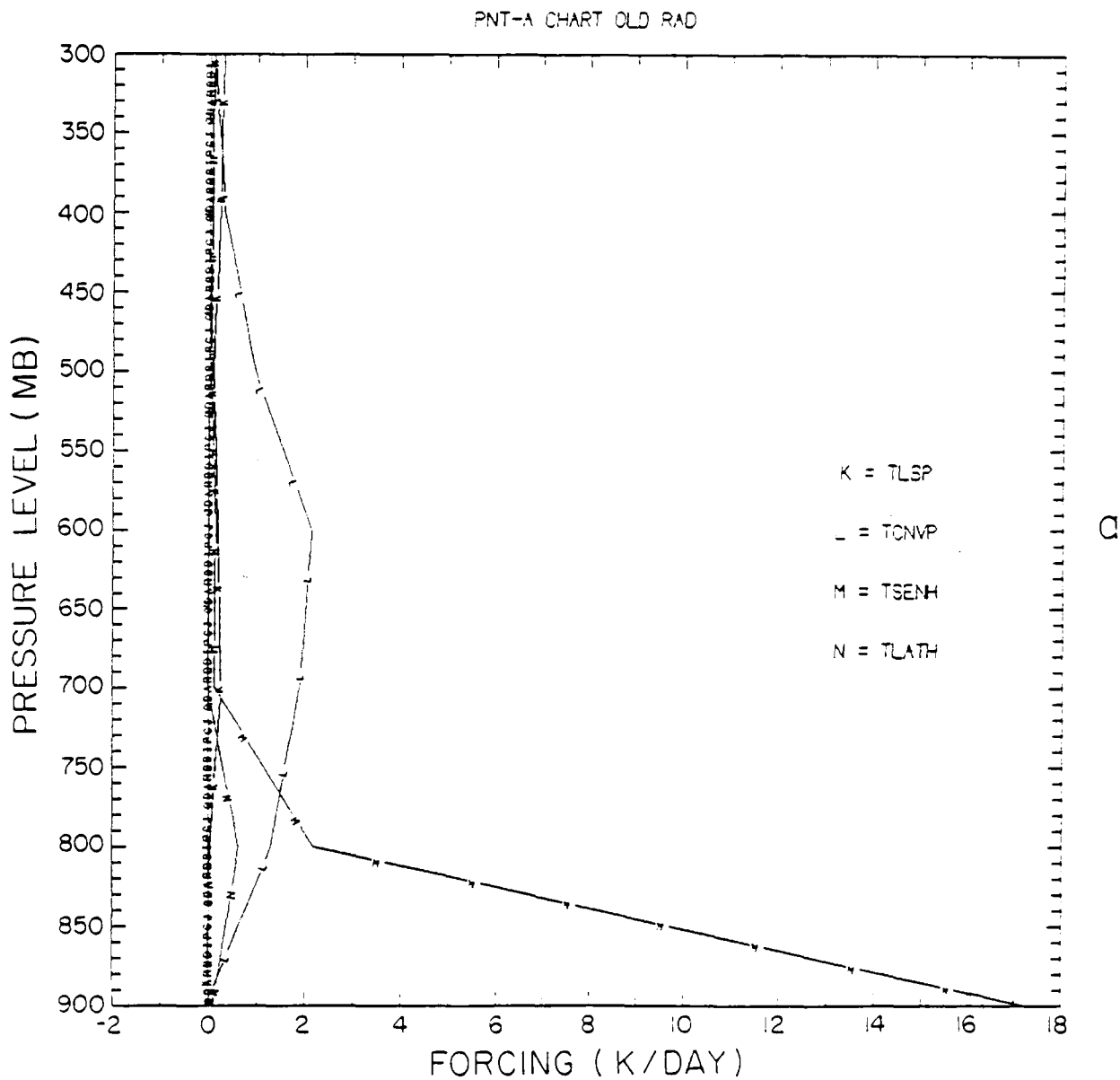
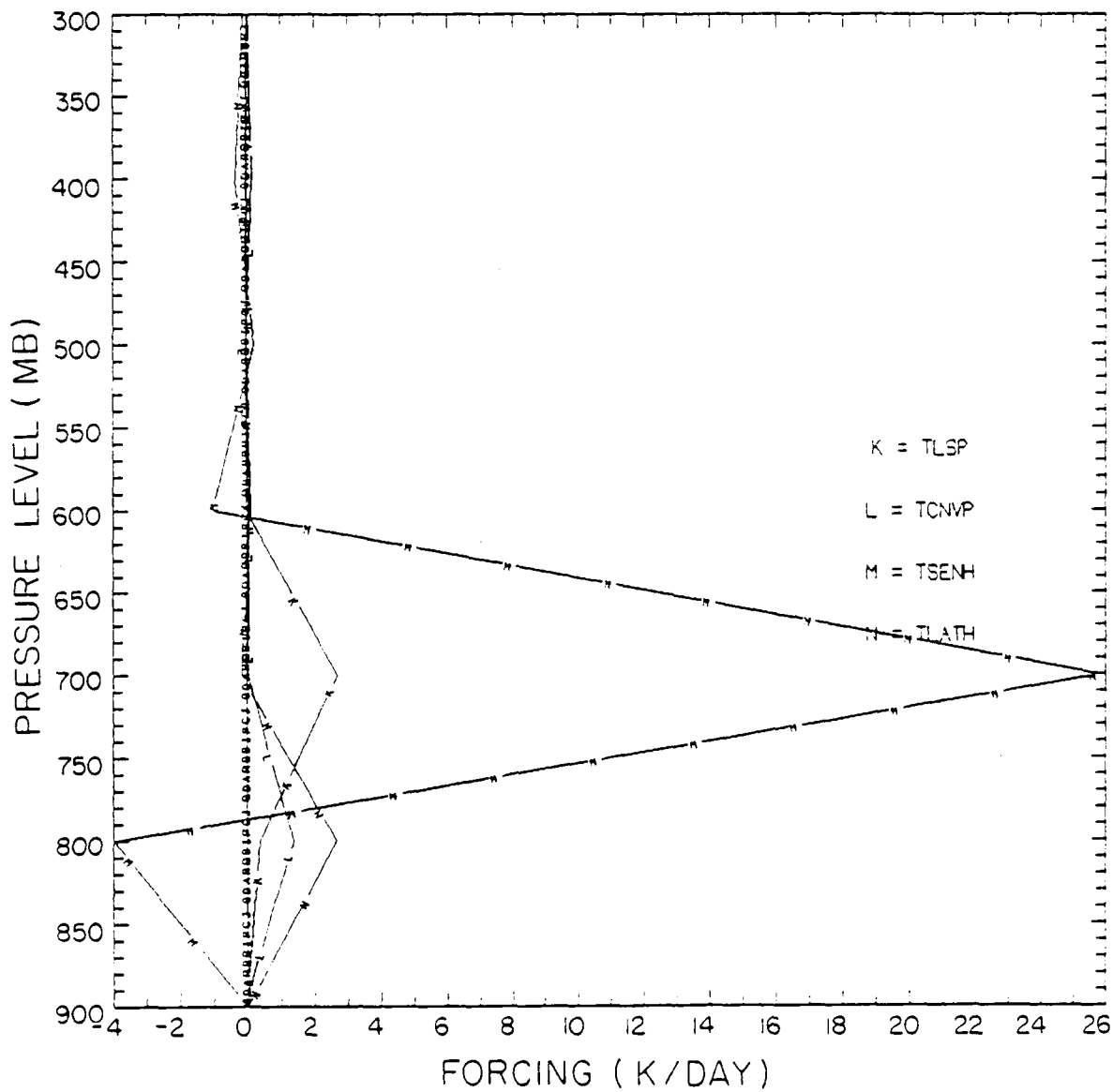


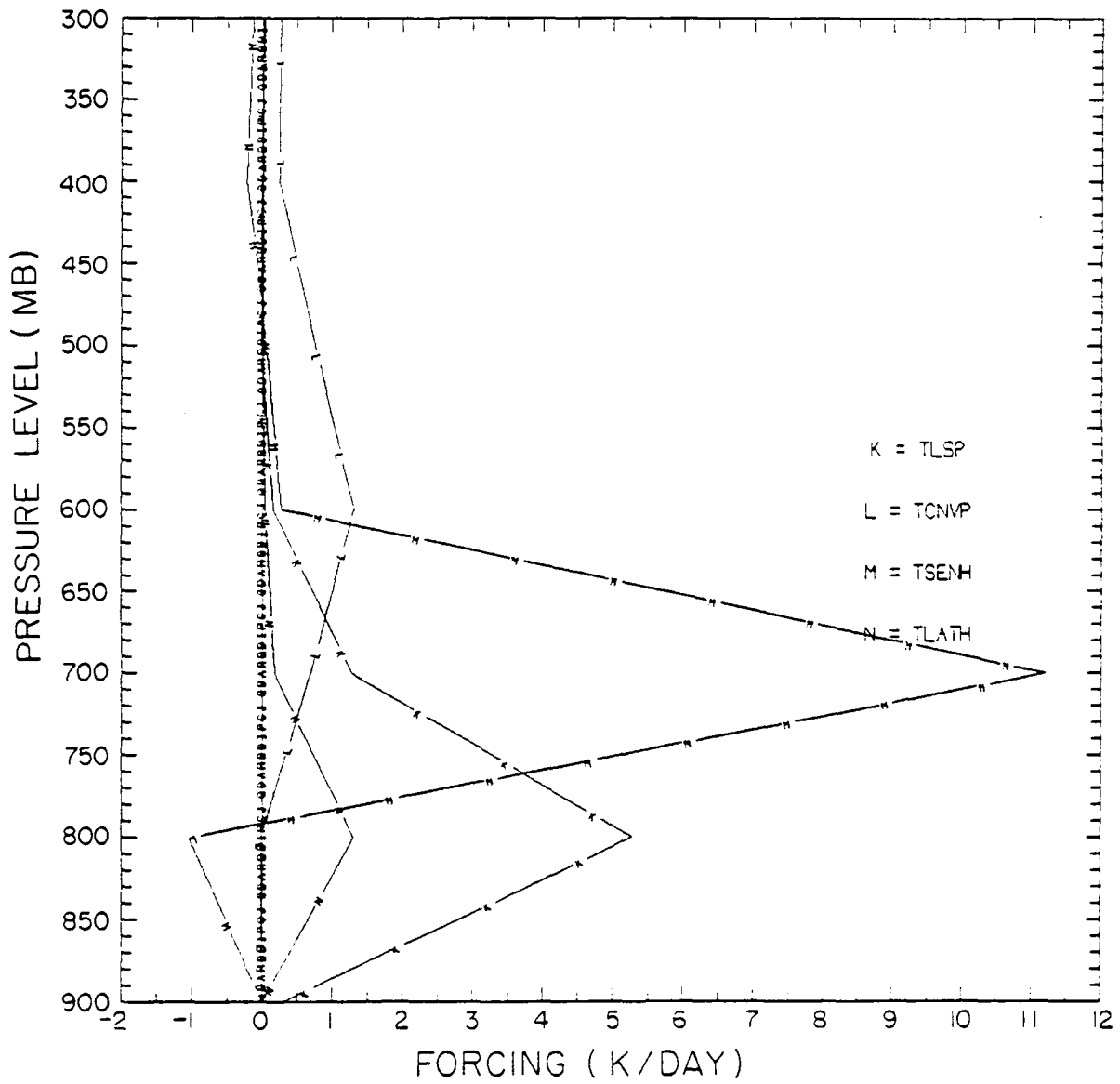
Figure 7.8a, b, and c The components of the apparent heat source as function of pressure level for the old radiation experiment at points A, B, and C. (See text for a description of the points.)

PNT-B CHART OLD RAD



b

PNT-C CHART OLD RAD



C

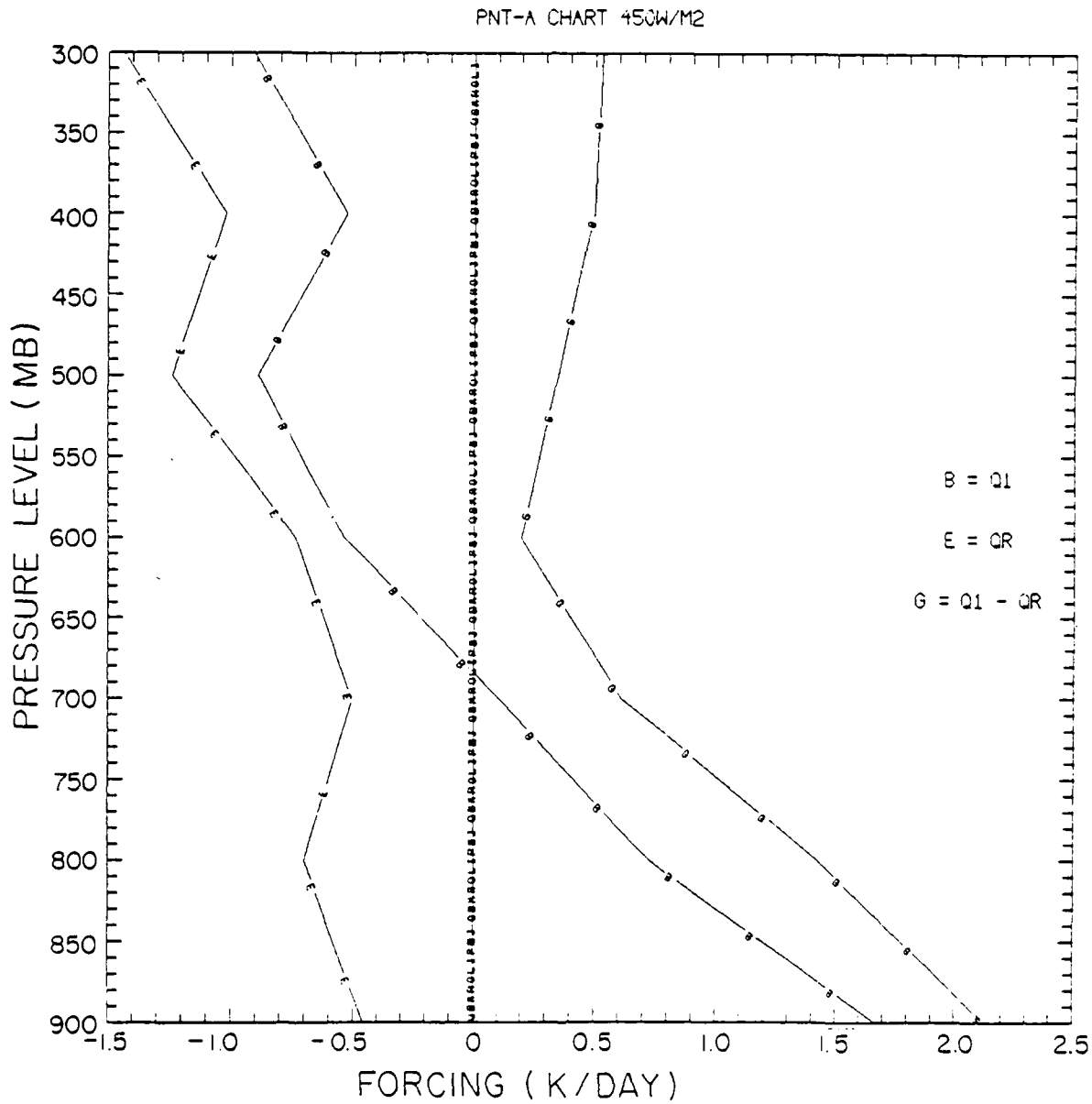
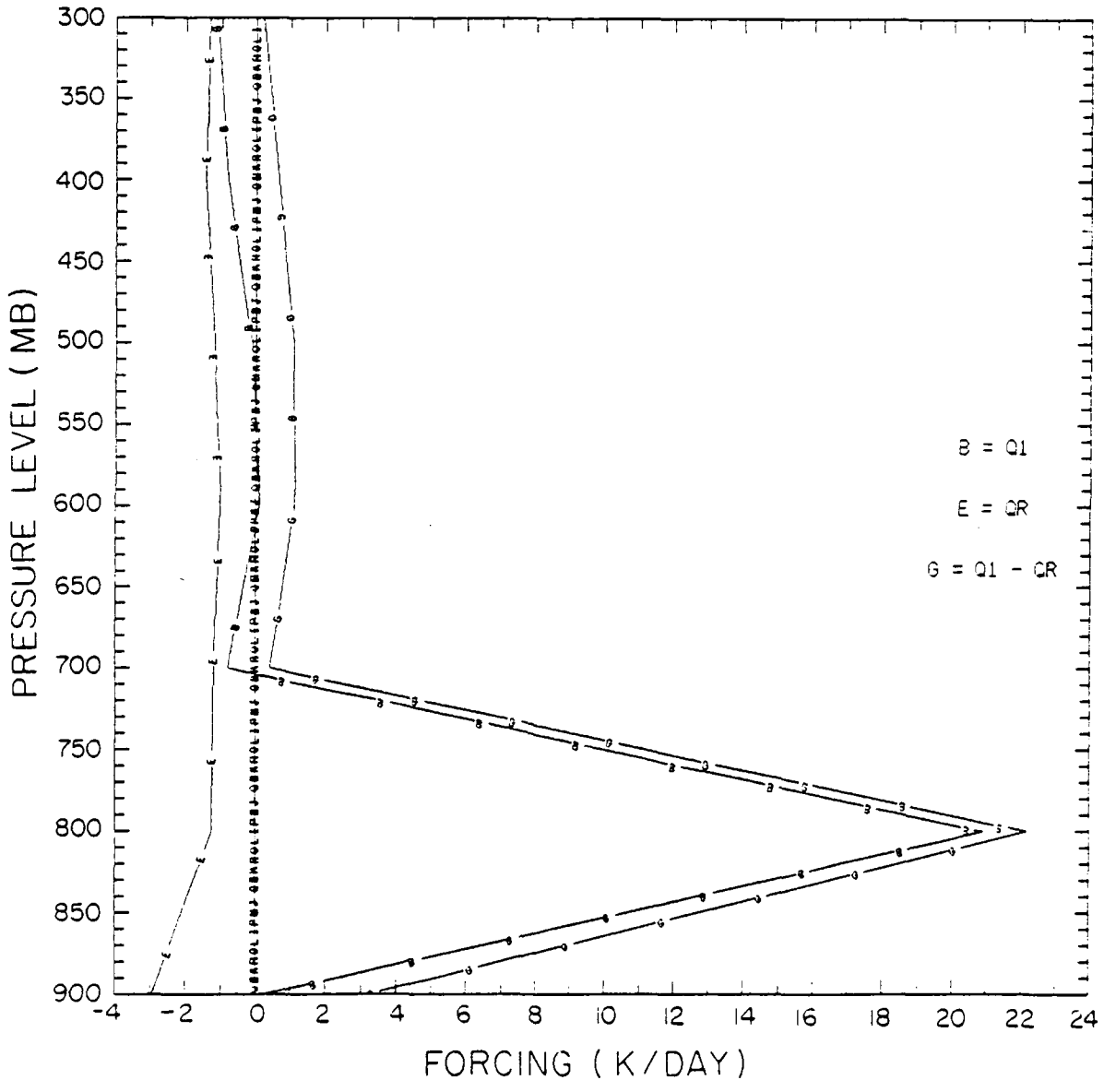


Figure 7.9a, b, and c The apparent heat source as function of pressure level of the control experiment at points A, B, and C. (See text for a description of the points.)

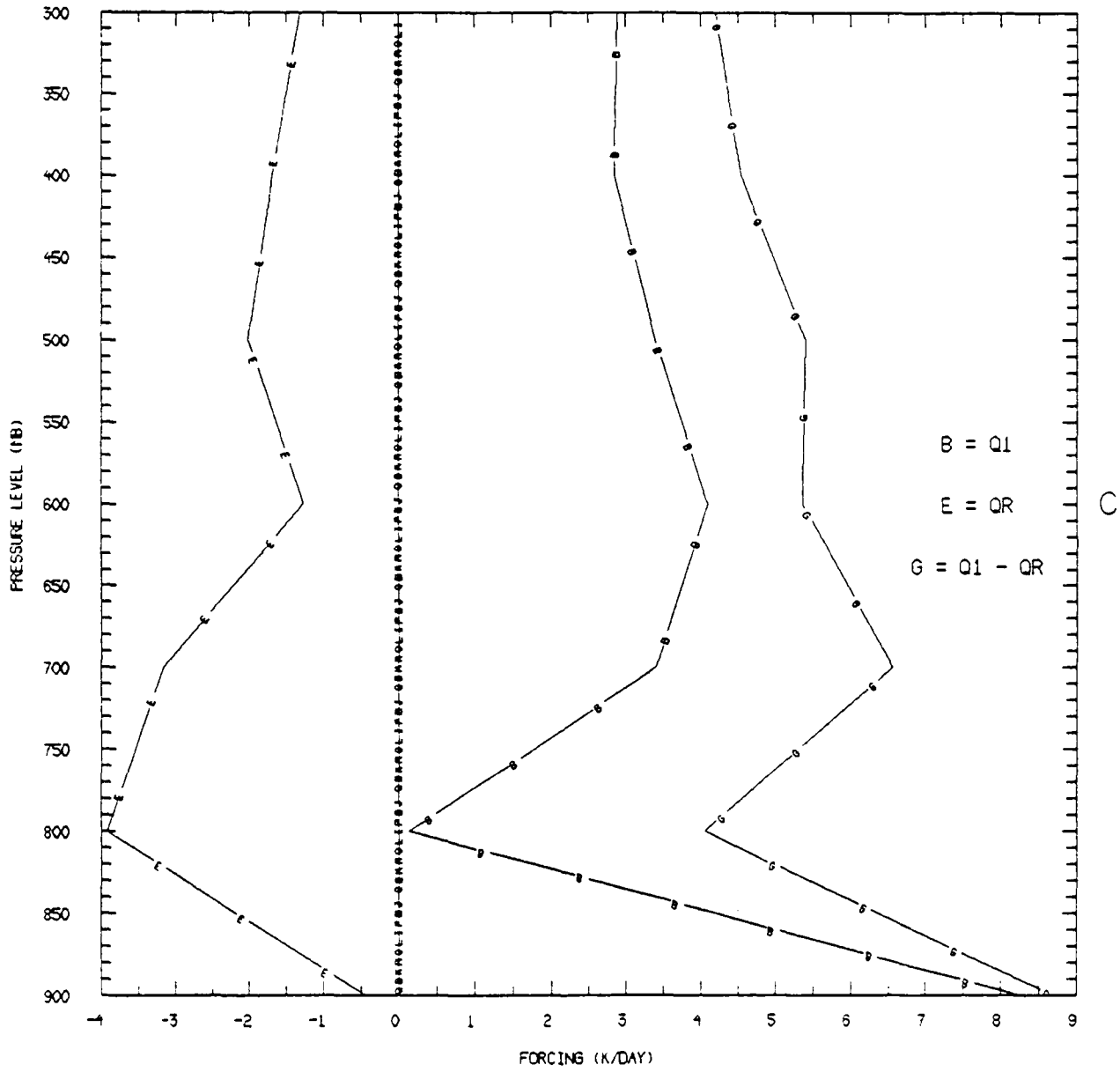
PNT-8 CHART 450W/M2



B = Q1  
 E = QR  
 G = Q1 - QR

b

PNT-C CHART 450W/M2



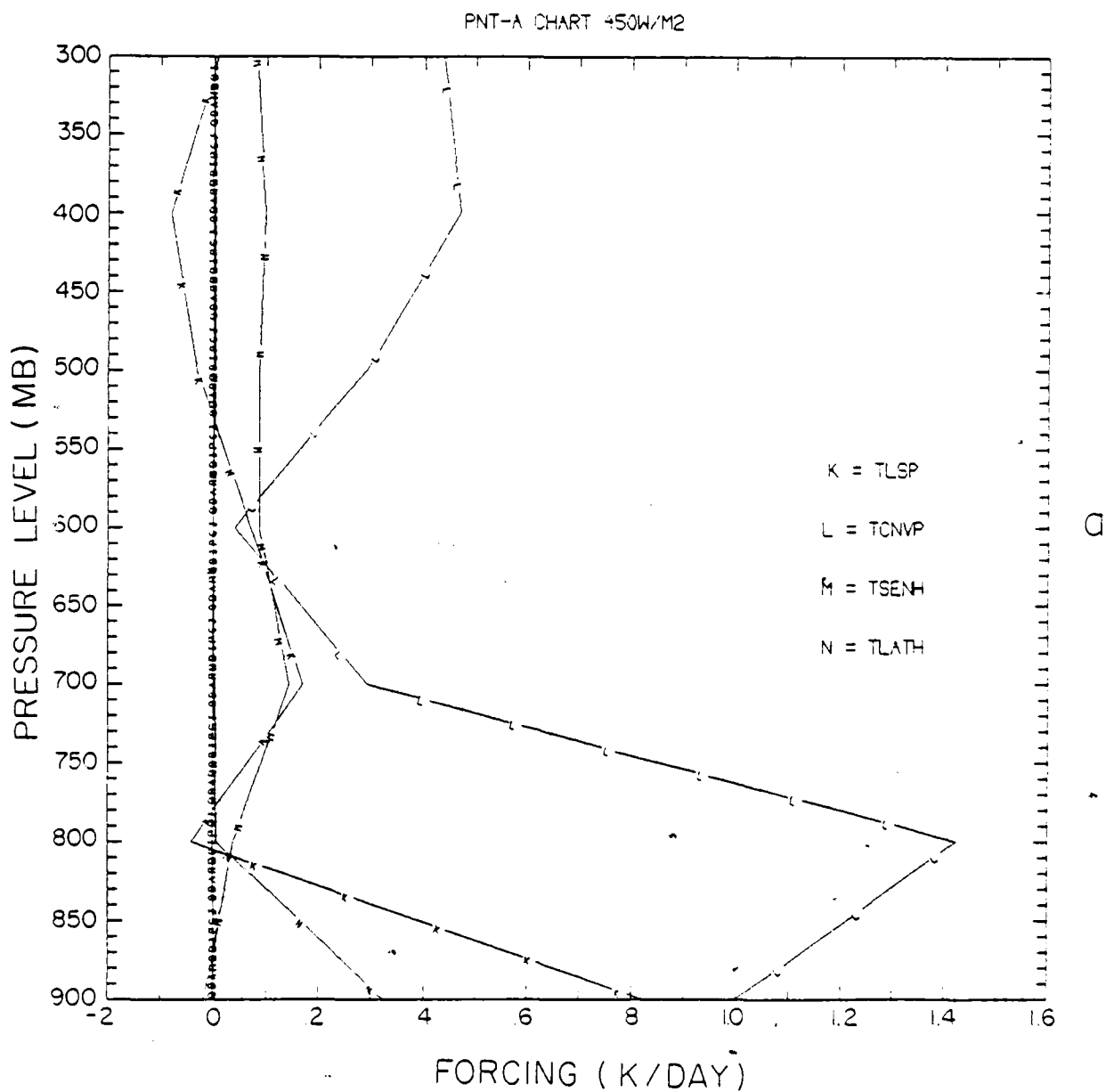
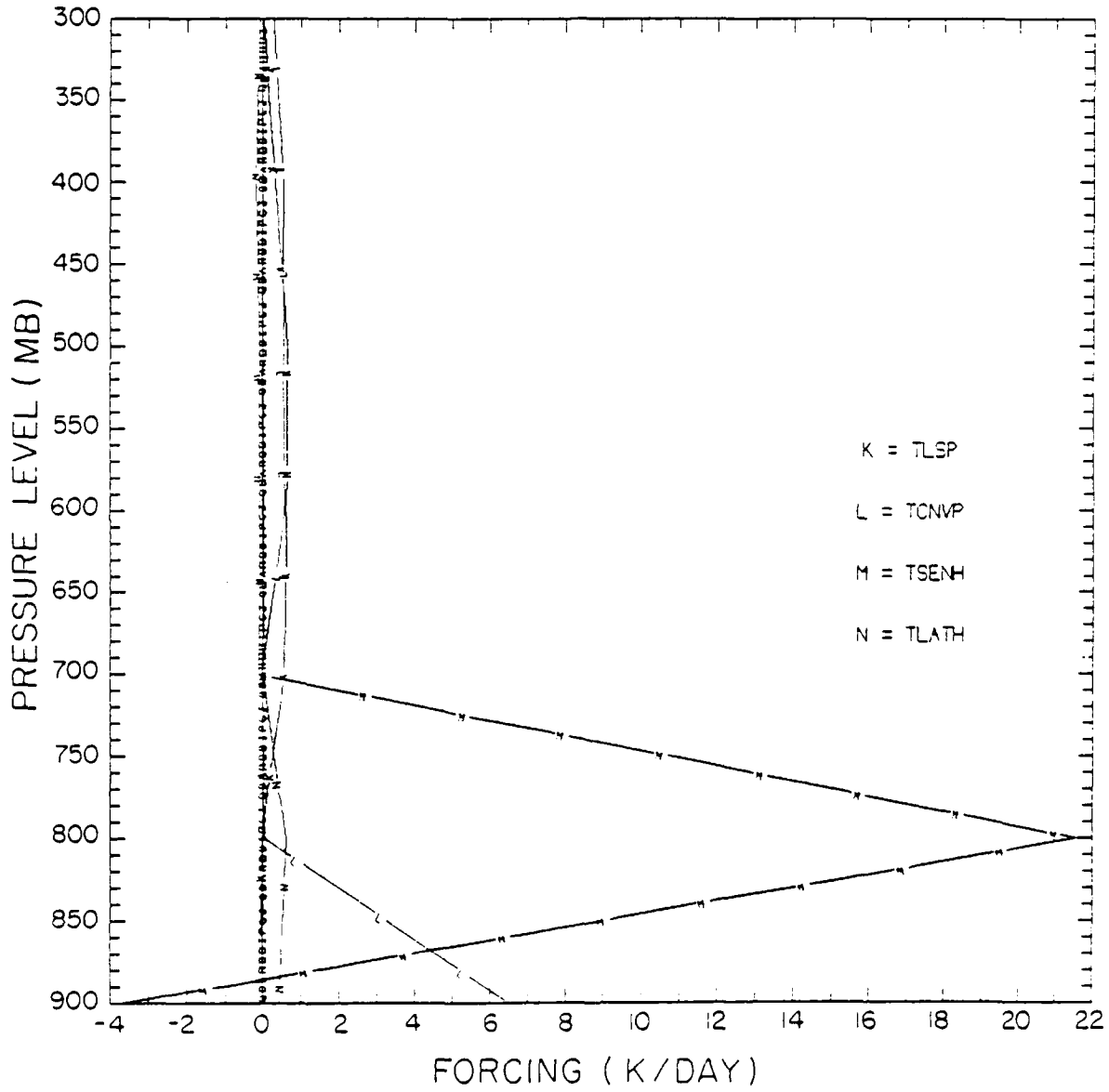


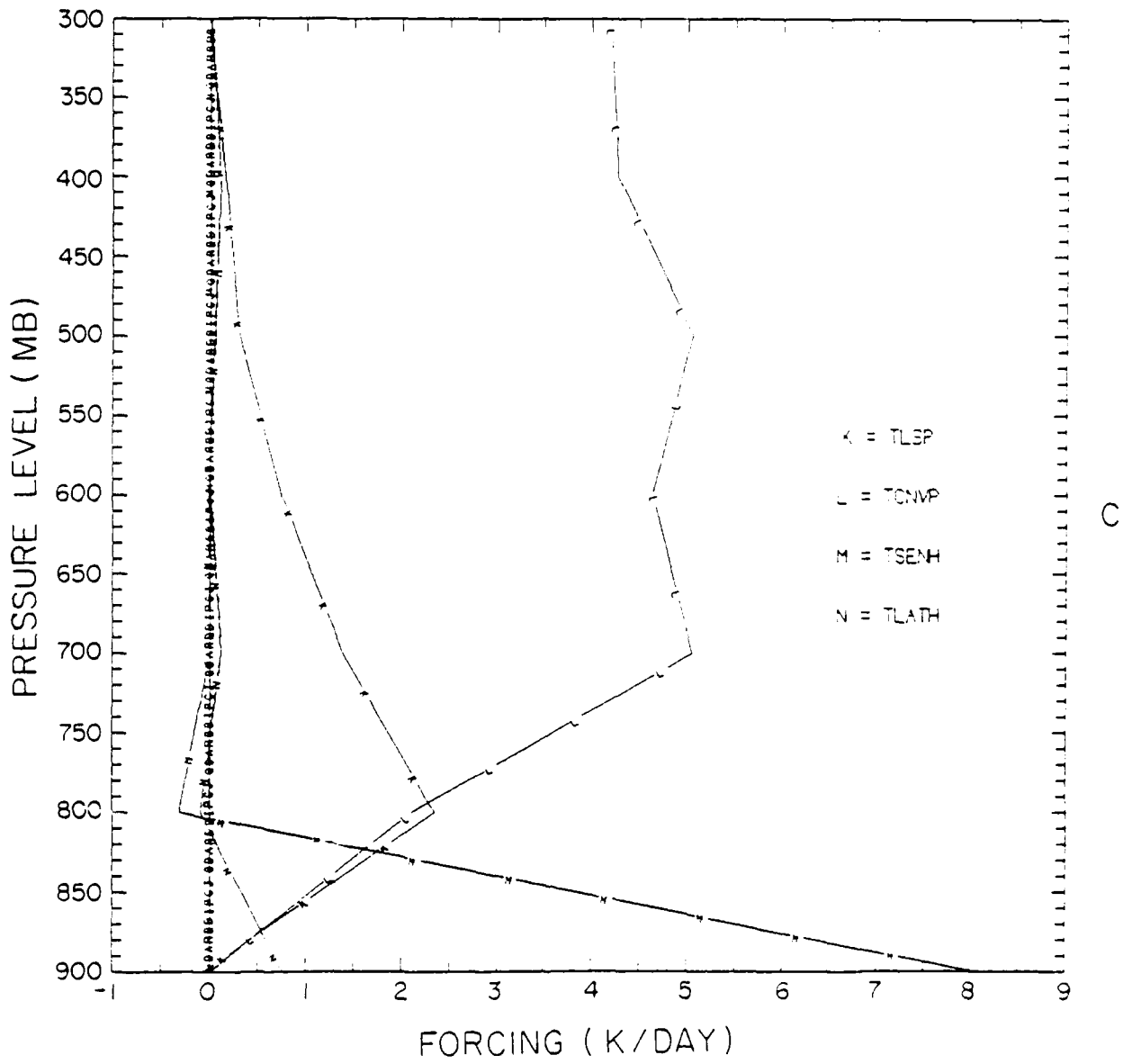
Figure 7.10a, b, and c The components of the apparent heat source as function of pressure level for the control experiment at points A, B, and C. (See text for a description of the points.)

PNT-B CHART 450W/M2



b

PNT-C CHART 450W/M2



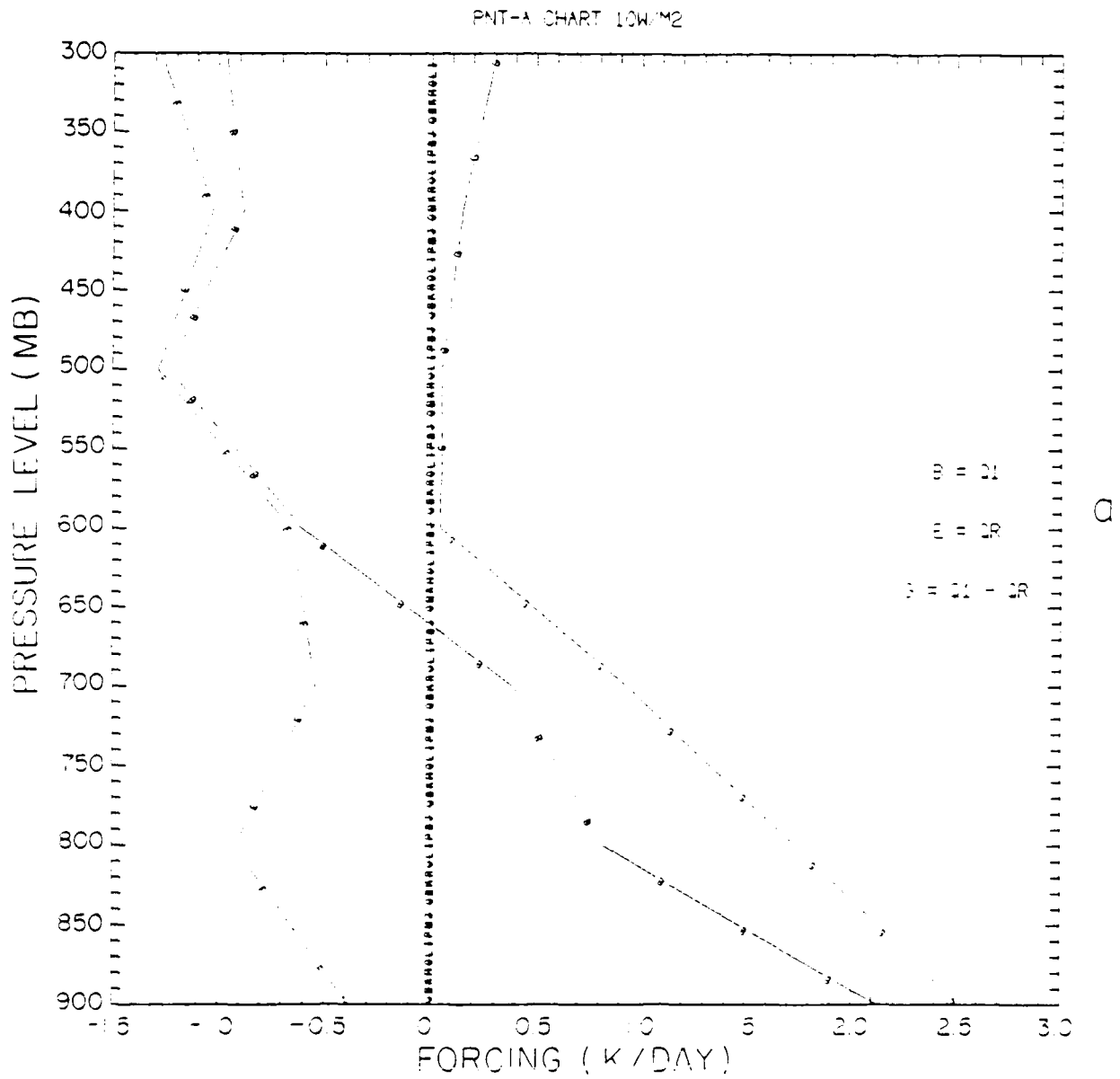
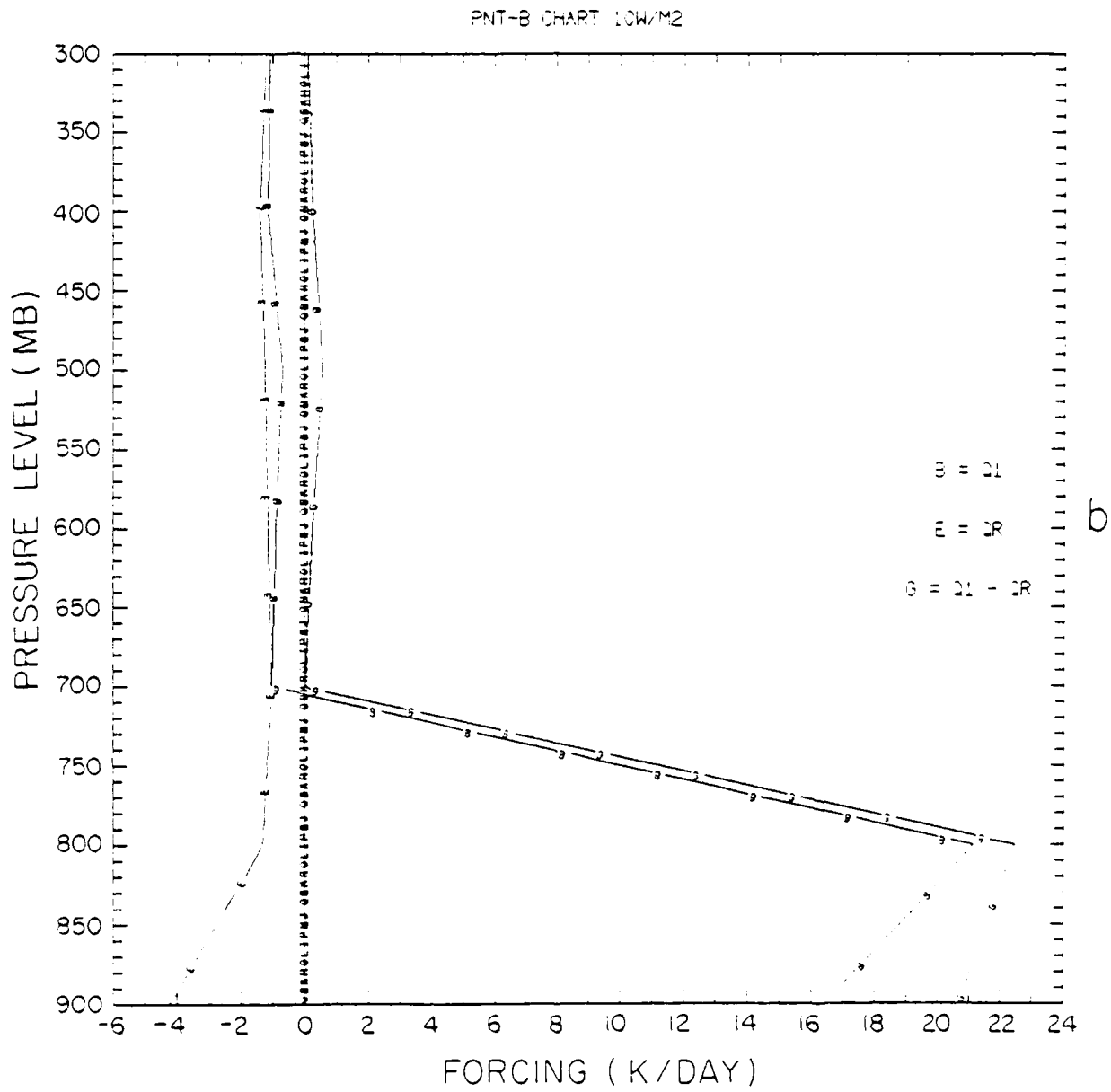
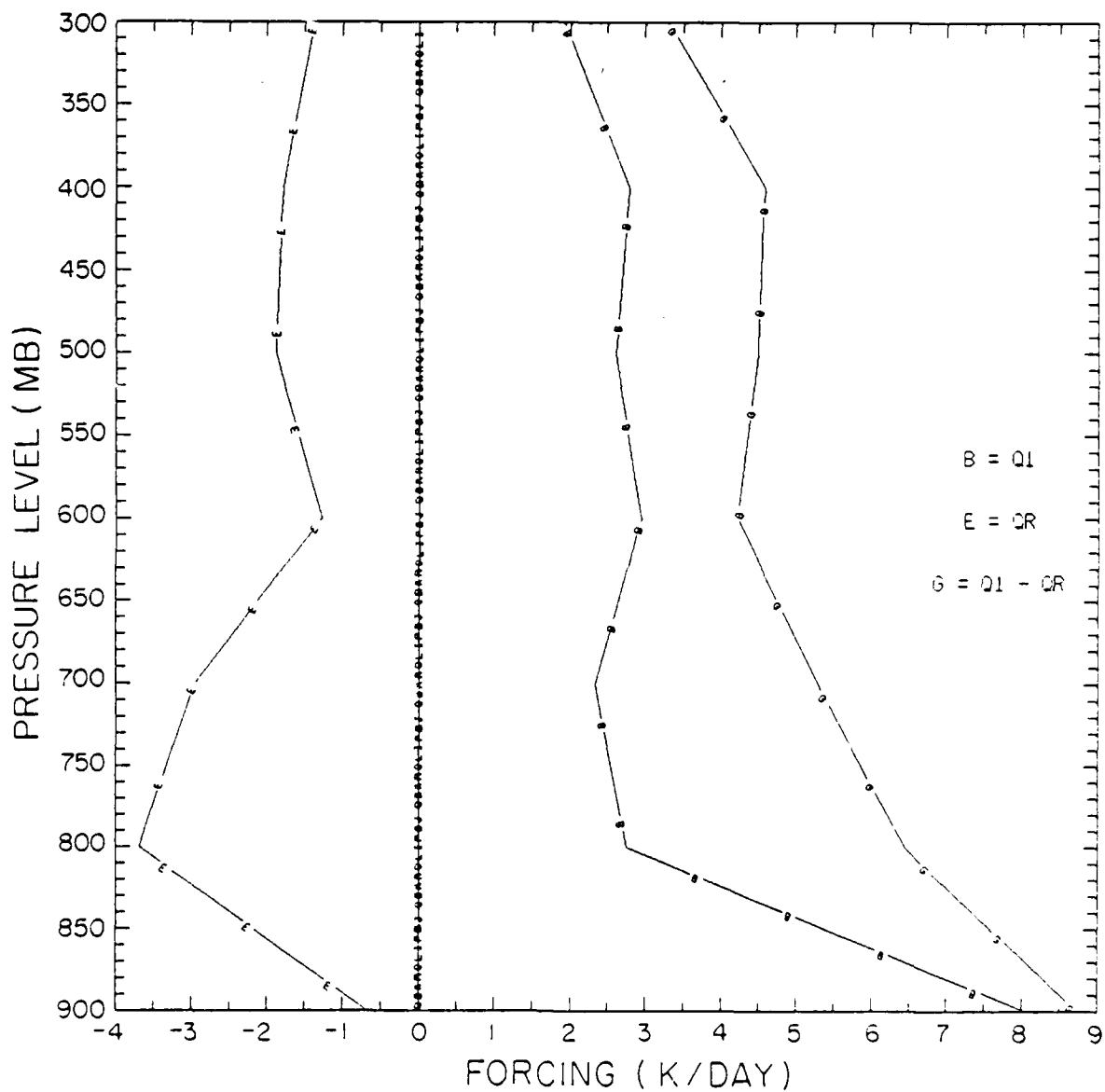


Figure 7.11a, b, and c The apparent heat source as function of pressure level of the moisture initialization experiment at points A, B, and C. (See text for a description of the points.)



PNT-C CHART 10W/M2



C

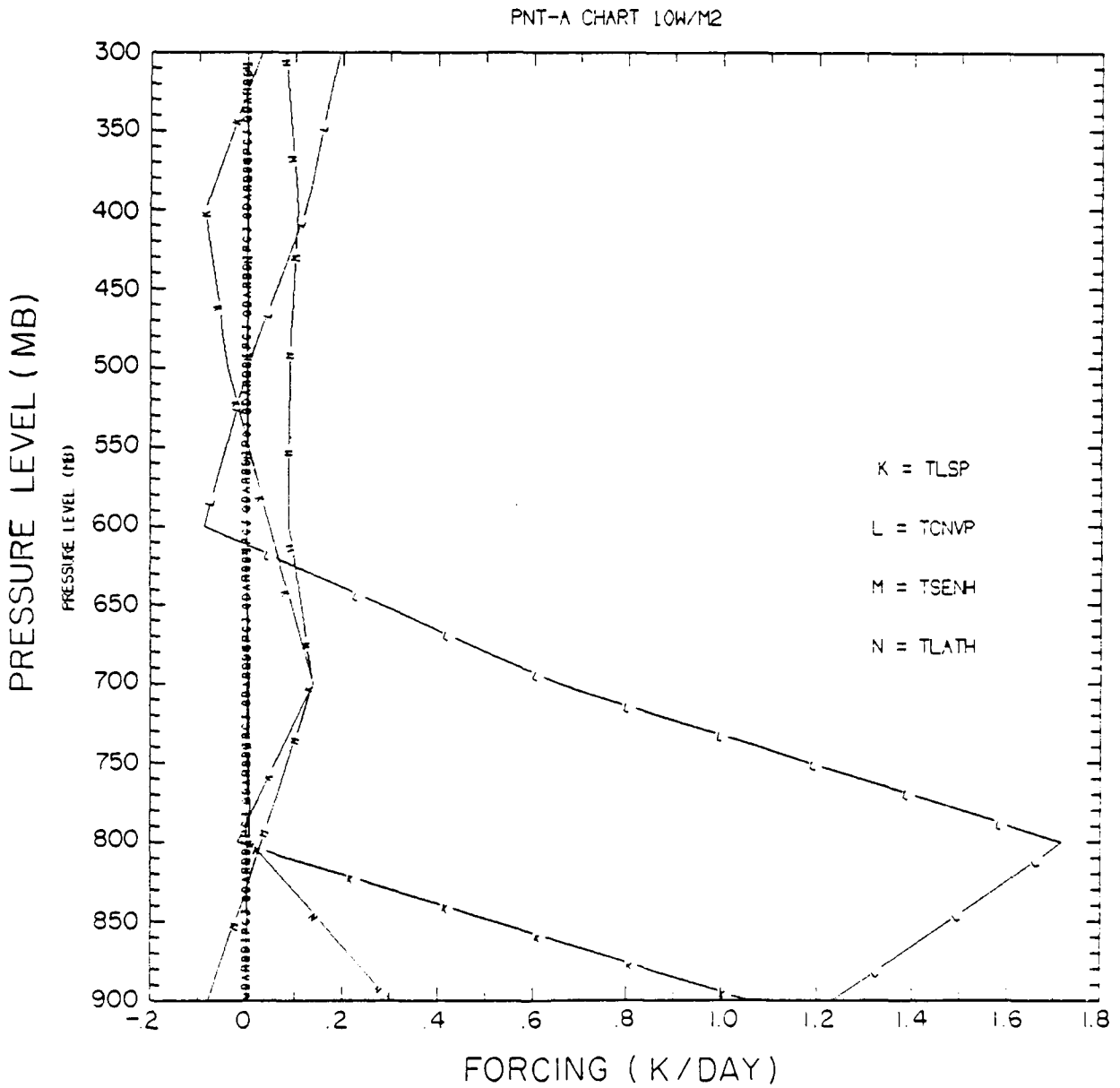
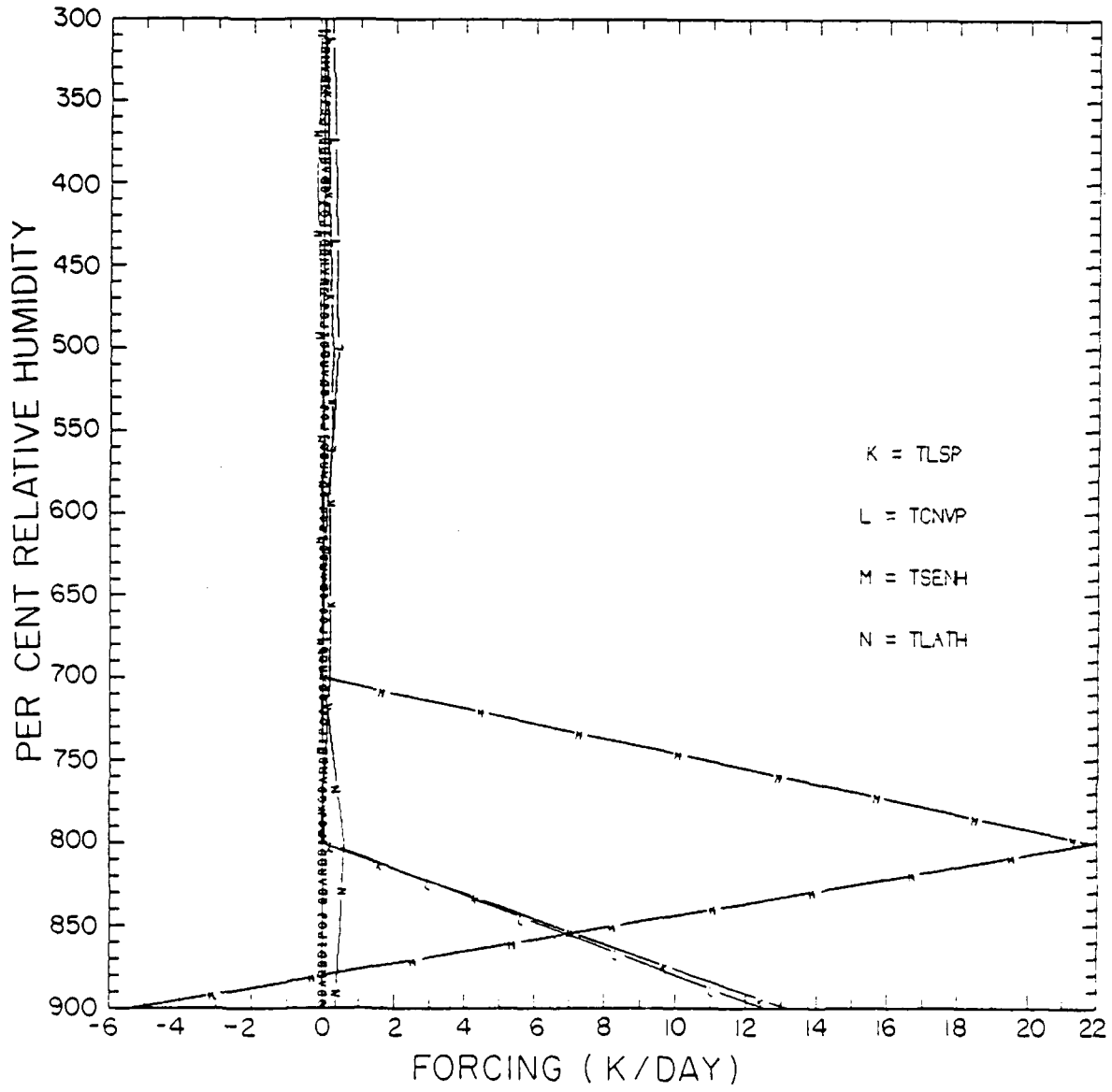
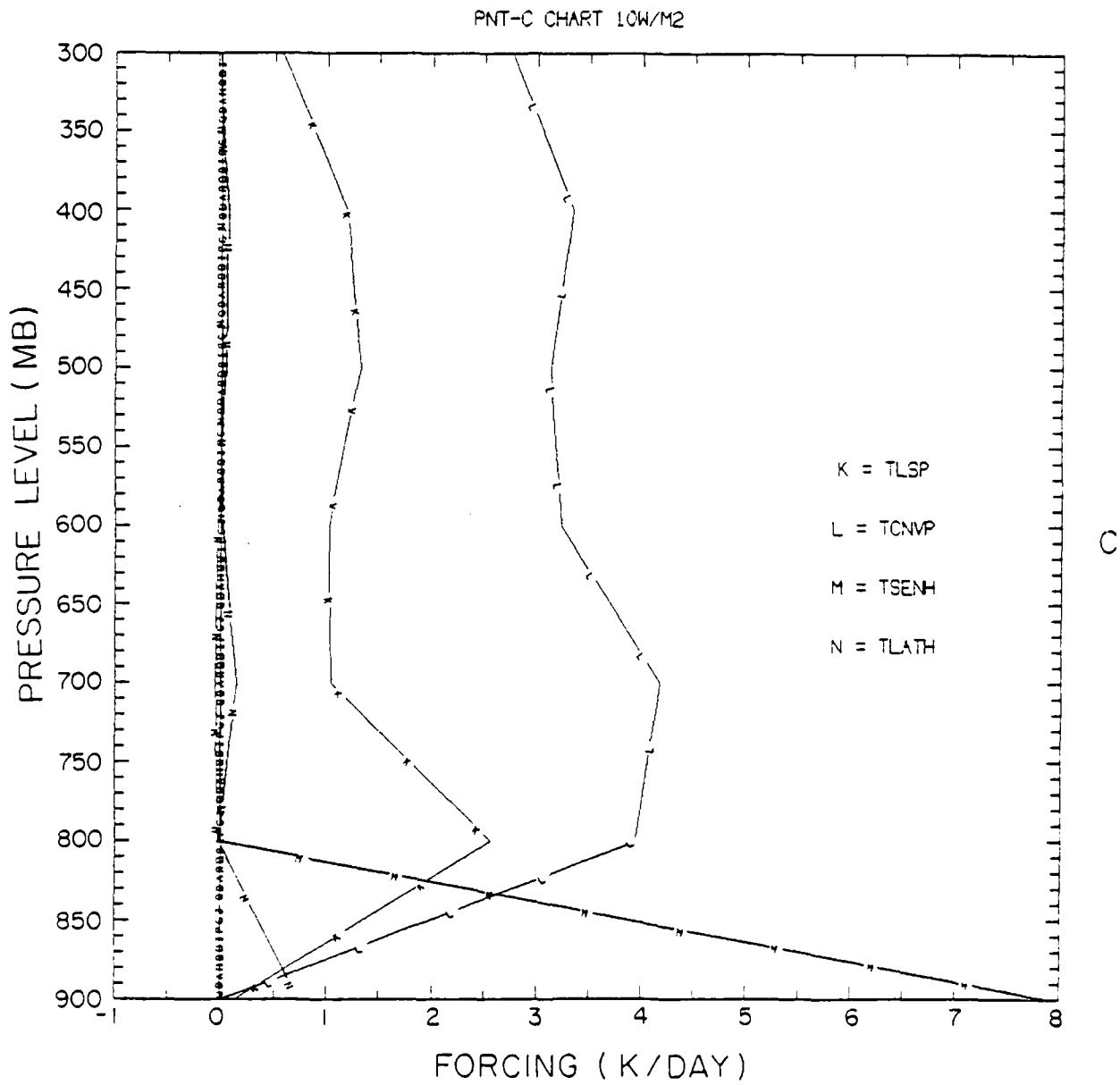


Figure 7.12a, b, and c The components of the apparent heat source as function of pressure level for the moisture initialization experiment at points A, B, and C. (See text for a description of the points.)

PNT-B CHART LOW/M2



b



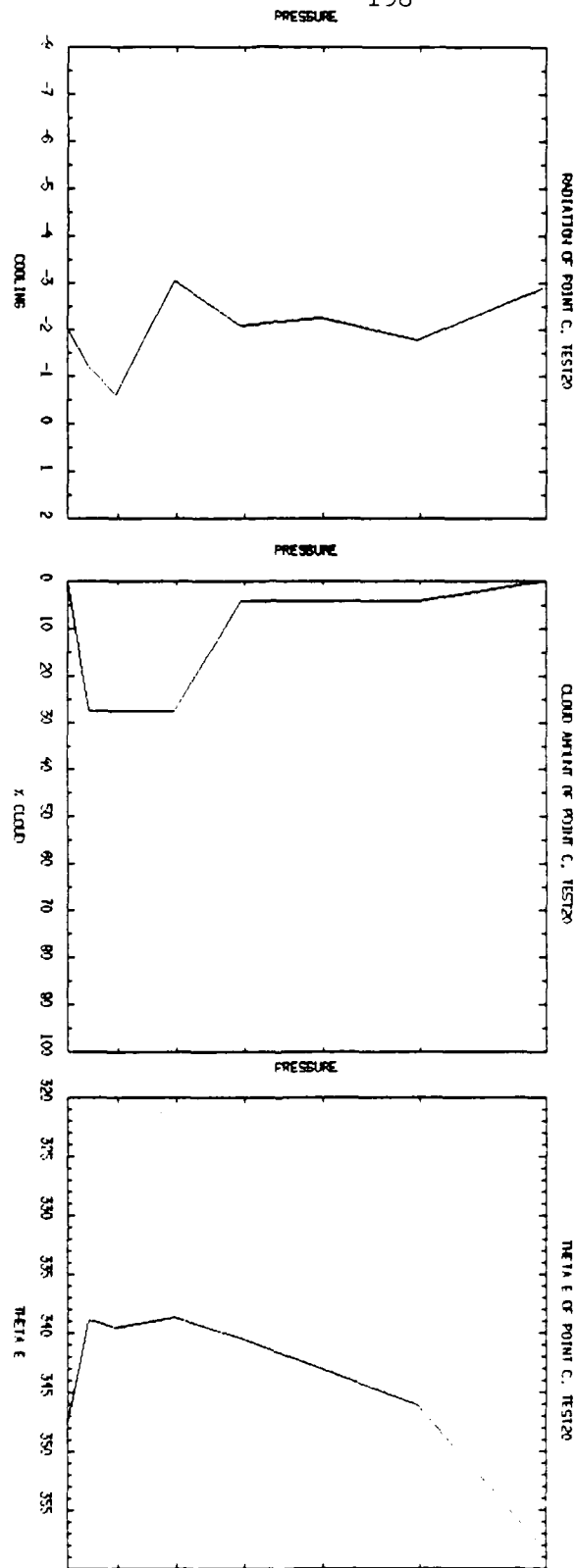


Figure 7.13 Longwave radiational cooling and clouds as a function pressure for Point C of the moisture initialization experiment.

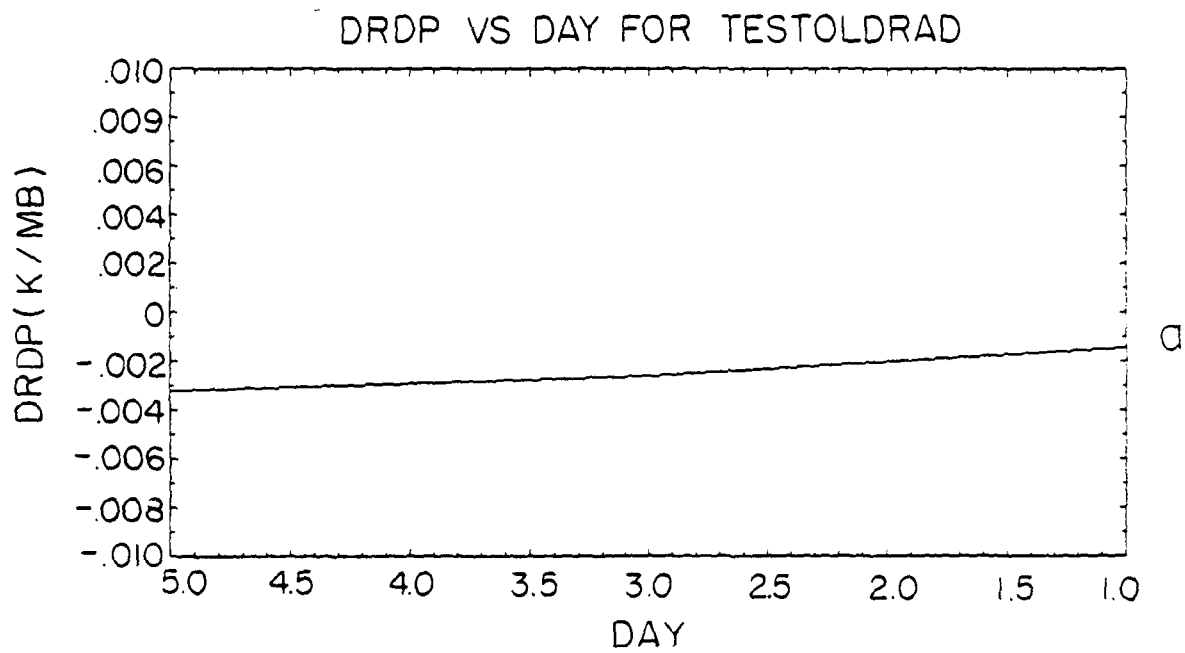
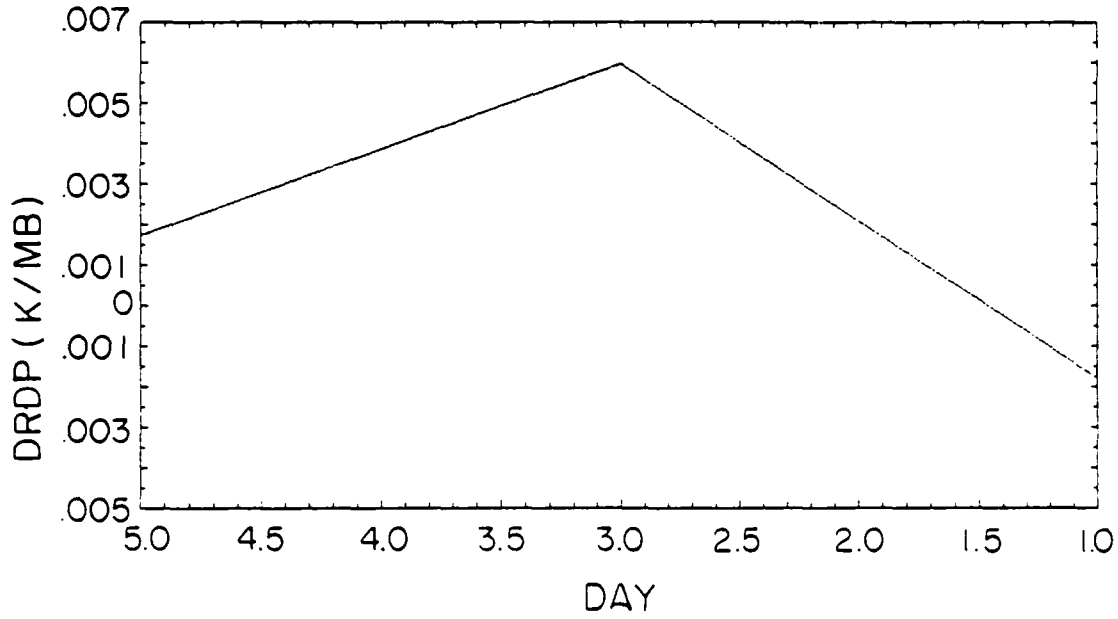


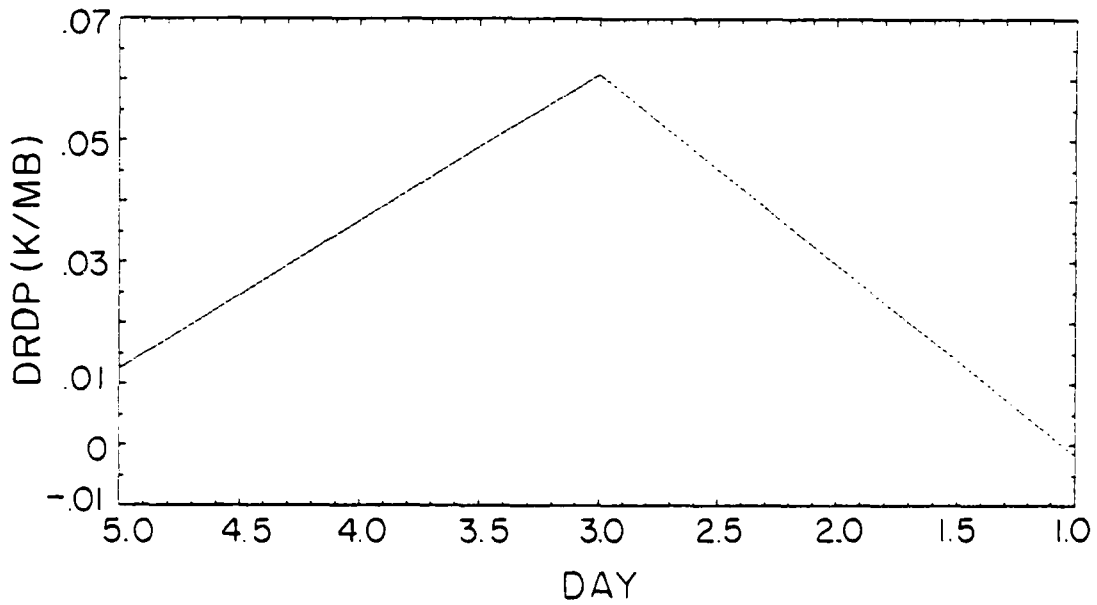
Figure 7.14a, b, and c Radiative destabilization as a function of time as parcels for the three experiments approach the ITCZ. Chart a is the old radiation experiment, chart b is the control experiment, and chart c is the moisture initialization experiment.

DRDP VS DAY FOR TEST 17



b

DRDP VS DAY FOR TEST 20



c

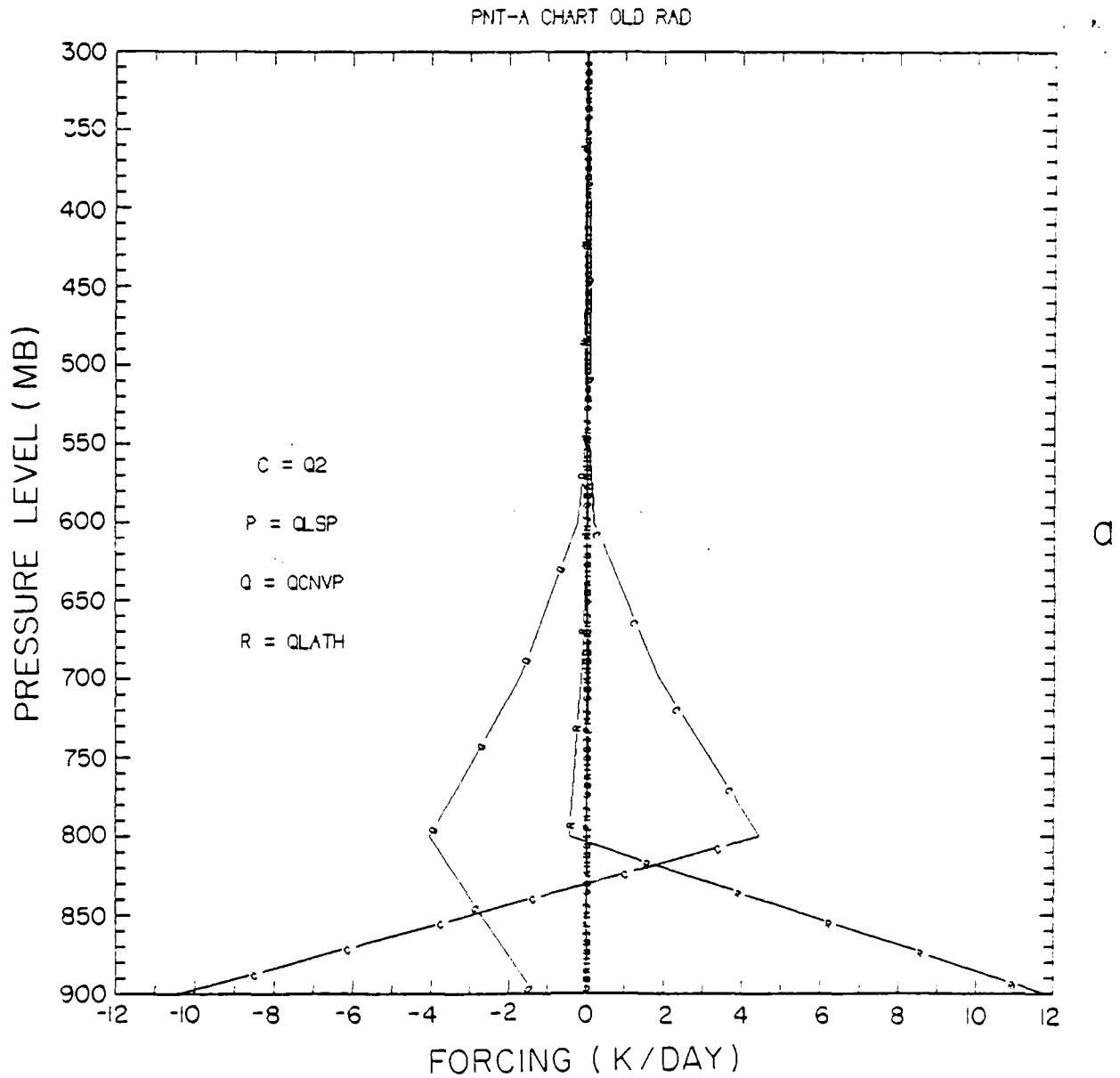
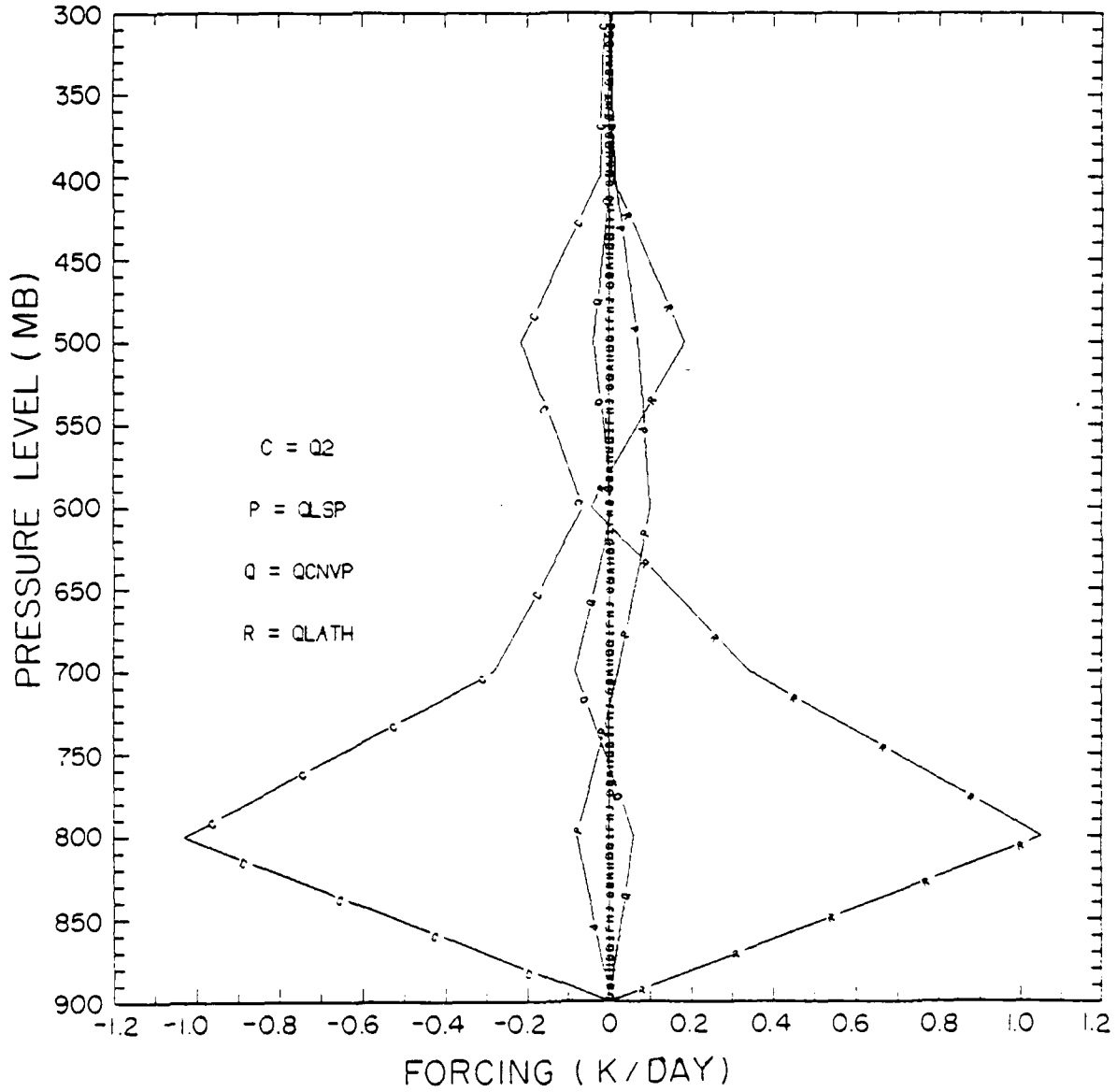


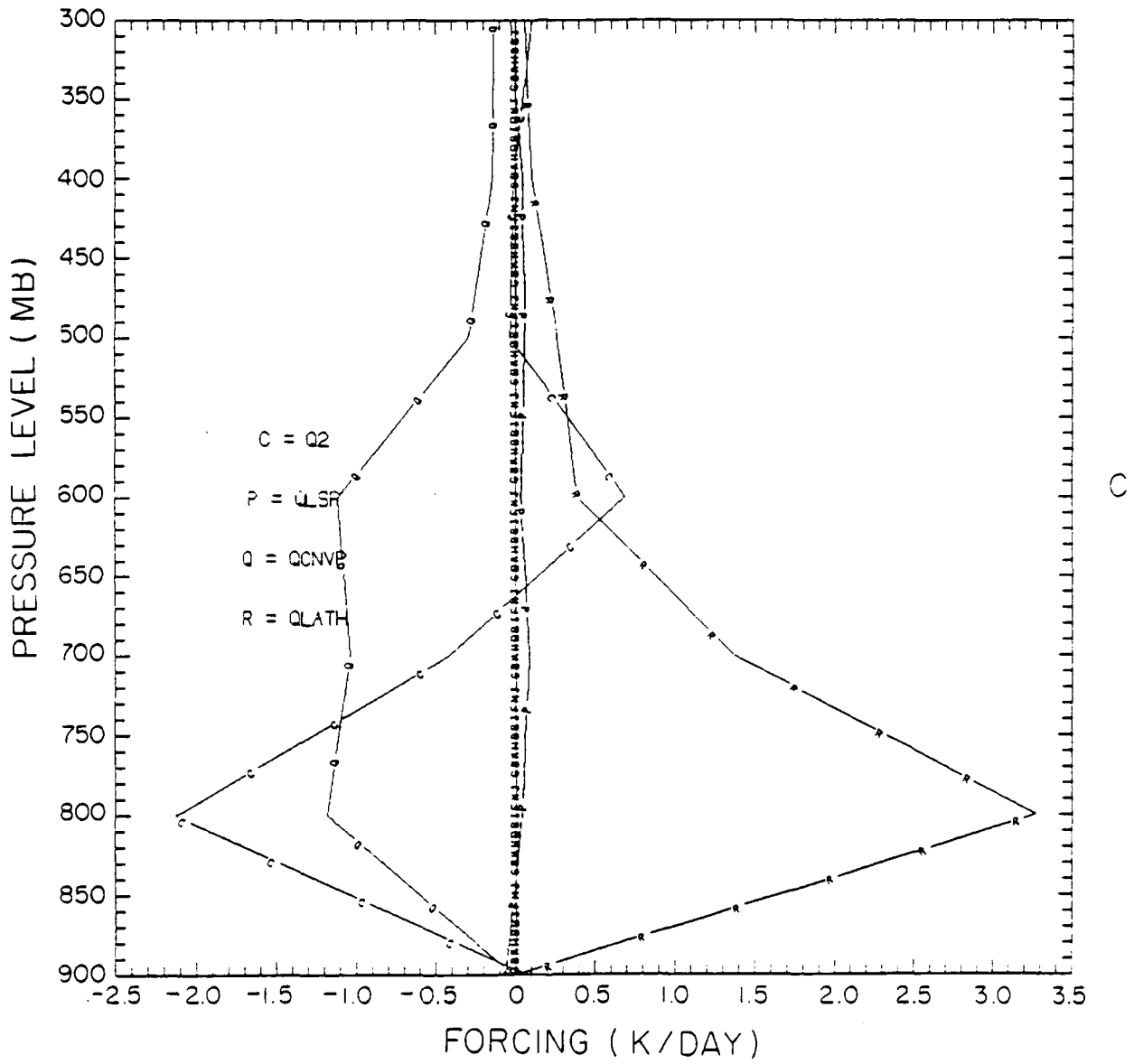
Figure 7.15a, b, and c The apparent moisture sink as function of pressure level for the old radiation experiment at points A, B, and C. (See text for a description of the points.)

PNT-B CHART OLD RAD



b

PNT-C CHART OLD RAD



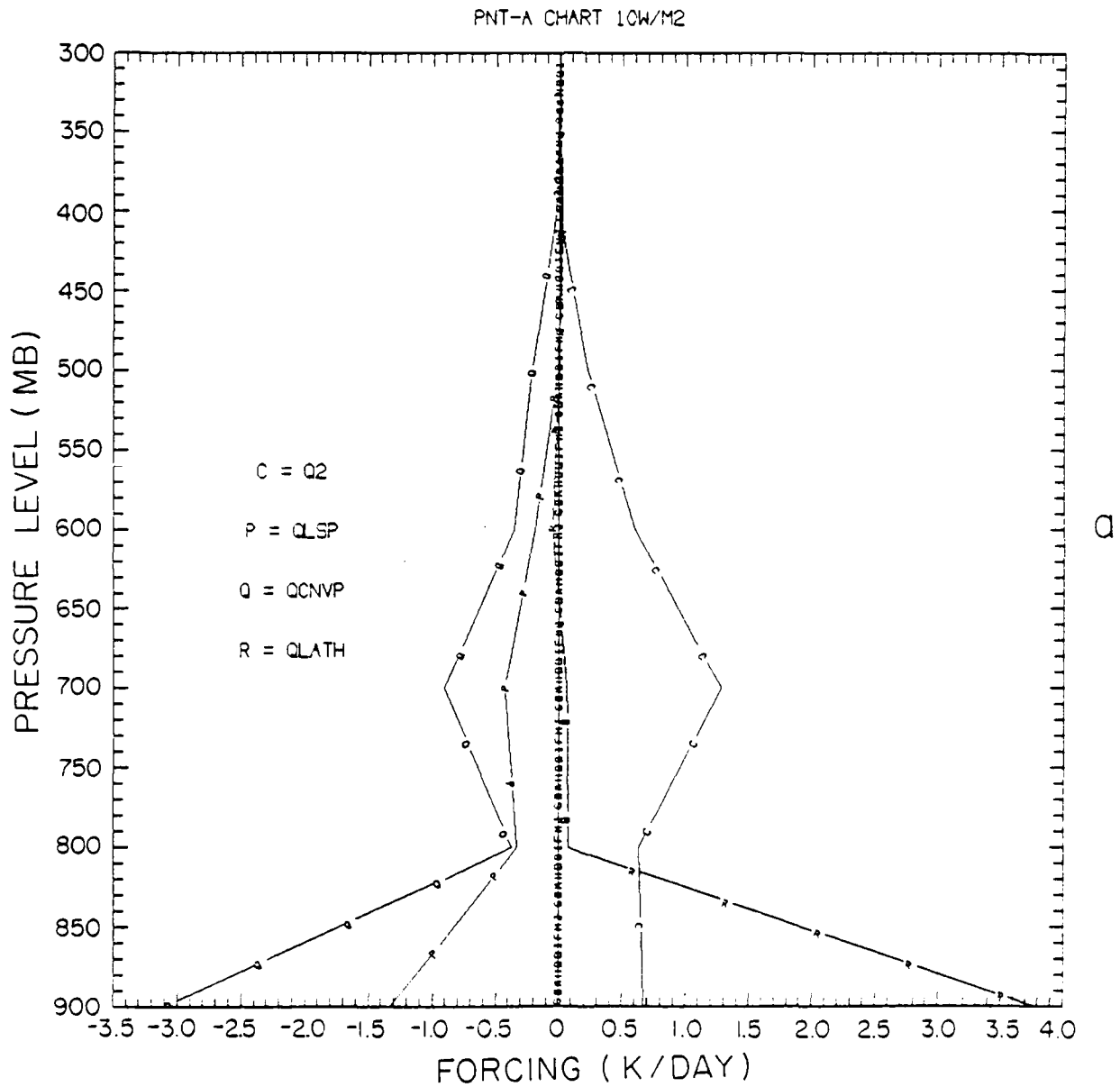
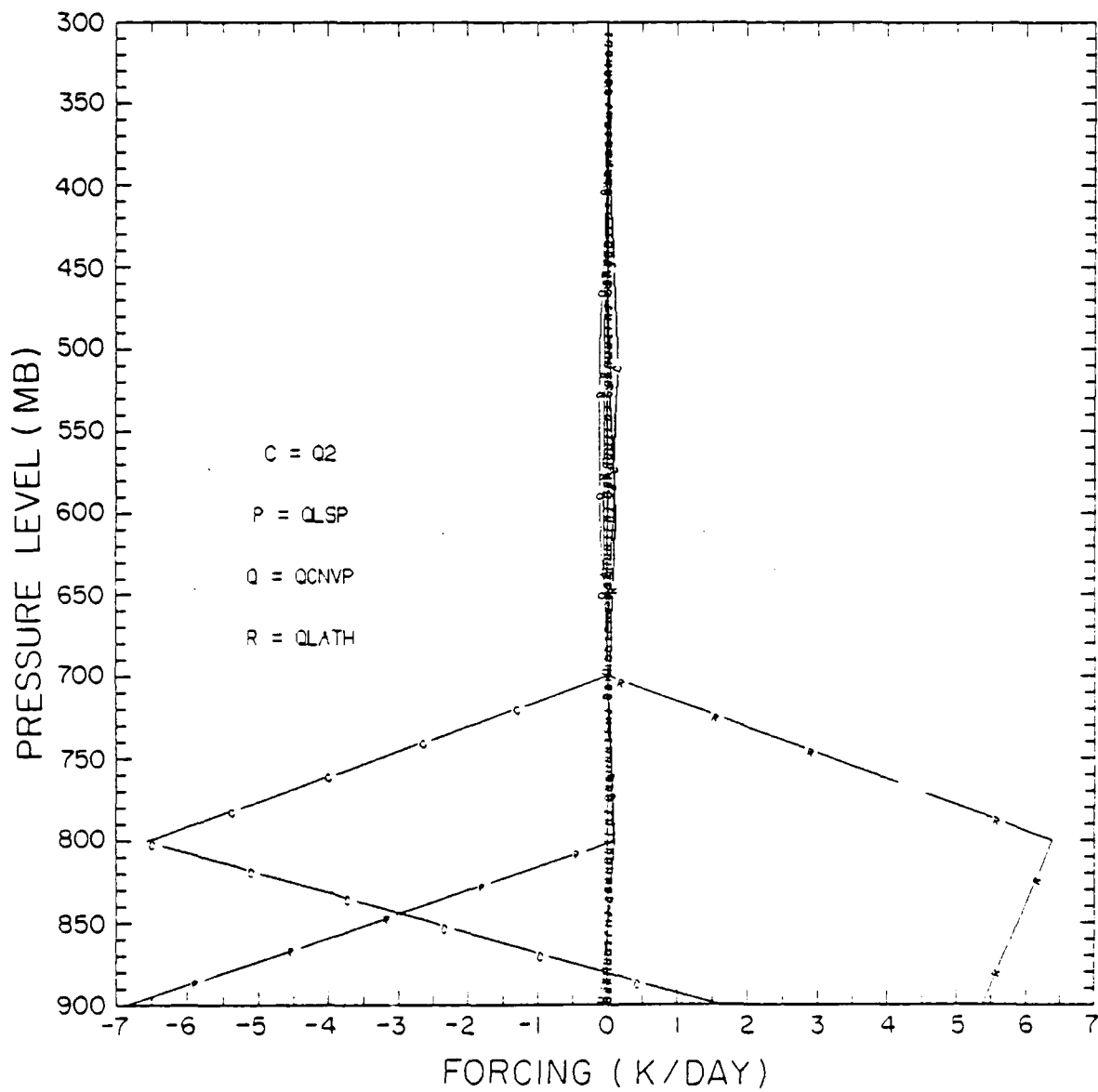


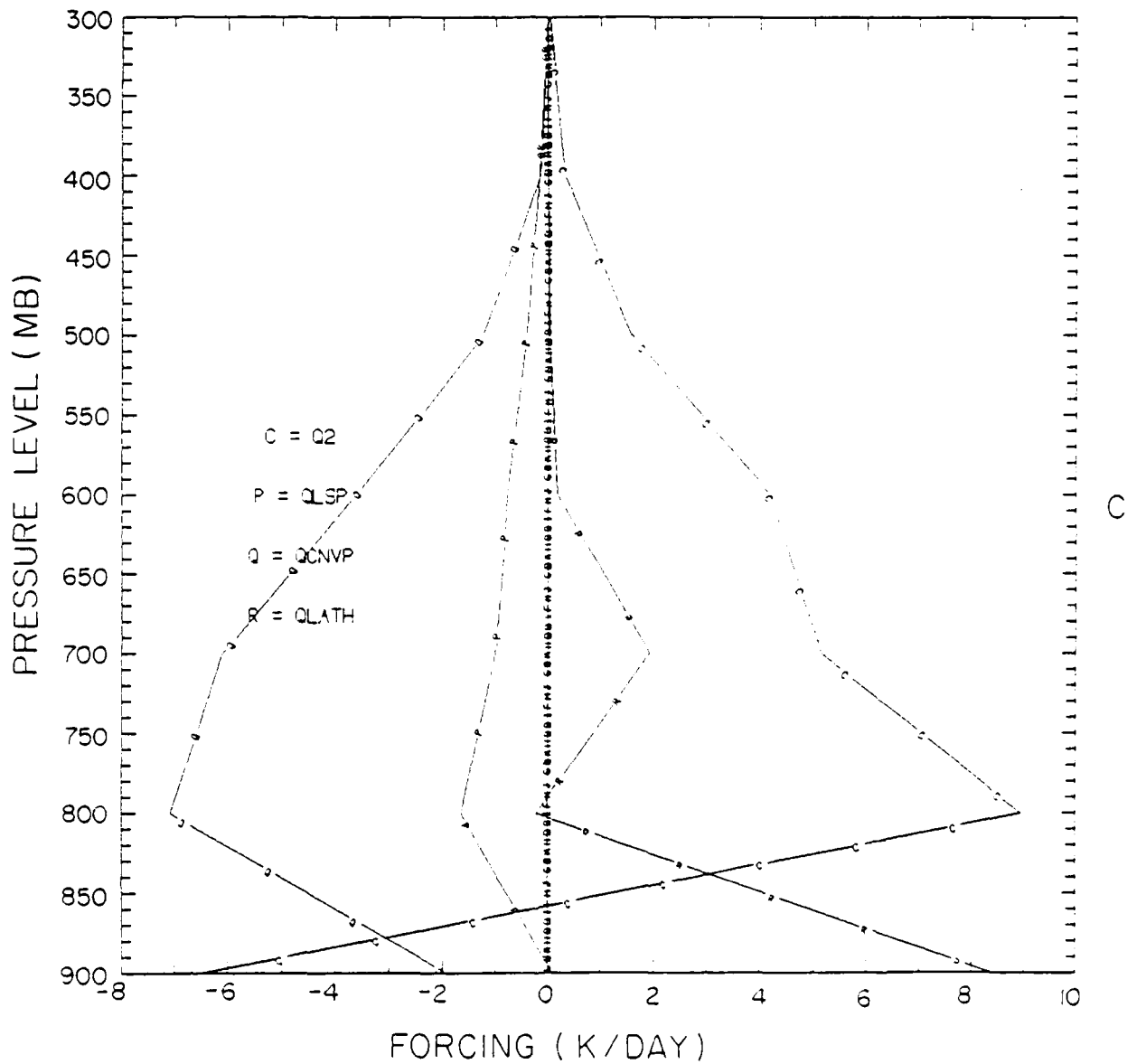
Figure 7.16a, b, and c The apparent moisture sink as function of pressure level for the moisture initialization experiment at points A, B, and C. (See text for a description of the points.)

## PNT-B CHART LOW/M2



b

PNT-C CHART 10W/M2



### 7.9 Summary

Moisture initialization, as explained in Chapter 4.1, was performed on a FGGE IIIb data set. The three cases examined after 96 hours of model integration were: Typhoon Hope, the monsoon, and the Atlantic ITCZ. In each case, there were differences between the control and the initialized case. These differences produced stronger and better defined tropical systems; a stronger, faster typhoon, a monsoon with greater cloud cover, and a more vigorous ITCZ. The residual free  $Q_1$  and  $Q_2$  budgets were also shown for the Atlantic ITCZ. These budgets clearly show that the moisture initialization procedure increased the temperature forcing of the convective precipitation by twice that of the control experiment. The radiative destabilization forcing of the moisture initialization was an order of magnitude larger than that of the control experiment. The results show that the moisture initialization procedure had a large and beneficial impact on the FSUGSM. This impact is still evident after 120 hours of integration proving that the moisture initialization not only affects the zero hour fields diagnosed from moisture (OLR, clouds, *etc.*), but also affects the medium range forecast of complex meteorological systems on a synoptic scale.

CHAPTER VIII  
SENSITIVITY OF RAINFALL  
TO  
MOISTURE INITIALIZATION

8.1 Introduction

In this set of experiments, the initial moisture fields have been perturbed and the FSUGSM has been modified to conserve global moisture. It is, therefore, of interest to determine how this perturbation affects the precipitation fields. The FSUGSM precipitation currently is a result of the large scale supply of moisture, the nonmeasurable mesoscale (subgrid scale) moisture supply, and a moistening parameter (as discussed in section 2.3.2). The subgrid scale moisture supply and the moistening parameter have been determined from a regression on the vertically-averaged large-scale vertical velocity and the 700 mb relative vorticity of the FGGE IIIb data set (Krishnamurti *et al.*, 1983). Results show that the increase in the skill of cloud forecasts of the moisture initialization experiment cause a decrease in the large scale moisture supply. This also causes a decrease in model precipitation. Two additional methods to diagnose precipitation from OLR are presented. Janowiak and Arkin (1990) have developed a scheme in which polar orbiting OLR data are regressed against rainfall estimates from geostationary satellites. Krishnamurti *et al.* (1983) have

regressed polar orbiting satellite OLR data against raingauge data. Both of these methods are used to compute rainfall from model diagnosed OLR. This rainfall is then compared against rainfall diagnosed from the satellite observed OLR. In both of these methods, the moisture initialization experiment compares more favorably to the satellite observed OLR derived rainfall than the control experiment. In addition, the method of Krishnamurti *et al.* (1983) has been used as a first guess for a Cressman analysis of raingauge data to produce precipitation fields for the same time period. This precipitation analysis shall also be presented.

## 8.2 FSUGSM precipitation

The precipitation of the FSUGSM is a result of the large scale supply of moisture, the mesoscale moisture supply, and a moistening parameter (Krishnamurti *et al.*, 1983):

$$R = I_1 (1 + \eta) (1 - b) \quad (8.1)$$

where:

R = rainfall rate

$I_1$  = large scale supply of moisture

$I_1\eta$  = nonmeasureable mesoscale moisture supply

b = moistening parameter

The large scale supply of moisture is defined as:

$$I_1 = \frac{1}{g} \int_{p_b}^{p_t} \omega \frac{\partial q}{\partial p} dp \quad (8.2)$$

where:

$g$  = gravity

$p_t$  = cloud top pressure

$p_b$  = cloud bottom pressure

$\omega$  = vertical velocity

$q$  = specific humidity

The parameters  $\eta$  and  $b$  are defined as:

$$\eta = [(a_1 + a_2)\zeta + (b_1 + b_2)\bar{\omega} + (c_1 + c_2)] - 1.0 \quad (8.3)$$

$$b = \frac{a_1\zeta + b_1\bar{\omega} + c_1}{(a_1 + a_2)\zeta + (b_1 + b_2)\bar{\omega} + (c_1 + c_2)} \quad (8.4)$$

where:

$\zeta$  = 700 mb relative vorticity

$\bar{\omega}$  = vertically averaged large scale vertical velocity

$a_1 = 0.158 \times 10^5 \text{ s}$

$a_2 = 0.107 \times 10^5 \text{ s}$

$b_1 = 0.304 \times 10^3 \text{ mb}^{-1}\text{s}$

$b_2 = 0.107 \times 10^3 \text{ mb}^{-1}\text{s}$

$c_1 = 0.476$

$c_2 = 0.870$

The coefficients  $a_1$  through  $c_2$  are regression coefficients determined from GATE data

by Krishnamurti *et al.* (1983). Figure 8.1b (the control experiment) and 8.1c (the moisture initialization experiment) are the FSUGSM produced rainfall rates. Inspection of the two charts shows that the control experiment has greater amounts of accumulated tropical precipitation than the moisture initialization experiment. This is an expected result. Equation 8.2 related the large scale supply of moisture to the vertical differential of moisture. The cloud charts of Chapter 5 showed that the control experiment was much drier in the upper levels than the moisture initialization experiment, but with a smaller difference in the lower levels. This causes the vertical differential of moisture, and consequently the large scale supply of moisture, to be smaller in the moisture initialization experiment. Due to this decrease, the total accumulated rainfall also decreases over the tropics. The only area in the tropics with comparable heavy rainfall in the two experiments is Taiwan and the Western Pacific Ocean immediately adjacent to Taiwan. The rainfall in this area is predominantly due to the nonmeasureable mesoscale moisture supply rather than the large scale supply of moisture. Equation 8.3 demonstrates that  $\eta$  is a function of the 700 mb relative vorticity and the vertically averaged large scale vertical velocity. Since this geographical area is that of the lifecycle of Super Typhoon Hope, the vorticity and the vertical velocity are much larger than the rest of the tropics. Thus, the rainfall in this region is comparable in the two experiments, even though the large scale supply of moisture may be smaller.

Verification of the two precipitation fields is impossible to accomplish. At present, there is no definitive synoptic precipitation analysis available. This is due to a number of reasons, primarily that precipitation is a discontinuous field and the necessary observing network would not be practical on a global scale. Nevertheless, there are a few sources available for precipitation estimates. One such source is

Krishnamurti *et al.* (1983). They have provided 24 hour precipitation totals from a mix of raingauge and satellite observations. Satellite OLR observations are used to create a first-guess field of large scale precipitation. A Cressman analysis is then performed using the raingauge data as observations. The resultant analysis is shown in figure 8.1a. This figure is not intended to be an absolute measure of precipitation, but rather it is to be used as a general frame of reference to compare against the two experiments. Earlier, it was noted that the moisture initialization experiment was drier than the control experiment, but neither could be identified as correct. Figure 8.2 is a comparison of selected tropical precipitation areas. Each histogram shows the three tropical fields of figure 8.1: the analysis fields of Krishnamurti *et al.* (1983) as "OBS"; the control experiment as "450W/M2"; and the moisture initialization experiment as "ABV5". Each histogram shows the zero to five day accumulated precipitation in the foreground and the five to ten day accumulated precipitation in the background. Each of the histograms show the control experiment as having the greatest amount of rainfall, with the exception of the tropical East Atlantic Ocean. (An examination of the clouds in this area shows a lack of high clouds in the moisture initialization experiment, which causes the large scale supply of moisture to be larger in this area.) Using the analysis in figure 8.1a and the histograms of figure 8.2, it is clear that the control experiment presents a better overall tropical precipitation field due to the fact that the corrected cloud fields have caused a decrease in the large scale supply of moisture. This shows that under the present definition of clouds and precipitation, both cannot be simultaneously forecast correctly. Either the cloud forecast will suffer at the expense of the precipitation forecast, or the precipitation forecast will suffer at the expense cloud forecast. The next section demonstrates two additional methods to forecast the precipitation from the model forecast of OLR.

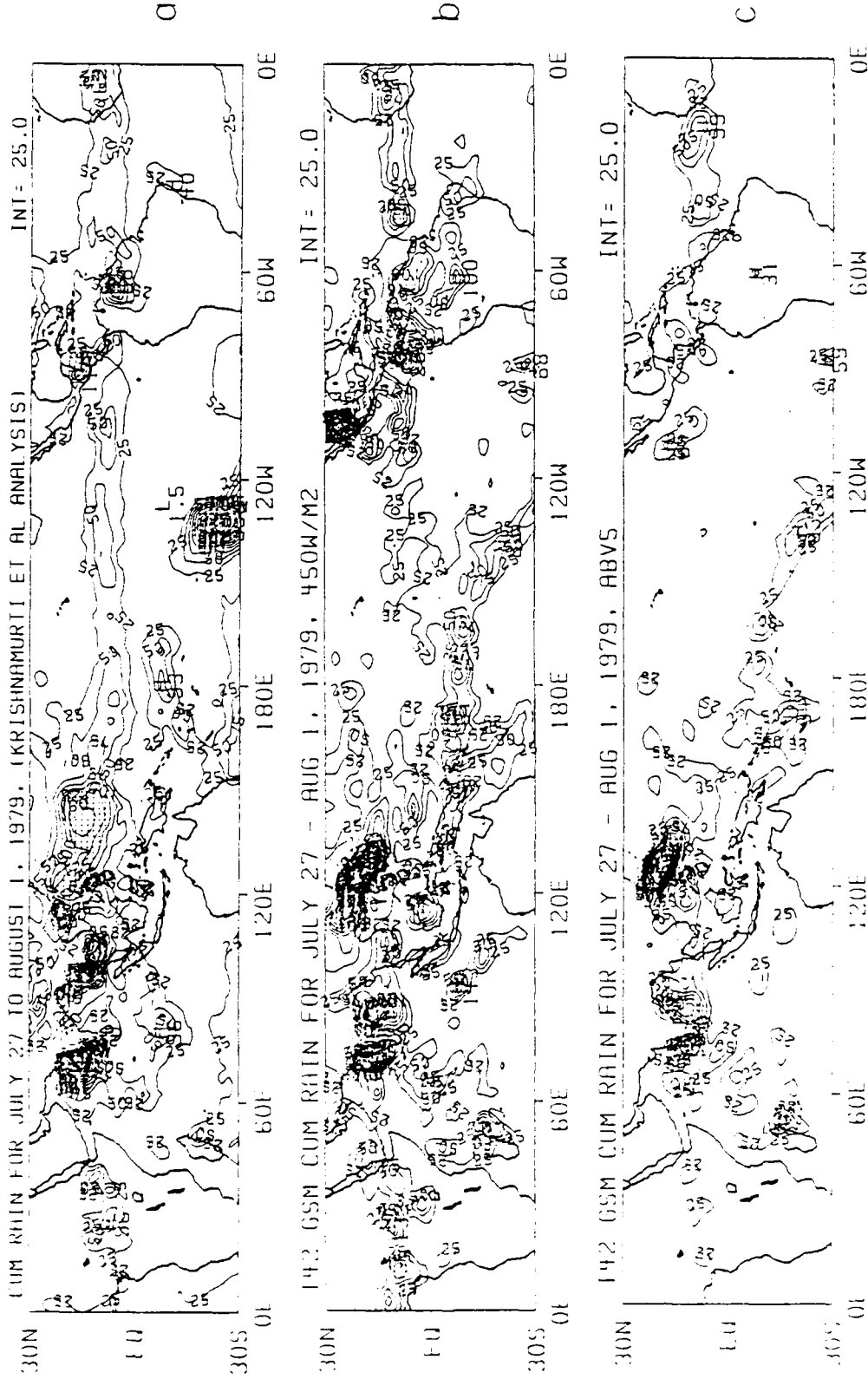


Figure 8.1 a, b, and c Cumulative tropical rainfall for the period July 27, 1979 through August 1, 1979. Chart a is from the analysis of Krishnamurti *et al.* (1983), chart b is from the FSUGSM control experiment, and chart c is from the FSUGSM moisture initialization experiment.

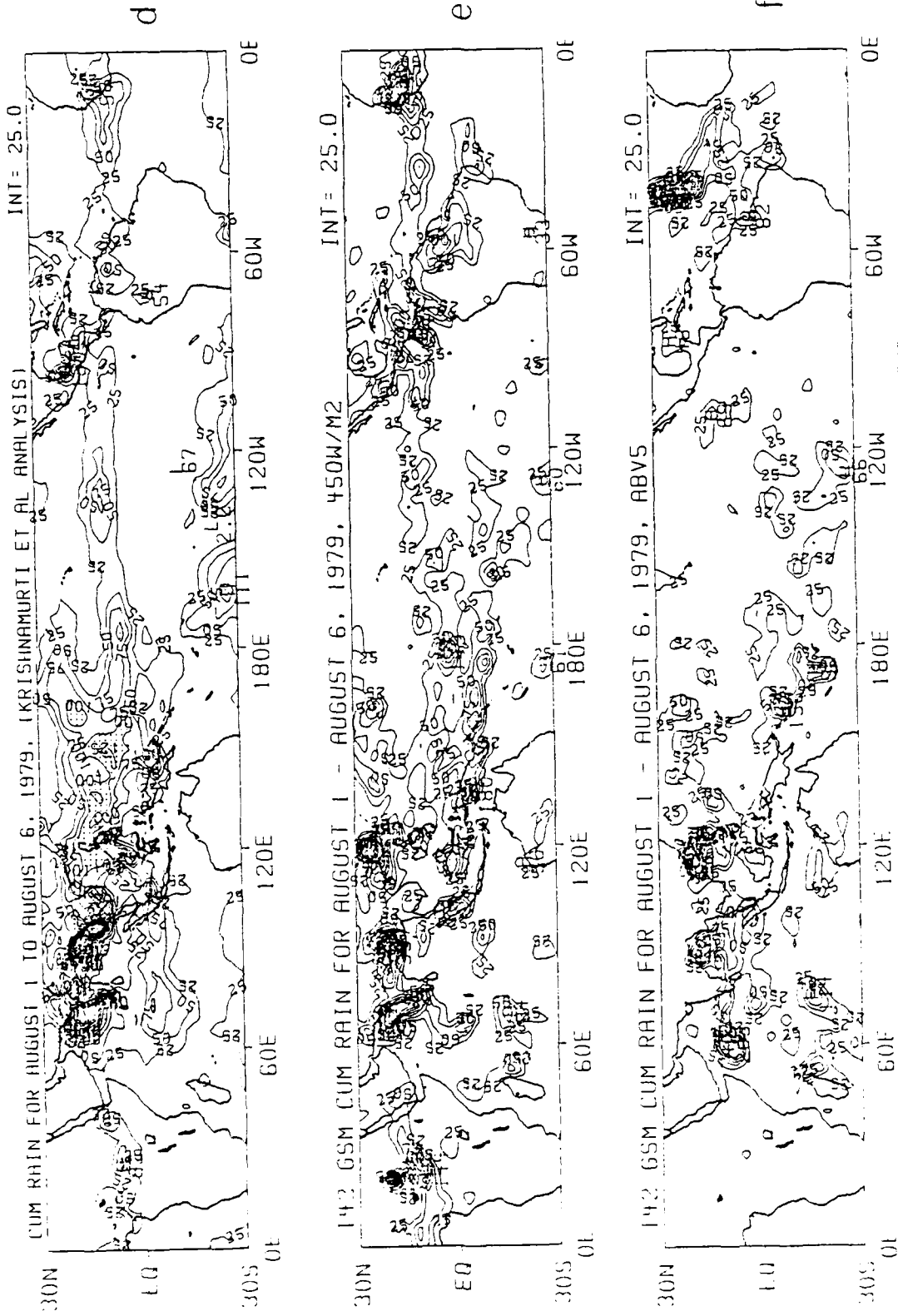
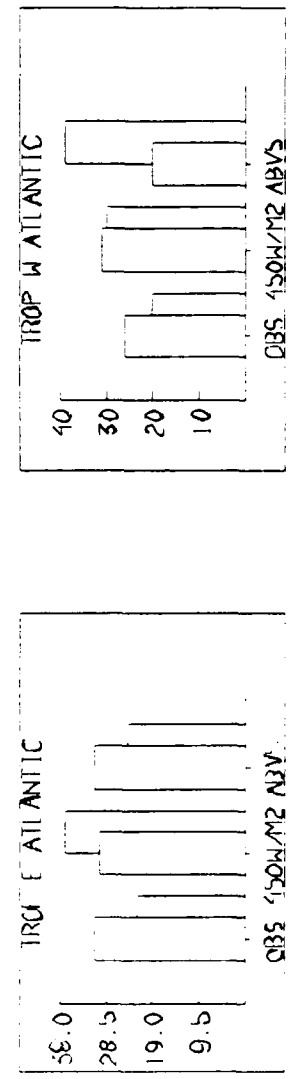
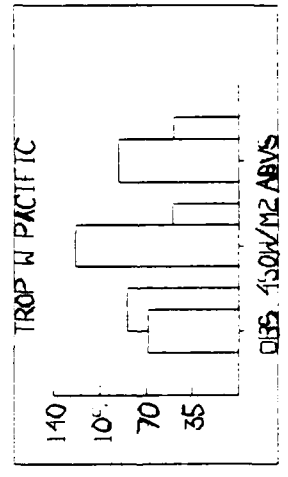
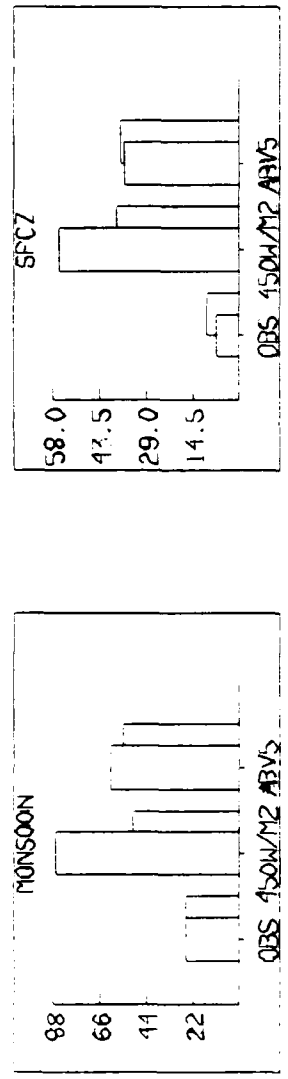


Figure 8.1 d, e, and f Cumulative tropical rainfall for the period August 1, 1979 through August 6, 1979. Chart a is from the analysis of Krishnamurti *et al.* (1983), chart b is from the FSUGSM control experiment, and chart c is from the FSUGSM moisture initialization experiment.



MONSOON RAINFALL COMPARISONS IN MM  
 Figure 8.2 Histogram of average cumulative rainfall for selected tropical areas. The foreground is the accumulated rainfall from July 27, 1979 through August 1, 1979. The background is the accumulated rainfall from August 1, 1979 through August 6, 1979.

### 8.3 FSUGSM OLR precipitation

The FSUGSM currently forecasts precipitation through parameterization of physical processes. Two additional methods can diagnose precipitation through regression equations, using OLR as the basic predictor. The first method was developed by Janowiak and Arkin (1990) for the Global Precipitation Climatology Project, which was part of the World Climate Research Programme. This method was not meant to provide a definitive precipitation analysis, but only a precipitation estimate of the large scale. It was based on the earlier work of Richards and Arkin (1981), who developed a linear regression relating GATE observed rainfall to the fractional coverage of cold clouds. The cold cloud amount was determined by the number of pixels in a 2.5° latitude/longitude area. Janowiak and Arkin (1990) have related the rainfall estimates from the geostationary method to the mean OLR flux of polar orbiting satellites. The resulting regression equation is:

$$R = \frac{(OLR - 255.15)}{-0.684} ; OLR < 255.15 \text{ Wm}^{-2} \quad (8.5)$$

$$R = 0.0; OLR \geq 255.15 \text{ Wm}^{-2} \quad (8.6)$$

where:

R = five day accumulated rainfall

OLR = average OLR flux

Janowiak and Arkin (1990) found that the geostationary satellite regression method and the polar orbiting satellite regression method were highly correlated. Eliminating the cases when both methods estimated zero precipitation, the mean correlation coefficient

is 0.885. They also found that in 92 % of the 15,893 gridpoints, the difference between the two methods was less than 25 mm for the five day accumulation. Figure 8.3a is the tropical precipitation estimate from the satellite observed OLR. It is immediately obvious that this estimate is very low in some areas, such as the Atlantic and Pacific ITCZ's. However, the purpose of using this method is not to evaluate its exactness, but to use it as a comparison for the precipitation estimates of the model diagnosed OLR. Figures 8.3b and 8.3c are the precipitation estimates based on the model diagnosed OLR of the control and moisture initialization experiments. The control experiment, which had a poor OLR verification, also shows a poor precipitation field. This is due to the generally warmer OLR of the control, caused by a lack of proper cloud distribution. The moisture initialization experiment, which had a better OLR verification, shows a more realistic precipitation field. This is due to a more proper distribution of clouds in the tropics. Figure 8.4 shows histograms of selected areas of the precipitation fields using the Janowiak and Arkin (1990) method. The histograms also show that the control experiment lacks precipitation throughout the tropics, while the moisture initialization experiment does not. This method shows that the diagnosed precipitation fields of the moisture initialization experiment are clearly better than the control experiment's diagnosed precipitation fields.

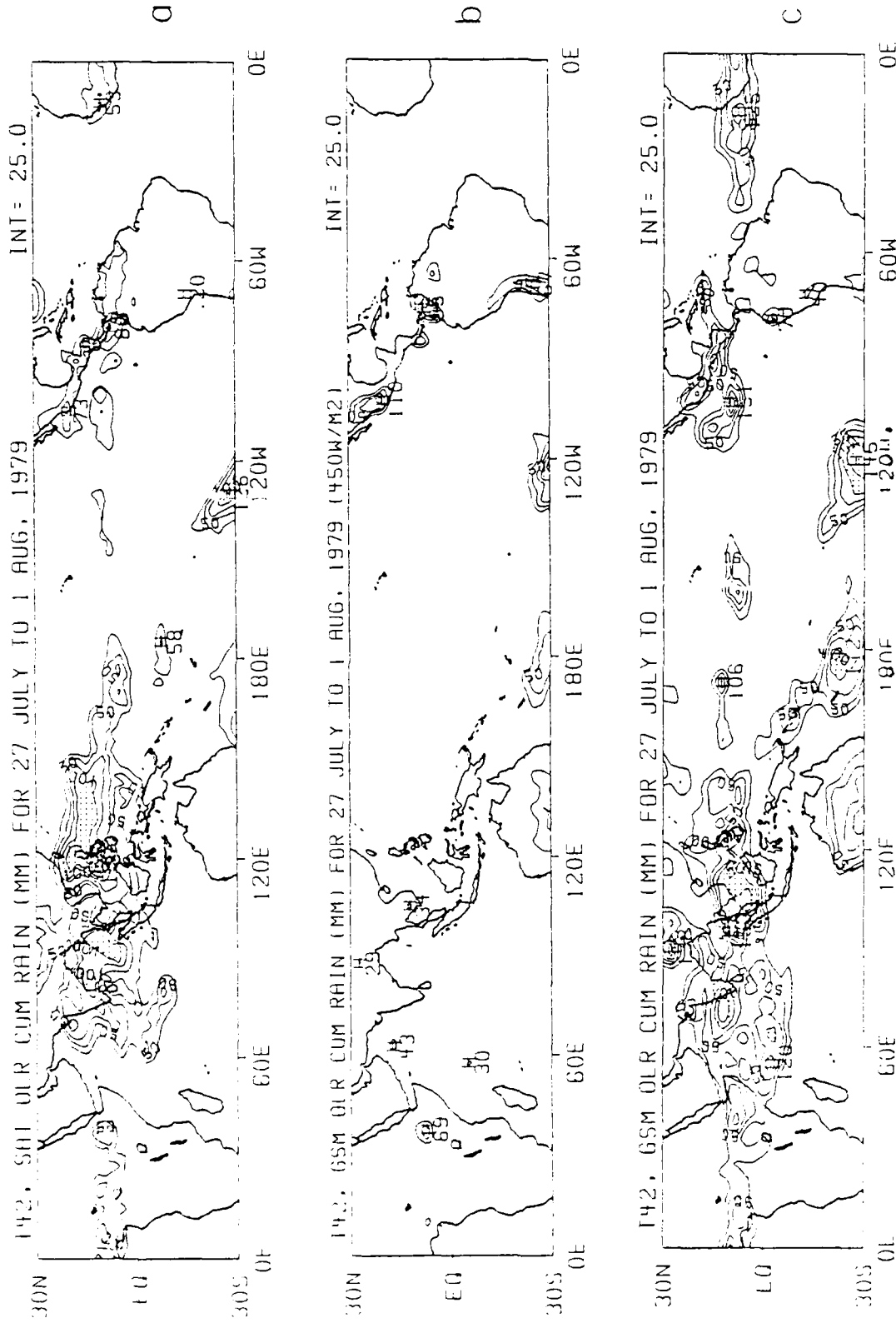


Figure 8.3 a, b, and c Cumulative tropical rainfall for the period July 27, 1979 through August 1, 1979 computed from the method of Janowiak and Arkin (1990). Chart a uses the satellite observed OLR, chart b uses the OLR of the FSUGSM control experiment, and chart c uses the OLR of the FSUGSM moisture initialization experiment.

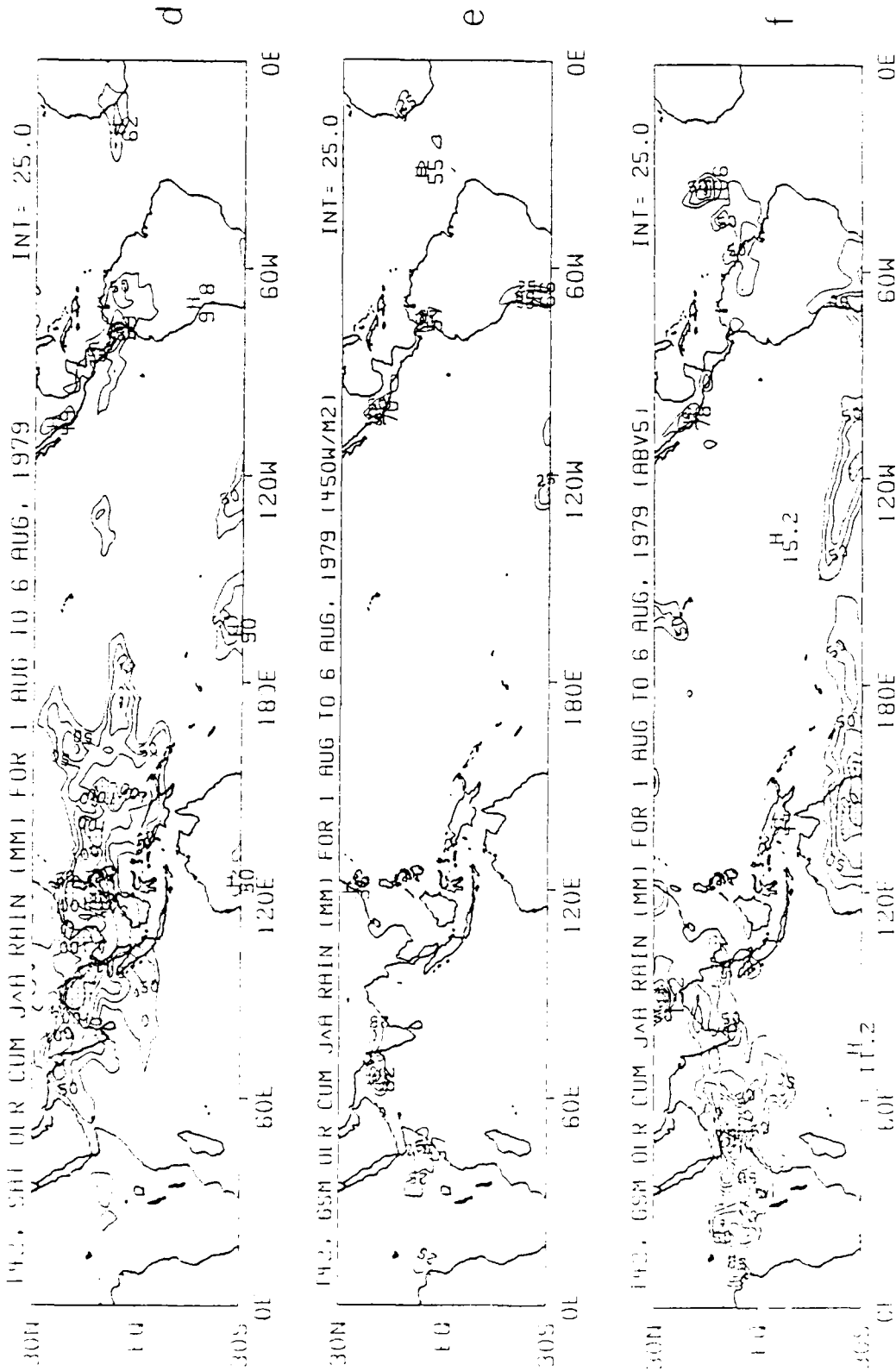
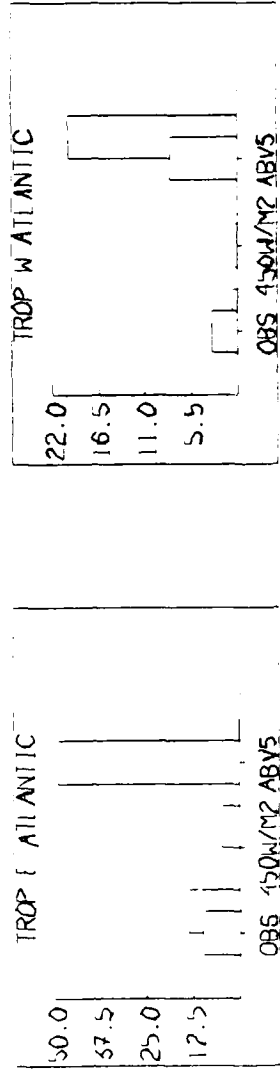
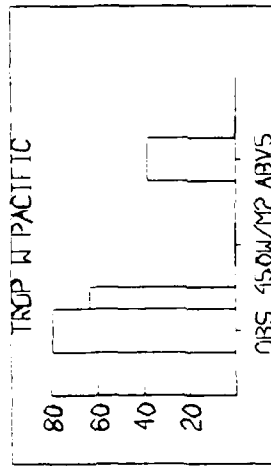
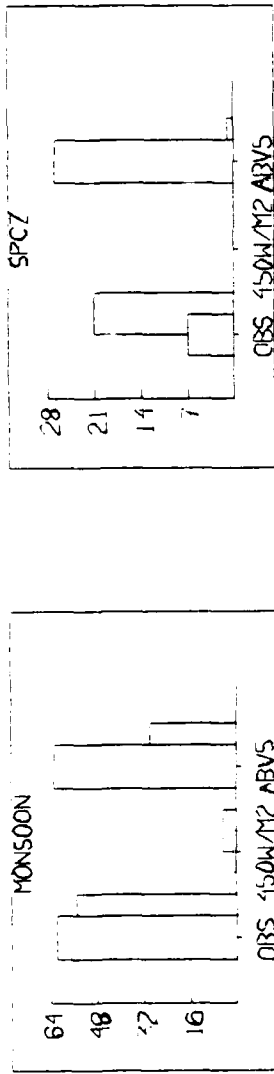


Figure 8.3 d, e, and f Cumulative tropical rainfall for the period August 1, 1979 through August 6, 1979 computed from the method of Janowiak and Arkin (1990). Chart a uses the satellite observed OLR, chart b uses the OLR of the FSUGSM control experiment, and chart c uses the OLR of the FSUGSM moisture initialization experiment.



J&A MILLION RAINFALL COMPARISONS IN MM

Figure 8.4 Histogram of average cumulative rainfall for selected tropical areas. The foreground is the accumulated rainfall from July 27, 1979 through August 1, 1979. The background is the accumulated rainfall from August 1, 1979 through August 6, 1979.

Another method of diagnosing precipitation from polar orbiting satellite OLR was developed by Krishnamurti *et al.* (1983), who related satellite OLR directly to raingauge observations. Over 275,000 observations from the FGGE IIc data base were used to create the regression coefficients. The regression equation is:

$$R = a*OLR + b*\frac{\partial OLR}{\partial t} + c \quad (8.7)$$

where:

R = daily accumulated rainfall

OLR = average OLR

t = time

a = - 0.1838

b = - 1.1955

c = 53.91

The five day precipitation estimate using satellite observed OLR is shown in figure 8.5a. It distinctly shows the precipitation areas associated with the Atlantic and Pacific ITCZ's and the monsoon over India. Similar to the Janowiak and Arkin (1990) method, the control experiment yields a poor precipitation field. The moisture initialization experiment yields a precipitation field that is very realistic. The histograms of figure 8.6 show that there is a strong ITCZ in the Pacific and the Atlantic Oceans, that the monsoon is very evident over India, and that there is a strong South Pacific Convergence Zone.

Both methods presented in this section are not considered to be exact precipitation analyses, but estimates. They show conclusively that the precipitation

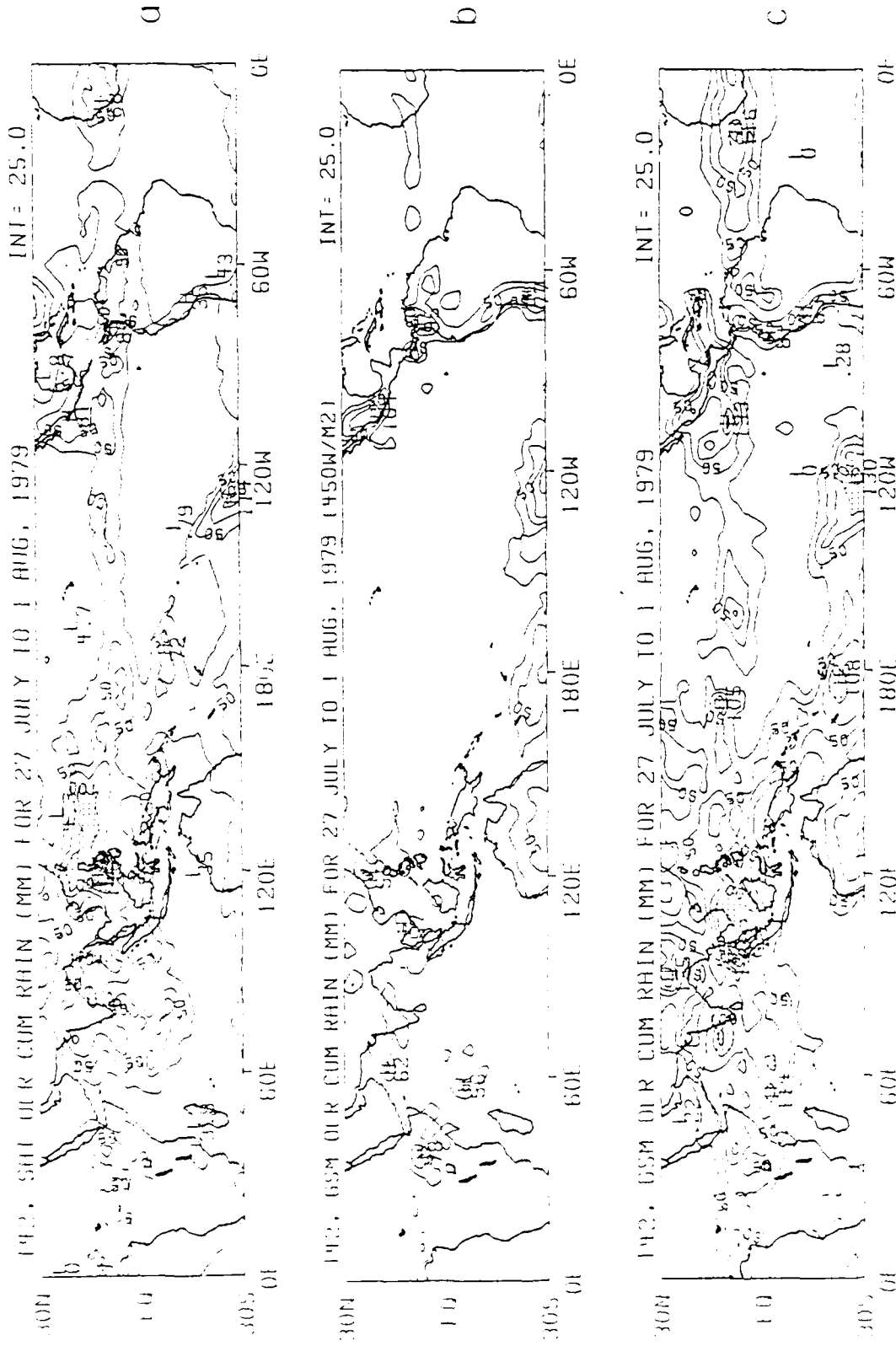


Figure 8.5 a, b, and c Cumulative tropical rainfall for the period July 27, 1979 through August 1, 1979 computed from the method of Krishnamurti *et al.* (1983). Chart a uses the satellite observed OLR, chart b uses the OLR of the FSUGSM control experiment, and chart c uses the OLR of the FSUGSM moisture initialization experiment.

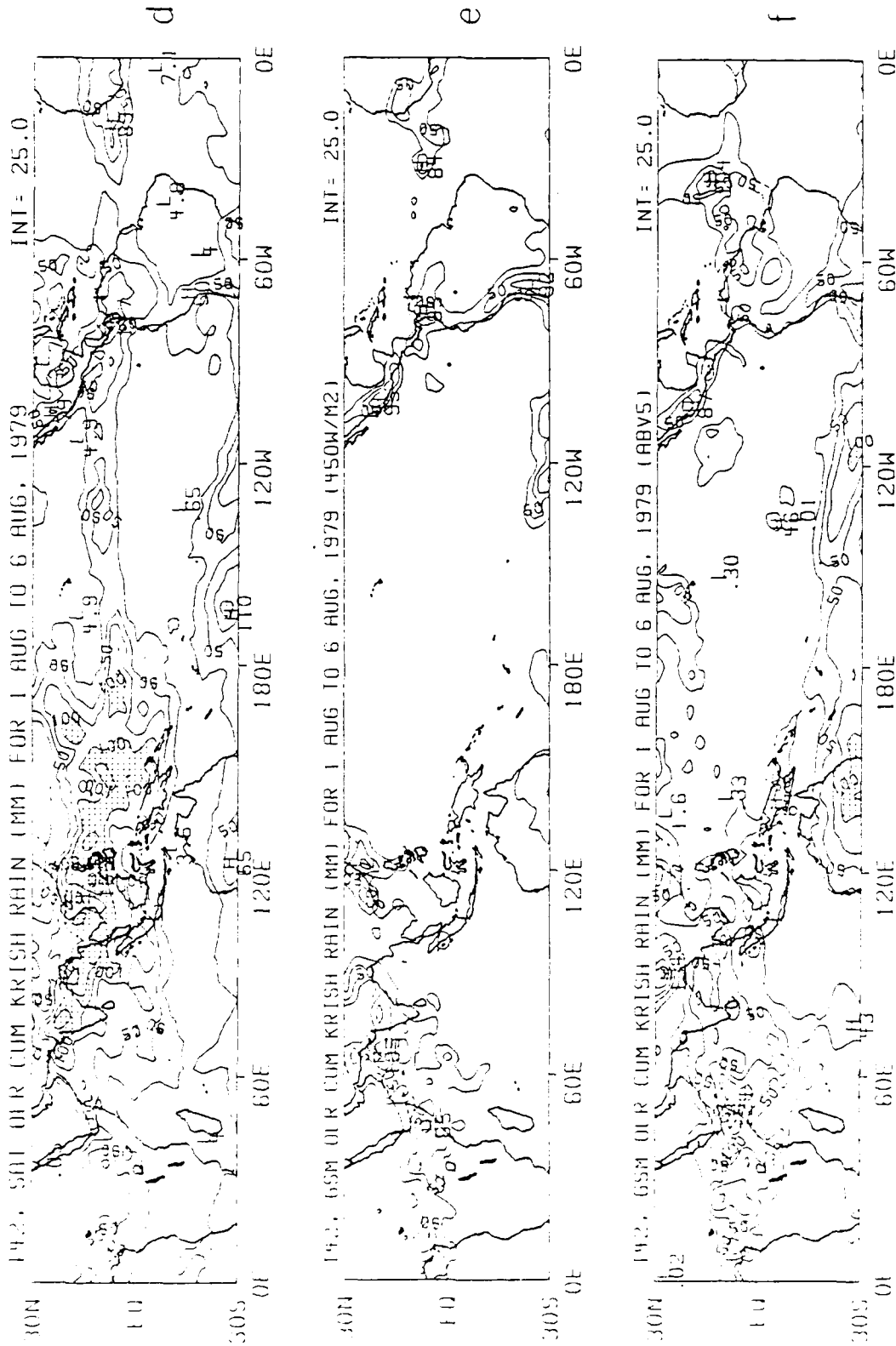
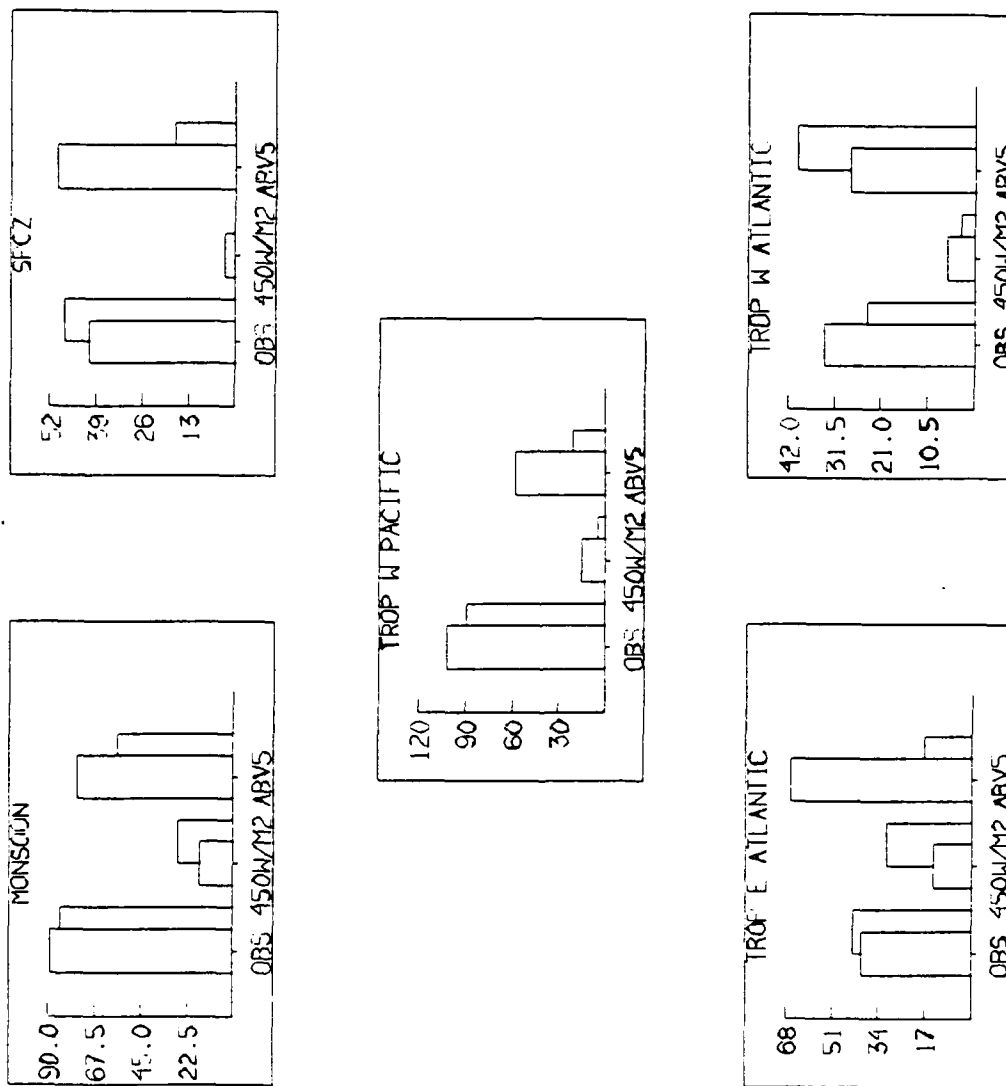


Figure 8.5 d, e, and f Cumulative tropical rainfall for the period August 1, 1979 through August 6, 1979 computed from the method of Krishnamurti *et al.* (1983). Chart a uses the satellite observed OLR, chart b uses the OLR of the FSUGSM control experiment, and chart c uses the OLR of the FSUGSM moisture initialization experiment.



KRISH METHOD RAINFALL COMPARISONS IN MM

Figure 8.6 Histogram of average cumulative rainfall for selected tropical areas. The foreground is the accumulated rainfall from July 27, 1979 through August 1, 1979. The background is the accumulated rainfall from August 1, 1979 through August 6, 1979.

estimates from the moisture initialization experiment are qualitatively better than the control experiment.

#### 8.4 Summary and conclusions

Three methods of calculating the tropical precipitation have been presented in this chapter. The first method was a physical parameterization and is currently part of the FSUGSM. When the moisture initialization experiment was conducted, there was a decrease in the model precipitation. The decrease was attributed to the improved forecast of moisture and clouds in the upper levels, which caused the values of the vertical differential of moisture to decrease. As the physical parameterization process is now formulated, any improvement in the upper level moisture forecast will lead to a decrease in the precipitation forecast (with certain noted exceptions, such as with a super typhoon). Two additional methods of diagnosing precipitation from OLR were also presented. Both of these methods yielded qualitative, rather than quantitative results. They did conclusively show that the moisture initialization experiment has the potential to forecast precipitation much better than the control experiment. This result has a tremendous impact on future precipitation studies of the FSUGSM. Instead of the nonmeasurable mesoscale moisture supply and the moistening parameter being a function of only the 700 mb relative vorticity and the vertically averaged vertical velocity, they should also be a function of OLR as calculated by the model. If this were accomplished, then as the moisture and cloud forecasts improved, the precipitation forecast would improve as well.

## CHAPTER IX

### SUMMARY AND CONCLUSIONS

#### 9.1 Summary

The use of satellite observed OLR in a global spectral model is a new concept which can improve the model forecast. Chapter I presented a broad overview of these improvements, many of which involved using climatological averages to determine the strengths and weaknesses of specific model forcings. Slingo and Slingo (1988) used the satellite observed OLR to study the effect of cloud radiative forcing and found that this forcing warmed the upper troposphere by more than 4 K and cooled the lower stratosphere by more than 6 K. Morette (1989) used comparisons of global spectral model produced OLR and satellite observed OLR to evaluate changes to his forecast model. He found that the changes produced OLR fields with increased contrast, rather than the smooth fields he was producing. Satellite observed OLR has also been used to make improvements to medium range forecast models. Slingo *et al.* (1988) used satellite observed OLR to make improvements to their shallow convection schemes and revised the formulation of subgrid scale turbulent exchanges by recognizing weak areas in their radiation budget while examining satellite observed OLR. Puri and Miller (1990) have used satellite observed OLR in the specification of the convective heating for the diabatic initialization routines of their global spectral model. They deduced

heating rates from satellite observed OLR data and then used these heating rates in the diabatic normal modes initialization to derive an initialized divergence field. They also modified the moisture fields so that the heating rates would be consistent with those used in the initialization. The research of this dissertation uses satellite observed OLR as a new method of initialization. In this procedure, the clouds and radiation of the FSUGSM are initialized through the interpretation of satellite observed OLR. This research shows that the new initialization procedure dramatically improves the FSUGSM cloud and radiation forecasts. This is in agreement with the generalized findings of Arpe *et al.* (1985), who found that the quality of a forecast was dependent on only two factors: the analysis and the forecast model. The analysis is the primary source of error for time scales less than two days and time scales greater than five days. This initialization procedure improves the moisture fields to the extent that the initialization experiment's five day forecast has approximately the same OLR verification score as the initial OLR of the control experiment.

Three methods for the initialization of clouds and radiation were attempted. The first method of initialization attempted was a single parameter initialization, using the satellite observed OLR as the only criterion for convergence. Three different methods of root convergence were formulated for this experiment. The first two methods (false position and secant) were found to be unsuitable for the initialization due to the non-linear functions being operated upon. The bisection method, which is based on the Intermediate Value Theorem (Burden and Faires, 1985), did converge to the correct root in a satisfactory manner. Using the bisection method, the moisture profile was repeatedly modified until the diagnosed OLR converged to the value of the satellite observed OLR. This single parameter method, using the bisection method of root convergence, was chosen to continue the initialization experiments. Both of the

methods not chosen for the initialization scheme were six parameter methods. The six parameters used for the convergence criteria were the five cloud layers of the ISCCP data and the satellite observed OLR. In the first six parameter method, a gaussian distribution of random deviations for the moisture profile was calculated. These deviations were operated upon a specified number of times, and the iteration with the smallest convergence error was considered to be the initialized value. However, this method required greater than two orders of magnitude more computation time than the other methods and was therefore eliminated from use. The second six parameter method used the bisection method, operating solely on moisture, to determine the convergence of the five ISCCP cloud layers and the satellite observed OLR. When this method of initialization was attempted, the cloud analysis in the 600 to 800 mb layer of the initialization experiment had a lower verification than the control experiment, while all other layers had no significant differences. The forecast, using this initialization procedure, had the same verification at all levels, except the 600 to 800 mb layer, where the control experiment verified lower. The fact that the analysis had a lower verification than the forecast is attributed to several factors, primarily the inability to successfully translate the ISCCP cloud data to that inferred by a global spectral model (Krishnamurti *et al.*, 1988). Because of the inconsequential effect at four of the five cloud layers, and the unpredictable nature of the 600 to 800 mb layer, this method was not selected to continue the experiment.

In Chapter V, it was shown that the single parameter initialization of clouds and radiation lead to a dramatic improvement in the OLR and cloud forecasts. The verification of the zero hour forecast was near 100 % for the initialization experiment, while the control experiment verified at only 60 %. The initialization experiment initially had a rapid decrease in the verification score, down to 65 % in the first 24

hours of integration, but then remained constant for the remainder of the forecast. The control experiment exhibited a continuous drop in verification throughout the forecast. By the fifth day, the verification had dropped to 27 %, less than half of the initialization experiment's score. The improvement in the initialization experiment's OLR forecast was so great that its five day forecast of OLR verified approximately the same as the zero hour forecast of the control experiment (see figure 5.1). The effect of the initialization procedure on the cloud forecast is just as dramatic as it was on the radiation forecasts. Figures 5.5 through 5.10 depict the tropical distribution of clouds for the initialization experiment. There is an unrealistic lack of clouds in the high clouds of the control experiment. In sharp contrast, the initialization experiment begins with high cloud signatures obviously indicative of the monsoon, the ITCZ, and the African rainbelts. Even after five days of integration the initialization experiment still shows these synoptic features. The middle cloud charts show the same situation. The control experiment is basically dry and featureless. At the end of the five day forecast, there is little moisture left to discern any synoptic feature. Once again the initialization experiment is in sharp contrast to the control experiment. The synoptic features are clearly delineated by the cloud signatures initially, and remain obvious at the end of the five day forecast. The low cloud forecasts of both experiments are similar to each other at the start of the forecast. However, by the fifth forecast day, the low clouds of the control experiment are spotty and cover small areas. Conversely, the five day forecast of the initialization experiment displays broader areas of clouds.

The cloud and radiation initialization impacted other meteorological variables. The initialization procedure increased the atmospheric instabilities of many systems. The moist static stability of a typhoon was examined after 96 hours of integration. It was found that the peripheral areas of minimum equivalent potential temperature had a

greater vertical gradient for the initialized storm than the control storm, showing that the initialized storm was continuing to grow while the control storm was weakening. The monsoon also showed the effects of the initialization on the moist static stability at 96 hours. The initialized monsoon was better organized and allowed more unstable air to reach it. The tendency of the moist static stability was also sensitive to the initialization. The control typhoon was almost symmetrical about its eye, while the initialized storm was slightly more negative on the western side, indicating movement in that direction. The initialized monsoon experiment also demonstrated stronger unstable tendencies than the control experiment. In the case of the Atlantic Ocean ITCZ, the control experiment contained mostly positive tendencies, with some slightly negative tendencies. The initialized experiment had strong negative tendencies in its updraft region, indicating a more active ITCZ. The residual free  $Q_1$  and  $Q_2$  budgets were also presented in Chapter VIII for air parcels as they approached the Atlantic ITCZ. The  $Q_1$  budget of the control experiment had a minimum at 800 mb which was not present in the initialized experiment because the convective precipitation forcing was only half as strong in the control experiment. This shows that the effect of the initialization procedure is still apparent after 120 hours of integration.

The precipitation of the FSUGSM was found to be sensitive to the initialization procedure. Unfortunately, there is no definitive precipitation analysis to compare against as absolute truth. Because of this, several precipitation algorithms were examined. The FSUGSM produced precipitation was examined first. The initialized experiment produced much less precipitation than the control experiment. The decrease was shown to be due to the FSUGSM formulation of the large scale moisture supply decreasing as a result of the increase in the high and middle cloud amounts. Two different methods of deriving precipitation from the computed FSUGSM OLR

were also shown (Janowiak and Arkin, 1990 and Krishnamurti *et al.*, 1983). In both of these comparisons, the initialized experiment produced more precipitation than the control experiment, showing that it was feasible to calculate an improved precipitation field from the model OLR using the initialization experiment, but not the control experiment.

## 9.2 Conclusions and suggestions for future study

A new procedure for the initialization of cloud and radiation in the FSUGSM has been presented. This procedure greatly improves the cloud and radiation forecasts. The radiation of the FSUGSM improved to such a great extent that the five day OLR forecast verified approximately the same as the initial OLR of the control experiment and more than a factor of two better than the five day forecast of the control experiment. The cloud forecasts of the control experiment were unrealistically dry, while the initialized experiment provided cloud signatures for many synoptic features of the tropics. These findings show that the initialization procedure definitely improves the cloud and radiation forecasts of the FSUGSM.

To ensure that the impact of the initialization was favorable on other meteorological variables, the equivalent potential temperature profile and moist static stability tendencies of several synoptic features were examined. The effect of the initialization was to strengthen these features through stronger vertical gradients and stronger negative tendencies. The effect on the apparent heat source of the tropical ITCZ also shows strengthening due to an increased forcing of convective precipitation. The precipitation fields were also examined. These fields showed that an increase in middle and high clouds will decrease the large scale moisture supply, and therefore, the precipitation. This conclusion is independent of the method that increases the clouds

(the initialization of cloud and radiation). However, the FSUGSM OLR-produced precipitation was more realistic for the initialized experiment than the control experiment, suggesting that the model-produced OLR be incorporated into the precipitation algorithm.

Several suggestions for follow-on studies to this research may be noted.

1.) The understanding and definition of satellite observed clouds should be revisited. At the current levels of knowledge, there is a great problem translating the ISCCP cloud to those inferred by global spectral models. Teams from Florida State University, the National Meteorological Center (in the United States), and the Japanese Meteorological Agency are currently researching this issue (Krishnamurti *et al.*, 1983), but have not yet reached a solution.

2.) The computer time required for the randomized six parameter initialization method is currently too prohibitive to use. When the next generation of supercomputers is available, this method will be more feasible.

3.) The first twenty-four hours of the forecast produces a rapid decrease in the OLR verification of the initialization experiment (from approximately 100 % to 65 %). The reason for this decay should be researched and corrected. This could enable the cloud and radiation forecasts to verify with higher scores for longer forecast periods.

4.) The current formulation of the FSUGSM precipitation should be redetermined to include the model produced OLR. This could be done by making the mesoscale moisture supply and the moisture parameter dependant on the triad of OLR, 700 mb relative vorticity, and the vertically averaged vertical velocity, instead of just the 700 mb relative vorticity and the vertically integrated vertical velocity.

## REFERENCES:

- Arpe, K., A. Hollingsworth, M. S. Tracton, A. C. Lorenc, S. Uppala, and P. Kallberg, 1985: The response of numerical weather prediction systems to FGGE level IIb data. Part II: Forecast verifications and implications for predictability. *Quart. J. Roy. Met. Soc.*, 111, 67 – 101.
- Bedi, H.S. and T.N. Krishnamurti, 1989: Residue Free Budgets and Maintenance of Tropical Disturbances. 118th Conference on Hurricanes and Tropical Meteorology, American Meteorological Society.
- Bjorheim, K., P. Julian, M. Kanamitsu, P. Kallberg, P. Price, S. Tracton, S. Uppala, 1981: The Global Weather Experiment, *Daily Global Analysis* June 1979 to August 1979. European Centre for Medium Range Weather Forecasts.
- Borger, G. R. and A. D. Vernekar, 1988: Validation of outgoing longwave radiation in a general circulation model. *Mon. Wea. Rev.*, 116, 106 – 119.
- Businger, J.A., J.C. Wyngaard, Y. Izumi, and E.F. Bradley, 1971: Flux–profile relationship in the atmosphere surface layer. *J. Atmos. Sci.*, 28, 181–189.
- Chang, C.B., 1979: On the influence of solar radiation and diurnal variation of surface temperatures on African Disturbances. Rep. No. 79–3. Dept. of Meteorology, Florida State University, Tallahassee, FL 32306, 157 pp.
- Charlock, T. P., K. M. Cattany–Carnes, F. Rose, 1988: Fluctuation statistics of outgoing longwave radiation in a general circulation model and in satellite data. *Mon. Wea. Rev.*, 116, 1540–1554.
- Chou, M. D., 1984: Broadband water vapor transmission functions for atmospheric IR flux computations. *J. Atmos. Sci.*, 41, 1775–1778.
- \_\_\_\_\_, and A. Arking, 1980: Computation of infrared cooling rates in the water vapor bands. *J. Atmos. Sci.*, 37, 855–867.
- \_\_\_\_\_, and A. Arking, 1981: An efficient method for computing the absorption of solar radiation by water vapor. *J. Atmos. Sci.*, 38, 798–807.
- \_\_\_\_\_, and L. Kouvaris, 1981: An Efficient Routine for Infrared Radiative Transfer in a Cloudy Atmosphere. *NASA Tech. Mem.* 83830, Goddard Space Flight Center, Greenbelt Md.
- \_\_\_\_\_, and L. Peng, 1983: A parameterization of the absorption in the 15 mm CO region with application to climate sensitivity studies. *J. Atmos. Sci.*, 40, 2183–2192.

- Daley, R.C., C. Girard, J. Henderson and I. Simmonds, 1976: Short-term forecasting with a multi-level spectral primitive equation model. Part 1: Model formulation. *Atmosphere*, 14, 98-116.
- Eliassen, E. B., B. Machenhauer, and E. Rasmussen, 1970: On a numerical method for integration of the hydrodynamical equations with a spectral representation of the horizontal fields. Institute of Theoretical Meteorology, University of Copenhagen Report No. 2, Haraldsgade 6, DK 2200, Copenhagen, Denmark, 37 pp.
- Harshvardhan and T. G. Corsetti, 1984: Longwave Parameterization for the UCLA/GLAS GCM. *NASA Tech. Mem.* 86072, Goddard Space Flight Center, Greenbelt, Md.
- \_\_\_\_\_, D. Randall, and T. Corsetti, 1986: Cloud and Radiation Experiments with a General Circulation Model. Research Review - 1985, Global Modeling and Simulation Branch, Laboratory for Atmospheres, Goddard Space Flight Center, Greenbelt Md.
- \_\_\_\_\_, R. Davies, D.A. Randall, and T.G. Corsetti, 1987: A Fast radiation parameterization for atmospheric circulation models. *J. Geophys. Res.*, 92, 1009-10016.
- \_\_\_\_\_, D. A. Randall, T. G. Corsetti, and D. A. Dazlich, 1989: Earth radiation budget and cloudiness simulations with a general circulation model. *J. Atmos. Sci.*, 46, 1922 - 1942.
- Hartmann, D.L., V. Ramanathan, A. Berroir, and G.E. Hunt, 1986: Earth radiation budget data and climate research. *Rev. Geophys.*, 24, 439-468.
- Janowiak, J. E., and P. A. Arkin, 1990: Rainfall variations in the tropics during 1986 - 1989, as estimated from observations of cloud-top temperature. *J. Geophys. Res.* in print.
- Koeing, G., K. N. Liou, and M. Griffin, 1987: An investigation of cloud/radiation interactions using three dimensional nephanalysis and Earth Radiation Budget data bases. *J. Geophys. Res.*, 92, 5540-5554.
- Krishnamurti, T.N., S. Low-Nam, and R. Pasch, 1983: Cumulus parameterization and rainfall rates II. *Mon. Wea. Rev.*, 111, 8116-828.
- \_\_\_\_\_, H. S. Bedi, W. Heckley, and K. Ingles, 1988: Reduction of the spinup time for evaporation and precipitation in a global spectral model. *Mon. Wea. Rev.*, 116, 907-920.
- \_\_\_\_\_, H.S. Bedi, K. Ingles, A. Weiner, K. Kuma, K.A. Campana, and M. Kimoto, 1988: Comparison of Cloud Cover from Global Models and ISCCP Data Sets. Fourth Session of the CAS/JSC-WGNE.
- \_\_\_\_\_, S. Cocke, R. Pasch, and S. Low-Nam, 1983: Precipitation estimates from raingauge and satellite observations, summer MONEX. Florida State

Report No. 83-7; Department of Meteorology, Florida State University, Tallahassee, Florida, 323306.

- \_\_\_\_\_, K. S. Yap, and D. K. Oosterhof, 1990: Sensitivity of tropical storm forecast to radiative destabilization. *J. Atmos. Sci.*, In print.
- Louis, J.F., 1979: A parametric model of the vertical eddy fluxes in the atmosphere. *Bound. Layer Meteor.*, 17, 187,202.
- MacVean, M.K., 1983: The effects of horizontal diffusion on baroclinic development in a spectral model. *Quart. J. Roy. Met. Soc.*, 109, 771-789.
- Madden, R. A. and F. E. Robitaille, 1970: A comparison of the equivalent potential temperature and the static energy. *J. Atmos. Sci.*, 27, 327 - 329.
- Manobianco, J., 1988: On the observational and Numerical Aspects of explosive east coast cyclogenesis. Department of Meteorology, Florida State University, Tallahassee, FL 32306, 58 pp.
- Martin, C., R. Platt, and Harshvardhan, 1988: Temperature dependence of cirrus extinction: implications for climate feedback. *J. Geophys. Res.*, 93, 11051-11058.
- Morcrette, J. J. 1989: Impact of changes to the radiation scheme in the ECMWF model. ECMWF Research Department Technical Report Number 64, 13 pp., ECMWF, Reading, U. K.
- Moursund, D.G. and C.S. Duris, 1967: Elementary Theory and Application of Numerical Analysis, McGraw-Hill Book Co., New York, 21 pp.
- Norquist, D.C., 1988: Alternate forms of humidity information in global data assimilation. *Mon. Wea. Rev.*, 116, 452-471.
- Puri, K. and M. J. Miller, 1990: The use of satellite data in the specification of convective heating for diabatic initialization and moisture adjustment in numerical weather prediction models. *Mon. Wea. Rev.*, 118, 67 - 93.
- Ostrowski, A.M., 1966: Solution of Equations and Systems of Equations, Academic Press, New York, 26 pp.
- Paltridge, G.W., 1987: Comparison of Nimbus 7 wide-angle earth budget measurements with the output of four cloud-generating numerical climate models. *J. Geophys. Res.*, 92, 4097-4106.
- Platt, C. M. R., and A. C. Dilley, 1981: Remote sounding of high clouds. IV: observed temperature variations in cirrus optical properties. *J. Atmos. Sci.*, 38, 1069-1082.
- Press, W.H., B.P. Flannery, S.A. Teukolsky, and W.T. Vetterling, 1986: Numerical Recipes - The Art of Scientific Computing, Cambridge University Press, New York, 240 pp.

- Ralston, A., 1965: A First Course in Numerical Analysis, McGraw-Hill Book Co., New York, 323 pp.
- Ramanathan, V., 1987: The Role of Earth Radiation Budget Studies in Climate and General Circulation Research. *J. Geophys. Res.*, 92, 4075-4095.
- Richards, F. and P. A. Arkin, 1988: On the relationship between satellite observed cloud cover and precipitation. *Mon. Wea. Rev.*, 5, 1081 - 1093.
- Robert, A. J., J. Henderson, and C. Turnbull, 1972: An implicit time integration scheme for baroclinic models of the atmosphere. *Mon. Wea. Rev.*, 100, 329-335.
- Roberts, R. E., J. E. A. Selby, L. M. Biberman, 1976: Infrared continuum absorption by atmospheric water vapor in the 8 - 12 mm window. *Appl. Opt.*, 15, 2085 - 2090.
- Rodgers, C. D., 1968: Some extensions and applications of the new random model for molecular band transmission. *Quart. J. Roy. Meteor. Soc.*, 94, 99-102.
- Rossow, W.B., L.C. Garder, P.J. Lu, and A. Walker, 1988: International Satellite Cloud Climatology Project (ISCCP) - documentation of data., August 1988, World Meteorological Organization, Geneva.
- Saito, K. and A. Baba, 1988: A statistical relation between the relative humidity and the GMS observed cloud amount. *J. Met. Soc. Jap.*, 66, 187-192.
- Slingo, A., and J. M. Slingo, 1988: The response of a general circulation model to cloud longwave radiative forcing. I: introduction and initial experiments. *Q. J. Meteorol. Soc.*, 114, 1027-1062.
- Slingo, A., R. C. Wilderspin, and R. N. B. Smith, 1988: The Effect of Improved Physical Parameterizations on Simulations of Cloudiness and the Earth's Radiation Budget. Dynamical Climatology Technical Note 65, Meteorological Office, Bracknell.
- Tiedtke, M., 1984: The sensitivity of the time-mean large-scale flow to cumulus convection in the ECMWF model. Workshop on the convection in large-scale numerical models. ECMWF, 28 Nov. - 1 Dec. 1983, 297 - 316.
- Teitz., N. W., ed, 1976: Fundamentals of Clinical Chemistry. W. B. Saunders Company, 64-77.
- Yanai, M., S. Esbensen, and J. Chu., 1973: Determination of bulk properties of tropical cloud clusters from large-scale heat and moisture budgets. *J. Atmos. Sci.*, 30, 611 - 627.

## BIOGRAPHICAL SKETCH

Allan M. Weiner was born November 23, 1955 in Columbia, South Carolina. He is currently serving as a Major in the United States Air Force. He received his Bachelor's in biochemistry from Canisius College in 1976, and Master's in Atmospheric Science from Creighton University in 1982. His meteorology experience includes 2 years as the Officer in Charge of the Global Clouds and Icing Section at the Air Force Global Weather Central, 3 years as the Officer in Charge of the Maintenance Unit for the Numerical Models Section of the Air Force Global Weather Central, and 2 years as the Meteorological Satellite Weather Officer at Lajes Field, Azores, Portugal.